Mestrado em Engenharia Eletrotécnica

LLC Resonant Charger with Variable Inductor Control

Trabalho de Projeto apresentado para a obtenção do grau de Mestre em Engenharia Eletrotécnica – Área de Especialização em Automação e Comunicações em Sistemas Industriais

Autor

Válter de Sousa Costa

Orientador

Professora Doutora Marina Mendes Sargento Domingues Perdigão

Departamento de Engenharia Eletrotécnica – Instituto Superior de Engenharia de Coimbra – Instituto Politécnico de Coimbra (DEE-ISEC-IPC); Instituto de Telecomunicações – Coimbra (IT-Coimbra)

Co-Orientador

Professor Doutor André Manuel dos Santos Mendes

Departamento de Engenharia Eletrotécnica e de Computadores – Universidade de Coimbra (DEEC-FCTUC); Instituto de Telecomunicações – Coimbra (IT-Coimbra)

Coimbra, março, 2017

ACKNOWLEDGMENTS

With the conclusion of this work I would like to thank, firstly to Professor Marina Perdigão (*Departamento de Engenharia Eletrotécnica – Instituto Superior de Engenharia de Coimbra – Instituto Politécnico de Coimbra*, DEE-ISEC-IPC and *Instituto de Telecomunicações* – Coimbra, IT-Coimbra) and Professor André Mendes (IT-Coimbra and, *Departamento de Engenharia Eletrotécnica e de Computadores – Universidade de Coimbra*, DEEC-UC) for guiding me and helping me in order to complete this work.

To ISEC-IPC that received me and, where I took by bachelor degree in Electrotechnical Engineering and where I am now taking the master degree in Electrotechnical Engineering.

To IT-Coimbra for receiving me, allowing me to complete this work in the *Laboratório de Sistemas Energéticos*, and for the financial support that allowed building the experimental prototype.

To all of the professors in general that in the last few years have been helping me improve myself and gain knowledge in this field.

To all my colleagues from the *Laboratório de Sistemas Energéticos*, for their help and cooperation.

To all my family and friends for the cooperation, comprehension and moral support in the most trouble days.

Thank you: *Válter de Sousa Costa*

ABSTRACT

The present work pretends to study the operation and behavior of the LLC resonant converter topology considering a battery charging application, using the traditional switching frequency control and a new control variable, the variable inductance, provided by a current controlled device, the Variable Inductor (VI).

During this work, a brief state of the art regarding general types of power converters and resonant power converters is presented. The LLC resonant converter topology and its advantages and disadvantages are described. The VI principle of operation and structure is presented and discussed and, in the end some information about batteries and its behavior under charging and discharging conditions is presented. The considered batteries characteristics for the studied battery charger are shown and the adopted charging profile is presented.

In the following chapters, a theoretical analysis of the LLC resonant converter operation and behavior under switching frequency or VI control is performed and presented. A design methodology is proposed for the converter considering both switching frequency and VI control, separately or simultaneously. Simulations of the converter operation under open-loop condition were made, and simulation results were obtained and discussed.

A prototype was built and test results were obtained. The prototype uses a SiC MOSFET (Silicon Carbide Metal Oxide-Semiconductor Field Effect Transistor) based inverter working at 100 kHz controlled with fiber optic drivers. To build the prototype, Printed Circuit Boards (PCB) were designed, manufactured and built. An high-frequency transformer and a VI were also design and built. Finally, theoretical, simulation and experimental results are confronted in order to reach conclusions regarding to the proposed design methodology and the prototype operation. This final analysis allows validating the LLC-VI resonant converter as a good option for a battery charger.

Keywords: LLC Resonant Converter; Variable Inductor; DC-DC Power Converters; Resonant Inverters; Battery Chargers.

RESUMO

O presente trabalho apresenta um estudo sobre o comportamento e operação do conversor ressonante LLC considerando uma aplicação de carregamento de baterias. Esta análise considera o tradicional método de controlo usando a frequência de comutação e, implementando uma nova variável de controlo para este tipo de conversores de potência, a Bobina de Indutância Variável (BIV) – *Variable Inductor* (VI).

Os conversores de potência baseados em topologias ressonantes têm vantagens relativamente aos tradicionais conversores controlados usando técnicas de PWM (*Pulse-Width Modulation*). Algumas das vantagens são: a possibilidade de trabalhar a frequências de comutação mais elevadas, reduzindo assim o tamanho dos conversores; operação em modo ZVS (*Zero Voltage Switching*), reduzindo as perdas por comutação. A topologia utilizada, o conversor ressonante LLC tem vindo a ser estudada nos últimos anos devido a estas vantagens quando comparada a outras topologias ressonantes, como o conversor ressonante série ou o conversor ressonante paralelo.

A Bobina de Indutância Variável é um elemento magnético que permite, de forma controlada, variar o valor da indutância da bobina através da regulação do nível de saturação do núcleo. Este elemento magnético tem tido aplicações variadas no que respeita ao controlo de conversores de eletrónica de potência, nomeadamente em aplicações de energias renováveis, controlo de lâmpadas LED (*Light Emitting Diode*) e, em particular, em conversores ressonantes.

Neste trabalho é apresentado um breve estado da arte sobre os tipos de conversores de potência assim como os tipos de conversores ressonantes, introduzindo a topologia em estudo, o conversor ressonante LLC, bem como as suas vantagens e desvantagens. O princípio de funcionamento e estrutura da BIV são apresentados. Por fim, informação adicional sobre o funcionamento e comportamento das baterias durante os processos de carga e descarga é apresentada e discutida. São ainda apresentadas as características das baterias consideradas para a aplicação em estudo bem como os perfis de carregamento adoptados.

De seguida, a topologia típica do conversor ressonante LLC é descrita, bem como as alterações efectuadas por forma a obter a topologia proposta, o conversor ressonante LLC controlado com BIV. É apresentada a análise teórica do conversor através de expressões matemáticas e de gráficos que permitem compreender o comportamento e funcionamento do

conversor. Por fim, o impacto da frequência de comutação e da BIV no funcionamento do conversor ressonante LLC é analisado.

A análise teórica efectuada permite compreender o funcionamento e comportamento do conversor ressonante LLC quando controlado através da frequência de comutação ou, utilizando o método de controlo proposto, utilizando uma BIV. Uma metodologia de cálculo é proposta, a qual permite dimensionar o conversor para ser controlado usando a frequência de comutação ou a BIV, separadamente ou em simultâneo. Desta análise resultou um ficheiro em *Mathcad* que implementa a metodologia de cálculo proposta, permitindo assim projetar o conversor ressonante LLC para uma determinada aplicação. Os principais parâmetros para projetar o conversor ressonante LLC são: o nível de tensão do barramento DC que alimenta o conversor, a frequência de comutação do inversor de meia-ponte e, os valores de tensão e corrente de saída. Através dos resultados teóricos e de gráficos obtidos, é possível analisar o comportamento e operação do conversor em função das variáveis de controlo (frequência de comutação e BIV) e da carga. Durante a análise teórica considera-se que a carga é uma carga resistiva com valor equivalente que permite emular o comportamento, neste caso, da bateria num determinado ponto de operação específico, equivalente a um estado de carga.

Simulações são então conduzidas utilizando o *software* PSIM (*Power Electronics Simulation Software*), que permite obter formas de onda e medidas de valores de tensão e de corrente em diversos pontos do circuito, que permitem comprovar o seu funcionamento. Os resultados foram obtidos com controlo em malha aberta.

Relativamente aos resultados experimentais, foi inicialmente construído um protótipo a operar a cerca de 10 kHz. Este protótipo inicial integrava um inversor de meia-ponte comercial da SEMIKRON baseado em IGBTs (*Insulated Gate Bipolar Transistor*), estando limitado a uma frequência de comutação máxima de 20 kHz. Este primeiro protótipo foi utilizado apenas para testar e comprovar a resposta do conversor ressonante LLC quando controlado com uma BIV. Durante os testes laboratoriais, os resultados foram obtidos igualmente com controlo em malha aberta. Os resultados deste protótipo não são apresentados neste trabalho mas foram publicados num artigo para a conferência IEEE IECON 2016. Mais tarde, um novo protótipo foi desenvolvido, usando um inversor de meia-ponte baseado em transístores SiC MOSFET (*Silicon Carbide Metal Oxide-Semiconductor Field Effect Transistor*) a comutar a 100 kHz controlados por *drivers* comandados por impulsos por fibra ótica. O *setup* experimental é composto por várias Placas de Circuito Impresso (PCI) – *Printed Circuit Boards* (PCB). As PCBs foram projetadas, construídas e testadas em ambiente laboratorial. Para completar o protótipo, foi ainda necessário projetar e construir: um transformador de alta frequência que

faz parte do circuito ressonante, permitindo o isolamento galvânico entre a entrada e a saída do conversor; e o protótipo de uma BIV, que permite efetuar o controlo do conversor mantendo a frequência de comutação constante. Após montagem do *setup* experimental, foi possível realizar testes experimentais e obter resultados relativamente à operação e comportamento do conversor ressonante LLC.

Resultados teóricos, de simulação e experimentais são confrontados ao longo do trabalho por forma a comprovar a veracidade do método de cálculo proposto, bem como a operação do protótipo do conversor ressonante LLC controlado usando a BIV. Os resultados teóricos e simulados são muito similares o que prova a veracidade da metodologia de projeto proposta. Os objetivos inicialmente previstos foram atingidos no que diz respeito à validação da topologia proposta, com este parâmetro de controlo alternativo, com a finalidade de aplicação em carregadores de baterias. No entanto, visto que o protótipo ainda se encontra em fase de otimização, os testes foram apenas efetuados a um nível de potência mais baixo quando comparado com o valor nominal. Pretende-se como trabalho de continuação, a implementação do controlo em malha fechada, e do teste com o banco de baterias de acordo com as especificações escolhidas. A eficiência obtida nessas condições deverá melhorar no que diz respeito ao registo obtido na fase experimental.

O trabalho foi desenvolvido no Laboratório de Sistemas Energéticos (LSE) do Instituto de Telecomunicações – Coimbra (IT-Coimbra), onde foi possível realizar a análise teórica e de simulação, bem como, proceder ao projeto e construção do protótipo e do *setup* experimental necessário para obtenção dos resultados experimentais. As PCBs projetadas foram fabricadas no Gabinete Técnico de Electrotecnia (GTE) do Instituto Superior de Engenharia de Coimbra (ISEC) – Instituto Politécnico de Coimbra (IPC). As PCBs foram então montadas e testadas no LSE.

A realização deste trabalho permitiu algumas contribuições para o grupo de investigação do IT-Coimbra e não teria sido possível sem o apoio de ambas as instituições envolvidas, o ISEC e o IT.

A realização deste trabalho permitiu ainda a publicação de dois artigos em duas conferências internacionais, um na conferência UPEC 2016 intitulado "*Analysis and Simulation of the LLC Resonant Converter under Different Control Methods*", e outro na conferência IECON 2016, intitulado "*Evaluation of a Variable-Inductor-Controlled LLC Resonant Converter for Battery Charging Applications*". Um terceiro artigo está ainda a ser preparado para submissão a uma revista do IEEE.

Palavras-Chave: Conversor Ressonante LLC; Bobina de Indutância Variável (BIV); Conversor de potência DC-DC; Inversores Ressonantes; Carregadores de Baterias.

INDEX

LIST OF FIGURES

LIST OF TABLES

LIST OF SYMBOLS

A_e	Area of the core cross-section [m^2]
C	Capacitor [F]
C	Battery Capacitance [Ah]
C_o	Output Capacitor [F]
C_r	Resonant Capacitor [F]
d	Duty Cycle [%]
f	Frequency [Hz]
f_p	Resonant frequency associated to L_p and C_r [Hz]
f_s	Switching frequency [Hz]
f_0	Resonant frequency associated to L_r and C_r [Hz]
$i; I$	Current [A]
$I_{bat}; I_{out}$	Battery current [A]
i_{Co}	Output capacitor current [A]
i_D	Current at the output of the full-bridge rectifier diodes [A]
I_{dc}	DC control current [A]
$i_{D14}; i_{D23}$	Series rectifier diodes 1/2 and, 2/3 current [A]
i_{in}	Input current [A]
i_{Lvi}	Variable inductor current [A]
i_{Lm}	Magnetizing inductance current in the transformer [A]
$i_{out}; I_{out}$	Output current [A]
I_{o_float}	Minimum output current value / Float current [A]
i_{pri}	Transformer primary-side current [A]
$i_r; i_p$	Resonant current [A]
i_{sec}	Transformer secondary-side current [A]

$i_{S1}; i_{S2}$	Source current from switches 1 and 2 [A]
k	k parameter – Ratio between L_m and L_{lkp}
l	Length [m]
L	Inductor [H]
L_{lkp}	Transformer primary-side leakage inductance [H]
L_{lks}	Transformer secondary-side leakage inductance [H]
L_m	Magnetizing inductance of the transformer [H]
L_p	Parallel inductor [H]
L_r	Resonant inductor [H]
L_{vi}	Variable inductor inductance [H]
M	Voltage gain
n	Transformer turns ratio
N	Number of turns
P	Power [VA]
P_o	Output Power [VA]
Q	Load quality factor
$\Re$	Magnetic Reluctance
R_{ac}	Rectifier input equivalent resistance [Ω]
$R_{bat}; R_L; R_o$	Battery internal resistance [Ω]
R_{load}	Load resistance [Ω]
S_1 ; S_2	Half-bridge inverter switches 1 and 2
T	Period of time [s]
μ_0	Magnetic Permeability in the Vacuum [H/m]
μ_r	Magnetic Permeability [H/m]
$v; V$	Voltage [V]
$V_{bat}; V_{out}$	Battery Voltage [V]
v_{Co}	Output capacitor voltage [V]

v_{Cr}	Resonant capacitor voltage [V]
$v_{DS1}; v_{DS2}$	Drain-source voltage from switches 1 and 2 [V]
V_F	Rectifier diode voltage drop [V]
$v_{gs1}; v_{gs2}$	Square wave generator to gate-source from switches 1 and 2 [V]
v_{mos1_dsp}	Square wave for switch 1 created by the DSP control board [V]
v_{mos2_dsp}	Square wave for switch 2 created by the DSP control board [V]
v_{pri}	Transformer primary-side voltage [V]
$v_{in}; V_{in}; V_{IN}$	Input voltage [V]
v_{Lvi}	Variable inductor voltage [V]
$v_{out}; V_{out}; V_{OUT}$	Output voltage [V]
v_{sec}	Transformer secondary-side voltage [V]
$\underline{Z}_{in}$	Resonant circuit impedance [Ω]
ΔI_{out}	Output current ripple [A]
$\Delta V_{out}; V_{ripple}$	Output voltage ripple [A]
η	Efficiency [%]
φ	Phase angle between voltage and current [°]
φ_{in}	Phase of the input current [°]
ω	Angular frequency [rad/s]
ω_0	Angular resonant frequency associated to L_r and C_r [rad/s]
ω_p	Angular resonant frequency associated to L_p and C_r [rad/s]

Measure Units from S.I.:

A	**Ampère** – Unit of measure of electric current according to SI
F	**Faraday** – Unit of measure of capacitance according to SI
H	**Henry** – Unit of measure of inductance according to SI
Hz	**Hertz** – Unit of measure of frequency according to SI

rad	**Radian** – Unit of measure of angular degrees according to SI
s	**Second** – Unit of measure of time according to SI
V	**Volt** – Unit of measure of electric voltage according to SI
Ω	**Ohm** – Unit of measure of electric resistance according to SI
%	**Percentage** – Unit of measure of percentage according to SI

LIST OF ACRONYMS

AC	Alternating Current
CCM	Continuous Conduction Mode
CCS	Current Charging Stage
DC	Direct Current
DCM	Discontinuous Conduction Mode
DSP	Digital Signal Processors
EAGLE	Easily Applicable Graphical Layout Editor (Software for PCB design)
ETD	Type of magnetic core structure
EV	Electric Vehicle
ESR	Equivalent Series Resistance
EMC	Electromagnetic Compatibility
EMI	Electromagnetic Interference
FHA	First Harmonic Approximation
GTE	*Gabinete Técnico de Electrotecnia*
HEV	Hybrid Electric Vehicle
IGBT	Insulated Gate Bipolar Transistor
IPC	*Instituto Politécnico de Coimbra*
ISEC	*Instituto Superior de Engenharia de Coimbra*
IT-Coimbra	*Instituto de Telecomunicações* – Coimbra
LED	Light Emitting Diode
Li-Ion	Lithium Ion
LSE	*Laboratório de Sistemas Energéticos*
Ni-Cd	Niquel-Cadmium Battery
Ni-MH	Niquel-Metal Hybride Battery
PCB	Printed Circuit Board

PCI	*Placa de Circuito Impresso*
PFC	Power Factor Correction
PHEV	Plug-In Hybrid Electric Vehicle
PP	Parallel-Parallel
PRC	Parallel Resonant Circuit
PS	Parallel-Series
PSIM	Power Electronics Simulation Software
PWM	Pulse-Width Modulation
RMS	Root Mean Square
RSCC	Resonant Switched Capacitor Converter
SiC MOSFET	Silicon Carbide Metal Oxide-Semiconductor Field Effect Transistor
SOC	State of Charge
SRC	Series Resonant Circuit
SP	Series-Parallel
SS	Series-Series
VCS	Voltage Charging Stage
VI	Variable Inductor
ZCS	Zero Current Switching
ZVS	Zero Voltage Switching

GLOSSARY

Duty Cycle In a period of time, corresponds to the percentage in which the signal is at logic level '1', being at '0' in the rest of the period.

Ripple Is the AC component that adds to the mean value in a DC signal. It appears normally due to the rectifiers in the electronic circuit.

Resonance Tt's a phenomenon that occurs in a electronic circuit that is as capacitive (capacitive reactance, X_C) as inductive (inductive reactance, X_L) in such way that both capacitive and inductive reactance's are equal ($X_C = X_L$) and, in this case the current is not lagging or in advance to the voltage (what would happen normally in electronic circuits with capacitors and inductors). To the power source, at resonance the electronic circuit behaves like a resistive load.

ZVS Zero Voltage Switching is a converter operating mode where a transistor stops conducting when the current crosses through zero and inverts its value becoming to flow through the anti-parallel diode. In this case, the transistor gets out of conduction naturally when the current crosses zero leading to almost no switching losses.

ZCS Zero Current Switching is a converter operating mode where a transistor is turned on the anti-parallel diode is conducting which causes a very small voltage variation leading to almost no switching losses.

LCR Meter Equipment used to measure inductance, capacitance and resistance.

Dead-time Time between the turn-off and turn-on of two switches in one of the arms of a half-bridge or full-bridge inverter, for example, to guarantee that there will not happen short-circuit to the input source.

1. Introduction

The growing demand for transportation vehicles and for a more sustainable world leads to search for less pollutant and more reliable energy sources in order to reduce emissions to the atmosphere, which degrade the ozone layer. Therefore, instead of the typical vehicles with internal combustion engines with fossil based fuels, researchers across the world have been trying to explore new types of vehicles, such as Electric Vehicles (EV), Hybrid Electric Vehicles (HEV), Plug-In Hybrid Electric Vehicles (PHEV) and others. An HEV is a vehicle that has two engines, typically a gasoline powered internal combustion engine and an electric motor that allows reducing the effort of the combustion engine, resulting in a lower fuel consumption and emission reductions [1]. An EV is a vehicle that is entirely powered by electric motors (one or more) [2]. Because HEVs and EVs have electric motors they also require some kind of electricity storage unit, for instance fuel cells, batteries, and others. Existent battery charging systems are based on converters that provide a variable DC output to charge the batteries. In order to have output regulation typically these converters can be controlled using different control variables such as switching frequency, phase-shift, Pulse-With Modulation (PWM), among others. There are very complex battery charging algorithms, which also depend of the battery technology. However, the purpose of this work is to investigate a new converter topology with a new control technique by considering very simple battery charging scheme, based on constant current, Current Charging Stage (CCS), and constant voltage, Voltage Charging Stage (VCS).

Therefore, the main focus will be on the converter selection, design and implementation. The selected converter is an LLC resonant converter. Rather than focusing on the charging technique, the purpose of this work is to study the behaviour of the converter using a different control parameter, a variable inductance – L_{vi} – and its ability to provide a controllable output for charging applications. A current-controlled magnetic device called Variable Inductor (VI) provides this variable inductance L_{vi} that corresponds to the VI inductance value. Typically the operating principle of resonant converters is based on the variation of the switching frequency f_s, and consequently regulate the voltage gain of the converter. In this work, using the VI, the switching frequency of the converter can be kept constant and the variable inductance is used to change the resonant frequency allowing output voltage regulation.

Thus, the main goal of this work will be the study and the design of a LLC resonant converter, comparing the typical switching frequency control and the proposed control technique using a VI. Applied to a battery charger, the purpose of the system to be developed is to control the charging process, ensuring that battery requirements are met. In order to do this, a simple charging profile is considered, where the voltage varies linearly during the charging process in order to simplify the theoretical analysis. Although complex algorithms can be used to charge the batteries, the selected charging profile, thought simple, is sufficient to test the viability and operation of the converter. Therefore this work does not focus on the charging algorithm but only on the converter response.

1.1. Motivation and Main Objectives

Nowadays there are many commercial battery technologies (Lead-Acid, Niquel-Metal Hydride (Ni-MH), Lithium Ion (Li-Ion)) and consequently various types of battery chargers [3],[4]. Converters based on the LLC resonant topology have recently become very popular and have also been selected to implement battery chargers, using the classical topology or with few adjustments to improve its operation and efficiency [5]-[7]. In the LLC resonant converter the voltage gain can be changed by acting either on the switching frequency, on the resonant tank, or both. These two control methods will be further discussed and compared. An LLC-VI based converter will be presented as a viable battery charger. The general diagram of the system is presented in Figure 1.1 and will be briefly discussed.

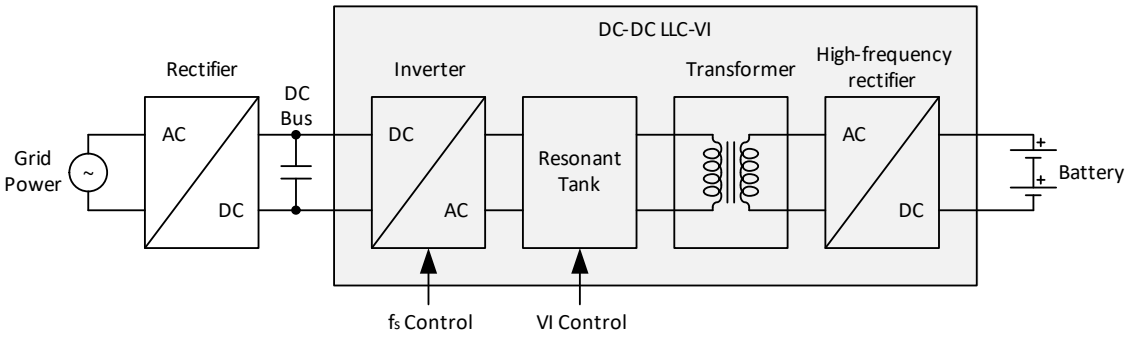

Figure 1.1 – General configuration of the battery charger

The charger is fed by the AC grid. In a first stage a rectifier converts the grid power into DC power creating a DC Bus (a Power Factor Correction (PFC) stage can be implemented in the future to try to improve the converter operation). The DC Bus feeds the DC-DC converter (gray block) to charge the batteries. The DC-DC converter can be divided into four blocks.

- The inverter, which is powered by the DC Bus, feeds the resonant tank. The inverter allows controlling the converter output power by acting on the switching frequency.

- The resonant tank allows resonant operation and, if a VI is introduced, the converter output power can also be controlled using the variable inductance.
- The transformer allows galvanic isolation from the input to the output. The transformer can also be part of the resonant tank.
- A high-frequency rectifier, which rectifies the output voltage of the transformer, feeds the batteries with low ripple voltage and current.

As previously mentioned, researchers across the world have been using the LLC resonant converter for various applications. Nevertheless the LLC-VI converter topology has not yet been studied for battery charging applications. This option is now discussed and its further potential will be investigated. The LLC-VI converter has inherent advantages: lower switching losses, due to resonant operation, constant switching frequency operation with low power losses in the magnetic device.

In a previous work, a different DC-DC resonant converter topology was studied considering VI based control (the DC-DC series-parallel resonant converter class D [8]). During that work, a VI prototype was built and tested. That application allowed selecting the battery output voltage and current levels. However, this topology was abandoned, an LLC resonant converter, which has become a hot topic in the last few years [9], was then selected, studied and analyzed.

The main goal of the present work is to study and develop a design methodology for building an LLC resonant converter for a battery charging application, considering both control techniques: the typical switching frequency control and the VI based control technique. A comprehensive simulation study of the converter operation is performed and a prototype is built and tested. The theoretical, simulation and experimental results are presented and discussed considering the viability of the converter as a battery charger.

The work was developed in the *Laboratório de Sistemas Energéticos* (LSE) from the *Instituto de Telecomunicações* – Coimbra (IT-Coimbra). In the LSE it was possible to develop the theoretical and simulation analysis, to design and build the prototype and perform experimental tests. The designed Printed Circuit Boards (PCB) were manufactured in the *Gabinete Técnico de Electrotecnia* (GTE) from the *Instituto Superior de Engenharia de Coimbra* (ISEC) – *Instituto Politécnico de Coimbra* (IPC). The PCBs were then assembled and tested in the LSE.

The work can be divided in the following steps:

- Firstly, a design methodology is proposed that allows understanding the LLC resonant converter behavior and operation. It will also allow designing the converter for the desired battery charger application considering the typical f_s control and the proposed controlled technique using a VI.
- Secondly, simulation studies will be performed and simulation results will be presented and analyzed. This analysis is made considering both f_s and VI control. Theoretical and simulation results are used to compare both control techniques for the LLC resonant converter. The possibility of using simultaneously both f_s and VI control techniques is also introduced.
- Thirdly, a prototype of the proposed converter will be implemented. The prototype will have a SiC MOSFET (Silicon Carbide Metal Oxide-Semiconductor Field Effect Transistor) half-bridge based inverter, working at 100 kHz, controlled with fiber optic based drivers. The prototype is designed to charge two sets of 8 serially connected lead-acid batteries in parallel with a 96 V nominal voltage that can vary between approximately 84 V and 116 V and that will be charged with a maximum 10 A DC current. The charging operation is controlled through the VI. Experimental results will be confronted with the theoretical and simulation results to reach conclusions regarding the validity of the design methodology and proposed converter topology.

During this work, different software programs were used:

- **PTC Mathcad Prime 3.1** – Software for computing mathematical equations used in the design of the converter and VI. The software also allows designing graphics to understand the behavior and operation of the converter.
- **PSIM version 9** – Software used to perform simulations of the converter and obtain results in the form of graphics and values (mean, rms (Root Mean Square), etc.).
- **Matlab R2012b** – Software used to perform auxiliary calculations for the design.
- **Matlab R2012b / Simulink library and Embedded Coder Support Package for Texas Instruments C2000 Processors Library** – Libraries from Matlab used to perform additional simulations of the converter, and to generate the code to program the DSP (Digital Signal Processors) control board – C2000 Peripheral Explorer Kit with a TMS320F28335 microprocessor from Texas Instruments – using CCS (Code Composer Studio).
- **Code Composer Studio 5.5** – Software used to program the DSP control board.
- **EAGLE 7.5.0 Light Edition** – Software used to draw the PCB schematics, the design of the boards and to generate the files to manufacture the PCBs.

- **LabVIEW 2015** – Software used to design the VI.

1.2. Outline of this Work

This work report is divided in 6 chapters. The overall structure and a brief introduction of each chapter is described as follows:

Chapter 1 - Introduction, gives a brief introduction to the developed work. The motivation and main goals are presented and the overall structure of this document is introduced.

Chapter 2 – State of the Art, presents the general types of power converters, followed by a summarized discussion on resonant power converter topologies. The Variable Inductor (VI) structure and principle of operation are presented. Batteries characteristics and the adopted battery charging profiles are presented.

In **Chapter 3 – LLC-VI Resonant Converter for a Battery Charger**, the LLC resonant converter topology is presented followed by the description of its operating principle, theoretical analysis and operation modes. The design methodology is performed considering the battery charging requirements. Finally the control variables impact on the converter output is presented.

Chapter 4 – Simulation Results, shows the simulation results of the LLC Resonant Converter considering both frequency and VI control methods.

In **Chapter 5 – Prototype and Experimental Results** the experimental results are shown considering the implemented prototype. Experimental results are confronted with simulation and theoretical results.

In **Chapter 6 – Conclusions, Contributions and Future Work**, the conclusions are presented and the main contributions and future work are identified.

The work described in the following chapters can be complemented with information provided in the **Appendix**.

2. State of the Art

In this chapter, general types of power converters are presented followed by classical resonant power converters topologies. The Variable Inductor (VI) structure and principle of operation are described. A brief state of the art describing batteries main characteristics and charging profile is also presented. The chapter ends with a brief description of general battery profiles. This analysis guides the options regarding the adopted charging scheme.

2.1. Types of Power Converters

Power converters are electronic circuits that are used to convert a type of energy (DC or AC) into another type of energy (DC or AC) that can be equal or different from the original with or without isolation from the input to the output. There are four main types of converters [8]:

- **AC-DC converter** or **Rectifier** – Converts an AC input into a DC output. The most common topologies are the half-bridge rectifier, full-bridge rectifier with center-tapped transformer and, full-bridge rectifier.
- **DC-DC converter** or **Chopper** – Converts a DC input into a DC output that can be smaller, equal or higher than the input and can be constant or variable. This converter can also be isolated if a high-frequency transformer is used.
- **DC-AC converter** or **Inverter** – Converts a DC input into an AC output, without a DC bus, that can have a fixed or variable amplitude and frequency. Some examples are half-bridge or full-bridge inverters.
- **AC-AC converter** – Converts an AC input into an AC output that can have a smaller, equal or higher amplitude and frequency.

Figure 2.1, presents the basic block diagrams corresponding to the four types of converter configurations described above.

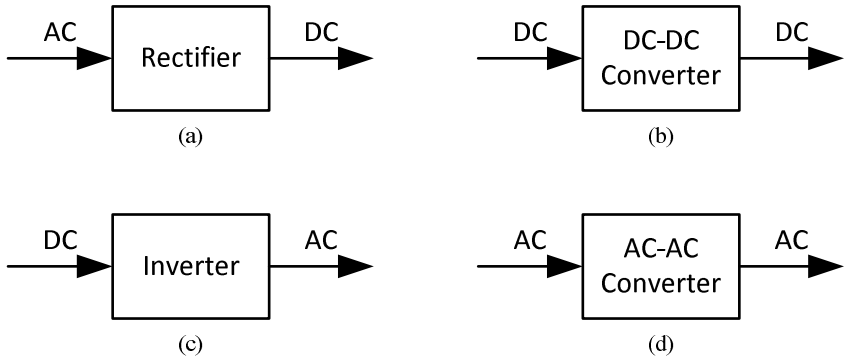

Figure 2.1 – Four basic converter configurations: a) AC-DC converter; b) DC-DC converterwith isolation; c) DC-AC converter; d) AC-AC converter [8]

A rectifier, shown in Figure 2.1 a), converts an AC voltage or current into a DC voltage. An inverter, shown in Figure 2.1 c), converts a DC voltage or current into an AC voltage or current output. A DC-DC converter Figure 2.1 b), converts a DC input into a DC output. An AC-AC converter Figure 2.1 d), converts an AC input into an AC output.

A DC-DC converter Figure 2.1 b), converts a DC input into a DC output. It can be an isolated or non-isolated topology. For example, Buck, Boost or Buck-Boost converters are simple non-isolated DC-DC converters topologies. In isolated topologies, there is an isolation high-frequency transformer and, in such case, the converter can be implemented by cascading an inverter followed by a rectifier, with a high-frequency transformer placed in between. An AC-AC converter Figure 2.1 d), converts an AC input into an AC output. It can be simply implemented using a cycloconverter, which converts directly an AC input into an AC output or, it can be composed by cascading a rectifier and an inverter. In such case, there is a DC Bus between both converters.

For many low and medium power applications, the converters are controlled using Pulse-With Modulation (PWM). The simplest PWM technique consists in having the converter switches commutating at constant frequency and, by controlling the duty cycle, the converter output is varied. These commutations interrupt the converter power flow, resulting in abrupt voltage or current changes (voltage/current square waveforms).This hard-switching results in high switching losses. The rectangular waveforms have high harmonics components which can potentially cause electromagnetic interferences (EMI). Hence, the PWM technique has some limitations in terms of operating frequencies, and can compromise the system efficiency due to switching losses. Because of the PWM technique limitations and because in many applications it is required a sinusoidal output of voltage/current, new converter topologies have been studied that allow generating sinusoidal shaped waveforms instead of rectangular shaped waveforms. In order to achieve sinusoidal voltage/current waveforms, a resonant circuit can be used in power converters. These types of converters are called *resonant*

converters. In resonant converters the switches (transistors and diodes) are softly-switched allowing either Zero-Voltage Switching (ZVS) or Zero-Current Switching (ZCS). Sinusoidal shaped waveforms are generated reducing significantly switching losses and EMI levels [8], [10].

2.2. Types of Resonant Converters

When compared to PWM based converter topologies (described before), resonance operation is advantageous because it allows resonant converters to have lower switching losses and lower electromagnetic interference levels (EMI) leading to higher efficiency and reliability. Increasing the operation frequency leads also to circuit miniaturization and improved EMC (Electromagnetic Compatibility) [11].

A resonant converter is a particular kind of converter which operation is based on the *resonant principle*. The *resonant circuit*, *resonant tank* or *resonant network* is an electric circuit composed by passive elements, capacitors and inductors (and can also have transformers incorporated) that are connected and designed in such way that allow operating at resonance achieving sinusoidal voltage/current waveforms.

The resonant tank can have various configurations. The main four configurations are:

- Series-Series (SS);
- Series-Parallel (SP);
- Parallel-Parallel (PP);
- Parallel-Series (PS).

These configurations depend on the way that the passive elements of the resonant tank are connected. The basic resonant circuit topologies are presented in Figure 2.2.

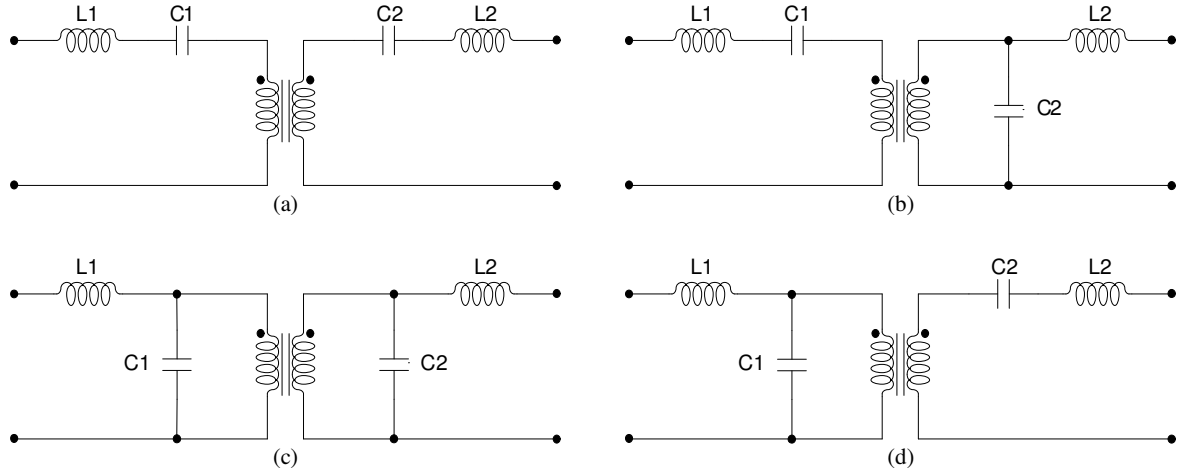

Figure 2.2 – Four basic resonant circuit configurations: a) SS topology; b) SP topology; c) PP topology; d) PS topology

These topologies allow galvanic isolation from the input to the output due to the existence of the transformer. Figure 2.2 a) shows the Series-Series topology where in the primary side the inductor L_1 is connected in series with capacitor C_1 and in the secondary side, the inductor L_2 is connected in series with capacitor C_2. Figure 2.2 b) shows the Series-Parallel topology where in the primary side the inductor L_1 is connected in series with capacitor C_1 and in the secondary side, the inductor L_2 is connected in parallel with the capacitor C_2. Figure 2.2 c) shows the Parallel-Parallel topology where in the primary side the inductor L_1 is connected in parallel with the capacitor C_1 and in the secondary side, the inductor L_2 is connected in parallel with the capacitor C_2. Figure 2.2 d) shows the Parallel-Series topology where in the primary side the inductor L_1 is connected in parallel with capacitor C_1 and in the secondary side, the inductor L_2 is connected in series with capacitor C_2.

Resonant converters can also allow AC-DC, DC-DC, DC-AC or AC-AC conversion depending on the design of the topology. For example, the DC-DC resonant converter can be obtained by cascading two converters, a resonant inverter (DC-AC converter) connected to a high-frequency rectifier (AC-DC converter). In this case, the DC input power is first converted into AC power by the resonant inverter and then, the AC power is converted back to DC power at the output by the rectifier. To allow isolation, a transformer can be inserted in the converter between the inverter output and the rectifier input. If the converter operates at high-frequency, the overall size of the converter can be reduced (note that a high-frequency transformer is much smaller than a low-frequency transformer) [8].

From this point on, the DC-DC resonant converter is analyzed. Representing the DC-DC resonant converter as the cascade of two converters is convenient because it allows a simpler analytical analysis. If the input of the rectifier is a sinusoidal voltage/current, it means that only the fundamental component is converted from AC to DC power. Having sinusoidal waveforms means that the rectifier can be replaced by its input impedance defined as the ratio between the fundamental components of the rectifier input voltage and current. This impedance will be called further in this work as R_{ac} and, it can be seen as an AC load for the inverter. This facilitates the project of the converter because the inverter and the rectifier can be analyzed and designed separately. If the resonant circuit load quality factor (Q) is high enough and if it is working near resonance (switching frequency f_s close to the resonant frequency f_0) the resonant inverter operates usually in continuous conduction mode (CCM) and forces either a near sinusoidal output current or voltage, depending on the resonant circuit topology. This means that the entire inverter can be replaced by a sinusoidal current or voltage source at the input of the rectifier. Therefore, the project of the converter can be made

in two steps, analyzing and designing the rectifier and the inverter separately and, after this, they can be cascaded as in other electronic systems cells/modules.

The cascaded inverter and rectifier need to be compatible with each other. This means that a rectifier requiring an input voltage source (voltage-driven rectifier or voltage-source rectifier) needs to be connected to an inverter whose output behaves like a voltage source (for example, inverters with a parallel-resonant circuit, forcing at the output a sinusoidal voltage). Similarly if the rectifier requires an input current source (current-driven rectifier or current-source rectifier), the inverter output should behave like a current source (for example, inverters with a series-resonant circuit, forcing at the output a sinusoidal current). Finally, to characterize the DC-DC converter, for example, the efficiency or the voltage transfer function, can be both obtained in a simple way as the product of the characteristics of the inverter and the rectifier [8].

Considering this, and in order to be able to design the converter it is considered that the converter will operate at or near resonance. The current and/or voltages are near sinusoidal so, the fundamental-frequency approach or first harmonic approximation (FHA) can be used. This approach considers only the fundamental components of voltage and/or currents (with no harmonic components) [9]. The FHA allows studying and characterizing the behavior of the converter. Nevertheless, note that if the resonant circuit load quality factor (Q) is very low and/or the converter is operating far from the resonance (switching frequency f_s much lower or higher than the resonant frequency f_0), the current waveforms may differ from sinusoidal waves (current has harmonic components) and the converter may operate in discontinuous conduction mode (DCM). In such cases, if FHA is used, it can lead to inaccurate design of the converter due to non-consideration of the harmonic components. In this case, other design approaches should be considered [8].

In order to design the converter, some considerations need to be accounted for. For example, for higher power density and smaller size power converters the switching frequency needs to be higher. Increasing the switching frequency allows reducing considerably the size of passive elements in the converter circuit, such as transformers, inductors and capacitors. Increasing the switching frequency in typical power converters means higher switching losses. However, using resonant converter topologies allows operating at higher frequencies with low switching losses [9]. In resonant converters, power is transferred in a sinusoidal manner and the switches are softly commutated reducing considerably these losses and noise.

Two basic resonant converters topologies are typically used: the series resonant converter (SRC) where the resonant tank is composed by an inductor in series with a capacitor and, the

parallel resonant converter (PRC) where the resonant tank is composed by an inductor in parallel with a capacitor. In the SRC shown in Figure 2.3 a), the circuit with the output rectifier and the load is connected in series with the LC resonant tank. In this case, the load behaves as a voltage divider. Acting on the switching frequency of half-bridge inverter changes the impedance of the resonant tank, which in turn changes the converter gain and allows controlling the converter output. Because the load behaves as a voltage divider, the output gain is always equal or lower than 1. At light load (no-load or open-circuit condition), the impedance of the load is very large when compared to the impedance of the resonant tank which makes it difficult to regulate the output of the converter. Theoretically, to regulate the output in light load conditions, the switching frequency should be infinite [9].

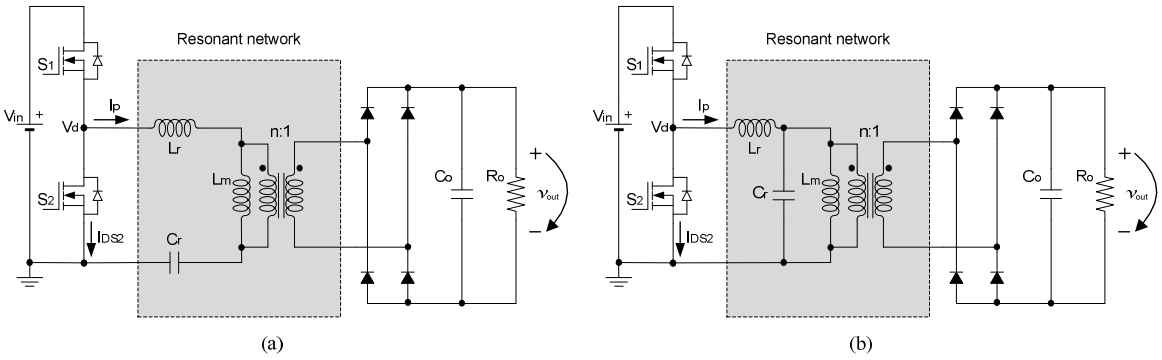

Figure 2.3 – Two basic topologies for resonant converters: a) Half-bridge series resonant converter; b) Half-bridge parallel resonant converter [9]

In the PRC shown in Figure 2.3 b), the circuit with the output rectifier and the load is connected in parallel with the resonant circuit. Because the load is connected in parallel, large amounts of circulating current appear. Because of the higher currents it is difficult to use this topology in high power applications [9].

In order to solve these limitations of the typical topologies SRC and PRC, the LLC resonant converter has been proposed in previous literature [9]. This topology has many advantages when compared with typical resonant converter topologies. For example, it allows output regulation, even when variations in the supply or load systems occur, with a small switching frequency variation of the inverter (typical control variable). Because of these advantages, the LLC resonant converter has been used in a high number of applications, from high-density DC-DC converters to low power LED (Light Emitting Diode) drivers [12], [13], or classical 48 V telecom power sources [14].

Due to the inherent resonant operation, resonant converters can also be used for battery charging applications. As batteries are charged with a DC current, a converter with a DC output is required. There are many possible configurations and topologies of resonant converters that can be used [5]-[7]. In the particular case of this work, the LLC resonant

converter will be considered. More detailed information about batteries will be presented below in this chapter.

2.3. Variable Inductor (VI)

The proposed converter will be controlled using a new control variable, based on the variable inductance concept. In order to control the converter the operating principle of the VI needs study, especially how the inductance can be regulated in order to control the charging process. In brief this section presents an introduction of the VI, its operating principle for an ETD shaped ferrite core and an explanation of how to regulate the inductance value. In mid-power applications, variable inductors have been researched and used to control the output current of high-frequency resonant circuits [15]. In [16] and [17], a LED driver based on a Resonant Switched Capacitor Converter (RSCC) controlled with a VI is proposed. Some of the previous knowledge presented in the RSCC converter served as reference for this work [18].

2.3.1. VI Principle of Operation

To understand the operating principle of the VI is necessary to know some basic concepts about inductors. In an inductor the inductance value can be calculated using (2.1).

$$L = \frac{N^2}{\Re} \tag{2.1}$$

where, L is the inductance [H], N is the number of turns and $\Re$ is the core reluctance [A/Wb], which can be calculated as:

$$\Re = \frac{l}{\mu_r \cdot \mu_0 \cdot A_e} \tag{2.2}$$

where, l is the length of the core [m], μ_r is the magnetic permeability of the core material [H/m], μ_0 is the magnetic permeability in the vacuum [H/m] ($\mu_0 = 4 * \pi * 10^{-7} H/m$) and A_e is the area of the core cross section [m^2].

The voltage across an inductor can be calculated as:

$$v_L(t) = L \cdot \frac{di_L(t)}{dt} \tag{2.3}$$

According to (2.1), the inductance value depends on the number of turns and the reluctance value. The number of turns is defined by the number of turns in the winding and the reluctance depends on the core material and size (length (l) and cross-section area (A_e)). In the VI if an auxiliary winding is inserted and if a DC current, I_{dc}, is injected in it, it allows

regulating the core saturation. By controlling this saturation, the magnetic permeability of the core (μ_r) will change, which causes variation of the core reluctance ($\Re$) changing the inductance value according to (2.1). By changing the DC current on the auxiliary winding, it is possible to control the inductance value on the VI.

The VI used in this work is based on an E shaped core, in particular an ETD ferrite core, as shown in Figure 2.4 a). To build the VI core, two ETD half cores are used which are assembled as in Figure 2.4 b). In the two external arms there is no air gap and, in the middle arm an air gap exists.

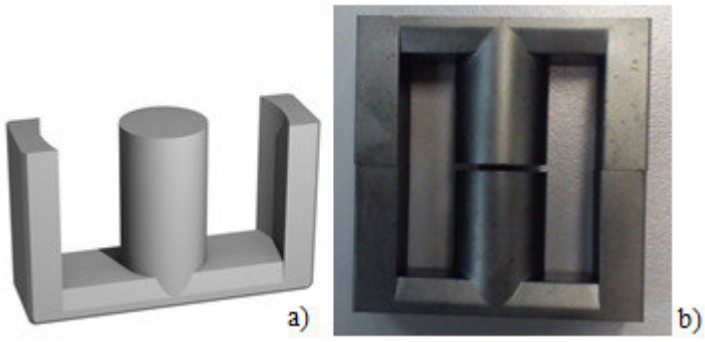

Figure 2.4 – VI core: a) ETD shaped core [19]; b) ETD core for VI construction

In VIs based on E-shaped cores there are three windings: two DC control windings and a main AC winding. Figure 2.5 shows the electrical connections of the VI windings and the magnetic flux contributions.

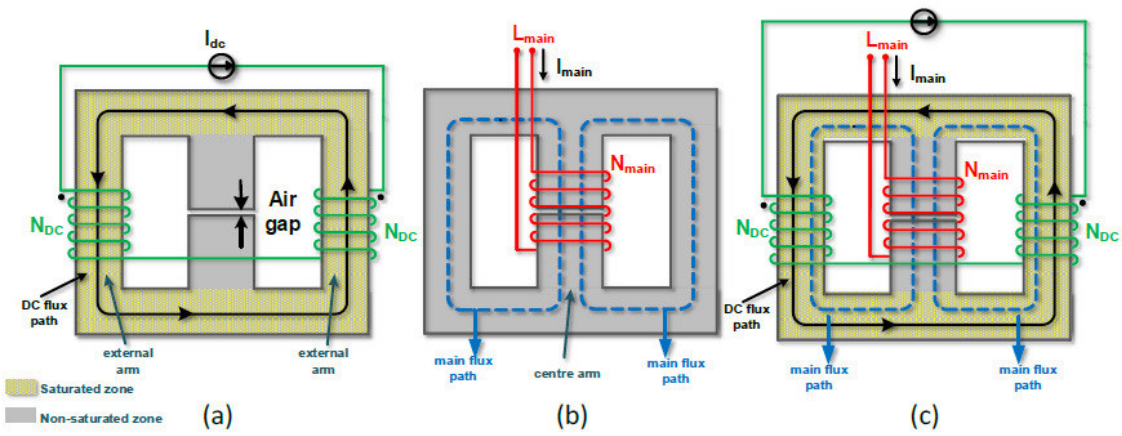

Figure 2.5 – Assembly and Magnetic contribution of the different windings in the VI: a) DC windings assembly and magnetic flux contribution; b) Main winding assembly and magnetic contribution; c) Complete VI model with DC and main windings assembled [16]

In Figure 2.5 a) the electric connections of the DC winding and its magnetic flux contribution is presented. The DC winding is composed by to windings placed in the external arms of the core and connected in anti-parallel as shown. In order to vary the main AC winding inductance, it is necessary to regulate the level of the core saturation. By injecting a DC current in the DC winding, a constant magnetic flux will flow around the external path of the

core as shown in Figure 2.5 a) by the black line. Because there is no air gap in the external arms it is easier to saturate this section of the core. By controlling the DC current in the DC windings, I_{DC}, the level of saturation of the core can be controlled which allows control the main AC winding inductance, L_{vi}. The yellow area represents the area that is most likely to be saturated by the DC windings.

In Figure 2.5 b) the electric connections of the main AC winding and its magnetic flux contribution is presented. The main AC winding is placed in the middle arm of the core which contains an air-gap in the middle. The air-gap allows decreasing the effective permeability of the core which reduces drastically the magnetic flux density.

In Figure 2.5 c) the general electric connections of the VI is presented as well as the flux directions created by the AC and DC windings. As can be observed there is a common path to both the main and DC flux path that is key for the VI operation [16].

In summary, as response to a DC control current, the global reluctance of the magnetic core is varied, and therefore the differential inductance of the inductor is controlled. Thus, the role of the L_{vi} is to change the characteristics of the resonant tank in order to have a controllable output in a similar manner to the classical f_s control. Adding the VI in series with the LLC resonant tank allows changing the resonant frequency and the converter gain. Changing the converter gain in a controlled way allows output regulation.

In this case, the f_s will be kept constant. However, if necessary both control variables might be use simultaneously in order to try to improve the performance and operation of the converter.

Although the VI concept is relatively simple, the equations that are used to explain its behavior and design are quite complex.

The design methodology used for the VI design is presented in the Appendix B. Further information about the VI design methodology, operation and behavior can be found in previous literature [16], [20], [21].

2.4. Batteries

Nowadays several battery technologies exist and new technologies are being investigated. In HEVs and EVs, the most common technologies are Lead-Acid, Ni-MH and Li-Ion. The batteries are commonly characterized by its nominal voltage V [V] and its capacitance C [Ah] which gives information about the current it can feed during a certain period of time. In other words, these parameters allow determining how long the battery can supply a circuit until it is

discharged. Although one of the battery characteristics is the output voltage, it depends on the battery State of Charge (SOC). Figure 2.6 shows the typical discharge curve for a battery as function of the capacity.

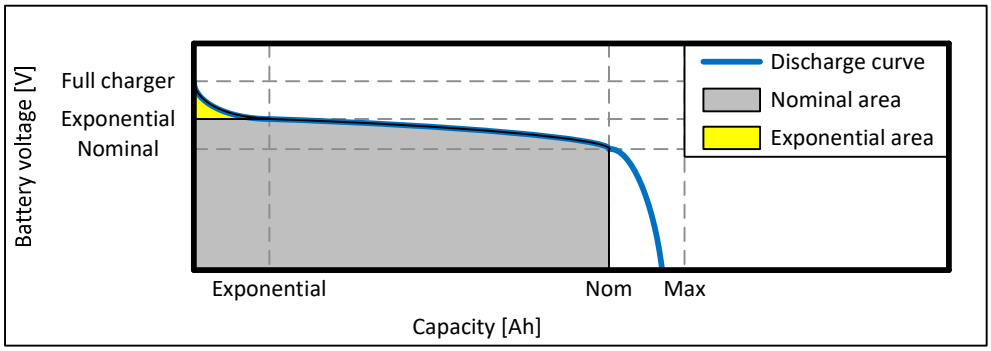

Figure 2.6 – Typical discharge characteristics for batteries [22]

The curve can be divided into three sections. As can be seen, in the first section, if the battery is fully charged the voltage is at its maximum value. When it starts to discharge, the voltage decreases exponentially as represented by the yellow area. This area is more or less wider depending on the battery type. In the second section, the grey area represents the available energy that can be used until the battery voltage reaches its nominal value. In the third section, the battery voltage is below the nominal value and if it continues to be discharged, the voltage drops very quickly.

To charge the battery, a current needs to be injected into the battery which implies that the battery current is negative and the charging follows the characteristics shown in Figure 2.7.

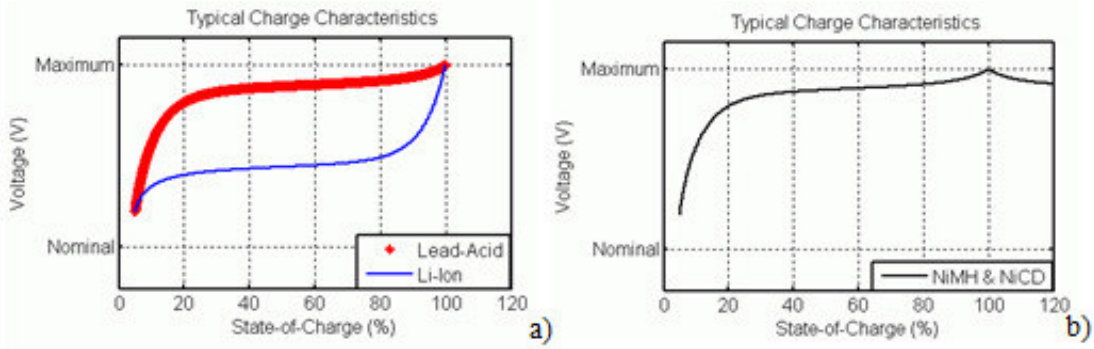

Figure 2.7 – Typical charging characteristics for batteries: a) Lead Acid and Li-Ion batteries; b) Ni-MH and Ni-CD batteries [22]

When discharging, the batteries feed energy to the system acting as a power supply. When charging, the batteries act like a load, harvesting energy from a power source and storing it in the battery. To charge the batteries, the corresponding charger needs to feed the batteries with either a current or voltage. Figure 2.7 shows the typical charging characteristics for Lead Acid, Li-Ion (Figure 2.7 a)), and Ni-MH and Ni-Cd (Niquel-Cadmium Battery) (Figure 2.7 b)) batteries. As can be seen, during the charging process the battery voltage increases from

the starting value, which depends on the SOC, until it reaches the maximum value at which the battery is fully charged. Figure 2.8 shows the problems that can appear during battery charging.

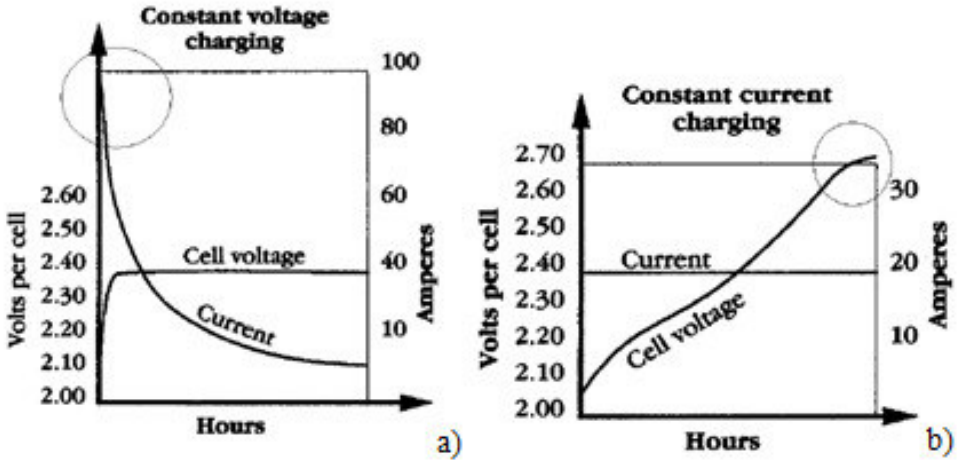

Figure 2.8 – Problems during charging: a) Constant voltage charging; b) Constant current charging [23]

If the charger imposes a constant voltage to charge the batteries, Figure 2.8 a), at the beginning of the charging, the voltage imposed by the charger is higher than the battery voltage. This imposes a very high starting current to feed the batteries, eventually decreasing as the battery charges. Therefore, there is a problem of current spikes in the beginning of the charging process.

If the charger imposes a constant current during the charging process, Figure 2.8 b), the battery will start charging with a controlled current and its voltage increases. When the battery is almost fully charged, if the current is maintained constant the battery voltage will keep increasing achieving possible very high values. Therefore, there is a problem of over-voltages at the end of the charging process.

In conclusion, the ideal charging procedure would start with a constant current and as the battery voltage increases from its initial value (when charging starts) to a value close to the maximum voltage, the charger needs to keep this voltage value under control. From this point on, the battery voltage will increase slowly until reaching its maximum voltage value. This implies that the charging current will decrease naturally to its minimum value, I_{o_float} (float value). Figure 2.9 shows the current and voltage in a battery during charging.

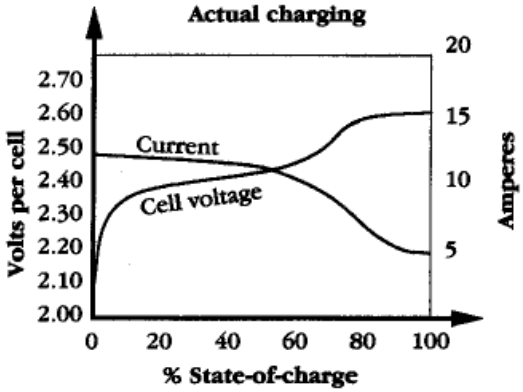

Figure 2.9 – Current and voltage of a battery during the charging process [23]

It can be seen that if the charging is controlled as described before there will be no current spikes or over-voltages which contributes to increase the battery life time. In this work, the first charging step with a constant current will be called as the Current Charging Stage (CCS) and the final charging step, which keeps a constant voltage, will be called as the Voltage Charging Stage (VCS). Because the battery voltage is not constant, either during charging or discharging, the battery charger needs to provide a variable DC output.

In the previous paragraphs, the behavior of the batteries during charging and discharging was analyzed. Now it is necessary to address the problem of how much time it takes to fully charge a battery. There are different types of commercial battery chargers for electric vehicles (EV and PHEV), which can be divided in three types [24]:

- **Normal charging:** The charging process is slow, takes about 8 hours. It is used in domestic applications and the charger is fed by the grid (230 V, 50 Hz, 16 A). The charger is an AC-DC converter that is placed on the vehicle and converts the AC grid power into DC power to charge the batteries.
- **Fast charging:** It is limited by the battery technology and by the power supply. Part of the converter is outside of the vehicle in the charging station and it is necessary communication between both to have safe charging. The system's power can go up to 45 kW, which can decrease the charging time to about 30 minutes. In fast charging, the charging station feeds DC power directly to the batteries in the vehicle.
- **Semi-fast charging:** It is similar to the fast-charging but with lower power capacity, about 22 kW, which increases the charging time but reduces the cost of the charging station.

So, the battery charger is composed by two main blocks as can be seen in Figure 2.10, the charging station and an on-board module in the vehicle. The charging station is fed by the grid and feeds the batteries in the vehicle.

Figure 2.10 – Battery charger for EV block diagram [25]

The charging system and the converters can be built in three different ways.

- Placed in the vehicle (Figure 2.11 a)). In this case, the charging station feeds the on-board converter from the AC power grid. The charging is controlled in the vehicle by the converter control system. This is used in normal charging systems, with lower power capacities and higher charging times. In this case, the volume of the on-board charger is higher due to the existence of the low-frequency rectifier.
- Placed part in the vehicle and part in the charging station (Figure 2.11 b)). This allows faster charging and higher power levels are involved. In this case, the charging station feeds directly the on-board DC-DC converter with DC power and, the on-board module does not need a rectifier as in Figure 2.11 b).
- Placed on the charging station. In this case, the on-board charger is not used and the batteries are directly fed by DC power from the charging station. This allows faster charging due to the higher power involved. In this case, communication between the charging station and the vehicle is needed to have a safe charging, because the charging is controlled directly by the charging station as in Figure 2.11 c).

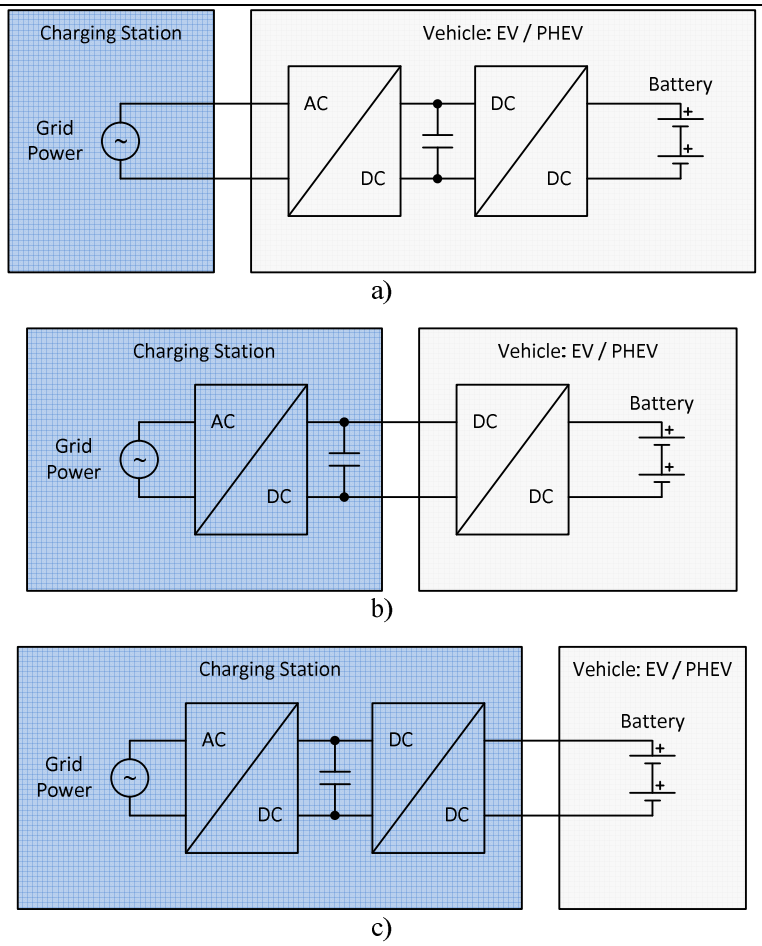

Figure 2.11 – Types of charging systems: a) On-board charger fed by AC power from the grid; b) On-board charger fed by DC power; c) Charger divided between the charging station and the vehicle; d) Battery charger on the charging station

In this chapter a brief state of the art regarding general topologies of resonant and non-resonant power converters, the VI principle of operation and batteries main characteristics were presented. The LLC resonant converter topology was selected due to its inherent resonant operation and advantages. Although this state of the art is necessary to introduce the theme of this work, the main goal is to study the behavior and design the LLC resonant converter for a battery charging application. This topology is studied in detail in the next chapter.

3. LLC Resonant Converter for a Battery Charger

In this chapter the LLC resonant converter topology is presented. The electrical scheme is shown; its components and principle of operation are addressed. A theoretical analysis is made and control variables are discussed.

3.1. Proposed Battery Charger Application

For battery charging applications different converter topologies can be used from simple non-controlled rectifiers to more complex converter topologies with complex control algorithms to improve the converter efficiency and prolong the batteries life time. For the present work, as referred before, a LLC resonant converter will be used to build the battery charger as shown in Figure 3.1:

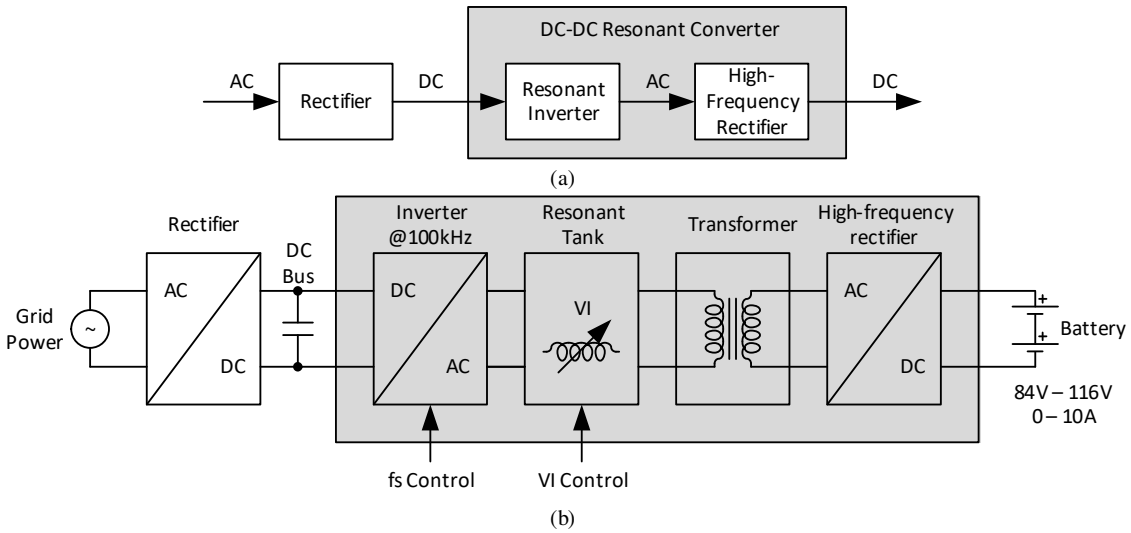

Figure 3.1 – Battery charger based on the LLC resonant converter block diagram: a) Simple block diagram; b) Block diagram with the block of the LLC resonant converter

The charger presented in Figure 3.1 a), is composed by a cascade of three converters, a rectifier (AC-DC conversion) fed by an AC power supply, followed by a resonant inverter (DC-AC conversion) followed by a high-frequency rectifier (AC-DC conversion) which in turn feeds the batteries. For this case study the AC power supply will be the national grid (230 V, 50 Hz in Portugal). Figure 3.1 b) presents a more detailed block diagram of the battery charger analyzed in this work. The focus will be on the DC-DC LLC resonant converter consisting of the resonant inverter, resonant tank, high-frequency transformer and the high-frequency rectifier (gray area). A 400 V DC bus created by a simple low-frequency rectifier

followed by a filter capacitor feeds the resonant inverter which works at a constant frequency of 100 kHz. The VI is introduced in the resonant tank. The resonant tank is followed by a high-frequency transformer connected to a high-frequency rectifier. Finally, the batteries are connected at the output of the rectifier. The converter can be controlled using two variables: the switching frequency of the inverter or the VI inductance value. In order to prove the design methodology presented in this work considering both control techniques a simple battery charger application is considered.

For the proposed charger application, Lead-Acid batteries are considered. The battery bank is composed by 16 individual 12 V Lead-Acid batteries, two sets of 8 serially connected batteries in parallel. The nominal voltage of the battery bank is 96 V and can vary between 84 V and 116 V depending on the SOC. The maximum charging current is of 10 A. Each individual battery has a 12 V nominal voltage that can vary between 10.5 V and 14.5 V and the maximum value for the charging current is 5 A.

As described previously (Figure 2.7), the battery voltage does not vary linearly during the charging process. Although this behavior happens in real batteries (Figure 2.9), for the present case study, to simplify the analysis, it will be considered a charging profile where the voltage increases linearly as function of the SOC. Figure 3.2 shows the simplified battery voltage and current profiles and Table 3.1 shows the main design specifications considered for the project of the LLC resonant converter based charger and the characteristics of the battery bank.

Table 3.1 – Design Specifications

Description	Specification
Main parameters	$V_{in} = 400V;\ f_s = 100kHz;\ d = 0.5$
Battery bank	$84V \leq V_o \leq 116V\ ;\ 0 \leq I_o \leq 10A$

The voltage and current are dependent on the state-of-charge (SOC) of the battery or battery bank. For this reason, during charging, the battery voltage V_{out} is not constant. The converter must cope with these changes and therefore must be capable of providing a wide output voltage range and safe-operation from no-load to short-circuit conditions [26], [27]. The LLC isolated converter is capable of dealing with these requirements, since ZVS is guaranteed in the primary side and ZCS is assured in the secondary [28]. These requirements will also be kept with the LLC-VI [29].

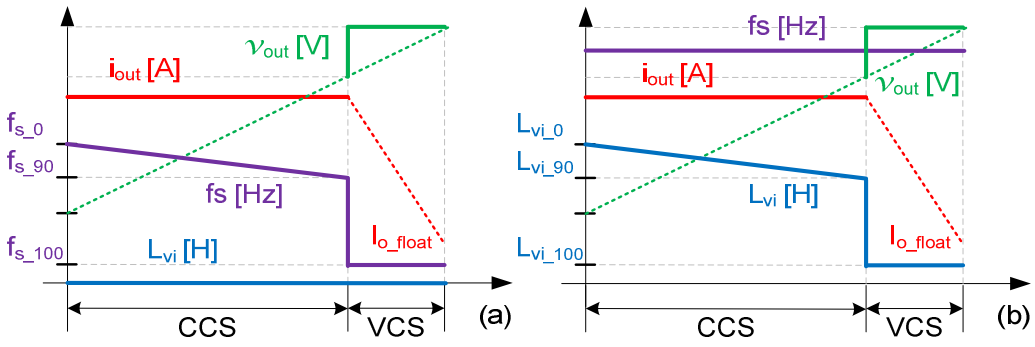

Figure 3.2 – Battery voltage and current profiles and, behavior of L_{vi} and f_s values along the charging process: (a) f_s control and, (b) L_{vi} control [29]

Figure 3.2 a) and Figure 3.2 b) show the voltage and current profiles. It is also shown the expected behavior of the control variables, inductance and switching frequency, L_{vi} and f_s, respectively.

Using the VI control method, the goal is to have a constant charging current, starting with an initial value for L_{vi}. Since the battery voltage is not constant, the controller needs to act on the inductance value to compensate the effect of the voltage variation. In this case, as the voltage increases from a minimum value, L_{vi} needs to decrease from L_{vi_0} (SOC ~0%), to maintain a constant charging current until an acceptable SOC is achieved (SOC~90% at L_{vi_90}). This mode is identified as current charging stage, CCS. In the next stage, identified as VCS (voltage charging stage), when the battery is almost fully charged, the voltage needs to be maintained at a constant maximum value as the charging current tends to decrease naturally to its floating level I_{o_float}. At this point, L_{vi} tends to its minimum value L_{vi_100} (SOC→ 100%). During the whole process f_s is kept constant. This simple approach is sufficient to prove the converter performance, however more complex charge control algorithms can be implemented to improve the efficiency of the application itself [29].

Using the frequency control method, the charging profile is similar to the previous one but, in this case, the variable inductor L_{vi} is not considered in the circuit and, the resonant inductor role is done by the leakage inductance of the transformer. The control variable is f_s. During CCS, f_s varies from f_{s_0} (SOC ~0%) to, f_{s_90} (SOC ~90%), to maintain a constant charging current as the battery voltage increases. During VCS, f_s tends to its minimum value f_{s_100} (SOC → 100%) maintaining the voltage at is maximum value as the charging current tends do its floating level I_{o_float}.

This simple approach presented in Figure 3.2 as described above is sufficient to prove the converter performance and validate the proposal; however, more complex charge control algorithms can be implemented to improve the efficiency of the application itself.

Having a battery bank as load, inductive operation is needed, therefore the converter will operate only at or above resonance. Above resonance, ZVS operation appears but the waveforms have more distortion [29].

Although the LLC resonant converter is studied considering a battery charger application, the theoretical analysis, simulation and experimental results were made considering a resistive load with an equivalent resistive value to emulate the battery at a specific operation point. The implemented prototype is not optimized. Therefore, the tests were conducted at a lower power level.

3.2. Converter Topology

Figure 3.3 shows the typical topology of a DC-DC LLC Resonant Converter.

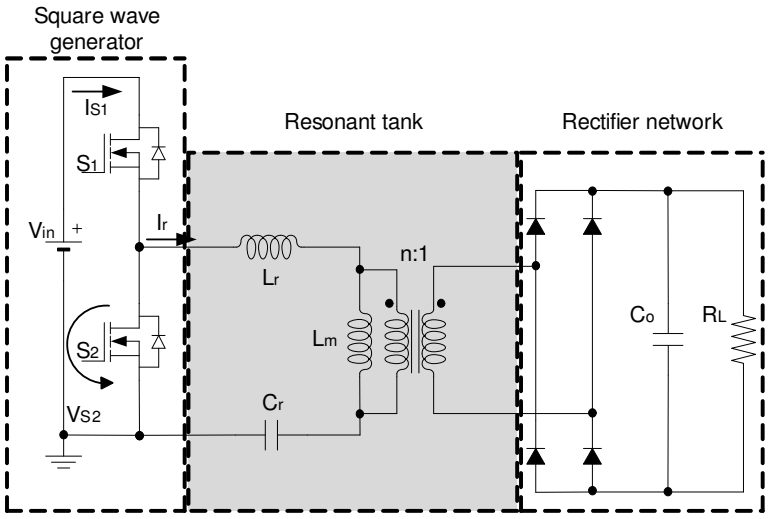

Figure 3.3 – LLC Resonant Converter – Typical Topology [10]

The typical LLC resonant topology can be divided in three modules as shown in Figure 3.3, [9].

- *Square wave generator*: The square wave generator is fed by a DC input voltage and is composed by two switches S_1 and S_2. By turning the switches S_1 and S_2 with 50% duty cycle and complementary to each other a square voltage wave v_{DS2} is created at the input of the resonant tank. In the present case study, a half-bridge inverter is used but a full-bridge inverter could also be an option.
- *Resonant tank*: The resonant tank is fed by a square wave voltage v_{DS2} and is composed by three components, a resonant inductor L_r, the magnetizing inductance of the transformer L_m and a resonant capacitor C_r. The relation between the values of the inductances and capacitances of these three elements will allow to work at, below or above resonance allowing ZVS or ZCS operation. At the output of the resonant tank,

an AC current is created. The goal of the resonant tank is to filter the higher harmonic currents in order to allow only the fundamental component of the current to flow through the resonant tank even when a square wave voltage is applied at the input.

- *Rectifier network*: The rectifier network is fed by an AC current which is rectified and transformed in a DC voltage applied to the load. This is done by a full-bridge rectifier with a output capacitor C_o, to filter the output voltage (a half-bridge or center-tapped rectifier could also be used) [9], [10].

The typical LLC resonant topology from Figure 3.3 as a disadvantageous of having two magnetic components, the resonant inductor L_r and the transformer (which is considered, in some cases, an ideal transformer for simplification) with a magnetizing inductance, L_m. In order to reduce the number of the magnetizing components (reducing the size of the converter) the role of the resonant inductor L_r can be made by considering the leakage inductance L_{lkp} of the primary-side of the transformer. Considering the leakage inductance of the transformer not only reduces the number of magnetic elements in the circuit but also, because the leakage will affect the gain equation, ignoring it leads to an incorrect design [10]. In this case, the topology scheme is shown in Figure 3.4. In Figure 3.4, L_m is the magnetizing inductance of the transformer; L_{lkp} and L_{lks} are respectively the primary and secondary-side leakage inductances of the transformer.

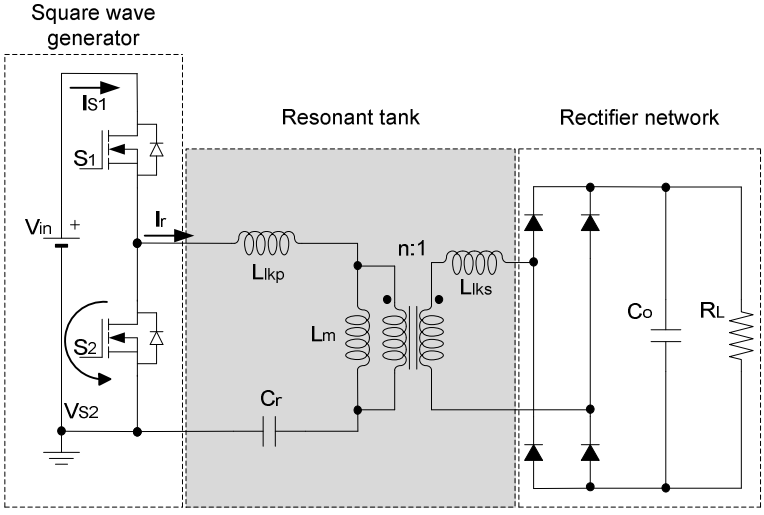

Figure 3.4 – LLC Resonant Converter – Simplified Topology [9]

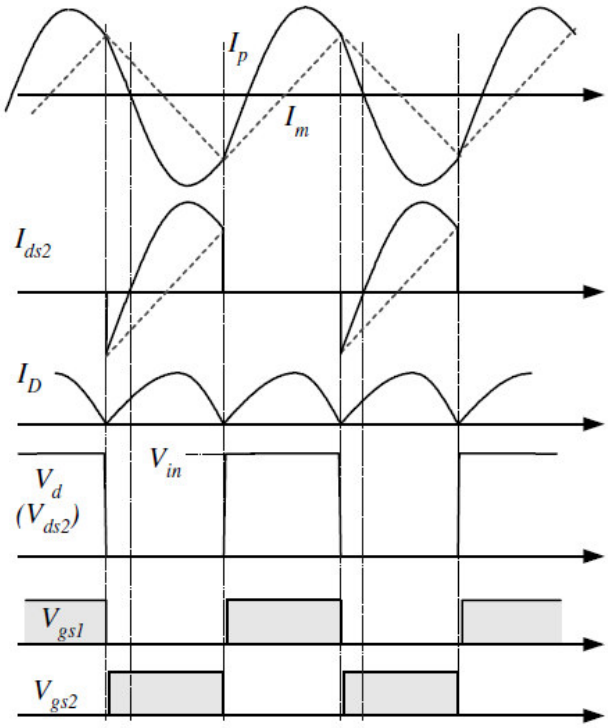

Figure 3.5 – Typical waveforms of the Half-bridge LLC Resonant Converter [9]

The operation of the converter can be depicted from the waveforms shown in Figure 3.5. Although the converter topology is slightly different from the SRC, its operation is similar. The difference is that, in this case, the magnetizing inductance of the transformer is relatively small and therefore a resonance appears between $L_m + L_{lkp}$ and C_r which affects the converter operation. From Figure 3.5 waveforms, it can be seen that, while switches 1 and 2 operate at constant frequency with 50% duty cycle a square voltage, v_{DS2} appears at the output of the square wave generator. Because v_{DS2} switches between 0 and V_{in} (half-bridge inverter) there is only input current, $I_{in} = I_{ds2}$ when $v_{DS2} = V_{in}$ and, when $v_{DS2} = 0$, $I_{in} = 0$. Depending on the values of the resonant tank parameters, resonant operation can be achieved and, in this case, the current in the resonant tank, $I_r = I_p$ (resonant current) is sinusoidal as shown. Because L_m is small there exists considerable amount of magnetizing current, I_m. This current is triangular shaped and it is in phase with I_r. At this point, I_r flows in the primary side of the transformer and a sinusoidal voltage appears at the terminals of the secondary side of the transformer v_{sec}. This voltage is rectified and the rectified current, I_D is just the rectified input current. Because there is an output capacitor in parallel with the load, C_o the voltage ripple will be reduced and a constant voltage and current can be achieved at the output for a resistive load. Note that if the output is open-circuited, the resonant current is equal to the magnetizing current, $I_r = I_m$ because there is no load.

The typical topology from Figure 3.3 can be simplified as shown in Figure 3.4. Although this simplification can be made in order to reduce the number of magnetizing components, the

design can be also improved because of considering the leakage inductances of the transformer which makes the design results more accurate. As the proposed technique is based on a variable resonant tank by using a Variable Inductor (VI), in the form of an inductor L_{vi}, an extra magnetizing component is introduced in series with the primary-side leakage inductance of the transformer as shown in Figure 3.6. So, the LLC resonant converter with VI (LLC-VI) is the proposed topology. In this case, the VI inductance L_{vi}, is connected in series with the transformer primary side, but the rest of the topology is kept.

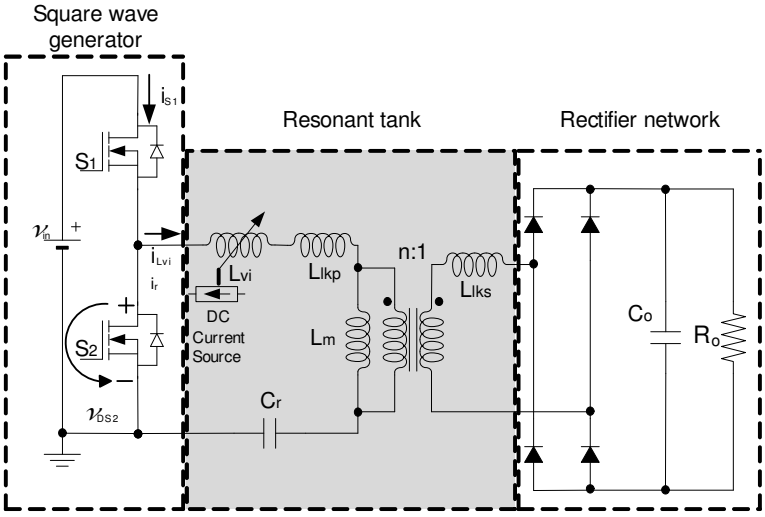

Figure 3.6 – LLC-VI Resonant Converter – Proposed Topology

In this case, adding the VI, allows operating the converter at constant switching frequency f_s or even using both control variables, f_s and L_{vi}, to regulate the converter output.

The converter generally provides galvanic isolation due to the transformer. For the purpose of this work, the load will be a battery bank but in the theoretical analysis, a simple resistor will be used to analyze the converter operation and behavior.

3.3. Behavior of the LLC Resonant Converter

The LLC resonant converter is known to be capable of providing a wide output voltage range and safe-operation from no-load to short-circuit conditions [26], [27]. When f_s is the control variable, it is natural to operate the converter around the resonant frequency, $f_0 = \frac{1}{2*\pi*\sqrt{L_r C_r}}$ associated to the series elements of the resonant tank, L_r and C_r. Around this frequency, the gain characteristics are almost independent of the load, as seen in Figure 3.7. Traditionally, the control is made by varying f_s. The required f_s range will be relatively small to guarantee enough controllability of the output gain (depending on the application) [27]. Therefore, narrow f_0 range with light load and ZVS capability with even no load are commonly described as key benefits. It can also be seen that the gain changes with the load when f_s is

different from f_0. The border between ZVS and ZCS operation is given by the peak gain, i.e. ZCS to the left and ZVS to the right, respectively. In case of no-load, the peak gain is maximum and it occurs when $f_s = f_p = \frac{1}{2*\pi*\sqrt{L_p C_r}}$ associated to the series-parallel elements of the resonant tank, L_p and C_r, where L_p is defined as the sum of the primary leakage inductance and the magnetizing inductance.

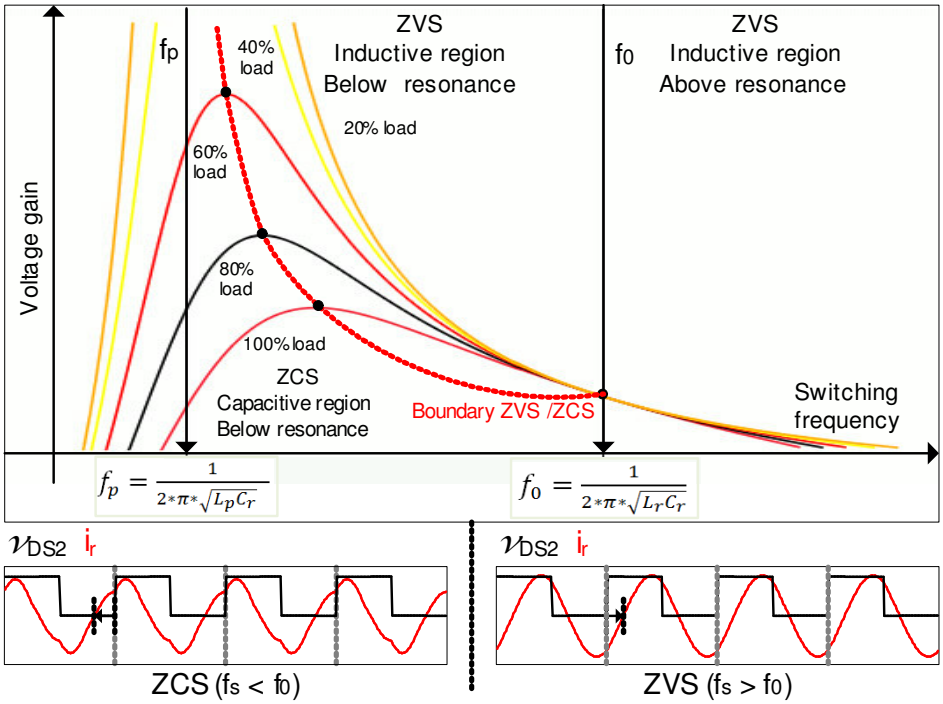

Figure 3.7 – Typical gain curves of LLC resonant converter for various loads and capacitive and inductive region waveforms [26]

It is also noticed that operating above f_0 the resonant tank is inductive and the input current, i_r ($i_r = i_{Lvi}$) lags the voltage applied to the resonant tank, v_{DS2}. The converter operates similar to a series resonant converter and therefore at f_0 the converter has only one operating point, which means no output regulation. Above f_0, switching losses will be minimized, due to ZVS. Working near resonance has the advantage of near sinusoidal waveforms. Below f_0 and above the boundary between ZVS/ZCS, formed by the peak of the family load vs. gain curves, the converter still operates in ZVS. This will not be the case if the converter is operated below the boundary leading to a capacitive operation [26].

3.3.1. Operating Modes

Figure 3.8 shows the steady-state equivalent circuit of the proposed converter and the correspondent operation modes for $f_s \geq f_0$ [30]. Four operation modes were identified (dead-time is not considered). The analysis of the circuit operation assumes the following: all switching devices are ideal (no on-state voltage drop or resistance), all capacitors are ideal (no

Equivalent Series Resistance – ESR), the output capacitor, C_o is large enough to consider the output voltage ripple small, the input voltage, V_{in} is also considered ideal; f_s is constant and the switches are turned on with ZVS.

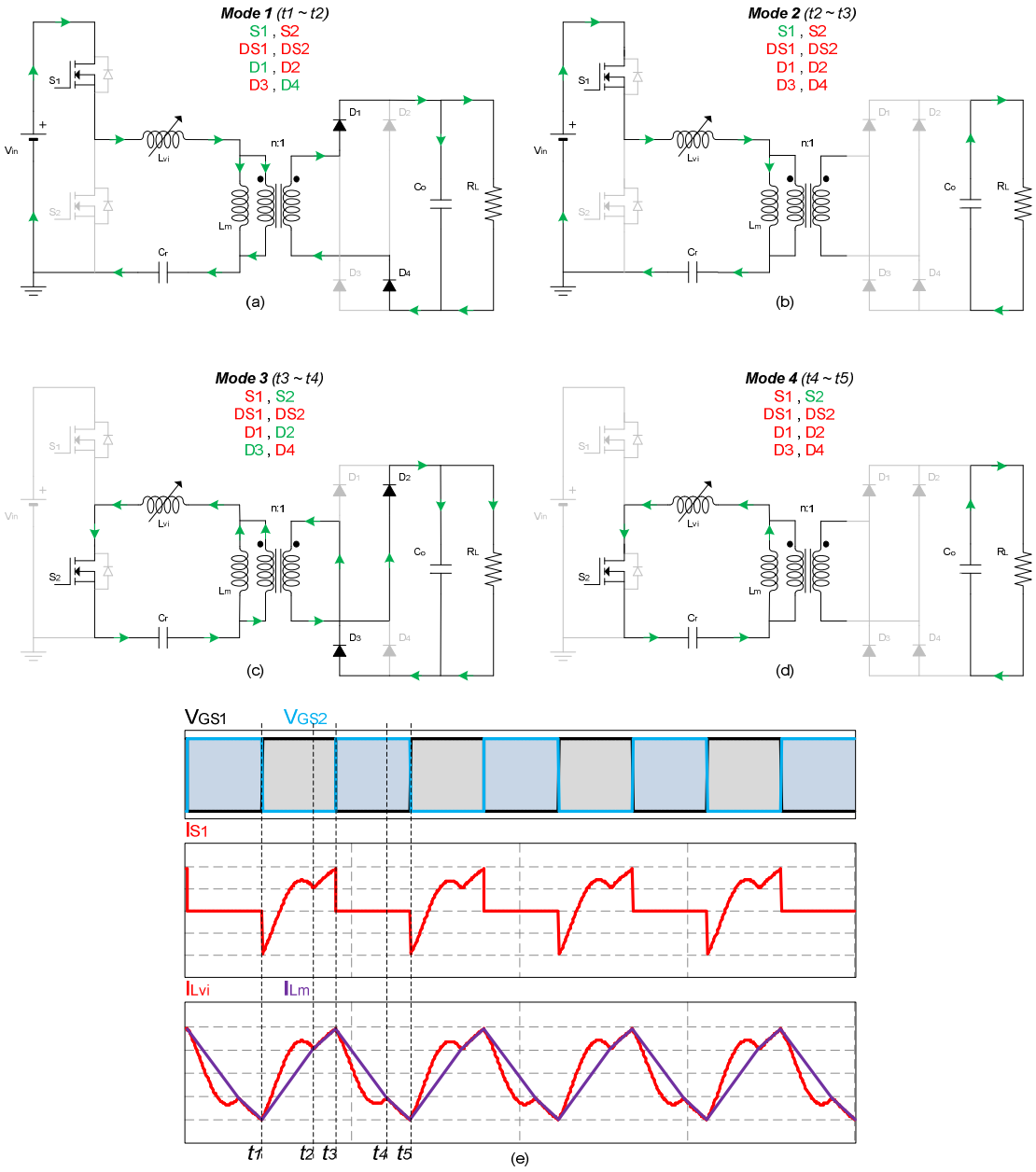

Figure 3.8 – Steady-state equivalent circuit and corresponding operating modes of the LLC-VI: (a) Mode 1 [t1~t2]; (b) Mode 2 [t2~t3]; (c) Mode 3 [t3~t4]; (d) Mode 4 [t4~t5]; and (e) Operating waveforms of the LLC-VI

During Modes 1 and 3 C_o is charged and, during Modes 2 and 4 C_o is discharged to the load. The main theoretical waveforms of the converter are also shown in Figure 3.8. Each operation mode can be described as follows [30]:

- *Mode 1 [t1~t2]:* S_1 turns on and current i_{Lvi} flows through the resonant tank. The magnetizing current i_{Lm} increases linearly in L_m. During this mode, $|I_{Lvi}| > |I_{Lm}|$ so, there is current flowing through the primary side of the transformer which creates a

voltage at the secondary side of the transformer v_{sec}, at the input of the full-bridge rectifier. Diodes D_1 and D_4 are forward-biased and C_o charges. When $i_{Lm} = i_{Lvi}$, this mode finishes.

- *Mode 2 [t2~t3]:* In this mode S_1 is still on, $i_{Lm} = i_{Lvi}$ so, there is no energy transferred to the secondary side, the output voltage V_o, is higher than v_{sec}, the rectifier diodes are reverse-biased and there is no current flowing from the source to the load. Capacitor C_o discharges to the load. When S_1 is turned off this mode ends.
- *Mode 3 [t3~t4]:* This mode is similar to mode 1. In this case, S_2 turns on and current i_{Lvi} flows through the resonant tank. The magnetizing current i_{Lm} decreases linearly in L_m. During this mode, $|I_{Lvi}| > |I_{Lm}|$ so, there is current flowing through the primary side of the transformer which creates a voltage v_{sec}, at the input of the full-bridge rectifier. Diodes D_2 and D_3 are forward-biased and C_o charges. When $i_{Lm} = i_{Lvi}$, this mode finishes.
- *Mode 4 [t4~t5]:* This mode is similar to mode 2, S_2 is still on, $i_{Lm} = i_{Lvi}$ so, there is no energy transferred to the secondary side, the output voltage V_o, is higher than v_{sec}, the rectifier diodes are reverse-biased and there is no current flowing from the source to the load. Capacitor C_o discharges to the load. When S_2 is turned off this mode ends.

3.4. LLC Analysis using FHA

In this section, the analysis and design of the converter will be discussed considering the proposed VI control method. The approach will be based on the evaluation of the converter using the fundamental harmonic approximation (FHA). Figure 3.9 presents the adopted current and voltage definitions. The battery bank is represented by a load resistance R_o.

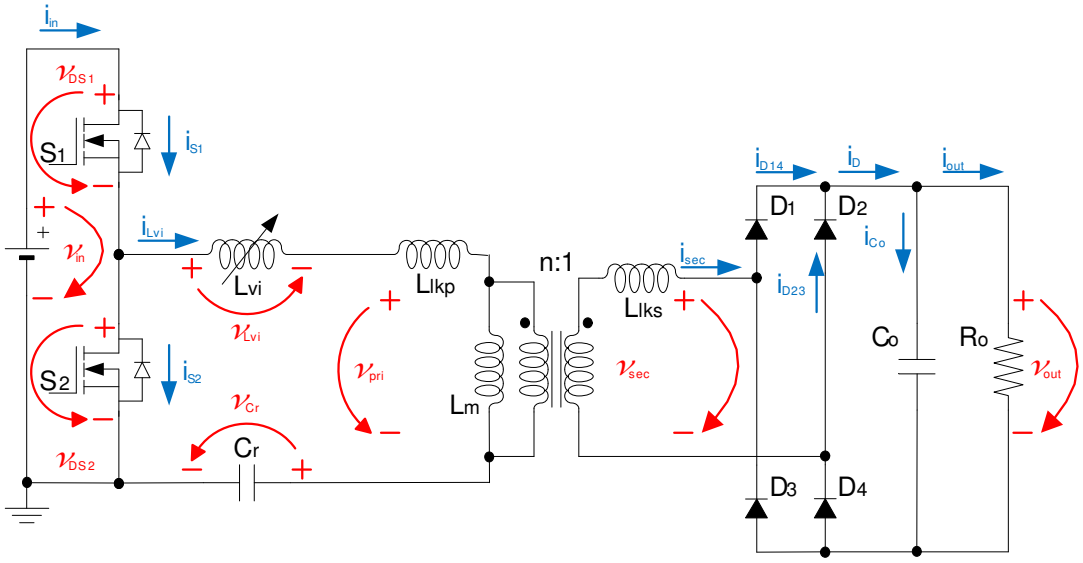

Figure 3.9 – Voltages and currents definitions

Typically, f_s is the control variable used for the LLC resonant converter and the design methodology can be found in previous literature [27]. In this work, since one of the goals is to control the converter operation using a VI, the design methodology needs to be adapted to this control technique. Moreover, to be able to compare both control techniques and even to analyze the behavior when both are used simultaneously a design methodology will be presented in order to do that.

In order to use the first harmonic approximation (FHA) it is assumed that the filtering action of the resonant tank is enough so that only the fundamental component of the square wave voltage v_{DS2} contributes to the power transfer to the output.

Considering the FHA the rectifier circuit at the output of the resonant tank acts as an impedance to the transformer [27], so the load resistance at the output of the resonant tank (equivalent load resistance, R_{ac}) is different from the actual load resistance R_o. In Figure 3.10 can be seen the principle used to derivate the equivalent load resistance. Using FHA only the fundamental component of v_{DS2} is considered. With this, at the transformer output almost sinusoidal current appears so, the resonant tank and square wave generator can be replaced by a sinusoidal current source, I_{ac} and a square wave of voltage, V_{Rac} appears at the rectifier input. Since the output current I_o is the average of I_{ac}, I_{ac} can be obtain as

$$I_{ac} = \frac{\pi \cdot I_o}{2} \cdot \sin(\omega t) \tag{3.1}$$

And V_{Rac} is given by

$$\begin{cases} V_{Rac} = +V_o, if\ \sin(\omega t) > 0 \\ V_{Rac} = -V_o, if\ \sin(\omega t) < 0 \end{cases} \tag{3.2}$$

Where V_o is the output voltage. With this, the fundamental component of the V_{Rac} voltage is given by

$$V_{Rac,1} = \frac{4 \cdot V_o}{\pi} \cdot \sin(\omega t) \tag{3.3}$$

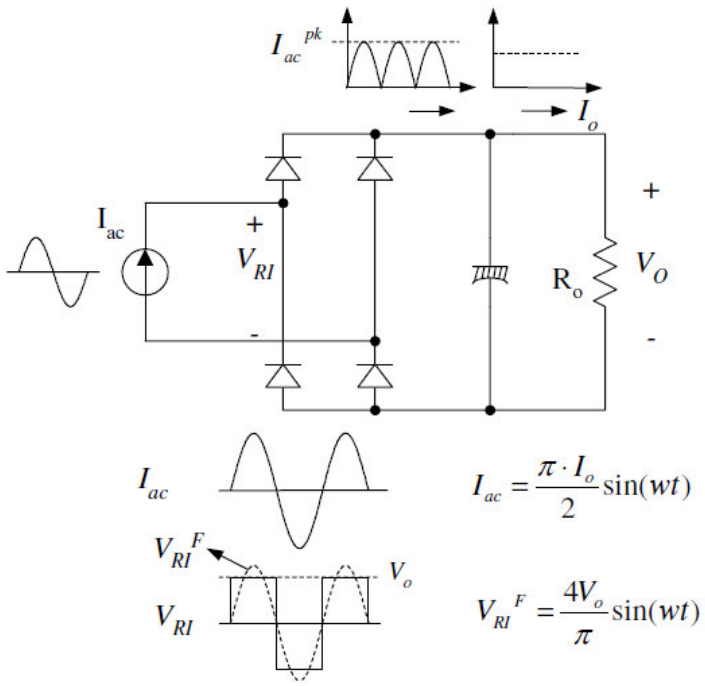

Figure 3.10 – Derivation of equivalent load resistance R_{ac} [27]

Using FHA, only the fundamental components of currents and voltages are considered so the harmonic components of V_{Rac} are not involved in the power transfer. Therefore, the AC equivalent load resistance can be obtained by dividing directly $V_{Rac,1}$ (3.3) by I_{ac} (3.1) obtaining:

$$R_{ac} = \frac{V_{Rac,1}}{I_{ac}} = \frac{\frac{4 \cdot V_o}{\pi} \cdot \sin(\omega t)}{\frac{\pi \cdot I_o}{2} \cdot \sin(\omega t)} = \frac{\frac{4 \cdot V_o}{\pi}}{\frac{\pi \cdot I_o}{2}} = \frac{8}{\pi^2} \cdot \frac{V_o}{I_o} = \frac{8}{\pi^2} \cdot R_o \tag{3.4}$$

Considering the transformer turns ratio ($n = N_p/N_s$), the equivalent load resistance R_{ac} shown in the primary side is obtained as:

$$R_{ac} = \frac{8 \cdot n^2}{\pi^2} \cdot R_o \tag{3.5}$$

Where $R_o = V_o/I_o$ is the load resistance (that represents the battery bank). The equivalent load resistance includes the effect of the output rectifier and load resistance.

Using the equivalent load resistance, the circuit from Figure 3.9 can be simplified to do the theoretical analysis using the AC equivalent circuit shown in Figure 3.11, where $V_{DS2,1}$ is the fundamental component of the square voltage wave V_{DS2} and, $V_{Rac,1}$ is the reflected output voltage.

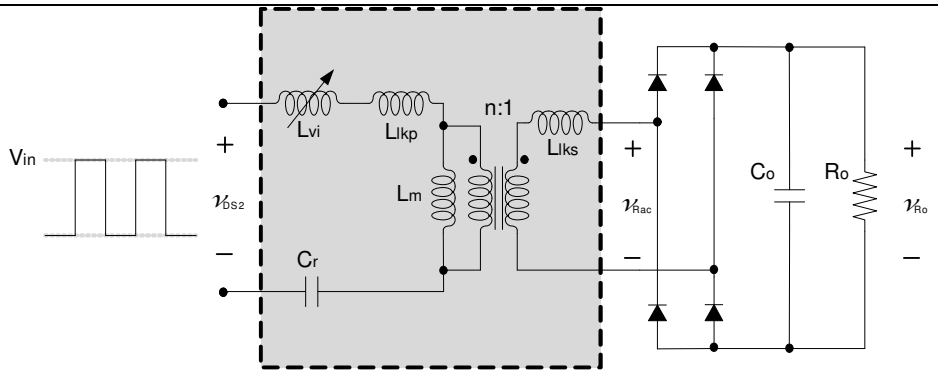

Figure 3.11 – AC equivalent circuit for LLC-VI resonant converter [29]

With the equivalent load resistance from (3.5) the voltage gain M, expression can be derived in order to characterize the LLC resonant converter. From the AC equivalent circuit from Figure 3.11, M can be obtained as [27]:

$$M = \frac{V_{Ro,1}}{V_{DS2,1}} = \frac{n \cdot V_{Rac,1}}{V_{DS2,1}} = \frac{\frac{4n \cdot V_o}{\pi} \cdot \sin(\omega t)}{\frac{4 \cdot V_o}{2 \cdot \pi} \cdot \sin(\omega t)} = \frac{2n \cdot V_o}{V_{in}} \tag{3.6}$$

3.4.1. Design Methodology and Converter Parameters Design

The design methodology starts by determining the resonant tank parameters (L_r, L_p and C_r) assuming the traditional FHA method followed by [27], considering the nominal operating point as reference.

The following condition is considered at the nominal operating point: $L_{vi} = 0$. As previously mentioned, the LLC converter has two resonant frequencies: $\omega_0 = 2\pi f_0$ determined by L_r and C_r and $\omega_p = 2\pi f_p$, determined by L_p and C_r, where $L_m = L_p - L_{lkp}$ and $L_r = L_{lkp} + L_m//(n^2 L_{lks})$. In a transformer if the secondary side winding is open or short-circuited, L_p and L_r can be measured, respectively. Following the procedure presented in [27] and assuming that $L_{lkp} = n^2 L_{lks}$ the voltage gain for this converter can be expressed as [10]:

$$M(j\omega) = \frac{2n \cdot V_o}{V_{in}} = \left| \frac{\left(\frac{\omega^2}{\omega_p^2}\right)\frac{k}{k+1}}{j\left(\frac{\omega}{\omega_0}\right) \cdot \left(1 - \frac{\omega^2}{\omega_0^2}\right) \cdot Q\frac{(k+1)^2}{2k+1} + \left(1 - \frac{\omega^2}{\omega_p^2}\right)} \right| \tag{3.7}$$

Where $Q = \frac{\sqrt{L_r/C_r}}{R_{ac}}$ and $k = \frac{L_m}{L_{lkp}}$ and is typically $k \in [5; 10]$ according to [9]. An analysis of the impact of the parameter k in the converter design is presented in the Appendix A.2. With this simplification, a minimum voltage gain at ω_0 can be obtained as $M_{\omega \to \omega_0} = M_{min} = \frac{k+1}{k}$.

Finally, Figure 3.11 may be redesigned in terms of L_p and L_r as shown in Figure 3.12, where an ideal transformer is included and $L_r = L_{lkp} + L_m // L_{lkp}$ and $L_p = L_{lkp} + L_m$. In this case, L_{vi} is kept at zero as referred before in order to determine the converter parameters for the nominal point of operation.

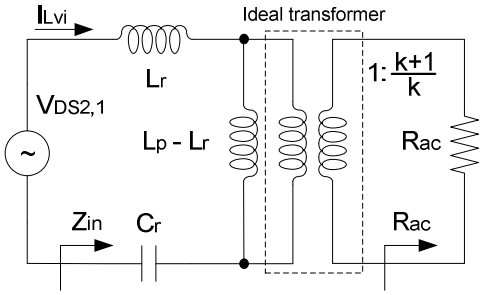

Figure 3.12 – Simplified AC equivalent circuit for LLC resonant converter [29]

Assuming an input voltage variation of 10% to 15%, the maximum gain can be calculated as:

$$M_{\max} = \frac{V_{in\_\max}}{V_{in\_\min}} \cdot M_{\min} \tag{3.8}$$

In order to identify the value of Q (for the calculation of the resonant parameters), it is necessary to find the peak gain curves as function of Q and intersect them with the specified maximum gain (assuming a variable range for V_{in}). These curves for different k values are shown in Figure 3.13 and were obtained using (3.7). For a selected Q range the voltage gain is determined and the peak gain value is identified. This is repeated for different values of k.

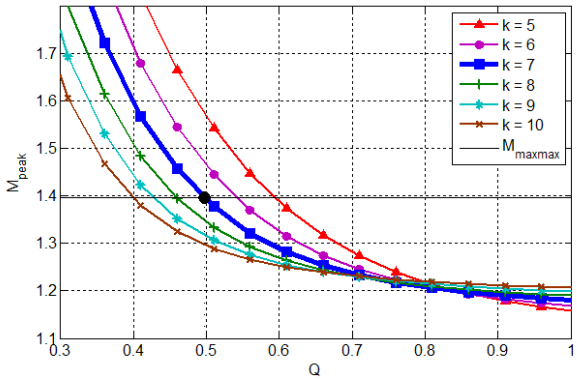

Figure 3.13 – Simplified AC equivalent circuit for LLC resonant converter [26]

The final value of Q is obtained from the intersection of the maximum gain, considering a margin of 10% ($M_{maxmax} = 1.1 * M_{max}$), and the peak gain curve for the selected k as shown in Figure 3.13. Knowing the value of Q, considering f_s and f_0, the resonant parameters can be calculated as [26]:

$$C_r = \frac{1}{2\pi Q \cdot f_0 \cdot R_{ac}} \tag{3.9}$$

$$L_r = \frac{1}{(2\pi f_0)^2 C_r} \tag{3.10}$$

$$L_p = \frac{(k+1)^2}{(2k+1)} \cdot L_r \tag{3.11}$$

Considering an output voltage ripple of 1%, the output capacitor C_o can be calculated as:

$$C_o = \frac{I_o}{V_{ripple} \cdot 2 \cdot f_s} \tag{3.12}$$

Finally, the transformer turns ratio is determined. Considering the rectifier diode voltage drop V_F, the transformer turns ratio can be determined as:

$$n = \frac{N_p}{N_s} = \frac{V_{in\_max}}{2(V_o + 2 \cdot V_F)} \cdot M_{\min} \tag{3.13}$$

3.4.2. VI Control Impact on the Design Methodology

In order to analyze the impact of the VI on the LLC converter operation, the voltage gain must be obtained as a function of this variable inductance parameter.

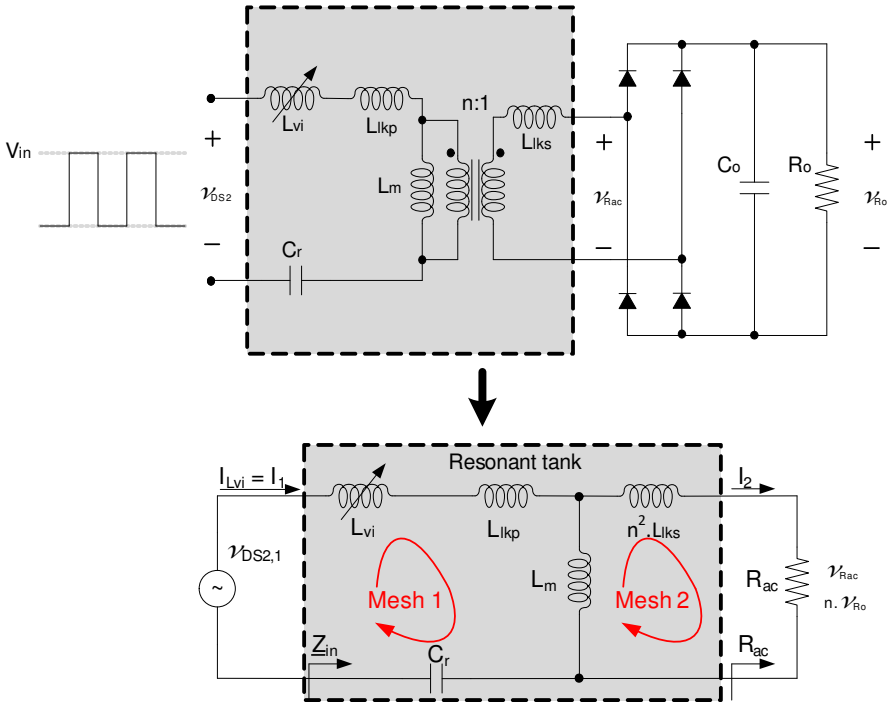

Figure 3.14 – AC equivalent circuit for LLC-VI resonant converter [29]

By analyzing the AC equivalent circuit from Figure 3.14 the input impedance of the resonant tank can be obtained as:

$$\underline{Z}_{in} = \frac{(Z_{Rac} + n^2 \cdot Z_{Llks}) \cdot Z_{Lm}}{(Z_{Rac} + n^2 \cdot Z_{Llks}) + Z_{Lm}} + Z_{Cr} + Z_{Llkp} + Z_{Lvi} \tag{3.14}$$

Where, $Z_{Rac} = R_{ac}$, $Z_{Lm} = j\omega L_m$, $Z_{Llkp} = j\omega L_{lkp}$, $Z_{Llks} = j\omega L_{lks}$, $Z_{Lvi} = j\omega L_{lvi}$ and $Z_{Cr} = \frac{1}{j\omega C_r}$. So, replacing this in (3.14) we have

$$\underline{Z}_{in} = \frac{\left(R_{ac} + n^2 \cdot j\omega L_{lks}\right) \cdot j\omega L_m}{\left(R_{ac} + n^2 \cdot j\omega L_{lks}\right) + j\omega L_m} + \frac{1}{j\omega C_r} + j\omega L_{lkp} + j\omega L_{vi} \tag{3.15}$$

And the phase angle of the input current is

$$\varphi_{in} = \arg\left(\frac{1}{Z_{in}}\right) \cdot \frac{180}{\pi} \tag{3.16}$$

Applying Kirchhoff's Laws to mesh 1 of Figure 3.14.

$$\begin{aligned}
\underline{V}_{in} &= \left(Z_{Cr} + Z_{Llkp} + Z_{Lvi}\right) \cdot \underline{I}_1 + Z_{Lm} \cdot \left(\underline{I}_1 - \underline{I}_2\right) \\
\underline{V}_{in} &= \left(Z_{Cr} + Z_{Llkp} + Z_{Lvi} + Z_{Lm}\right) \cdot \underline{I}_1 - Z_{Lm} \cdot \underline{I}_2 \\
\underline{V}_{in} &= \left(\frac{1}{j\omega C_r} + j\omega L_{lkp} + j\omega L_{vi} + j\omega L_m\right) \cdot \underline{I}_1 - j\omega L_m \cdot \underline{I}_2
\end{aligned} \tag{3.17}$$

And, in mesh 2

$$\begin{aligned}
0 &= \left(Z_{Rac} + n^2 \cdot Z_{Llks}\right) \cdot \underline{I}_2 + Z_{Lm}\left(\underline{I}_2 - \underline{I}_1\right) \\
0 &= \left(Z_{Rac} + n^2 \cdot Z_{Llks} + Z_{Lm}\right) \cdot \underline{I}_2 - Z_{Lm} \cdot \underline{I}_1 \\
0 &= \left(R_{ac} + j\omega n^2 L_{lks} + j\omega L_m\right) \cdot \underline{I}_2 - j\omega L_m \cdot \underline{I}_1
\end{aligned} \tag{3.18}$$

Rewriting (3.18) it turns into

$$\begin{aligned}
0 &= \left(R_{ac} + j\omega n^2 L_{lks} + j\omega L_m\right) \cdot \underline{I}_2 - j\omega L_m \cdot \underline{I}_1 \\
\left(R_{ac} + j\omega n^2 L_{lks} + j\omega L_m\right) \cdot \underline{I}_2 &= j\omega L_m \cdot \underline{I}_1 \\
\frac{\underline{I}_1}{\underline{I}_2} &= \frac{R_{ac} + j\omega n^2 L_{lks} + j\omega L_m}{j\omega L_m} \\
\underline{I}_1 &= \underline{I}_2 \cdot \left(\frac{R_{ac} + j\omega n^2 L_{lks} + j\omega L_m}{j\omega L_m}\right) \\
\underline{I}_1 &= \underline{I}_2 \cdot \left(\frac{R_{ac} + j\omega n^2 L_{lks}}{j\omega L_m} + 1\right)
\end{aligned} \tag{3.19}$$

From (3.17) and (3.19) we obtain

$$\begin{aligned}
\underline{V}_{in} &= \left(\frac{1}{j\omega C_r} + j\omega L_{lkp} + j\omega L_{vi} + j\omega L_m\right)\cdot\left(\frac{R_{ac} + j\omega n^2 L_{lks}}{j\omega L_m} + 1\right)\cdot \underline{I}_2 - j\omega L_m \cdot \underline{I}_2 \\
\underline{V}_{in} &= \left[\left(\frac{1}{j\omega C_r} + j\omega L_{lkp} + j\omega L_{vi} + j\omega L_m\right)\cdot\left(\frac{R_{ac} + j\omega n^2 L_{lks}}{j\omega L_m} + 1\right) - j\omega L_m\right]\cdot \underline{I}_2 \\
\frac{\underline{V}_{in}}{\underline{I}_2} &= \left(\frac{1}{j\omega C_r} + j\omega L_{lkp} + j\omega L_{vi} + j\omega L_m\right)\cdot\left(\frac{R_{ac} + j\omega n^2 L_{lks}}{j\omega L_m} + 1\right) - j\omega L_m \\
\underline{I}_2 &= \underline{V}_{in}\cdot\frac{1}{\left(\frac{1}{j\omega C_r} + j\omega L_{lkp} + j\omega L_{vi} + j\omega L_m\right)\cdot\left(\frac{R_{ac} + j\omega n^2 L_{lks}}{j\omega L_m} + 1\right) - j\omega L_m}
\end{aligned} \tag{3.20}$$

Considering the output voltage $\underline{V_O} = R_{ac} * \underline{I_2}$, and $\underline{I_2}$ (3.20), the output voltage can be written as:

$$\begin{aligned}
\underline{V}_o &= R_{ac}\cdot \underline{I}_2 \\
\underline{V}_o &= R_{ac}\cdot\frac{1}{\left(\frac{1}{j\omega C_r} + j\omega L_{lkp} + j\omega L_{vi} + j\omega L_m\right)\cdot\left(\frac{R_{ac} + j\omega n^2 L_{lks}}{j\omega L_m} + 1\right) - j\omega L_m}\cdot \underline{V}_{in}
\end{aligned} \tag{3.21}$$

Or as a ratio between voltages:

$$\frac{\underline{V}_o}{\underline{V}_{in}} = \frac{R_{ac}}{\left(\frac{1}{j\omega C_r} + j\omega L_{lkp} + j\omega L_{vi} + j\omega L_m\right)\cdot\left(\frac{R_{ac} + j\omega n^2 L_{lks}}{j\omega L_m} + 1\right) - j\omega L_m} \tag{3.22}$$

So, the voltage gain M can be obtained as:

$$M(j\omega) = \frac{\underline{V}_o}{\underline{V}_{in}} = \frac{R_{ac}}{\left(\frac{1}{j\omega C_r} + j\omega L_{lkp} + j\omega L_{vi} + j\omega L_m\right)\cdot\left(\frac{R_{ac} + n^2\cdot j\omega L_{lks}}{j\omega L_m} + 1\right) - j\omega L_m} \tag{3.23}$$

In order to calculate the limits of variation to the control variables range, the output power expression is needed.

$$P_o = \frac{V_o^2}{R_o} \tag{3.24}$$

From (3.6), the output voltage can also be written as

$$\begin{aligned}
M &= \frac{2n\cdot V_o}{V_{in}} \\
2n\cdot V_o &= M\cdot V_{in} \\
V_o &= M\cdot\frac{V_{in}}{2n}
\end{aligned} \tag{3.25}$$

So, the output power can be obtained as:

$$P_o = \frac{V_o^2}{R_o} = \frac{\left(\left|M(j\omega)\right| \cdot \frac{V_{in}}{2n}\right)^2}{R_o} = \frac{\left(\frac{V_{in}}{2n}\right)^2}{R_o} \cdot \left|M(j\omega)\right|^2 \tag{3.26}$$

Which leads to the final output power expression, using (3.23) and (3.26) shown in (3.27).

$$P_o = \frac{\left(\frac{V_{in}}{2n}\right)^2}{R_o} \cdot \left| \frac{R_{ac}}{\left(\frac{1}{j\omega C_r} + j\omega L_{lkp} + j\omega L_{vi} + j\omega L_m\right) \cdot \left(\frac{R_{ac} + n^2 \cdot j\omega L_{lks}}{j\omega L_m} + 1\right) - j\omega L_m} \right|^2 \tag{3.27}$$

At this point, the equations that allow designing the resonant circuit, understanding its behavior and operation and finally obtaining the range of the control variables to have the desire output variation were determined. The next section will present an analysis describing the impact of the control variables in use.

3.5. Control Variables Impact on the Design Methodology

In order to perform the control of the converter two control variables will be considered, f_s and L_{vi}. This section will analyze both their impact on the design methodology and converter operation.

3.5.1. VI Control Method

Using the VI principle as control method, L_{vi} is the control variable so, in (3.23) L_{vi} is variable and f_s is kept constant at the design value. Figure 3.15 presents the gain curves as function of L_{vi}, $M(L_{vi})$ at 10 kHz and 100 kHz using (3.23). Figure 3.15 a) presents these curves for different load values. It is possible to observe that a higher frequency leads to a narrower voltage gain peak. The previous resonance point considered in the design methodology, for $f_s = f_0$, occurs now when L_{vi} is zero. At this point, the voltage gain is independent of load and frequency variations. In this case since the value of L_{vi} changes, so does the resonance frequency. Mathematically, resonance may occur for negative values of L_{vi}. Since a negative value of L_{vi} is not possible, it implies that the real operating region will always be a ZVS inductive region. From Figure 3.15 b) it can be seen that for a given voltage gain variation, ΔM, when the frequency is higher (100 kHz) the variation of inductance needed to obtain that gain variation (ΔL_{vi}) is smaller when compared to a lower frequency (10 kHz) gain curve. Therefore, for the same inductance range, a higher value of f_s will lead

to a higher controllable range of the output. Increasing f_s enables circuit miniaturization and operating at constant f_s facilitates the design of the EMI filter [29].

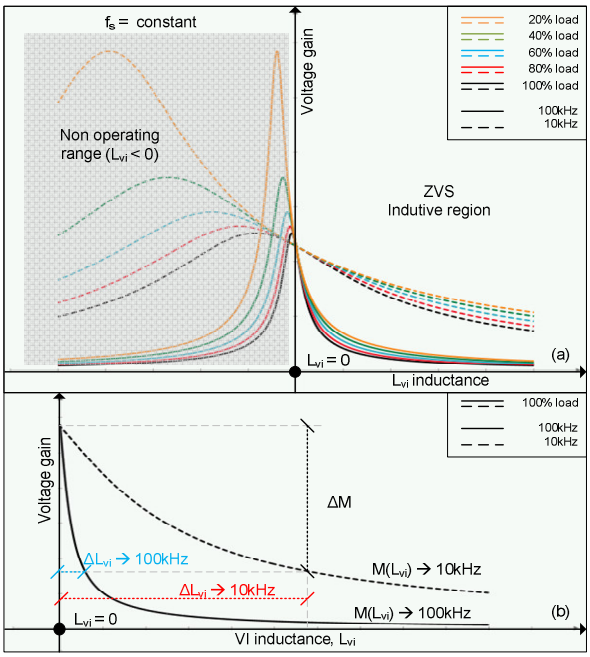

Figure 3.15 – Gain curves as function of L_{vi} at 10 kHz and 100 kHz: a) $M(L_{vi})$ at different load levels; b) $M(L_{vi})$ at full-load [29]

This converter has inherent no-load and short-circuit protection. For short-circuit conditions, the resonant current would be limited by L_{vi}. For no-load, this current is equal to the magnetizing current of the transformer. Therefore, using the variable inductance concept, the converter can provide a controllable output and be operated at constant switching frequency f_s, advantageous regarding EMC (electromagnetic compatibility) and miniaturization issues, without compromising reliability and performance [29]. Using VI control, and, since L_{vi} value cannot be negative, for the real implementation, the range of the VI as always values greater than zero with possibility of the minimum value being $L_{vi} = 0$.

In order to identify the required inductance range for the application, the output power must be calculated using (3.27).

Considering the voltage and current profiles presented in Figure 3.2 a), the output power for the three levels of SOC corresponding to L_{vi_0}, L_{vi_90} and, L_{vi_100} can be obtained by using (3.27). The results are shown in Figure 3.16.

By intersecting the gain curves of Figure 3.16 with the defined power levels, L_{vi_0}, L_{vi_90} and, L_{vi_100} are obtained. The inductance range is defined with L_{vi_0} and L_{vi_100}. The procedure for the construction of the VI can be found in previous literature [15], [21] and is presented in the Appendix B attached to this work.

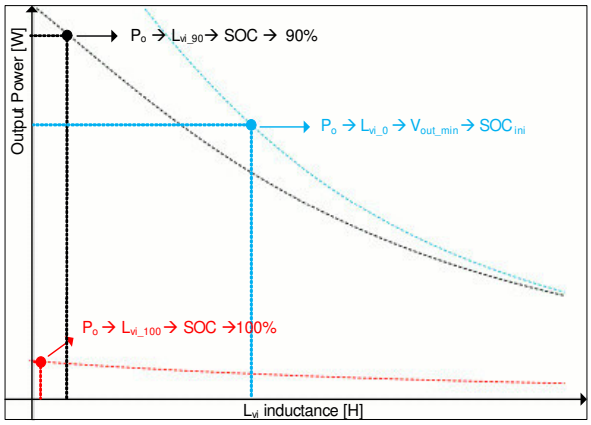

Figure 3.16 – Output power as function of of L_{vi}, $P_o(L_{vi})$ for the operating points corresponding to L_{vi_0}, L_{vi_90} and L_{vi_100} [29]

3.5.2. Switching Frequency Control Method

In order to analyze the impact of the switching frequency on the LLC resonant converter operation, the voltage gain must be obtained as a function of the switching frequency, f_s.

Similar to the VI control method, (3.23) can be used to obtain the gain curves as function of f_s. In this case, L_{vi} is not considered and is set to be zero in (3.23). The variation of f_s is made by knowing that $\omega = 2 * \pi * f_s$. Figure 3.17 presents the gain curves as function of f_s, $M(f_s)$ considering a design for 10 kHz and 100 kHz. Figure 3.17 a) presents these curves for different load values. In this case, unlike the previous one, it is possible to observe that considering the design for a lower frequency leads to a narrower voltage gain peak. At and around resonance, the voltage gain is independent of the load and frequency variation (this is one of the advantageous of this LLC frequency controlled resonant converter). As the resonant filter components are constant, f_0 is always constant even with f_s variation. Since the converter is designed initially to operate at resonance considering the maximum power in the output at this point, and that in normal operation, it will only operate at or above f_0 to regulate the output, ZVS is always guaranteed. From Figure 3.17 b) it can be seen that for a given voltage gain variation, ΔM, when the design frequency is higher (100 kHz) the variation of f_s needed to obtain that gain variation (Δf_s) is higher when compared to a lower frequency design (10 kHz) gain curve. Therefore, for the same f_s range, when the design is for a lower value of f_s it will lead to a higher controllable range of the output. Nevertheless, from Figure 3.17 a) above resonance, if the frequency of design is higher, the operation is less load dependent although it allows less output regulation with the same variation of f_s. Another advantage of increasing the design frequency is that enables circuit miniaturization.

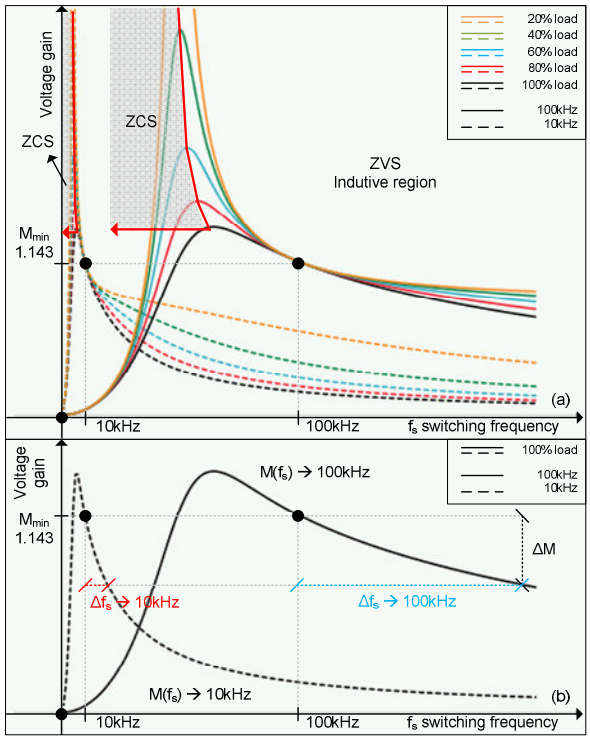

Figure 3.17 – Gain curves as function of f_s for 10 kHz and 100 kHz design: a) $M(f_s)$ at different load levels; b) $M(f_s)$ at full-load [29]

Using f_s control, the minimum and maximum values need to be limited because if f_s becomes lower, for a certain value the converter changes from ZVS to ZCS operation or vice-versa and depending on the application this may be critical. So, the controller must be able to limit the limits for f_s variation.

Similar to the previous case, in order to identify the required frequency range for the application, the output power must be calculated. In this case, the output power is calculated using (3.27) where $\omega = 2 * \pi * f_s$ and, L_{vi} is kept at zero ($L_{vi} = 0$). In this case, f_s is the control variable.

Considering the voltage and current profiles presented in Figure 3.2 b), the output power for the three levels of SOC corresponding to f_{s_0}, f_{s_90} and, f_{s_100} can be obtained using (3.27). The results are shown in Figure 3.18.

By intersecting the gain curves of Figure 3.18 with the defined power levels, f_{s_0}, f_{s_90} and, f_{s_100} are obtained. The frequency range is defined with f_{s_0} and f_{s_100}.

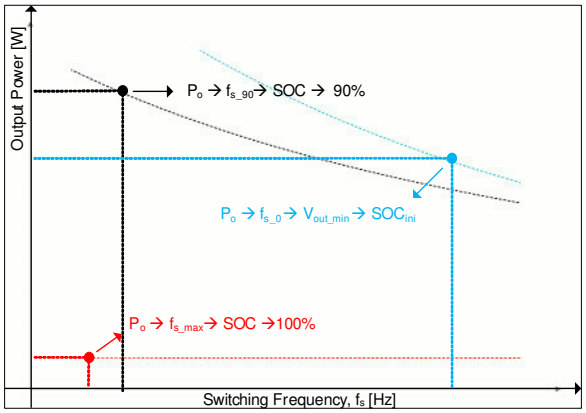

Figure 3.18 – Output power as function of of f_s, $P_o(f_s)$ for the operating points corresponding to f_{s_0}, f_{s_90} and f_{s_100} [29]

3.5.3. Simultaneous use of Both Control Methods

Figure 3.19 presents the gain curves as function of f_s, $M(f_s)$ considering a design for 100 kHz. From Figure 3.19, it can be seen that using both control methods simultaneously can be advantageous. It is possible to obtain the same gain M with a smaller value of f_s by increasing the L_{vi} value. This would imply pushing the operating point from A to B or C as shown in Figure 3.19.

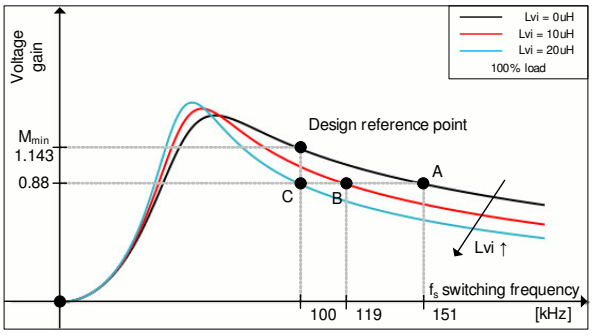

Figure 3.19 – Gain curves as function of f_s for 100 kHz design for three different values of L_{vi} at full-load (100% load) [29]

As can be seen, using either one of the control techniques the converter is able to have the needed output regulation to charge the batteries. Also, if the two control variables are used simultaneously, the converter as enough output regulation to control the charging of the batteries. The possibility of using both control variables simultaneously can be further studied in order to try to improve the converter efficiency and operation and possibly be more advantageous.

4. Simulation Results

In order to validate the proposed converter topology, simulations in PSIM (Power Electronics Simulation Software) were carried out. This chapter presents the simulation results obtained considering both control variables separately and also considering a particular case of mixing both control variables.

4.1. Converter Parameters

Considering the design methodology and equations presented in section 3.4 and considering the design specifications from Table 3.1 the design parameters were obtained and the results are present in Table 4.. The design procedure and results are presented with more detail in the Appendix A.1 attached to this work.

The converter parameters used in the simulation are presented in Table 4. which were obtained by applying the proposed design methodology presented above.

Table 4.1 – Converter parameters for simulation

Description		Specification
Main parameters		$V_{in} = 400V;\ f_s = 100kHz;\ d = 0.5$
Magnetic devices	L_{vi}	$L_{vi\_min} = 0.98\mu H\ ;\ L_{vi\_max} = 21.1\mu H$
	Transformer	$k = 7\ ;\ n = 1.95$
		$L_{lkp} = 15.11\mu H\ ;\ L_{lks} = 3.97\mu H\ ;\ L_m = 105.75\mu H$
C_r , C_o , Load		$89.42nF\ ;\ 43\mu F\ ;\ R_o \geq 8.4\Omega$

4.2. Simulation Results

The simulation results presented below were obtained under open-loop control condition and are referred to VI and frequency control methods, in sub-sections 3.5.1 and 3.5.2, respectively. Figure 4.1 shows the simulation schematic in PSIM software used to obtain the simulation results.

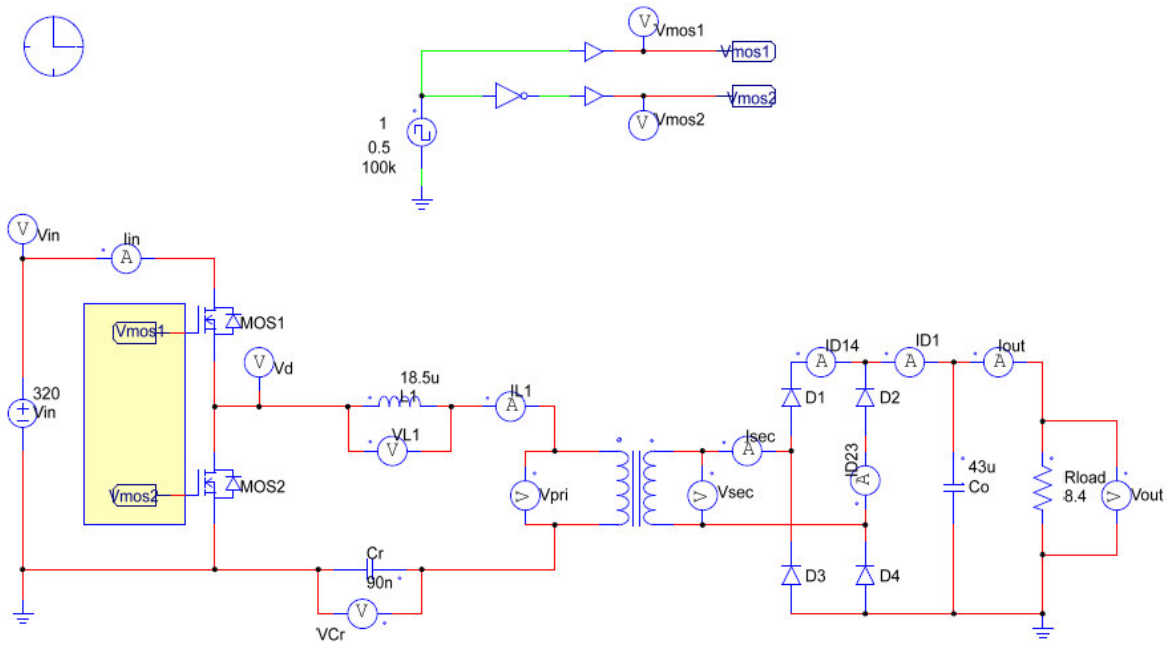

Figure 4.1 – PSIM circuit for obtaining the simulation results

4.2.1. VI Control Method

The simulation results referred to the VI control method are shown in Figure 4.2 and are referred to operating points L_{vi_0}, L_{vi_90} and L_{vi_100} (red, green and blue, respectively) obtained from Figure 3.2 b). Figure 4.2 a) and Figure 4.2 b) show respectively the driver signals for S_1 and S_2, v_{GS1} and v_{GS2} and the resonant filter input voltage, v_{DS2}. Figure 4.2 c), Figure 4.2 d), Figure 4.2 f) and Figure 4.2 g) show respectively the input current, i_{S1}, the current in the resonant tank, i_{Lvi}, the current in the rectifier diodes, i_D and the output current, i_{out}. Finally, Figure 4.2 e) and Figure 4.2 h) show respectively the voltage at the VI terminals, v_{Lvi} and the output voltage, v_{out}.

During the CCS the range of the VI is $[L_{vi\_0}; L_{vi\_90}]$. When charging begins, $L_{vi} = L_{vi\_0}$, $I_{out} = 10A$ and $V_{out} = 84V$ which corresponds to its minimum value. When CCS ends, $L_{vi} = L_{vi\_90}$, $I_{out} = 10A$ and $V_{out} = 112{,}8V$ (SOC $\approx 90\%$). The controller switches from CCS to VCS, and the battery voltage increases to its maximum value, $V_{out} = 116V$ and the charging current tends naturally to its float value. At this point, $L_{vi} \rightarrow L_{vi\_100}$.

The converter operates always above resonance with ZVS. When the charging process begins the rectifier diodes operate in CCM (continuous conduction mode). The analysis of i_D shows however that the converter enters in DCM (discontinuous conduction mode). When the batteries are almost fully charged the behavior of the converters tends to an open circuit and

the current through the VI, i_{Lvi_100} exhibits a triangular shape waveform similar to what would be expected for the magnetizing current, i_{Lm}.

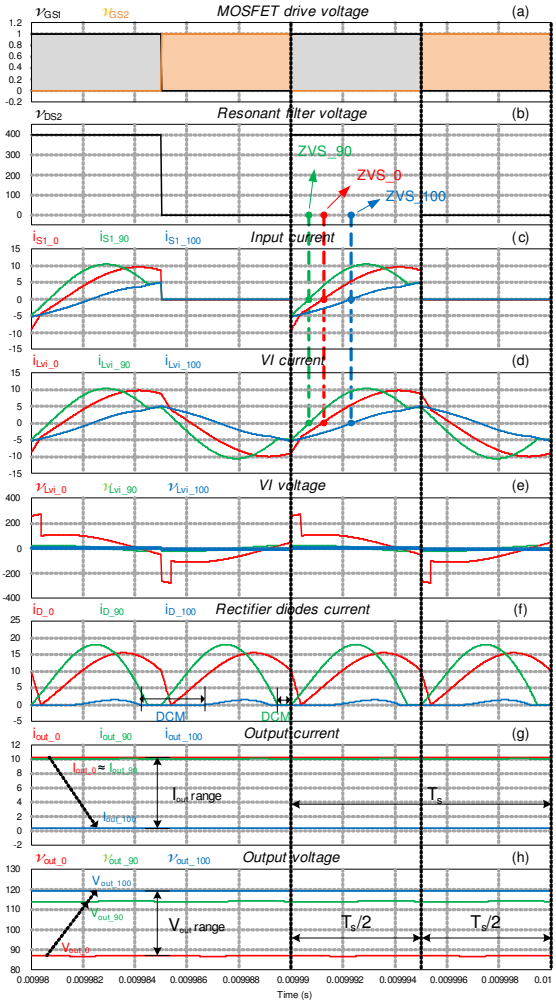

Figure 4.2 – Waveforms from simulation which represent the three points of operation correspondent to L_{vi_0}, L_{vi_90} and L_{vi_100}, in red, green and blue, respectively: (a) $v_{GS1}$and v_{GS2}; (b) v_{DS2} ; (c) i_{S1}; (d) i_{Lvi}; (e) v_{Lvi}; (f) i_D; (g) i_{out}; (h) v_{out} [29]

4.2.2. Switching Frequency Control Method

The simulation results referred to the frequency control method are shown in Figure 4.3 and are referred to operating points f_{s_0}, f_{s_90} and f_{s_100} (red, green and blue, respectively) obtained from Figure 3.2 a). Figure 4.3 a) to Figure 4.3 c) show respectively the driver signals for S_1 and S_2, v_{GS1} and v_{GS2}, for f_{s_0}, f_{s_90} and f_{s_100} respectively. Figure 35 d) shows the resonant filter input voltage, v_{DS2}. Figure 4.3 e), Figure 4.3 f), Figure 4.3 g) and Figure 4.3 h) show respectively the input current, i_{S1}, the current in the resonant tank, i_{Lvi}, the current in the rectifier diodes, i_D and the output current, i_{out}. Finally, Figure 4.3 i) shows the output voltage, v_{out}.

Similar to the previous case, during the CCS the range of the f_s is $[f_{s\_0}; f_{s\_90}]$. When charging begins, $f_s = f_{s\_0}$, $I_{out} = 10A$ and $V_{out} = 84V$ which corresponds to its minimum value.

When CCS ends, $f_s = f_{s\_90}$, $I_{out} = 10A$ and $V_{out} = 112{,}8V$ (SOC $\approx 90\%$). The controller switches from CCS to VCS, and the battery voltage increases to its maximum value, $V_{out} = 116V$ and the charging current tends naturally to its float value. At this point, $f_s \rightarrow f_{s\_100}$. The converter operates always above resonance with ZVS. When the charging process begins the rectifier diodes operate in CCM (continuous conduction mode). The analysis of i_D shows however that the converter enters in DCM (discontinuous conduction mode). When the batteries are almost fully charged the behavior of the converters tends to an open circuit and the current through the VI, i_{Lvi_100} exhibits a triangular shape waveform similar to what would be expected for the magnetizing current, i_{Lm}.

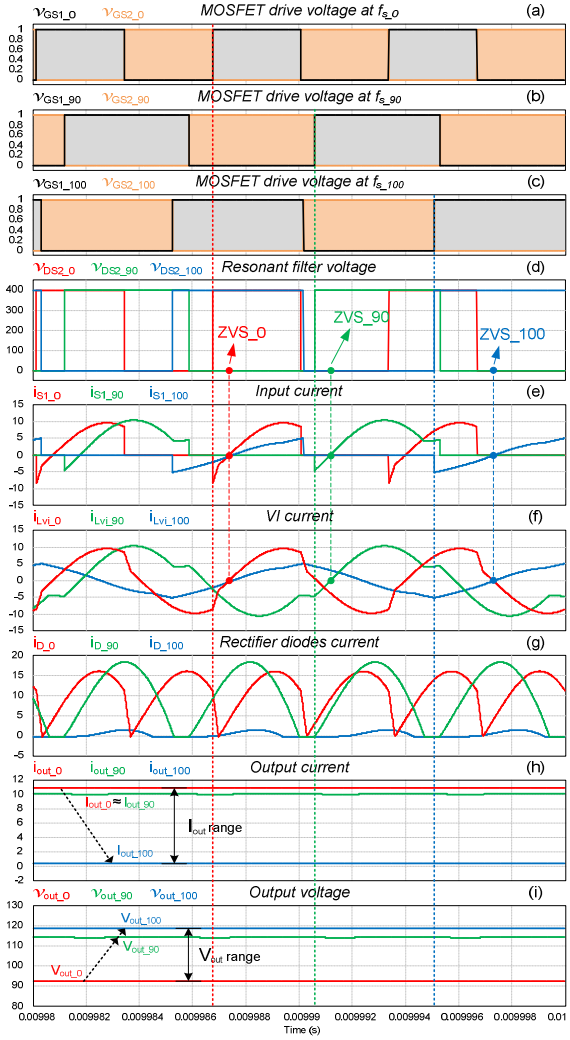

Figure 4.3 – Waveforms from simulation which represent the three points of operation correspondent to L_{vi_0}, L_{vi_90} and L_{vi_100}, in red, green and blue, respectively: (a) v_{GS1} and v_{GS2} for f_{s_0}; (b) v_{GS1} and v_{GS2} for f_{s_90}; (c) $v_{GS1}$and v_{GS2} for f_{s_100}; (d) v_{DS2} ; (e) i_{S1}; (f) i_{Lvi}; (g) i_D; (h) i_{out}; (i) v_{out} [29]

Table 4. shows the theoretical and simulation results considering VI and frequency control methods for the converter design parameters defined in Table 4.. As can be seen, the simulation results are similar to the expected theoretical results and the results for VI control are very similar to the results for frequency control.

Table 4.2 – Theoretical and simulation results

	Theoretical					Simulation		
SOC [%]	L_{vi} [µH]	f_s [kHz]	V_{out} [V]	I_{out} [A]	P_{out} [W]	V_{out} [V]	I_{out} [A]	P_{out} [W]
≈ 0	21.1	100	84	10	840	87.23	10.38	906
≈ 90	3.3	100	112.8	10	1128	114.41	10.14	1161
≈ 100	0.98	100	116	0.5	58	118.99	0.51	61
≈ 0	–	151	84	10	840	92.5	11.01	1019
≈ 90	–	106.3	112.8	10	1128	114.41	10.14	1161
≈ 100	–	101.65	116	0.5	58	118.99	0.51	61
≈ 0	10	120	84	10	840	89.38	10.64	951

From Table 4. the necessary range to regulate the output is about 20 μH considering only VI control, 50 kHz considering only f_s control and, 10 μH and 20 kHz considering VI and f_s control simultaneously. In conclusion, using both control techniques simultaneously allows the range of each control variable to be smaller when compared to the case of using only one control method.

5. Prototype and Experimental Results

In order to validate the proposed topology an experimental prototype was built. This chapter presents the details about the prototype design and experimental implementation and validation. Although the simulation results presented considered both control variables, L_{vi} and f_s, the experimental results are referred only to VI control and in open-loop condition.

During this work, two prototypes of the LLC resonant converter were built and tested. The first one using an IGBT (Insulated Gate Bipolar Transistor) based inverter operating at around 10 kHz controlled by a commercial driver from SEMIKRON. The transformer was already existent in the laboratory and the rest of the parameters were calculated and a VI prototype was built. This first prototype served only as proof of concept. The experimental results are not presented in this work but they were published at the IEEE IECON 2016 conference as can be seen in [26]. The paper can be found in the Appendix D. This prototype was built in order to verify the concept of controlling the converter using a variable resonant tank with a VI. Having validated the control method using a VI, a new prototype was built. The new prototype is presented in this chapter.

The prototype uses a SiC MOSFET based inverter operating at 100 kHz (constant frequency) controlled by a fiber optic based driver. For this prototype all of the PCB boards were designed and built in the laboratory with exception of the fiber optic drivers for the SiC MOSFET and the DSP control board. In addition, a simple rectifier was built to create the DC Bus to feed the LLC resonant converter. To simulate the load, instead of using the battery bank, a resistive load via a Programmable DC Electronic Load (BK PRECISION 8522 2400 W) with an equivalent value of the battery bank was used. The global block diagram of the build prototype is shown in Figure 5.1, as follows:

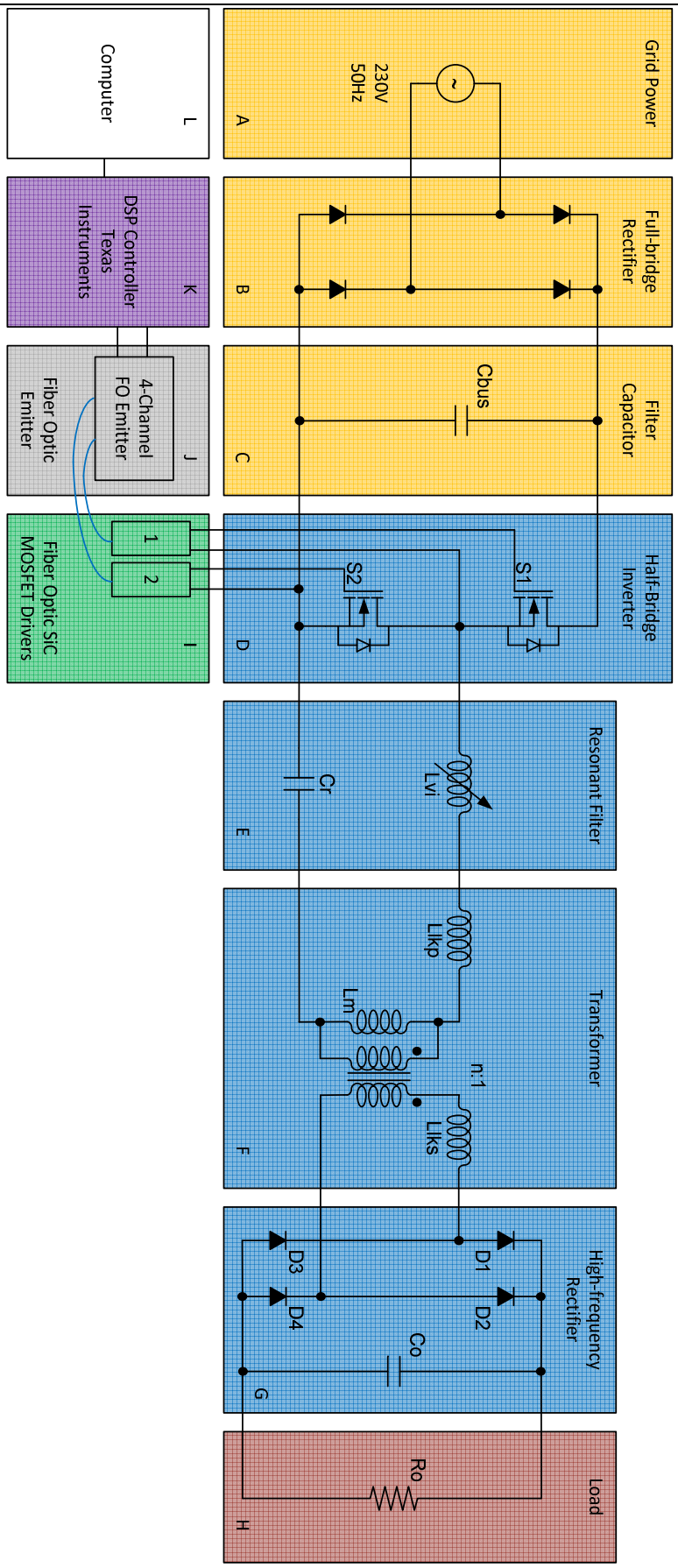

Figure 5.1 – Block diagram of the built prototype

Figure 5.1 is divided in 12 blocks, and each one corresponds to one PCB/equipment of the prototype:

- The orange blocks represent the power supply to generate the DC Bus to feed the LLC resonant converter: **A** corresponds to the grid; **B** corresponds to a full-bridge rectifier; **C** corresponds to the rectifier filter capacitor or DC bus. Block **C** generates the input voltage for the LLC resonant converter V_{in}.
- The blue blocks represent the PCBs designed to build the LLC-VI resonant converter: PCB **D** has two SiC MOSFET that constitute the half-bridge inverter; **E** has the VI, L_{vi}, and the resonant capacitor C_r; **F** has the transformer and finally **G** corresponds to the high-frequency full-bridge rectifier with filter capacitor to feed the load.
- The red block **H** corresponds to the load that is connected at the output of the LLC-VI resonant converter. During the experimental tests, the load was considered to be a programmable resistive load.
- The computer **L** is used to program the DSP control board **K** that generates the electrical signals to the fiber optic emitter **J** that converts them to fiber optic signals. The fiber optics are connected to the SiC MOSFET drivers **I** that are then connected to the SiC MOSFET in block **D**.

Experimental results will be confronted with the theoretical and simulation results to validate the design methodology and the proposed converter topology.

5.1. Converter Parameters

This work started by considering the specifications shown in Table 3.1. These specifications were used in the theoretical analysis and in the simulation to analyze the converter operation under f_s and L_{vi} control: 400 V DC Bus and 100 kHz switching frequency. When the first prototype was tested, the half-bridge inverter was built using IGBTs with commercial drivers from SEMIKRON which were limited to a 20 kHz maximum switching frequency. Therefore, a lower value, around 10 kHz was used. The converter design was adapted to obtain the converter resonant parameters. The second prototype was built using a SiC MOSFET half-bridge inverter that allows working at the initially specified 100 kHz switching frequency. Using a full-bridge rectifier to create the DC Bus from the monophasic national grid voltage, the DC Bus voltage level had to be decreased from 400 V to 320 V. Considering these changes, the converter design was done under the new system specifications and the new converter parameters are shown in Table 5..

Table 5.1 – Converter parameters for simulation and experimental prototype

Description		Specification
Main parameters		$V_{in} = 320V;\ f_s = 100\ kHz;\ d = 0.5$
SiC MOSFET (S_1 and S_2)		MOSFET Channel N – SPW24N60C3; $650V$; $24.3A$; 0.16Ω
D_1 , D_2, D_3 and D_4		80EPF12 ; $V_F = 1.2V$; $40A$; $1200V$
Theoretical design		
Magnetic devices	L_{vi}	$L_{vi\_min} = 3.5\mu H$; $L_{vi\_max} = 18.5\mu H$
	Transformer	$k = 7$; $n = 1.6$
		$L_{lkp} = 13.06\mu H$; $L_{lks} = 5.24\mu H$; $L_m = 91.41\mu H$
C_r , C_o , Load		$90nF$; $43\mu F$; $R_o \geq 8.4\Omega$
Simulation and experimental parameters		
Magnetic devices	L_{vi}	$L_{vi} = 5.56\mu H \rightarrow 17.66\mu H$
		$N_{ac} = 8$; $N_{dc} = 170\ (2\times)$
		ETD44/22/15 core ; N87 material ; $0.5mm$ air-gap
		$n = 1.6$; $N_p = 19$; $N_s = 12$
	Transformer	ETD 44/22/15 core ; N87 material ; $1mm$ air-gap
		$L_{lkp} = 13.06\mu H$; $L_{lks} = 5.24\mu H$; $L_m = 91.41\mu H$
C_r , C_o , Load		$90nF$; $680\mu F$; $R_o = 5.6\Omega \rightarrow 232\Omega$

The VI was designed and built considering the LabVIEW software presented in the Appendix B and using a Mathcad file also presented in Appendix B. The LabVIEW software was the result of a previous work done by Samuel Ferreira during his Master Thesis [16] and, the Mathcad file was adapted from a file used by Marco Martins during his Master Thesis [17]. The parameters for the construction of the VI are presented in Table 5..

5.2. Prototype Construction

In order to build the prototype different components and PCB boards were designed. The details of the PCBs design and construction are shown in the Appendix C. The full LLC-VI resonant converter assembly is shown in Figure 5.2.

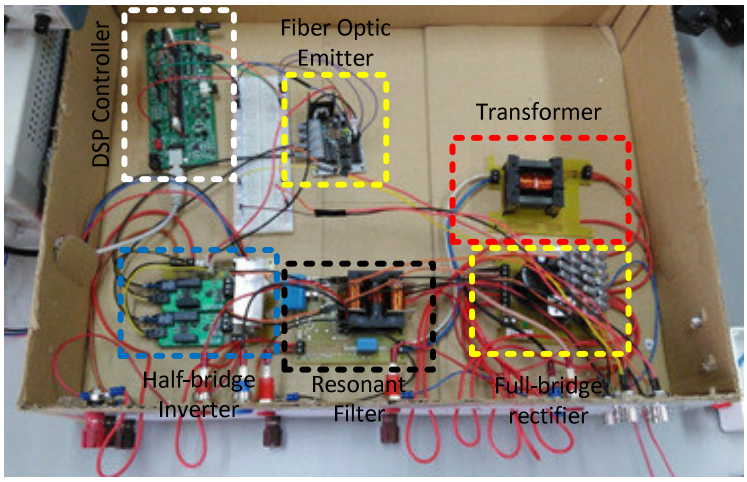

a)

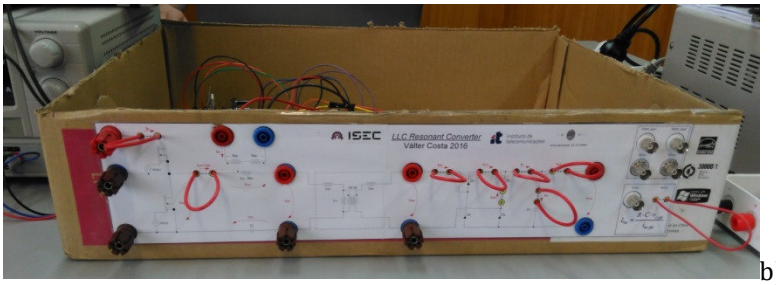

b)

Figure 5.2 – LLC-VI resonant converter full assembly: a) Top view (520 x 400 mm); b) Front view

The full experimental setup for testing the LLC-VI resonant converter and for obtaining the experimental results is shown in Figure 5.3.

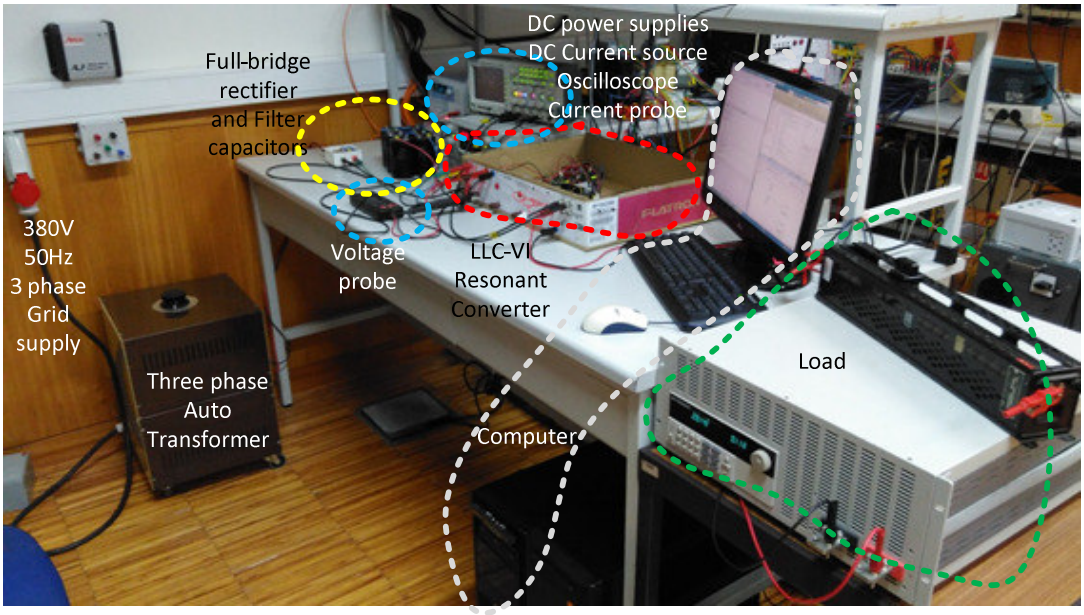

Figure 5.3 – Full experimental setup for the LLC-VI resonant converter

5.3. Experimental Results

The prototype assembly, shown in Figure 5.3 was tested in the laboratory and the experimental results are shown in this section. Since the prototype is not yet optimized, the experimental results were obtained at 1/4 of the input voltage nominal level ($V_{in} = 80\,V$ instead of $V_{in} = 320\,V$). The proper design of snubber circuits for the half-bridge inverter is still under development as well as the optimization of the transformer design. In addition closed loop control is being studied, which will enable attending higher voltage values. Nevertheless, it is possible to compare both theoretical, simulation and experimental results and validate the converter.

The theoretical results expected for $V_{in} = 80\,V$ are shown and the simulation was also adapted and performed with a DC bus of $V_{in} = 80\,V$. A snubber capacitor of 2.2 μF was inserted in parallel between the drain of S_1 and the source of S_2 in order to decrease the spikes of the square wave voltage v_{DS2}. The pulses for controlling the switching of the SiC MOSFET drivers are created by the DSP control board and converted to optic signals using the fiber optic emitter PCB built. The SiC MOSFET operate at 100 kHz with 100 ns dead-time as shown in Figure 5.4.

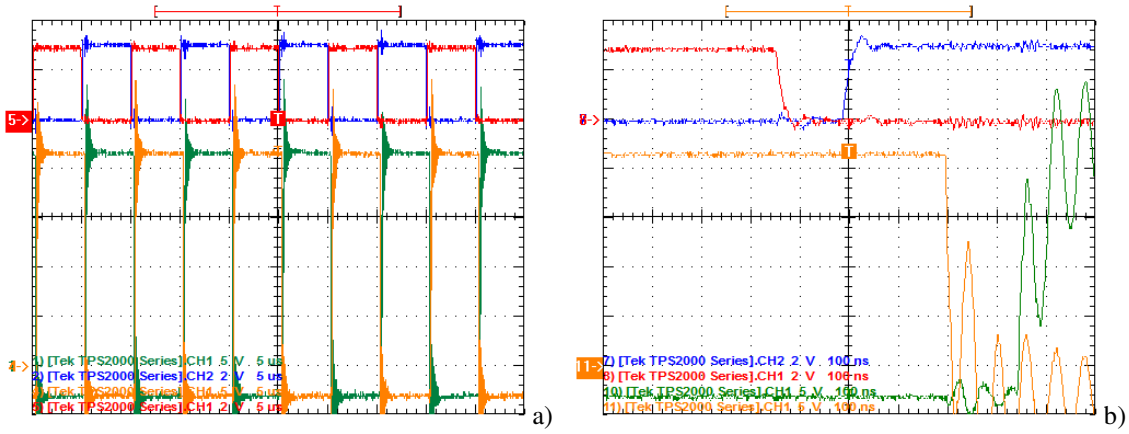

Figure 5.4 – Driver signals for S_1 and S_2. v_{mos1_dsp}, v_{mos2_dsp} in blue and red respectively (2V/div) and, v_{gs1} and v_{gs2} in green and orange respectively (5V/div): a) At 5us/div; b) At 100ns/div

As can be seen from Figure 5.4 b) the dead-time is about 100 ns, which corresponds to the time between the switching of v_{mos2_dsp} and v_{mos1_dsp}. As can be seen, the delay between the command from the DSP control board v_{mos2_dsp} and the signal of the driver to switch the SiC MOSFET transistor is about 350 ns (this delay is caused by the interface board of the fiber optic emitter, the fiber optic light propagation and the SiC MOSFET drivers operation).

The experimental tests to the prototype were made in two parts:

- Firstly, to evaluate the impact of the VI inductance variation in the converter operation
- Secondly, to simulate a charging cycle.

5.3.1. VI Impact in the Converter Operation

In this case, the load value was kept constant at 5.6 Ω (resistor load from Fig. C.13) and the VI inductance level was varied between two limit values, which correspond to $I_{dc\_max} = 1.5A$ and $I_{dc\_min} = 0A$. Note that the level of the DC Bus used was of $V_{in} = 80V$. Figure 5.5 shows the small-signal characteristic curve of the VI, $L_{vi}(I_{dc})$ obtained with a LCR meter.

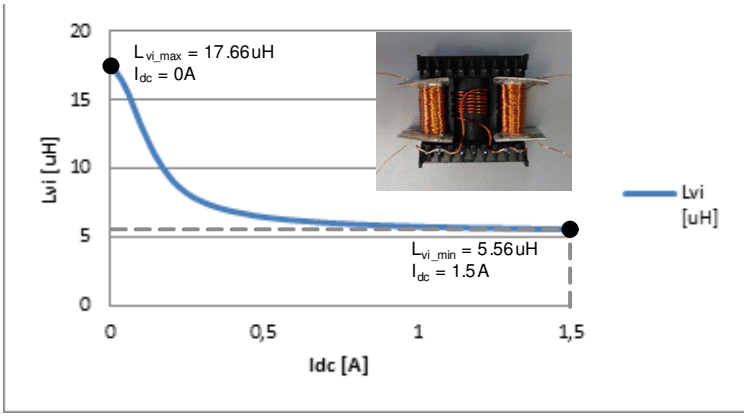

Figure 5.5 – $L_{vi}(I_{dc})$ curve

By changing the L_{vi} value between its maximum and minimum values, which correspond to a DC control current variation from 0 to 1.5 A it was possible to obtain the results shown in Figure 5.6. In Figure 5.6, the LLC-VI resonant converter voltage and current waveforms are presented. These waveforms allow understanding the converter operation. The load value was kept constant.

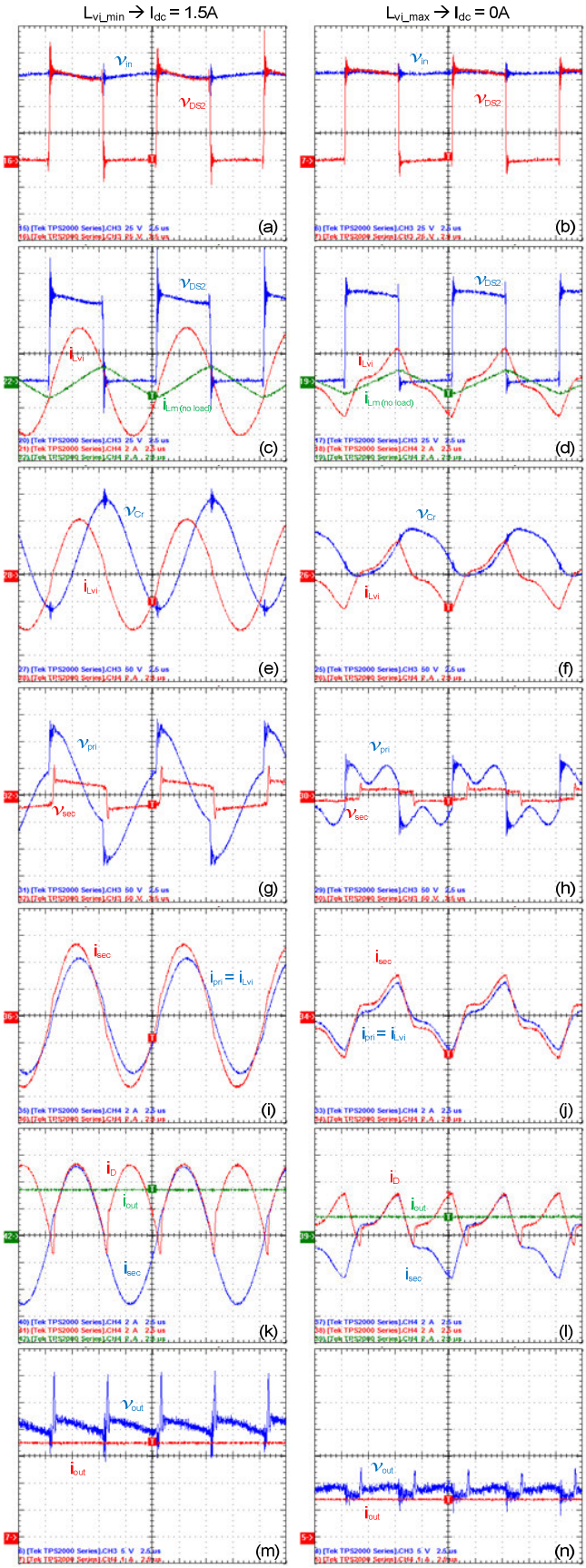

Figure 5.6 – Experimental results for L_{vimin} and L_{vimax}, left and right, respectively: (a) and (b) v_{DS2} and, V_{in}, 25V/div; (c) and (d) i_{Lvi}, v_{DS2} and, i_{Lm}, 50V/div, 2A/div; (e) and (f) i_{Lvi} and, v_{Cr}, 50V/div, 2A/div; (g) and (h) v_{sec} and, v_{pri}, 50V/div; (i) and (j) i_{sec} and, $i_{pri} = i_{Lvi}$,, 2A/div; (k) and (l) i_{sec}, i_D and, I_{out}, 2A/div; (m) and (n) I_{out} and, V_{out}, 5V/div, 1A/div; With 2.5us/div

The experimental waveforms obtained for the converter operation at the two VI prototype limits, L_{vi_min} and L_{vi_max} are shown in Figure 5.6. In the left side, the results correspond to L_{vi_min} for $I_{dc} = 1.5$ A and, in the right side, they correspond to L_{vi_max} for $I_{dc} = 0$ A.

Figure 5.6 a) and b) show the DC Bus voltage and the square wave voltage created by the half-bridge inverter, V_{in} and v_{DS2} respectively for L_{vi_min} and L_{vi_max}. It can be seen that changing the inductance value, the voltage level at the input and the square wave voltage maximum value is about the same with a slightly higher ripple and spikes in the commutation for L_{vi_min}.

Figure 5.6 c) and d) show v_{DS2} and the resonant current i_{Lvi} when the load is connected, in red, and when the load is disconnected (no-load), in green. At no-load, i_{Lvi} corresponds only to the magnetizing inductance of the transformer, i_{Lm} and is triangular shaped ($i_{Lvi} = i_{Lm}$ for L_{vi_min} and L_{vi_max}). As can be seen, the current i_{Lvi} leads the voltage v_{DS2} which means that between these two limits the converter operates always in ZVS.

Figure 5.6 e) and f) show i_{Lvi} and v_{Cr} for L_{vi_min} and L_{vi_max}. As can be seen for L_{vi_min} the waveforms are more sinusoidal shaped which means that the converter is near resonance and, as the inductance level increases the converter goes away from the resonance and the waveforms are less sinusoidal shaped.

Figure 5.6 g) and h) show v_{pri} and v_{sec} for L_{vi_min} and L_{vi_max} and, Figure 5.6 i) and j) show $i_{pri} = i_{Lvi}$ and i_{sec} for L_{vimin} and L_{vimax}. As can be seen, as the turns ratio is higher than 1, the secondary-side voltage, v_{sec} amplitude is higher than the primary-side voltage, v_{pri} and, $i_{pri} < i_{sec}$.

Figure 5.6 k) and l) show i_{sec}, i_D and I_{out}, for L_{vi_min} and L_{vi_max}. As the inductance level increases the output current decreases. It can also be seen that there is a small period of time, for which the rectifier diodes current i_D is negative. Theoretically, this value should be zero and it means that the converter is working in DCM. This is more noticeable for L_{vi_min} and, for L_{vi_max} the converter is close to CCM operation. From the results, i_D has negative values which is most likely due to the diodes recovery time. This means that when the current crosses zero they do not stop conducting immediately.

Figure 5.6 m) and n) show I_{out} and V_{out}, for L_{vi_min} and L_{vi_max}. As can be seen, increasing the inductance level, the current and voltage levels decrease, which means that the output power decreases, as expected. The current is almost constant with no ripple and the voltage has a ripple of about 15 V for L_{vi_min} and 8 V for L_{vi_max}.

Simulations were also carried out in order to obtain similar results. These simulation results are presented in Figure 5.7.

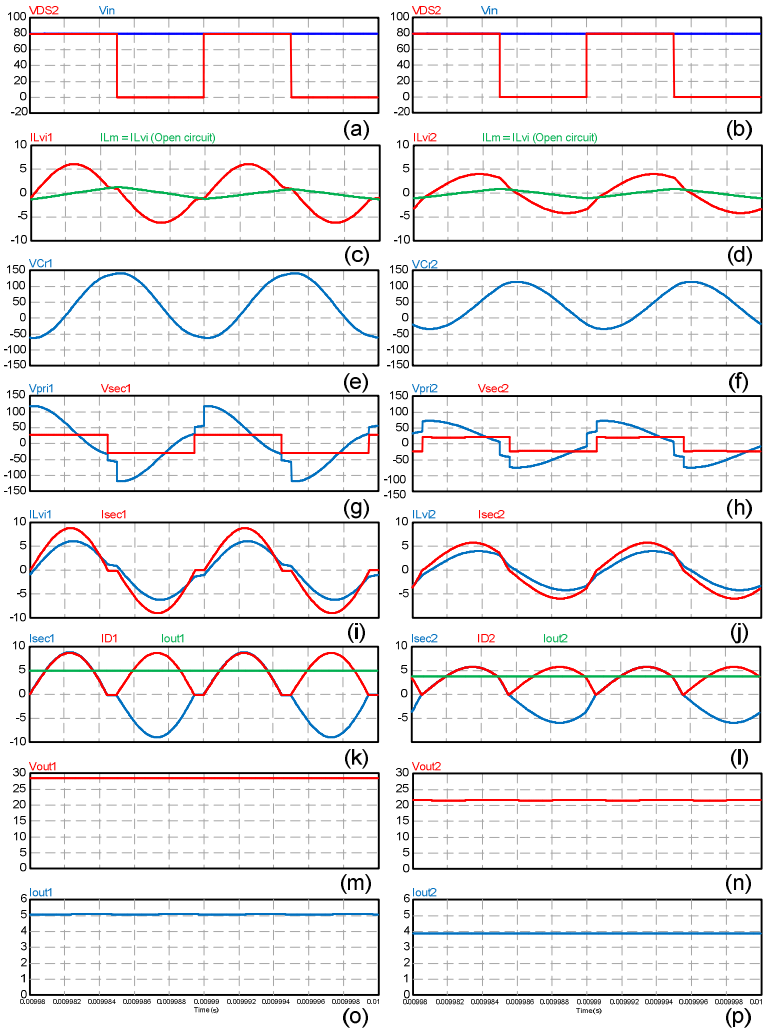

Figure 5.7 – Simulation results for L_{vimin} and L_{vimax}, left and right, respectively: (a) and (b) v_{DS2} and, V_{in}; (c) and (d) i_{Lvi} and, i_{Lm}; (e) and (f) v_{Cr}; (g) and (h) v_{sec} and, v_{pri}; (i) and (j) i_{sec} and, $i_{pri} = i_{Lvi}$; (k) and (l) i_{sec}, i_D and, I_{out}; (m) and (n) V_{out}; (o) and (p) I_{out}

As can be seen from Figure 5.7, the waveforms shapes are similar to the obtained experimental results. In this case, the behavior is as expected, by increasing the inductance level, the output current and voltage levels decreases which mean lower output power. When comparing the simulation and experimental waveforms it can be seen that in simulation, ZVS operation is more identifiable as well as DCM operation. In simulation the components are more ideal; the magnetic losses in the transformer and in the VI are not accounted for. The currents waveforms are more sinusoidal shaped then in the experimental results, because in the simulation, the magnetic behavior of the magnetic devices is not considered. The simulation allows analyzing only the electrical behavior of the converter.

In summary, the experimental and simulation results from Figure 5.6 and Figure 5.7, respectively allow seeing that for L_{vi_min} the circuit operates in DCM because there is a time

period where the diodes current is zero which means that no current is being fed by the converter and all the current going from the input is stored in the output capacitor. For L_{vi_max} the circuit operates in CCM and the output is always fed by the converter. When comparing i_{Lvi} with i_{Lm} ($i_{Lm} = i_{Lvi}$ at no-load) it is clearly possible to see the difference between DCM and CCM. For the case of L_{vi_min} when $i_{Lm} = i_{Lvi}$, the output diodes are not conducting ($I_D = 0$) and the circuit is operating in DCM. In the other side, for the case of L_{vi_max} the circuit is operating in CCM.

During the experimental tests as well as obtaining the waveforms of the voltages and currents, some measurements were acquired and the results are shown in Figure 5.8.

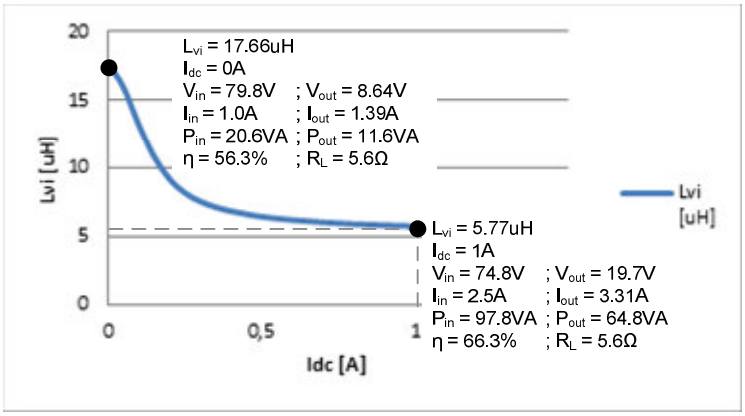

Figure 5.8 – $L_{vi}(I_{dc})$ measured curved with experimental results

From the results shown in Figure 5.8 it can be seen that by increasing the I_{dc} value (decreasing the inductance value of the VI) the output voltage and current increases from 8.64 V to 19.7 V and from 1.39 A to 3.31 A, respectively. Because the input voltage is kept constant the input current also increases to feed the load at the required power level. The power increases with the increase of I_{dc}, from 11.6 VA to 64.8 VA and, the test results allowed achieving a maximum efficiency around 66.3% when $L_{vi} = L_{vi\_min}$. This low efficiency value is expected since the prototype is not operating at the nominal power level.

Simulation and theoretical results were adapted in order to obtain the same operating conditions as in experimental tests. The results are shown in Table 5. and allow comparing the theoretical, simulation and experimental results. As expected, the simulation results are close to the theoretical results. The experimental values exhibit some variation essentially due to coupling losses in the power transformer and due to the prototype efficiency.

Table 5.2 – Converter parameters for simulation and experimental prototype

VI prototype range		Theoretical results			Simulation Results			Experimental Results		
I_{dc}	L_{vi}	V_{out}	I_{out}	P_{out}	V_{out}	I_{out}	P_{out}	V_{out}	I_{out}	P_{out}
[A]	[µH]	[V]	[A]	[W]	[V]	[A]	[W]	[V]	[A]	[W]
1	5.77	27.9	4.98	139	28.44	5.08	144.4	19.7	3.31	64.8
0	17.66	18.63	3.33	62	21.73	3.88	84.30	8.64	1.39	11.6

For the current and voltage values the error between the experimental and simulation results is around 30% and 65%, respectively. Nevertheless at this point, it was only intended to prove the capability of this topology regarding output regulation.

5.3.2. Simulation of a Charging Cycle

A charging cycle of the batteries was simulated and the results are now presented. The load resistance value was varied between 5.6 Ω, 11.28 Ω and 232 Ω (resistor load from Fig. C.13) and the VI inductance level adjusted to simulate the respective operating point through the I_{dc} current level. In this case, the level of the DC Bus used was also of $V_{in} = 80V$. In this case, four points of operation were analyzed:

- $SOC \approx 0\%$, $I_{dc} = 0A$, $L_{vi} \cong 17.66\mu H$, $R_L = 5.6\Omega$;
- $SOC = 90\%$, $I_{dc} = 1.45A$, $L_{vi} \cong 5.6\mu H$, $R_L = 11.28\Omega$;
- $SOC = 100\%$, $I_{dc} = 1.5A$, $L_{vi} \cong 5.56\mu H$, $R_L = 232\Omega$;

The minimum possible inductance VI value is 5.56 µH. Theoretically, this value should be zero. Therefore, a fourth case is analyzed, where the VI is short-circuited:

- $SOC = 100\%$, $I_{dc} = 0A$, $L_{vi} \cong 0uH$, $R_L = 232\Omega$ → VI short-circuited.

Figure 5.9 a) presents the charging profile with the L_{vi} expected variation as function of the SOC for the experimental points to be tested. Figure 5.9 b) shows the correlation between these L_{vi} values and the I_{dc} value according to the $L_{vi}(I_{dc})$ measured small-signal curve.

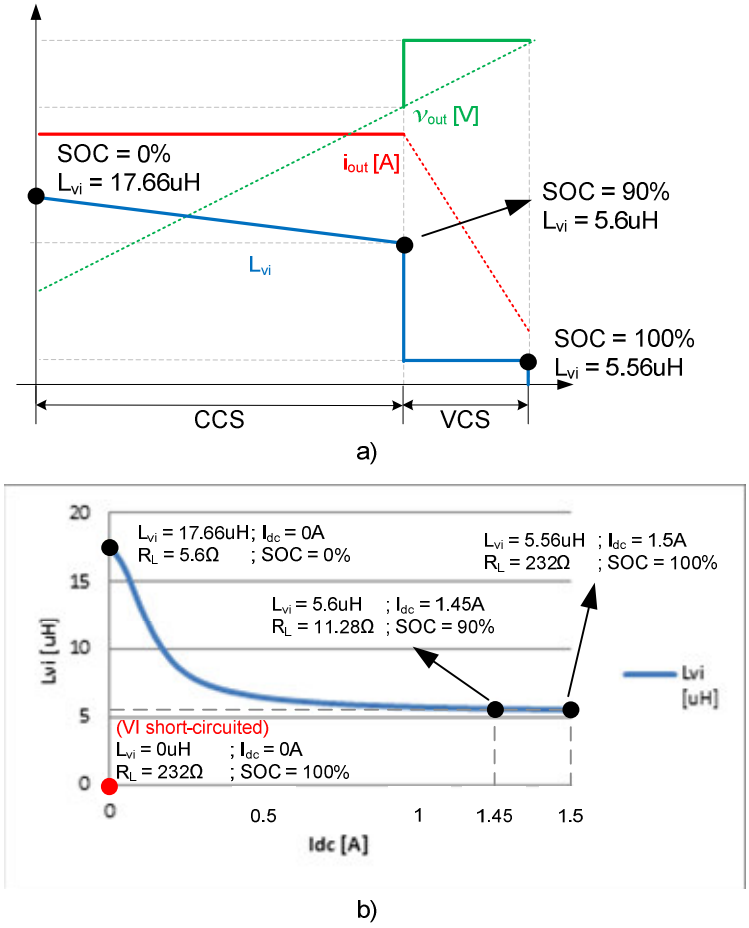

Figure 5.9 – a) Charging profile SOC expected points; b) $L_{vi}(I_{dc})$ curve

In Figure 5.9 b) the four cases described before are shown, including the case when the VI is short-circuited, in order to obtain the minimum possible value. The first point considered, corresponds to SOC ≈ 0% where the load is at the minimum value, the VI inductance is maximum and, therefore, minimum I_{dc} current value. The second point corresponds to SOC = 90%. The load increases because the battery voltage has increased, although the same charging current is maintained. In this point, the L_{vi} value should drop to 5.6 μH and therefore I_{dc} increases to 1.45 A. In the last case, SOC = 100%, the I_{dc} is at the maximum value (1.5 A). So the VI inductance value should be at its minimum (5.56 μH). If the VI is short-circuited, the minimum theoretical value for the VI inductance (≈ 0µH)) can be obtained. In this case the load is maximum and corresponds to the equivalent resistive load of when the batteries are fully charged.

The obtained experimental waveforms are presented in Figure 5.10, and show the operation of the converter at the previous presented points.

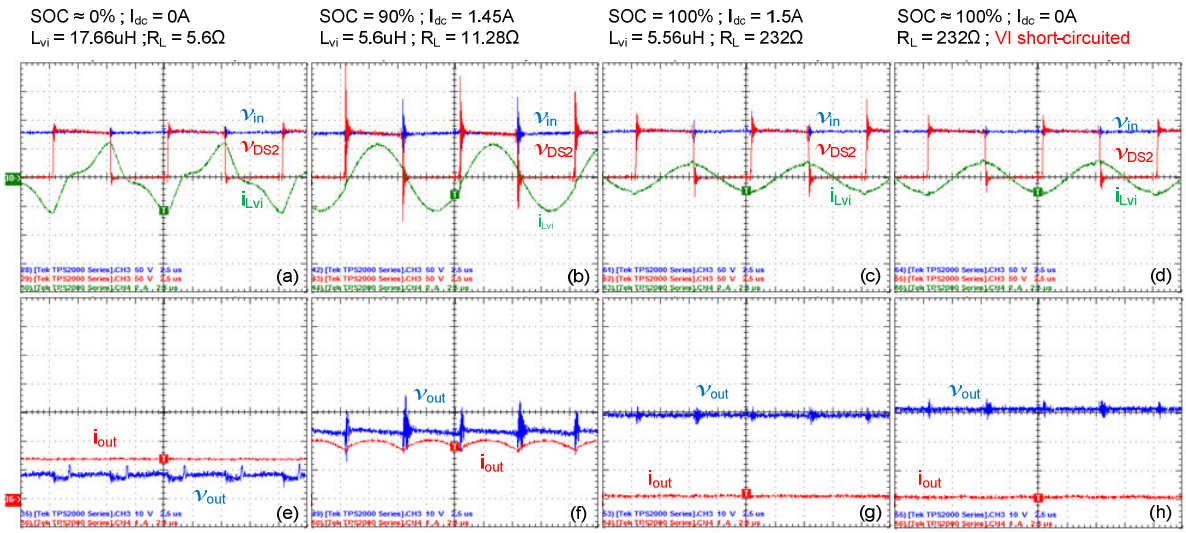

Figure 5.10 – Experimental results for the simulated charging cycle: (a), (b), (c) and (d) V_{in}, v_{DS2} and, i_{Lvi}, 50V/div, 2A/div; (e), (f), (g) and (h) i_{out} and v_{out},10V/div, 1A/div; With 2.5us/div

Figure 5.10 in the top shows V_{in}, v_{DS2} and, i_{Lvi} for the four cases considered and, in the bottom, it shows v_{out} and i_{out}. From left to right, the waveforms correspond to all of the considered SOCs. As can be seen, the current i_{Lvi} leads the voltage v_{DS2} which means, that during the simulated charging cycle, the converter operates always in ZVS. For $SOC = 90\%$ the circuit is near resonance (sinusoidal shaped current i_{Lvi}) and this operating point corresponds to the highest output power level. Figure 5.10 bottom shows I_{out} and V_{out}, for the same SOCs. It can be seen that from the first to the second point of operation, the output voltage and current increase therefore, the output power increases. Then, for the third and fourth cases, clearly, the output power decreases. In the third case, $SOC = 100\%$, the voltage increases and the current is almost zero (I_{o_float}). When the VI is short-circuited, in the last case, the L_{vi} value drops to almost zero and the output voltage increases to it maximum value. The output current decreases to its minimum possible, I_{o_float}. I_{o_float} corresponds to the current that will feed the battery when it is almost 100% charged.

During the experimental tests as well as obtaining the waveforms of the voltages and currents, also some measurements were acquired and the results are shown in Figure 5.11.

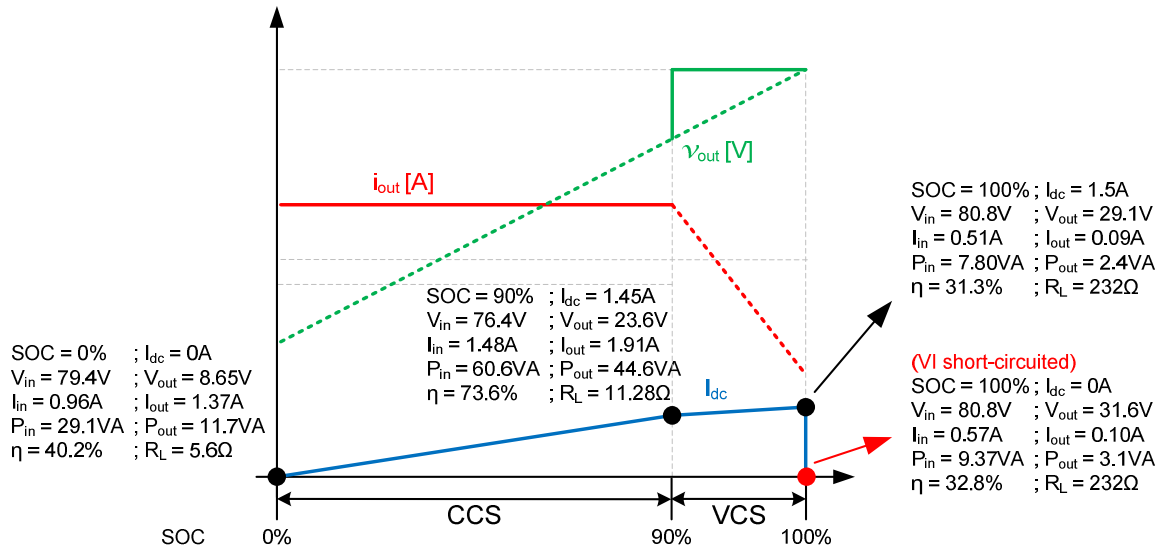

Figure 5.11 – Simulation of a charging cycle with experimental measured results

From the results shown in Figure 5.11 it can be seen that by increasing the I_{dc} value (which means decreasing the inductance value of the VI) the output power increases from $SOC = 0\%$ to $SOC = 90\%$, from 11.7 VA to 44.6 VA, and then decreases to 2.4 VA when $SOC = 100\%$, and 3.1 VA if the VI is short-circuited. The test results allowed achieving a maximum efficiency of around 73.6% when $I_{dc} = 1.45$ A that corresponds to the highest output power level obtained.

The simulation and theoretical results were adapted in order to allow obtaining results for the same operation conditions as in experimental tests and perform a comparison between them. The results are shown in Table 5.. As expected, the simulation results are close to the theoretical results. The experimental values exhibit some variation essentially due to coupling losses in the power transformer and due to the prototype efficiency. It should be noticed again, that the converter was operating at 1/4 of the nominal power with a DC bus voltage of $V_{in} = 80$ V. In practice, it means that the output of the converter will feed the load with the enough power to charge 2 batteries in series (24 V nominal voltage) and with a maximum current of almost 2 A as shown in Table 5..

Table 5.3 – Theoretical vs. Simulation vs. Experimental Results

		Theoretical			Simulation			Experimental		
L_{vi} [μH]	R_o [Ω]	V_{out} [V]	I_{out} [A]	P_{out} [VA]	V_{out} [V]	I_{out} [A]	P_{out} [VA]	V_{out} [V]	I_{out} [A]	P_{out} [VA]
17.66	5.6	18.63	3.33	62.0	21.73	3.88	84.3	8.65	1.37	11.7
5.6	11.28	28.2	2.50	70.5	28.58	2.53	72.4	23.6	1.91	44.6
5.56	232	28.29	0.12	3.45	28.88	0.12	3.60	29.1	0.09	2.44
0	232	30.35	0.13	3.97	31.32	0.13	4.23	31.6	0.10	3.07

Such values of efficiency – 66.3% in section 5.3.1 and, 73.6% in section 5.3.2 – can be justified because the prototype was non-optimized and still working under open-loop

condition. The snubber circuit for the half-bridge inverter is yet to be optimized and therefore high spikes in the input voltage and v_{DS2} voltage appear, contributing to losses increase. It was seen that the VI core was sustaining an increase of temperature, mainly due to the higher levels of I_{DC} current, contributing also for the losses and consequently for a lower efficiency. However, the lower efficiency level is also due to the fact that the converter is still working at a lower power level. Once the closed loop operation is implemented the efficiency is expected to increase.

Considering the adopted charging profiles from Figure 3.2 b), and the results from Table 5., it is possible to conclude that the charging profile is followed. Initially V_{out} is minimum and increases from $SOC = 0\%$ to $SOC = 90\%$ from 8.65 V to 23.6 V. The output current level I_{out} increases slightly, from 1.37A to 1.91A, which is not constant due to open-loop operation. From $SOC = 90\%$ on, the voltage still increases to $V_{out} = 29.1$ V and I_{out} decreases to its I_{o_float} value of 0.09 A for $SOC = 100\%$. If the VI is short-circuited, the minimum value of L_{vi} is obtained and because of that if the load is the same, the output voltage increases to its maximum allowed value of 31.6 V and the output current is almost equal at 0.10 A. In terms of output power, at the beginning of the charging cycle, the output power is 11.7 VA. As the SOC increases, so does the output power to 44.6 VA ($SOC = 90\%$). When $SOC = 100\%$, the output power deceases drastically to 2.44 VA due to the low level of output current $I_{out} = I_{o\_float}$. When the VI is short-circuited, the output power increases slightly to 3.07 VA due to the increase of the output voltage inherent to the lower L_{vi} inductance value.

Although this behavior validates the use of a constant-frequency, LLC-VI resonant converter for the proposed application, it will be necessary to optimize the converter (snubber circuit, transformer, VI) in order to be able to test it at the nominal power. Close-loop operation needs to be implemented which will allow increasing the converter efficiency. As last step the load needs to be changed from the resistive load to the real batteries in order to see the converter operation and behavior as battery charger.

6. Conclusions, Contributions and Future Work

The main goal of designing and implementing a constant-frequency LLC resonant converter with VI control for a battery charger was achieved.

6.1. Conclusions

Theoretical and simulation analysis were made considering both f_s and VI control techniques. Mathcad software was used to design and calculate the converter parameters. This allowed designing the converter considering either switching frequency and/or VI control methods. Then simulations were performed using PSIM software. The simulations results were obtained in open-loop condition. Theoretically, both control parameters can be used to control the output of the LLC resonant converter achieving always ZVS: using a VI while keeping f_s constant or using f_s while the resonant parameters are kept constant. A higher f_s leads to converter miniaturization and the range of the VI needed to obtain a specific output regulation will be smaller. However, if f_s is the control variable, the range is higher. It was concluded that a mix between both controls methods may lead to an improved performance. In the end, a prototype was built, working at 1/4 of the nominal power, and test results were obtained, the PCBs for the prototype were designed and built according to the specifications. Considering the obtained results, the proposed topology is validated although the converter was not tested at nominal power and close-loop control has not yet been implemented.

6.2. Contributions

With the conclusion of this work, the contributions for the research group are as follows:

- A Mathcad file that allows understanding the behavior of the LLC resonant converter as well as analyzing the converter operation under different operating conditions. This file allows designing the LLC resonant converter considering as main design parameters the switching frequency (f_s) design value, the input voltage value at the DC Bus (V_{in}) and, the output voltage and current (V_o and I_o respectively), for different applications.

- Simulation files in Mathcad and PSIM that allow, not only, understanding the behavior of the converter under f_s and/or VI control but also allow a comparative study between both methods (open-loop control).
- Project and PCB boards for half-bridge configurations controlled with fiber optic based drivers (fiber optic emitter and the SiC MOSFETs drivers for half or full-bridge inverters for different projects).
- A complete LLC-VI resonant converter hardware has been implemented, including a Variable Inductor and High-frequency transformer.
- Two articles were published in international conferences (UPEC 2016 and IECON 2016) and a third article is being prepared for submission to an IEEE journal.

6.3. Future Work

To expand this work, future changes can be made to improve the prototype operation and efficiency. It will be necessary to implement close-loop control, which means introducing voltage and current sensors in the prototype, design a PI controller and implement it using the DSP control board to control the I_{dc} current level and the converter voltage gain. In order to improve the converter efficiency it is mandatory to work at the nominal power level, which means that is necessary to improve the snubber circuit of the half-bridge inverter.

Moreover, a mix of both f_s and VI control techniques can be further investigated trying to improve the converter operation, efficiency and reliability.

Furthermore, a way to integrate both the VI and the transformer in only one magnetic element (variable transformer) shall be studied. This new magnetic device allows reducing the number of magnetic elements and simplifies the prototype.

It can also be studied different resonant topologies in order to evaluate their performance and compare them with the LLC resonant converter studied in this work.

Finally, instead of using a simple low-frequency rectifier to create the DC Bus to feed the resonant inverter, a Power Factor Correction (PFC) stage can be used to improve the circuit operation.

6.4. Published Articles

This work allowed two articles to be written, submitted and accepted for publication in two different conferences, UPEC 2016, 51st International Universities Power Engineering

Conference, 2016 (Coimbra – Portugal) and one in IECON 2016, 42nd Annual Conference of IEEE Industrial Electronics Society Conference (Florence – Italy) as follows:

- Valter S. Costa, M. S. Perdigão, A. S. Mendes, J. M. Alonso, **"Analysis and Simulation of the LLC Resonant Converter under Different Control Methods"**, 51st International Universities Power Engineering Conference, 2016.
- Valter S. Costa, M. S. Perdigão, A. S. Mendes, J. M. Alonso, **"Evaluation of a Variable-Inductor-Controlled LLC Resonant Converter for Battery Charging Applications"**, 42nd Annual Conference of IEEE Industrial Electronics Society Conference, 2016.

References

[1]. Hybrid Electric Vehicle (Searched in 25-Nov-2016): https://pt.wikipedia.org/wiki/Autom%C3%B3vel_h%C3%ADbrido_el%C3%A9trico

[2]. Electric Vehicle (Searched in 25-Nov-2016): https://pt.wikipedia.org/wiki/Ve%C3%ADculo_el%C3%A9trico

[3]. Battery (electricity) (Searched in 25-Nov-2016: https://en.wikipedia.org/wiki/Battery_(electricity)

[4]. Charging Station (searched in 25-Nov-2016): https://en.wikipedia.org/wiki/Charging_station

[5]. Y. J. Choi, S. Y. Choi and R. Y. Kim, "An integrated voltage-current compensator of LLC resonant converter for Li-ion battery charger applications," *2016 IEEE 8th International Power Electronics and Motion Control Conference (IPEMC-ECCE Asia)*, Hefei, 2016, pp. 3783-3790.

[6]. K. H. Park, Y. J. Choi, S. Y. Choi and R. Y. Kim, "Design consideration of CC-CV controller of LLC resonant converter for Li-ion battery charger," *2015 IEEE 2nd International Future Energy Electronics Conference (IFEEC)*, Taipei, 2015, pp. 1-6.

[7]. C. Liu, J. Wang, K. Colombage, C. Gould, B. Sen and D. Stone, "Current ripple reduction in 4kW LLC resonant converter based battery charger for electric vehicles," *2015 IEEE Energy Conversion Congress and Exposition (ECCE)*, Montreal, QC, 2015, pp. 6014-6021.

[8]. Marian K. Kazimierczuk and Dariusz Czarkowski, “Resonant Power Converters”; Second Edition; John Wiley & Sons Inc., 2011

[9]. Hangseok Choi, " Design Considerations for an LLC resonant Converter," Farichild Power Seminar 2007

[10]. Hang-Seok Choi, “Design Consideration of Half-Bridge LLC Resonant Converter”, Journal of Power Electronics, Vol. 7, No. 1, January 2007

[11]. M. Youssef, J. A. A. Qahouq and M. Orabi, "Electromagnetic Compatibility results for an LCC resonant inverter for the tranportation systems," *2010 Twenty-Fifth Annual IEEE Applied Power Electronics Conference and Exposition (APEC)*, Palm Springs, CA, 2010, pp. 1800-1803.

[12]. Y. Wang, Y. Guan, J. Huang, W. Wang and D. Xu, "A Single-Stage LED Driver Based on Interleaved Buck–Boost Circuit and LLC Resonant Converter," in IEEE Journal of Emerging and Selected Topics in Power Electronics, vol. 3, no. 3, pp. 732-741, Sept. 2015.

[13]. Shuze Zhao, Jiale Xu and O. Trescases, "Burst-Mode Resonant LLC Converter for an LED Luminaire With Integrated Visible Light Communication for Smart Buildings," in IEEE Transactions on Power Electronics, vol. 29, no. 8, pp. 4392-4402, Aug. 2014.

[14]. R. L. Lin and C. W. Lin, "Design criteria for resonant tank of LLC DC-DC resonant converter," IECON 2010 - 36th Annual Conference on IEEE Industrial Electronics Society, Glendale, AZ, 2010, pp. 427-432. doi: 10.1109/IECON.2010.5674988

[15]. M. S. Perdigão, M. F. Menke, A. R. Seidel, R. A. Pinto and J. M. Alonso, "A Review on Variable Inductors and Variable Transformers: Applications to Lighting Drivers," in *IEEE Transactions on Industry Applications*, vol. 52, no. 1, pp. 531-547, Jan.-Feb. 2016.

[16]. FERREIRA, Samuel Filipe Soares – "Estudo do comportamento electromagnético de uma bobina variável controlada através de uma corrente DC", 2016, Master Thesis.

[17]. MARTINS, Marco André Cunha – "LED Lamp Driver Based on a Resonant Switched Capacitor Converter with a Variable Resonant Tank", 2015, Master Thesis.

[18]. M. Martins, M. S. Perdigão, A. S. Mendes, R. A. Pinto and J. M. Alonso, "Dimmable LED driver with variable inductor based on a resonant switched-capacitor topology," *2015 IEEE Energy Conversion Congress and Exposition (ECCE)*, Montreal, QC, 2015, pp. 5329-5336.

[19]. Magnetic core (Searched in 25-Nov-2016): https://en.wikipedia.org/wiki/Magnetic_core#.22E.22_core

[20]. PERDIGÃO, Marina Mendes Sargento Domingues – "Research and Development on New Control Techniques for Electronic Ballasts based on Magnetic Regulators", 2011, PhD Thesis.

[21]. M. S. Perdigao, S. F. Ferreira, M. Martins, A. S. Mendes and J. M. Alonso, "Finite element analysis of a variable inductor for an RSCC based LED lamp driver," Industry Applications Society Annual Meeting, 2015 IEEE, Addison, TX, 2015, pp. 1-8.

[22]. Battery Mathworks help (Searched in 25-Nov-2016): https://www.mathworks.com/help/physmod/sps/powersys/ref/battery.html?requestedDomain=www.mathworks.com&requestedDomain=www.mathworks.com

[23]. Lecture notes from the class "Tração e Veículos Elétricos", from the MACSE Master – ISEC – IPC, 2013/2014, from Professor Paulo Pereirinha

[24]. Notes "Sistemas de Armazenamento de Energia – Capítulo 3" from the class "Tração e Veículos Elétricos", from the MACSE Master – ISEC – IPC, 2013/2014, from Professor Paulo Pereirinha

[25]. Figure conductive charging (Searched in 25-Nov-2016): https://www.google.pt/search?q=electric+vehicles+charging&client=firefox-b-ab&source=lnms&tbm=isch&sa=X&ved=0ahUKEwjWpLPI_KXPAhXCchQKHfM4DqAQ_AUICCgB&biw=1366&bih=635#imgrc=qCyWRRxRPHEfSM%3A

[26]. V. S. Costa, M. S. Perdigão, A. S. Mendes and J. M. Alonso, "Evaluation of a variable-inductor-controlled LLC resonant converter for battery charging applications," *IECON 2016 - 42nd Annual Conference of the IEEE Industrial Electronics Society*, Florence, 2016, pp. 5633-5638.

[27]. Hangseok Choi, "AN-4151, Half-Bridge LLC Resonant Converter Design Using FSFR-Series Fairchild Power Switch (FPSTM)", 2007.

[28]. Z. Fang, T. Cai, S. Duan and C. Chen, "Optimal Design Methodology for LLC Resonant Converter in Battery Charging Applications Based on Time-Weighted Average Efficiency," in IEEE Transactions on Power Electronics, vol. 30, no. 10, pp. 5469-5483, Oct. 2015.

[29]. Valter S. Costa, M. S. Perdigão, A. S. Mendes, J. M. Alonso, "Analysis and Simulation of the LLC Resonant Converter under Different Control Methods", 51st International Universities Power Engineering Conference, 2016.

[30]. C. A. Cheng, H. W. Chen, E. C. Chang, C. H. Yen and K. J. Lin, "Efficiency study for a 150W LLC resonant converter," *2009 International Conference on Power Electronics and Drive Systems (PEDS)*, Taipei, 2009, pp. 1261-1265.

Appendix

A. Theoretical Analysis of the LLC Resonant Converter

A.1. LLC Resonant Converter Design

This section of the appendix presents the calculation performed using Mathcad Prime 3.1 software that allows designing the LLC resonant converter. This file allows understanding the behavior of the converter under VI and switching frequency control (curves of the gain and the output power as function of the VI inductance and switching frequency, $M(L_{vi})$, $P_o(L_{vi})$, $M(f_s)$ and $M(f_s)$). It also presents the auxiliary Matlab Code used to determine the Q parameter value for the converter design.

At the end of this section an analysis of the influence of the k parameter in the converter design is presented, in particular the impact of the value of k in the gain of the converter, and the resonant frequencies behavior, $M(L_{vi})$, $f_0(L_{vi})$ and $f_p(L_{vi})$.

Design of the LCC Resonant Converter:

Half-Bridge LLC Resonant Converter Design

Design specifications

- Nominal input voltage: 325.269V (230Vef ; 50Hz line frequency)
- Output:
  - Vo = 84V to 116V
  - Io = 0A to 10A

Step 1 - Define the system specifications

$j := \sqrt{-1}$

$V_{in\_ac\_ef} := 230$

$V_{in\_ac} := V_{in\_ac\_ef} \cdot \sqrt{2} = 325.269$

$I_o := 10$

$V_o := 116$

$P_o := V_o \cdot I_o = 1.16 \cdot 10^3$

$P_{o\_max} := P_o = 1.16 \cdot 10^3$

$V_{in\_ac\_ef} = 230$

$I_o = 10$

$V_o = 116$

$P_o = 1160$

Estimated efficency: Tipically, η=0.88~0.92 for low voltage output applications and η=0.92~0.96 for high voltage output applications.

$\eta := 0.95$

$P_{in} := \frac{P_o}{\eta} = 1.221 \cdot 10^3$

$V_\gamma := 0.7$ $f_{in} := 50$ $Ripple := 1\%$ Assumption of 1% input voltage allowed variation

$V_{in\_max} := V_{in\_ac} - 2 \cdot V_\gamma = 323.869$

$V_{Ripple} := Ripple \cdot V_{in\_max} = 3.239$

$V_{in\_min} := V_{in\_max} - V_{Ripple} = 320.63$ $V_{in} := 320$

$I_{in\_dc} := \frac{P_{in}}{V_{in\_max}} = 3.77$

$C_{in} := \frac{I_{in\_dc}}{2 \cdot f_{in} \cdot V_{Ripple}} = 11.641 \cdot 10^{-3}$

$C_{in} = 11.6 \cdot 10^{-3}$

Step 2 - Determine the Maximum and Minimum Voltage Gains of the Resonant Network

Is tipically to set k to be between 5~10, which results in a voltage gain of 1.1~1.2 at the resonant frequency (f0)

$k := 7$ k = ratio between Lm and Llkp

$k = 7$

$M_{min} := \frac{k+1}{k} = 1.143$

$M_{max} := \frac{V_{in\_max}}{V_{in\_min}} \cdot M_{min} = 1.154$

Step 3 - Determine the transformer Turns Ratio (n=Np/Ns)

$V_F := 0.6$ Secondary-side rectifier diode voltage drop

$n := \frac{V_{in\_max}}{2 \cdot (V_o + 2 \cdot V_F)} \cdot M_{min} = 1.58$

$n = 1.579$

Step 4 - Calculate the Equivalent Load Resistance (Rac)

$R_{ac} := \frac{8 \cdot n^2}{\pi^2} \cdot \frac{V_o^2}{P_o} = 23.445$

$R_{ac} = 23.445$

Step 5 - Design the Resonant Network

$M_{max} = 1.154$

Considering a 10% margin:

$margin := 0.1$

$M_{maxmax} := (1 + margin) \cdot M_{max} = 1.27$

$M_{min} = 1.143$

$M_{max} = 1.154$

$M_{maxmax} = 1.2698$

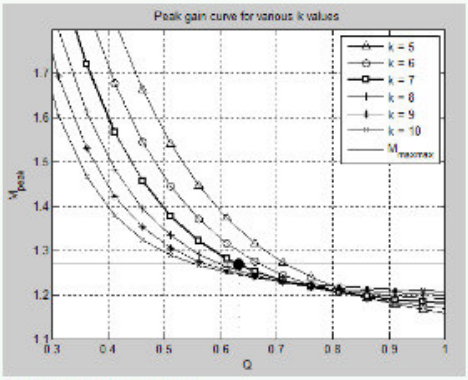

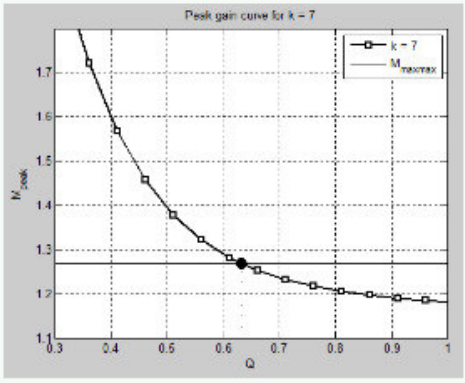


```
########################
Mmaxmax = 1.269
Q = 0.63150
########################
```

$M_{maxmax} = 1.2698$

$Q := 0.6315$

From the graphic: peak gain vs Q

$M_{min} = 1.143$

$M_{max} = 1.154$

$M_{maxmax} = 1.27$

$Q = 0.6315$

$f := 100 \cdot 10^3$ Switching frequency $f = 100 \cdot 10^3$

$\omega := 2 \cdot \pi \cdot f = 6.283 \cdot 10^5$

$f_0 := 100 \cdot 10^3$ Resonant frequency $f_0 = 100 \cdot 10^3$

$$C_r := \frac{1}{2 \cdot \pi \cdot Q \cdot f_0 \cdot R_{ac}} = 107.496 \cdot 10^{-9} \qquad C_r = 107 \cdot 10^{-9}$$

$$L_r := \frac{1}{(2 \cdot \pi \cdot f_0)^2 \cdot C_r} = 23.564 \cdot 10^{-6} \qquad L_r = 24 \cdot 10^{-6}$$

$$L_p := \frac{(k+1)^2}{(2 \cdot k + 1)} \cdot L_r = 100.540 \cdot 10^{-6} \qquad L_p = 101 \cdot 10^{-6}$$

$$L_{lkp} := \frac{L_p}{k+1} = 12.567 \cdot 10^{-6} \qquad L_{lkp} = 13 \cdot 10^{-6}$$

$$L_m := L_p - L_{lkp} = 87.972 \cdot 10^{-6} \qquad L_m = 88 \cdot 10^{-6}$$

$$L_{lks} := \frac{L_{lkp}}{n^2} = 5.04 \cdot 10^{-6} \qquad L_{lks} = 5 \cdot 10^{-6}$$

$$Q := \frac{\sqrt{\frac{L_r}{C_r}}}{R_{ac}} = 0.6315 \qquad Q = 0.6315$$

$$f_0 := \frac{1}{2 \cdot \pi \cdot \sqrt{L_r \cdot C_r}} = 100.000 \cdot 10^3 \qquad \omega_0 := 2 \cdot \pi \cdot f_0 = 6.283 \cdot 10^5 \qquad f_0 = 100.000 \cdot 10^3$$

$$f_p := \frac{1}{2 \cdot \pi \cdot \sqrt{L_p \cdot C_r}} = 48.412 \cdot 10^3 \qquad \omega_p := 2 \cdot \pi \cdot f_p = 3.042 \cdot 10^5 \qquad f_p = 48.412 \cdot 10^3$$

Summary

$k = 7$

$V_o = 116$

$I_o = 10$

$n = 1.579$

$C_r = 107.50 \cdot 10^{-9}$

$L_r = 23.56 \cdot 10^{-6}$

$L_p = 100.54 \cdot 10^{-6}$

$L_{lkp} = 12.57 \cdot 10^{-6}$

$k_{proj} := \frac{L_m}{L_{lkp}} = 7$

$L_m = 87.97 \cdot 10^{-6}$

$L_{lks} = 5.04 \cdot 10^{-6}$

$Q = 0.6315$

Graphic of Cain vs. Switching frequency

$f = 100 \cdot 10^3$

$f_0 = 100 \cdot 10^3$

$f_p = 48.412 \cdot 10^3$

$f_{sw\_min} := 0 \cdot 10^3$

$f_{sw\_max} := 200 \cdot 10^3$

$f_s := f_{sw\_min}, f_{sw\_min} + 100 .. f_{sw\_max}$

$P_{o\_100} := 1 \cdot P_o = 1.16 \cdot 10^3$ $\quad R_{ac\_100} := \frac{8 \cdot n^2}{\pi^2} \cdot \frac{V_o^2}{P_{o\_100}} = 23.445$ $\quad Q_{100} := \sqrt{\frac{L_r}{C_r}} \cdot \frac{1}{R_{ac\_100}} = 0.632$

$P_{o\_80} := 0.8 \cdot P_o = 928$ $\quad R_{ac\_80} := \frac{8 \cdot n^2}{\pi^2} \cdot \frac{V_o^2}{P_{o\_80}} = 29.307$ $\quad Q_{80} := \sqrt{\frac{L_r}{C_r}} \cdot \frac{1}{R_{ac\_80}} = 0.505$

$P_{o\_60} := 0.6 \cdot P_o = 696$ $\quad R_{ac\_60} := \frac{8 \cdot n^2}{\pi^2} \cdot \frac{V_o^2}{P_{o\_60}} = 39.076$ $\quad Q_{60} := \sqrt{\frac{L_r}{C_r}} \cdot \frac{1}{R_{ac\_60}} = 0.379$

$P_{o\_40} := 0.4 \cdot P_o = 464$ $\quad R_{ac\_40} := \frac{8 \cdot n^2}{\pi^2} \cdot \frac{V_o^2}{P_{o\_40}} = 58.613$ $\quad Q_{40} := \sqrt{\frac{L_r}{C_r}} \cdot \frac{1}{R_{ac\_40}} = 0.253$

$P_{o\_20} := 0.2 \cdot P_o = 232$ $\quad R_{ac\_20} := \frac{8 \cdot n^2}{\pi^2} \cdot \frac{V_o^2}{P_{o\_20}} = 117.227$ $\quad Q_{20} := \sqrt{\frac{L_r}{C_r}} \cdot \frac{1}{R_{ac\_20}} = 0.126$

$$M_{100}(f_s) := \left| \frac{\left(\frac{(2 \cdot \pi \cdot f_s)^2}{\omega_p^2}\right) \cdot \frac{k}{k+1}}{j \cdot \left(\frac{2 \cdot \pi \cdot f_s}{\omega_0}\right) \cdot \left(1 - \frac{(2 \cdot \pi \cdot f_s)^2}{\omega_0^2}\right) \cdot Q_{100} \cdot \frac{(k+1)^2}{2 \cdot k + 1} + \left(1 - \frac{(2 \cdot \pi \cdot f_s)^2}{\omega_p^2}\right)} \right|$$

$$M_{80}(f_s) := \left| \frac{\left(\frac{(2 \cdot \pi \cdot f_s)^2}{\omega_p^2}\right) \cdot \frac{k}{k+1}}{j \cdot \left(\frac{2 \cdot \pi \cdot f_s}{\omega_0}\right) \cdot \left(1 - \frac{(2 \cdot \pi \cdot f_s)^2}{\omega_0^2}\right) \cdot Q_{80} \cdot \frac{(k+1)^2}{2 \cdot k + 1} + \left(1 - \frac{(2 \cdot \pi \cdot f_s)^2}{\omega_p^2}\right)} \right|$$

$$M_{60}(f_s) := \left| \frac{\left(\frac{(2\cdot\pi\cdot f_s)^2}{\omega_p^2}\right)\cdot\frac{k}{k+1}}{j\cdot\left(\frac{2\cdot\pi\cdot f_s}{\omega_0}\right)\cdot\left(1-\frac{(2\cdot\pi\cdot f_s)^2}{\omega_0^2}\right)\cdot Q_{60}\cdot\frac{(k+1)^2}{2\cdot k+1}+\left(1-\frac{(2\cdot\pi\cdot f_s)^2}{\omega_p^2}\right)} \right|$$

$$M_{40}(f_s) := \left| \frac{\left(\frac{(2\cdot\pi\cdot f_s)^2}{\omega_p^2}\right)\cdot\frac{k}{k+1}}{j\cdot\left(\frac{2\cdot\pi\cdot f_s}{\omega_0}\right)\cdot\left(1-\frac{(2\cdot\pi\cdot f_s)^2}{\omega_0^2}\right)\cdot Q_{40}\cdot\frac{(k+1)^2}{2\cdot k+1}+\left(1-\frac{(2\cdot\pi\cdot f_s)^2}{\omega_p^2}\right)} \right|$$

$$M_{20}(f_s) := \left| \frac{\left(\frac{(2\cdot\pi\cdot f_s)^2}{\omega_p^2}\right)\cdot\frac{k}{k+1}}{j\cdot\left(\frac{2\cdot\pi\cdot f_s}{\omega_0}\right)\cdot\left(1-\frac{(2\cdot\pi\cdot f_s)^2}{\omega_0^2}\right)\cdot Q_{20}\cdot\frac{(k+1)^2}{2\cdot k+1}+\left(1-\frac{(2\cdot\pi\cdot f_s)^2}{\omega_p^2}\right)} \right|$$

$f_{s\_min} := 98\cdot10^3$

$f_{s\_max} := 100\cdot10^3$

From the graphic below: Gain vs switching frequency
fs_min = frequency to the maximum gain Mmax (considering a margin)

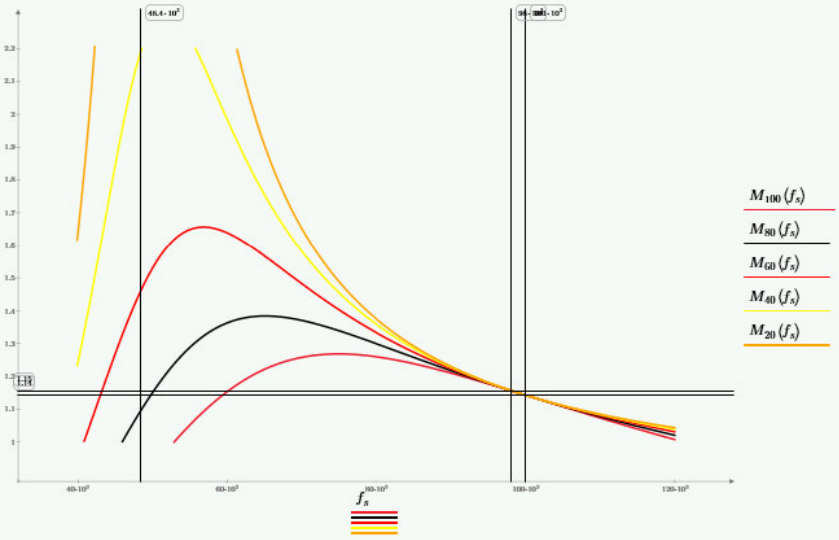

Step 6 - Design the Transformer

$n = 1.5791$ $f_{s\_min} = 98\cdot10^3$ $V_o = 116$ $V_F = 0.6$

ETD 44/22/15 Ferrite Core

$\Delta B_2 := 0.3$

$A_{e2} := 173\cdot10^{-6}$

$$N_{p\_min2} := \frac{n\cdot(V_o+2\cdot V_F)}{2\cdot f_{s\_min}\cdot\Delta B_2\cdot A_{e2}} = 18.193$$

Choose Ns so that the resultant Np is greater than Np_min

$N_{s2} := 12$ $N_{s2} = 12$

$N_{p2} := n\cdot N_{s2} = 18.949$ greater then Np_min $N_{p2} = 19$

$N_2 := \frac{N_{p2}}{N_{s2}} = 1.579$ $N_2 = 1.6$

Step 7 - Transformer Construction

ETD 44/22/15 Core $N_{p2}=19$ $N_{s2}=12$ $N_2=1.6$

Lp measured with secondary open
Lr measured with secondary short

$gap_{core21}:=1\cdot10^{-3}$ $L_{p21}:=104.47\cdot10^{-6}$ $L_{r21}:=28.15\cdot10^{-6}$

$R_{p21}:=1.656$ $R_{s21}:=0.6296$

$L_{lkp21}:=\frac{L_{p21}}{k+1}=13.059\cdot10^{-6}$ $L_{m21}:=L_{p21}-L_{lkp21}=91.411\cdot10^{-6}$ $L_{lks21}:=\frac{L_{lkp21}}{N_2^2}=5.237\cdot10^{-6}$

$R_p:=R_{p21}=1.656$ $R_s:=R_{s21}=629.6\cdot10^{-3}$

$L_p=100.54\cdot10^{-6}$ $L_r=23.564\cdot10^{-6}$ $L_{lkp}=12.567\cdot10^{-6}$ $L_m=87.972\cdot10^{-6}$ $L_{lks}=5.04\cdot10^{-6}$

$gap_{core21}=1\cdot10^{-3}$ $L_{p21}=104.47\cdot10^{-6}$ $L_{r21}=28.15\cdot10^{-6}$ $L_{lkp21}=13.059\cdot10^{-6}$ $L_{m21}=91.411\cdot10^{-6}$ $L_{lks21}=5.237\cdot10^{-6}$

ETD 44/22/15 Ferrite Core

$N_p:=N_{p2}=19$

$N_s:=N_{s2}=12$

$n=1.579$ $N_2=1.6$

$gap:=gap_{core21}=1\cdot10^{-3}$

$L_p=100.54\cdot10^{-6}$ $L_{p21}=104.47\cdot10^{-6}$

$L_r=23.564\cdot10^{-6}$ $L_{r21}=28.15\cdot10^{-6}$

$L_{lkp}=12.567\cdot10^{-6}$ $L_{lkp21}=13.059\cdot10^{-6}$

$L_m=87.972\cdot10^{-6}$ $L_{m21}=91.411\cdot10^{-6}$

$L_{lks}=5.04\cdot10^{-6}$ $L_{lks21}=5.237\cdot10^{-6}$

Introducing the transformer caracteristics

ETD 44/22/15 core

$N_p:=N_{p2}=19$

$N_s:=N_{s2}=12$

$n:=N_2=1.579$

$gap:=gap_{core21}=1\cdot10^{-3}$

$n=1.579$ $R_{ac}=23.445$

$n=1.579$

$R_{ac}:=\frac{8\cdot n^2}{\pi^2}\cdot\frac{V_o^2}{P_o}=23.445$ $R_{ac}=23.445$

$L_{lkp}=12.567\cdot10^{-6}$

$L_{lkp}:=L_{lkp21}=13.059\cdot10^{-6}$ $L_{lkp}=13\cdot10^{-6}$

$L_m=87.972\cdot10^{-6}$

$L_m:=L_{m21}=91.411\cdot10^{-6}$ $L_m=91\cdot10^{-6}$

$L_{lks}=5.04\cdot10^{-6}$

$L_{lks} := L_{lks21} = 5.237 \cdot 10^{-6}$ $L_{lks} = 5 \cdot 10^{-6}$

$L_p = 100.54 \cdot 10^{-6}$

$L_p := L_{p21} = 104.47 \cdot 10^{-6}$ $L_p = 104 \cdot 10^{-6}$

$L_r = 24 \cdot 10^{-6}$ $M_{min} = 1.143$ $L_m = 91.411 \cdot 10^{-6}$ $L_p = 104.47 \cdot 10^{-6}$

$L_r := L_{r21} = 28.15 \cdot 10^{-6}$ $L_r = 28 \cdot 10^{-6}$

$C_r = 107 \cdot 10^{-9}$ $Q = 0.6315$ $R_{ac} = 23.445$ $L_r = 28.15 \cdot 10^{-6}$

$$C_{r1} := \frac{L_r}{(Q \cdot R_{ac})^2} = 1.284 \cdot 10^{-7} \qquad C_r = 107 \cdot 10^{-9}$$

Considering the built transformer:

$n = 1.579$

$R_{ac\_2} := R_{ac} = 23.445$

$L_{r\_2} := L_r = 28.15 \cdot 10^{-6}$

For f0 = 100kHz; Q = ? and, Cr = ?

$f_{0\_2} := f_0 = 100 \cdot 10^3$

$$C_{r\_21} := \frac{\left(\frac{1}{2 \cdot \pi \cdot f_{0\_2}}\right)^2}{L_{r\_2}} = 89.983 \cdot 10^{-9}$$

$$C_{r\_21} := \frac{1}{(2 \cdot \pi \cdot f_{0\_2})^2 \cdot L_{r\_2}} = 89.983 \cdot 10^{-9}$$

$$f_{0\_21} := \frac{1}{2 \cdot \pi \cdot \sqrt{L_{r\_2} \cdot C_{r\_21}}} = 100.000 \cdot 10^3 \qquad f_{0\_2} := f_0 = 100 \cdot 10^3$$

$$Q_1 := \frac{\sqrt{\frac{L_{r\_2}}{C_{r\_21}}}}{R_{ac\_2}} = 0.7544 \qquad Q = 0.6315$$

$$C_{r\_22} := \frac{L_{r\_2}}{(Q \cdot R_{ac\_2})^2} = 128.416 \cdot 10^{-9}$$

$$Q_2 := \frac{\sqrt{\frac{L_{r\_2}}{C_{r\_22}}}}{R_{ac\_2}} = 0.6315 \qquad Q = 0.6315$$

$$f_{0\_22} := \frac{1}{2 \cdot \pi \cdot \sqrt{L_{r\_2} \cdot C_{r\_22}}} = 83.709 \cdot 10^3 \qquad f_{0\_2} := f_0 = 100 \cdot 10^3$$

$$C_{r\_23} := \frac{1}{2 \cdot \pi \cdot Q \cdot f_{0\_2} \cdot R_{ac\_2}} = 107.496 \cdot 10^{-9}$$

$$Q_3 := \frac{\sqrt{\frac{L_{r\_2}}{C_{r\_23}}}}{R_{ac\_2}} = 0.69022 \qquad Q = 0.6315$$

$$f_{0\_23} := \frac{1}{2 \cdot \pi \cdot \sqrt{L_{r\_2} \cdot C_{r\_23}}} = 91.493 \cdot 10^3 \qquad f_{0\_2} := f_0 = 100 \cdot 10^3$$

For Q = 0.6315; f0 = ? and, Cr = ?

$Q_2 := Q = 0.6315$

$$C_{r\_24} := \frac{L_{r\_2}}{(Q_2 \cdot R_{ac\_2})^2} = 128.416 \cdot 10^{-9}$$

$$Q_3 := \frac{\sqrt{\frac{L_{r\_2}}{C_{r\_24}}}}{R_{ac\_2}} = 0.6315 \qquad Q = 0.6315$$

$$f_{0\_23} := \frac{1}{2 \cdot \pi \cdot \sqrt{L_{r\_2} \cdot C_{r\_24}}} = 83.709 \cdot 10^3 \qquad f_{0\_2} := f_0 = 100 \cdot 10^3$$

$$C_{r\_25} := \frac{\left(\frac{1}{2 \cdot \pi \cdot f_{0\_2}}\right)^2}{L_{r\_2}} = 89.983 \cdot 10^{-9}$$

$$C_{r\_25} := \frac{1}{(2 \cdot \pi \cdot f_{0\_2})^2 \cdot L_{r\_2}} = 89.983 \cdot 10^{-9}$$

$$Q_4 := \frac{\sqrt{\frac{L_{r\_2}}{C_{r\_25}}}}{R_{ac\_2}} = 0.7544 \qquad Q = 0.6315$$

$$f_{0\_24} := \frac{1}{2 \cdot \pi \cdot \sqrt{L_{r\_2} \cdot C_{r\_25}}} = 100.000 \cdot 10^3 \qquad f_{0\_2} := f_0 = 100 \cdot 10^3$$

$$C_{r\_26} := \frac{1}{2 \cdot \pi \cdot Q \cdot f_{0\_2} \cdot R_{ac\_2}} = 107.496 \cdot 10^{-9}$$

$$Q_5 := \frac{\sqrt{\frac{L_{r\_2}}{C_{r\_26}}}}{R_{ac\_2}} = 0.69022 \qquad Q = 0.6315$$

$$f_{0\_25} := \frac{1}{2 \cdot \pi \cdot \sqrt{L_{r\_2} \cdot C_{r\_26}}} = 91.493 \cdot 10^3 \qquad f_{0\_2} := f_0 = 100 \cdot 10^3$$

$L_r := L_{r\_2} = 28.15 \cdot 10^{-6}$ $\qquad R_{ac} = 23.445$

$C_r := C_{r\_21} = 89.983 \cdot 10^{-9}$ $\qquad C_r = 90 \cdot 10^{-9}$

$$Q := \frac{\sqrt{\frac{L_r}{C_r}}}{R_{ac}} = 0.7544$$

$$f_0 := \frac{1}{2 \cdot \pi \cdot \sqrt{L_r \cdot C_r}} = 100.000 \cdot 10^3$$

$$f_p := \frac{1}{2 \cdot \pi \cdot \sqrt{L_p \cdot C_r}} = 51.909 \cdot 10^3$$

Summary

$k = 7$

$V_o = 116$

$I_o = 10$

$n = 1.579$

$C_r = 89.98 \cdot 10^{-9}$

$L_r = 28.15 \cdot 10^{-6}$

$L_p = 104.47 \cdot 10^{-6}$

$L_{lkp} = 13.06 \cdot 10^{-6}$

$L_m = 91.41 \cdot 10^{-6}$

$L_{lks} = 5.24 \cdot 10^{-6}$

$Q = 0.7544$

$f_0 = 100.000 \cdot 10^3$ $\quad \omega_0 := 2 \cdot \pi \cdot f_0 = 6.283 \cdot 10^5$ $\quad k_{transf} := \frac{L_m}{L_{lkp}} = 7$ $\quad k := k_{transf} = 7$

$f_p = 51.909 \cdot 10^3$ $\quad \omega_p := 2 \cdot \pi \cdot f_p = 3.262 \cdot 10^5$

Graphic of Cain vs. Switching frequency

$f = 100 \cdot 10^3$

$f_0 = 100 \cdot 10^3$

$f_p = 51.909 \cdot 10^3$

$f_{sw\_min} := 0 \cdot 10^3$

$f_{sw\_max} := 200 \cdot 10^3$

$f_s := f_{sw\_min}, f_{sw\_min} + 100 .. f_{sw\_max}$

$P_{o\_100} := 1 \cdot P_o = 1.16 \cdot 10^3$ $\quad R_{ac\_100} := \frac{8 \cdot n^2}{\pi^2} \cdot \frac{V_o^2}{P_{o\_100}} = 23.445$ $\quad Q_{100} := \sqrt{\frac{L_r}{C_r}} \cdot \frac{1}{R_{ac\_100}} = 0.754$

$P_{o\_80} := 0.8 \cdot P_o = 928$ $\quad R_{ac\_80} := \frac{8 \cdot n^2}{\pi^2} \cdot \frac{V_o^2}{P_{o\_80}} = 29.307$ $\quad Q_{80} := \sqrt{\frac{L_r}{C_r}} \cdot \frac{1}{R_{ac\_80}} = 0.604$

$P_{o\_60} := 0.6 \cdot P_o = 696$ $\quad R_{ac\_60} := \frac{8 \cdot n^2}{\pi^2} \cdot \frac{V_o^2}{P_{o\_60}} = 39.076$ $\quad Q_{60} := \sqrt{\frac{L_r}{C_r}} \cdot \frac{1}{R_{ac\_60}} = 0.453$

$P_{o\_40} := 0.4 \cdot P_o = 464$ $\quad R_{ac\_40} := \frac{8 \cdot n^2}{\pi^2} \cdot \frac{V_o^2}{P_{o\_40}} = 58.613$ $\quad Q_{40} := \sqrt{\frac{L_r}{C_r}} \cdot \frac{1}{R_{ac\_40}} = 0.302$

$P_{o\_20} := 0.2 \cdot P_o = 232$ $\quad R_{ac\_20} := \frac{8 \cdot n^2}{\pi^2} \cdot \frac{V_o^2}{P_{o\_20}} = 117.227$ $\quad Q_{20} := \sqrt{\frac{L_r}{C_r}} \cdot \frac{1}{R_{ac\_20}} = 0.151$

$$M_{100}(f_s) := \left| \frac{\left(\frac{(2 \cdot \pi \cdot f_s)^2}{\omega_p^2}\right) \cdot \frac{k}{k+1}}{j \cdot \left(\frac{2 \cdot \pi \cdot f_s}{\omega_0}\right) \cdot \left(1 - \frac{(2 \cdot \pi \cdot f_s)^2}{\omega_0^2}\right) \cdot Q_{100} \cdot \frac{(k+1)^2}{2 \cdot k + 1} + \left(1 - \frac{(2 \cdot \pi \cdot f_s)^2}{\omega_p^2}\right)} \right|$$

$$M_{80}(f_s) := \left| \frac{\left(\frac{(2 \cdot \pi \cdot f_s)^2}{\omega_p^2}\right) \cdot \frac{k}{k+1}}{j \cdot \left(\frac{2 \cdot \pi \cdot f_s}{\omega_0}\right) \cdot \left(1 - \frac{(2 \cdot \pi \cdot f_s)^2}{\omega_0^2}\right) \cdot Q_{80} \cdot \frac{(k+1)^2}{2 \cdot k + 1} + \left(1 - \frac{(2 \cdot \pi \cdot f_s)^2}{\omega_p^2}\right)} \right|$$

$$M_{60}(f_s) := \left| \frac{\left(\frac{(2 \cdot \pi \cdot f_s)^2}{\omega_p^2}\right) \cdot \frac{k}{k+1}}{j \cdot \left(\frac{2 \cdot \pi \cdot f_s}{\omega_0}\right) \cdot \left(1 - \frac{(2 \cdot \pi \cdot f_s)^2}{\omega_0^2}\right) \cdot Q_{60} \cdot \frac{(k+1)^2}{2 \cdot k + 1} + \left(1 - \frac{(2 \cdot \pi \cdot f_s)^2}{\omega_p^2}\right)} \right|$$

$$M_{40}(f_s) := \left| \frac{\left(\frac{(2 \cdot \pi \cdot f_s)^2}{\omega_p^2}\right) \cdot \frac{k}{k+1}}{j \cdot \left(\frac{2 \cdot \pi \cdot f_s}{\omega_0}\right) \cdot \left(1 - \frac{(2 \cdot \pi \cdot f_s)^2}{\omega_0^2}\right) \cdot Q_{40} \cdot \frac{(k+1)^2}{2 \cdot k + 1} + \left(1 - \frac{(2 \cdot \pi \cdot f_s)^2}{\omega_p^2}\right)} \right|$$

$$M_{20}(f_s) := \left| \frac{\left(\frac{(2 \cdot \pi \cdot f_s)^2}{\omega_p^2}\right) \cdot \frac{k}{k+1}}{j \cdot \left(\frac{2 \cdot \pi \cdot f_s}{\omega_0}\right) \cdot \left(1 - \frac{(2 \cdot \pi \cdot f_s)^2}{\omega_0^2}\right) \cdot Q_{20} \cdot \frac{(k+1)^2}{2 \cdot k + 1} + \left(1 - \frac{(2 \cdot \pi \cdot f_s)^2}{\omega_p^2}\right)} \right|$$

$f_{s\_min} := 104.5 \cdot 10^3$ From the graphic below: Gain vs switching frequency
fs_min = frequency to the maximum gain Mmax (considering a margin)

$f_{s\_max} := 106 \cdot 10^3$

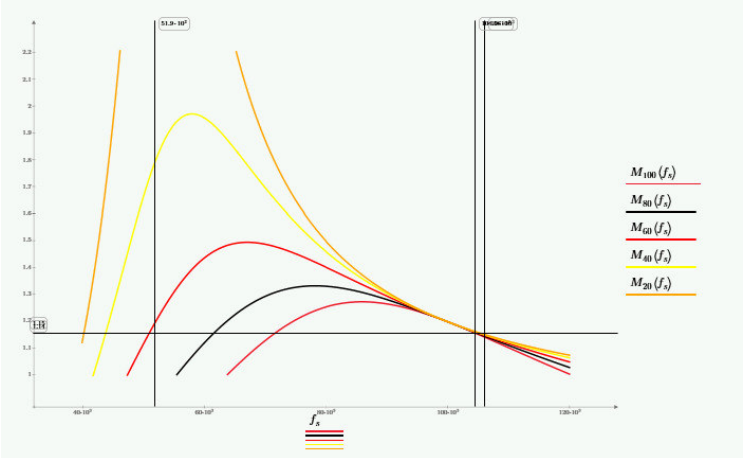

$k := 7$

$L_{vi\_g} := -1000 \cdot 10^{-6}, -999 \cdot 10^{-6} .. 2000 \cdot 10^{-6}$

$$M_{100\_2}(L_{vi\_g}) := \left| \frac{R_{ac\_100}}{\left(\frac{1}{j \cdot \omega \cdot C_r} + j \cdot \omega \cdot L_{lkp} + j \cdot \omega \cdot L_{vi\_g} + j \cdot \omega \cdot L_m\right) \cdot \left(\frac{R_{ac\_100} + n^2 \cdot j \cdot \omega \cdot L_{lks}}{j \cdot \omega \cdot L_m} + 1\right) - j \cdot \omega \cdot L_m} \right|$$

$$M_{80\_2}(L_{vi\_g}) := \left| \frac{R_{ac\_80}}{\left(\frac{1}{j \cdot \omega \cdot C_r} + j \cdot \omega \cdot L_{lkp} + j \cdot \omega \cdot L_{vi\_g} + j \cdot \omega \cdot L_m\right) \cdot \left(\frac{R_{ac\_80} + n^2 \cdot j \cdot \omega \cdot L_{lks}}{j \cdot \omega \cdot L_m} + 1\right) - j \cdot \omega \cdot L_m} \right|$$

$$M_{60\_2}(L_{vi\_g}) := \left| \frac{R_{ac\_60}}{\left(\frac{1}{j \cdot \omega \cdot C_r} + j \cdot \omega \cdot L_{lkp} + j \cdot \omega \cdot L_{vi\_g} + j \cdot \omega \cdot L_m\right) \cdot \left(\frac{R_{ac\_60} + n^2 \cdot j \cdot \omega \cdot L_{lks}}{j \cdot \omega \cdot L_m} + 1\right) - j \cdot \omega \cdot L_m} \right|$$

$$M_{40\_2}(L_{vi\_g}) := \left| \frac{R_{ac\_40}}{\left(\frac{1}{j \cdot \omega \cdot C_r} + j \cdot \omega \cdot L_{lkp} + j \cdot \omega \cdot L_{vi\_g} + j \cdot \omega \cdot L_m\right) \cdot \left(\frac{R_{ac\_40} + n^2 \cdot j \cdot \omega \cdot L_{lks}}{j \cdot \omega \cdot L_m} + 1\right) - j \cdot \omega \cdot L_m} \right|$$

$$M_{20\_2}(L_{vi\_g}) := \left| \frac{R_{ac\_20}}{\left(\frac{1}{j \cdot \omega \cdot C_r} + j \cdot \omega \cdot L_{lkp} + j \cdot \omega \cdot L_{vi\_g} + j \cdot \omega \cdot L_m\right) \cdot \left(\frac{R_{ac\_20} + n^2 \cdot j \cdot \omega \cdot L_{lks}}{j \cdot \omega \cdot L_m} + 1\right) - j \cdot \omega \cdot L_m} \right|$$

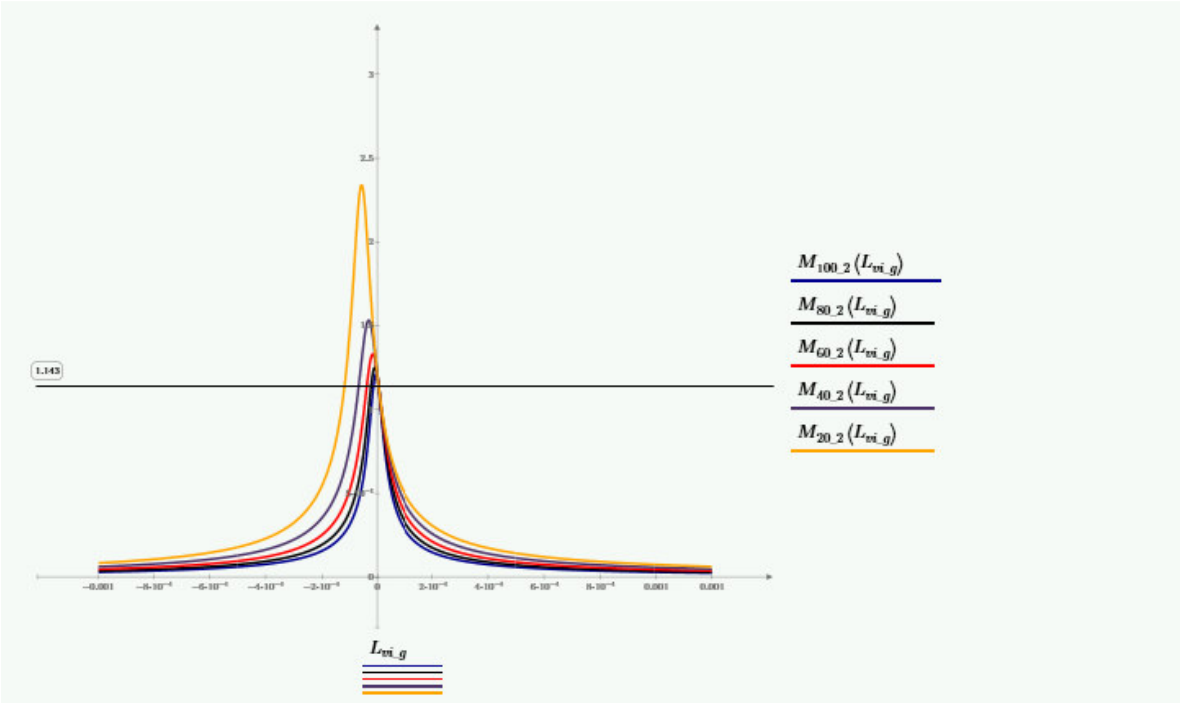

1º point: considering SOC = 0%

$V_{o\_min} := 84 \qquad V_{o\_max} := 116$

$I_{o\_max} := 10$

$P_{Lvi\_0} := V_{o\_min} \cdot I_{o\_max} = 840 \qquad R_{o\_Lvi\_0} := \frac{V_{o\_min}}{I_{o\_max}} = 8.4 \qquad R_{ac\_Lvi\_0} := \frac{8 \cdot n^2}{\pi^2} \cdot R_{o\_Lvi\_0} = 16.978$

2º point: considering SOC = 25%

$V_{o\_25} := \left(\left(V_{o\_max} - V_{o\_min} \right) \cdot 0.25 \right) + V_{o\_min} = 92$

$P_{Lvi\_25} := V_{o\_25} \cdot I_{o\_max} = 920 \qquad R_{o\_Lvi\_25} := \frac{V_{o\_25}}{I_{o\_max}} = 9.2 \qquad R_{ac\_Lvi\_25} := \frac{8 \cdot n^2}{\pi^2} \cdot R_{o\_Lvi\_25} = 18.595$

3º point: considering SOC = 50%

$V_{o\_50} := \left(\left(V_{o\_max} - V_{o\_min} \right) \cdot 0.5 \right) + V_{o\_min} = 100$

$P_{Lvi\_50} := V_{o\_50} \cdot I_{o\_max} = 1 \cdot 10^3 \qquad R_{o\_Lvi\_50} := \frac{V_{o\_50}}{I_{o\_max}} = 10 \qquad R_{ac\_Lvi\_50} := \frac{8 \cdot n^2}{\pi^2} \cdot R_{o\_Lvi\_50} = 20.211$

4º point: considering SOC = 75%

$V_{o\_75} := \left(\left(V_{o\_max} - V_{o\_min} \right) \cdot 0.75 \right) + V_{o\_min} = 108$

$P_{Lvi\_75} := V_{o\_75} \cdot I_{o\_max} = 1.08 \cdot 10^3 \qquad R_{o\_Lvi\_75} := \frac{V_{o\_75}}{I_{o\_max}} = 10.8 \qquad R_{ac\_Lvi\_75} := \frac{8 \cdot n^2}{\pi^2} \cdot R_{o\_Lvi\_75} = 21.828$

5º point: considering SOC = 90%

$V_{o\_90} := \left(\left(V_{o\_max} - V_{o\_min} \right) \cdot 0.9 \right) + V_{o\_min} = 112.8$

$P_{Lvi\_90} := V_{o\_90} \cdot I_{o\_max} = 1.128 \cdot 10^3 \qquad R_{o\_Lvi\_90} := \frac{V_{o\_90}}{I_{o\_max}} = 11.28 \qquad R_{ac\_Lvi\_90} := \frac{8 \cdot n^2}{\pi^2} \cdot R_{o\_Lvi\_90} = 22.799$

CCS -> VCS point: considering SOC~90%

$V_{o\_90\_2} := V_{o\_max} = 116$

$R_{o\_Lvi\_90\_2} := R_{o\_Lvi\_90} = 11.28 \qquad R_{ac\_Lvi\_90\_2} := \frac{8 \cdot n^2}{\pi^2} \cdot R_{o\_Lvi\_90\_2} = 22.799 \qquad P_{Lvi\_90\_2} := \frac{V_{o\_90\_2}^2}{R_{o\_Lvi\_90\_2}} = 1.193 \cdot 10^3 \qquad I_{o\_90\_2} := \frac{P_{Lvi\_90\_2}}{V_{o\_90\_2}} = 10.284$

6º point: considering SOC = 92%

$I_{o\_92} := 8$

$P_{Lvi\_92} := V_{o\_max} \cdot I_{o\_92} = 928 \qquad R_{o\_Lvi\_92} := \frac{V_{o\_max}}{I_{o\_92}} = 14.5 \qquad R_{ac\_Lvi\_92} := \frac{8 \cdot n^2}{\pi^2} \cdot R_{o\_Lvi\_92} = 29.307$

7º point: considering SOC = 95%

$I_{o\_95} := 5$

$P_{Lvi\_95} := V_{o\_max} \cdot I_{o\_95} = 580 \qquad R_{o\_Lvi\_95} := \frac{V_{o\_max}}{I_{o\_95}} = 23.2 \qquad R_{ac\_Lvi\_95} := \frac{8 \cdot n^2}{\pi^2} \cdot R_{o\_Lvi\_95} = 46.891$

8º point: considering SOC = 98%

$I_{o\_98} := 2$

$P_{Lvi\_98} := V_{o\_max} \cdot I_{o\_98} = 232 \qquad R_{o\_Lvi\_98} := \frac{V_{o\_max}}{I_{o\_98}} = 58 \qquad R_{ac\_Lvi\_98} := \frac{8 \cdot n^2}{\pi^2} \cdot R_{o\_Lvi\_98} = 117.227$

9º point: considering SOC = 99%

$I_{o\_99} := 1$

$P_{Lvi\_99} := V_{o\_max} \cdot I_{o\_99} = 116 \qquad R_{o\_Lvi\_99} := \frac{V_{o\_max}}{I_{o\_99}} = 116 \qquad R_{ac\_Lvi\_99} := \frac{8 \cdot n^2}{\pi^2} \cdot R_{o\_Lvi\_99} = 234.453$

10º point: considering SOC = 99.5%

$I_{o\_99.5} := 0.5$

$P_{Lvi\_99.5} := V_{o\_max} \cdot I_{o\_99.5} = 58 \qquad R_{o\_Lvi\_99.5} := \frac{V_{o\_max}}{I_{o\_99.5}} = 232 \qquad R_{ac\_Lvi\_99.5} := \frac{8 \cdot n^2}{\pi^2} \cdot R_{o\_Lvi\_99.5} = 468.906$

11º point: considering SOC = 100%

$I_{o\_float} := 0.01 \qquad V_{o\_max} := 116$

$P_{Lvi\_100} := V_{o\_max} \cdot I_{o\_float} = 1.16 \qquad R_{o\_Lvi\_100} := \frac{V_{o\_max}}{I_{o\_float}} = 1.16 \cdot 10^4 \qquad R_{ac\_Lvi\_100} := \frac{8 \cdot n^2}{\pi^2} \cdot R_{o\_Lvi\_100} = 2.345 \cdot 10^4$

$$P_{Lvi\_g\_0}\left(L_{vi\_g}\right) := \frac{V_{in}^2}{4 \cdot n^2 \cdot R_{ac\_Lvi\_0} \cdot \frac{\pi^2}{8 \cdot n^2}} \cdot \left| \frac{R_{ac\_Lvi\_0}}{\left(\frac{1}{j \cdot \omega \cdot C_r} + j \cdot \omega \cdot L_{lkp} + j \cdot \omega \cdot L_{vi\_g} + j \cdot \omega \cdot L_m \right) \cdot \left(\frac{R_{ac\_Lvi\_0} + n^2 \cdot j \cdot \omega \cdot L_{lks}}{j \cdot \omega \cdot L_m} + 1 \right) - j \cdot \omega \cdot L_m} \right|^2$$

$$P_{Lvi\_g\_25}\left(L_{vi\_g}\right) := \frac{V_{in}^2}{4 \cdot n^2 \cdot R_{ac\_Lvi\_25} \cdot \frac{\pi^2}{8 \cdot n^2}} \cdot \left| \frac{R_{ac\_Lvi\_25}}{\left(\frac{1}{j \cdot \omega \cdot C_r} + j \cdot \omega \cdot L_{lkp} + j \cdot \omega \cdot L_{vi\_g} + j \cdot \omega \cdot L_m \right) \cdot \left(\frac{R_{ac\_Lvi\_25} + n^2 \cdot j \cdot \omega \cdot L_{lks}}{j \cdot \omega \cdot L_m} + 1 \right) - j \cdot \omega \cdot L_m} \right|^2$$

$$P_{Lvi\_g\_50}\left(L_{vi\_g}\right) := \frac{V_{in}^2}{4 \cdot n^2 \cdot R_{ac\_Lvi\_50} \cdot \frac{\pi^2}{8 \cdot n^2}} \cdot \left| \frac{R_{ac\_Lvi\_50}}{\left(\frac{1}{j \cdot \omega \cdot C_r} + j \cdot \omega \cdot L_{lkp} + j \cdot \omega \cdot L_{vi\_g} + j \cdot \omega \cdot L_m \right) \cdot \left(\frac{R_{ac\_Lvi\_50} + n^2 \cdot j \cdot \omega \cdot L_{lks}}{j \cdot \omega \cdot L_m} + 1 \right) - j \cdot \omega \cdot L_m} \right|^2$$

$$P_{Lvi\_g\_75}(L_{vi\_g}) := \frac{V_{in}^2}{4\cdot n^2\cdot R_{ac\_Lvi\_75}\cdot\frac{\pi^2}{8\cdot n^2}}\cdot\left|\frac{R_{ac\_Lvi\_75}}{\left(\frac{1}{j\cdot\omega\cdot C_r}+j\cdot\omega\cdot L_{lkp}+j\cdot\omega\cdot L_{vi\_g}+j\cdot\omega\cdot L_m\right)\cdot\left(\frac{R_{ac\_Lvi\_75}+n^2\cdot j\cdot\omega\cdot L_{lks}}{j\cdot\omega\cdot L_m}+1\right)-j\cdot\omega\cdot L_m}\right|^2$$

$$P_{Lvi\_g\_90}(L_{vi\_g}) := \frac{V_{in}^2}{4\cdot n^2\cdot R_{ac\_Lvi\_90}\cdot\frac{\pi^2}{8\cdot n^2}}\cdot\left|\frac{R_{ac\_Lvi\_90}}{\left(\frac{1}{j\cdot\omega\cdot C_r}+j\cdot\omega\cdot L_{lkp}+j\cdot\omega\cdot L_{vi\_g}+j\cdot\omega\cdot L_m\right)\cdot\left(\frac{R_{ac\_Lvi\_90}+n^2\cdot j\cdot\omega\cdot L_{lks}}{j\cdot\omega\cdot L_m}+1\right)-j\cdot\omega\cdot L_m}\right|^2$$

$$P_{Lvi\_g\_90\_2}(L_{vi\_g}) := \frac{V_{in}^2}{4\cdot n^2\cdot R_{ac\_Lvi\_90\_2}\cdot\frac{\pi^2}{8\cdot n^2}}\cdot\left|\frac{R_{ac\_Lvi\_90\_2}}{\left(\frac{1}{j\cdot\omega\cdot C_r}+j\cdot\omega\cdot L_{lkp}+j\cdot\omega\cdot L_{vi\_g}+j\cdot\omega\cdot L_m\right)\cdot\left(\frac{R_{ac\_Lvi\_90\_2}+n^2\cdot j\cdot\omega\cdot L_{lks}}{j\cdot\omega\cdot L_m}+1\right)-j\cdot\omega\cdot L_m}\right|^2$$

$$P_{Lvi\_g\_92}(L_{vi\_g}) := \frac{V_{in}^2}{4\cdot n^2\cdot R_{ac\_Lvi\_92}\cdot\frac{\pi^2}{8\cdot n^2}}\cdot\left|\frac{R_{ac\_Lvi\_92}}{\left(\frac{1}{j\cdot\omega\cdot C_r}+j\cdot\omega\cdot L_{lkp}+j\cdot\omega\cdot L_{vi\_g}+j\cdot\omega\cdot L_m\right)\cdot\left(\frac{R_{ac\_Lvi\_92}+n^2\cdot j\cdot\omega\cdot L_{lks}}{j\cdot\omega\cdot L_m}+1\right)-j\cdot\omega\cdot L_m}\right|^2$$

$$P_{Lvi\_g\_95}(L_{vi\_g}) := \frac{V_{in}^2}{4\cdot n^2\cdot R_{ac\_Lvi\_95}\cdot\frac{\pi^2}{8\cdot n^2}}\cdot\left|\frac{R_{ac\_Lvi\_95}}{\left(\frac{1}{j\cdot\omega\cdot C_r}+j\cdot\omega\cdot L_{lkp}+j\cdot\omega\cdot L_{vi\_g}+j\cdot\omega\cdot L_m\right)\cdot\left(\frac{R_{ac\_Lvi\_95}+n^2\cdot j\cdot\omega\cdot L_{lks}}{j\cdot\omega\cdot L_m}+1\right)-j\cdot\omega\cdot L_m}\right|^2$$

$$P_{Lvi\_g\_98}(L_{vi\_g}) := \frac{V_{in}^2}{4\cdot n^2\cdot R_{ac\_Lvi\_98}\cdot\frac{\pi^2}{8\cdot n^2}}\cdot\left|\frac{R_{ac\_Lvi\_98}}{\left(\frac{1}{j\cdot\omega\cdot C_r}+j\cdot\omega\cdot L_{lkp}+j\cdot\omega\cdot L_{vi\_g}+j\cdot\omega\cdot L_m\right)\cdot\left(\frac{R_{ac\_Lvi\_98}+n^2\cdot j\cdot\omega\cdot L_{lks}}{j\cdot\omega\cdot L_m}+1\right)-j\cdot\omega\cdot L_m}\right|^2$$

$$P_{Lvi\_g\_99}(L_{vi\_g}) := \frac{V_{in}^2}{4\cdot n^2\cdot R_{ac\_Lvi\_99}\cdot\frac{\pi^2}{8\cdot n^2}}\cdot\left|\frac{R_{ac\_Lvi\_99}}{\left(\frac{1}{j\cdot\omega\cdot C_r}+j\cdot\omega\cdot L_{lkp}+j\cdot\omega\cdot L_{vi\_g}+j\cdot\omega\cdot L_m\right)\cdot\left(\frac{R_{ac\_Lvi\_99}+n^2\cdot j\cdot\omega\cdot L_{lks}}{j\cdot\omega\cdot L_m}+1\right)-j\cdot\omega\cdot L_m}\right|^2$$

$$P_{Lvi\_g\_99.5}(L_{vi\_g}) := \frac{V_{in}^2}{4\cdot n^2\cdot R_{ac\_Lvi\_99.5}\cdot\frac{\pi^2}{8\cdot n^2}}\cdot\left|\frac{R_{ac\_Lvi\_99.5}}{\left(\frac{1}{j\cdot\omega\cdot C_r}+j\cdot\omega\cdot L_{lkp}+j\cdot\omega\cdot L_{vi\_g}+j\cdot\omega\cdot L_m\right)\cdot\left(\frac{R_{ac\_Lvi\_99.5}+n^2\cdot j\cdot\omega\cdot L_{lks}}{j\cdot\omega\cdot L_m}+1\right)-j\cdot\omega\cdot L_m}\right|^2$$

$$P_{Lvi\_g\_100}(L_{vi\_g}) := \frac{V_{in}^2}{4\cdot n^2\cdot R_{ac\_Lvi\_100}\cdot\frac{\pi^2}{8\cdot n^2}}\cdot\left|\frac{R_{ac\_Lvi\_100}}{\left(\frac{1}{j\cdot\omega\cdot C_r}+j\cdot\omega\cdot L_{lkp}+j\cdot\omega\cdot L_{vi\_g}+j\cdot\omega\cdot L_m\right)\cdot\left(\frac{R_{ac\_Lvi\_100}+n^2\cdot j\cdot\omega\cdot L_{lks}}{j\cdot\omega\cdot L_m}+1\right)-j\cdot\omega\cdot L_m}\right|^2$$

$L_{vi\_0} := 18.5\cdot10^{-6}$

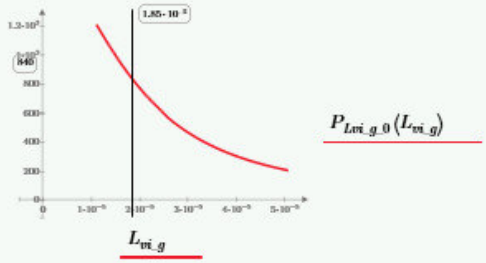

$L_{vi\_25} := 15.5\cdot10^{-6}$

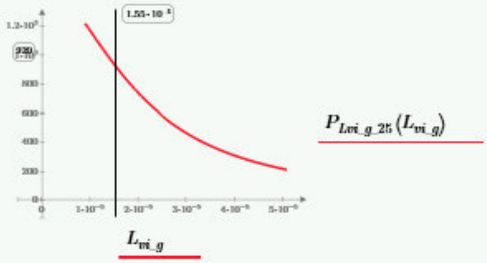

$L_{vi\_50} := 12\cdot10^{-6}$

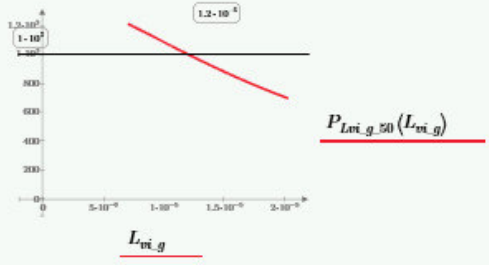

$L_{vi\_75} := 8.3\cdot10^{-6}$

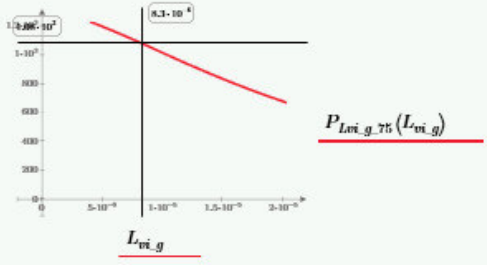

$L_{vi\_90} := 5.6 \cdot 10^{-6}$

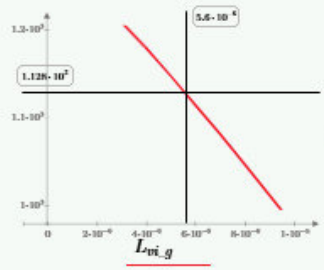

$P_{Lvi\_g\_90}(L_{vi\_g})$

$L_{vi\_90\_2} := 3.5 \cdot 10^{-6}$

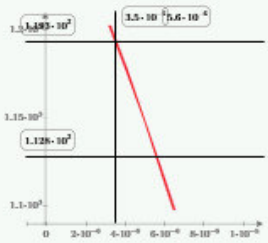

$P_{Lvi\_90\_2} = 1.193 \cdot 10^{3}$

$V_{o\_90\_2} = 116$

$I_{o\_90\_2} = 10.284$

$R_{o\_Lvi\_90\_2} = 11.28$

$L_{vi\_92} := 3.5 \cdot 10^{-6}$

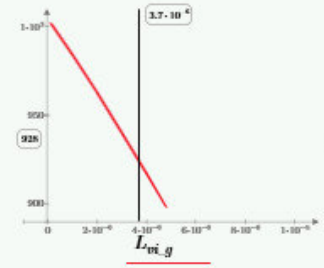

$P_{Lvi\_g\_92}(L_{vi\_g})$

$L_{vi\_95} := 3.5 \cdot 10^{-6}$

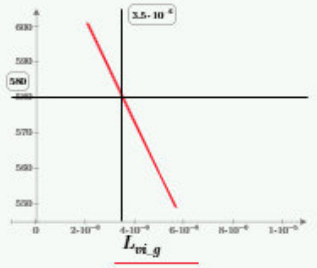

$P_{Lvi\_g\_95}(L_{vi\_g})$

$L_{vi\_98} := 3.5 \cdot 10^{-6}$

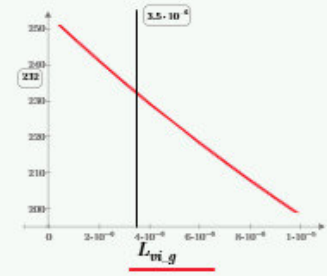

$P_{Lvi\_g\_98}(L_{vi\_g})$

$L_{vi\_99} := 3.5 \cdot 10^{-6}$

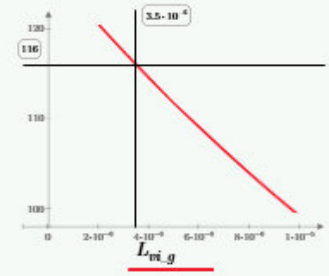

$P_{Lvi\_g\_99}(L_{vi\_g})$

$L_{vi\_99.5} := 3.5 \cdot 10^{-6}$

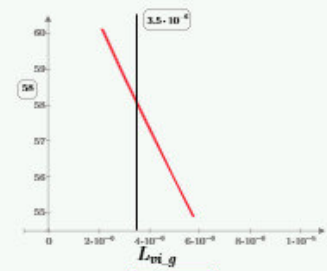

$P_{Lvi\_g\_99.5}(L_{vi\_g})$

$L_{vi\_100} := 3.5 \cdot 10^{-6}$

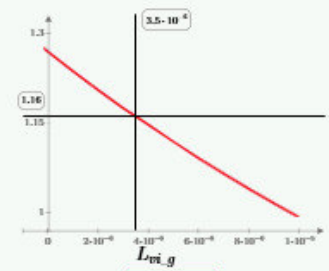

$P_{Lvi\_g\_100}(L_{vi\_g})$

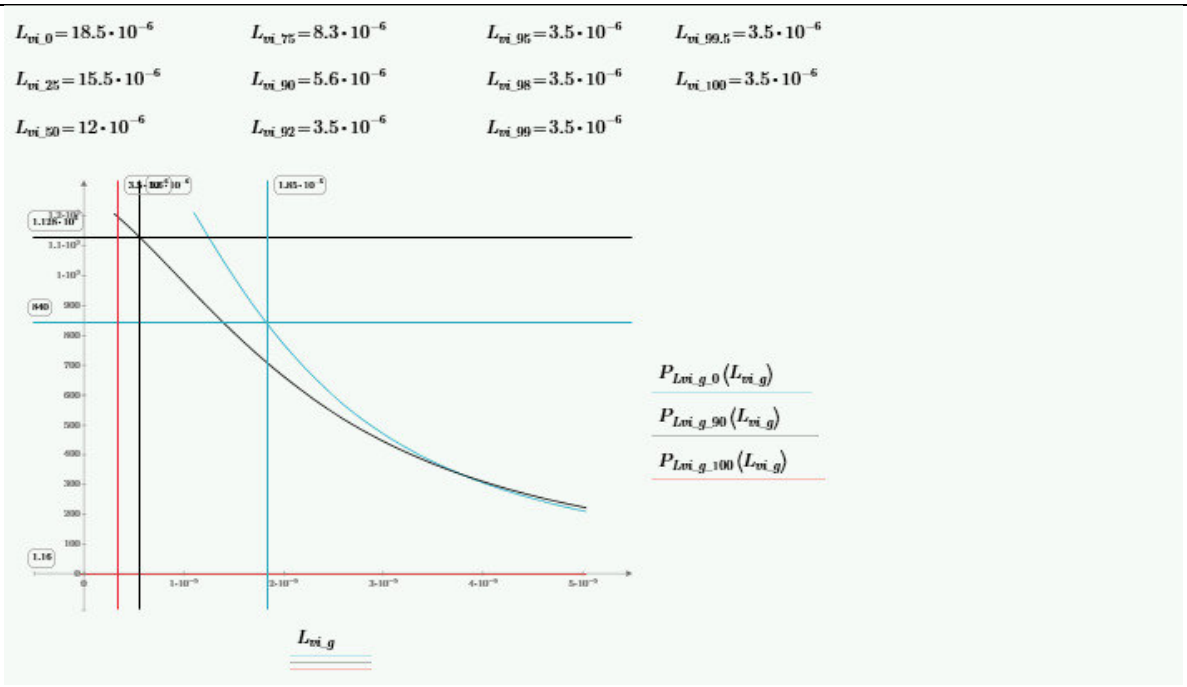

Tab. A.1 – Theoretical and simulation results for the output voltage, current and power as function of the SOC and the VI inductance value

f_s	100	kHz

Theoretical						Simulation		
SOC [%]	L_{vi} $[uH]$	V_{out_t} $[V]$	I_{out_t} $[A]$	R_o $[\Omega]$	P_{out_t} $[W]$	V_{out_sim} $[V]$	I_{out_sim} $[A]$	P_{out_sim} $[W]$
0	21,1	84	10	8,4	840	87,23	10,38	905,82
25	16,65	92	10	9,2	920	95,09	10,34	982,91
50	11,9	100	10	10	1000	102,87	10,29	1058,32
75	6,7	108	10	10,8	1080	109,91	10,18	1118,61
90	3,3	112,8	10	11,28	1128	114,41	10,14	1160,495
90.1	0,95	116	10,284	11,28	1192,944	117,51	10,42	1224,26
92	0,95	116	8	14,5	928	117,65	8,11	954,52
95	0,95	116	5	23,2	580	117,95	5,08	599,69
98	0,95	116	2	58	232	118,27	2,04	241,18
99	0,95	116	1	116	116	118,47	1,02	120,996
99.5	0,95	116	0,5	232	58	118,99	0,513	61,03
100	0,95	116	0,01	11600	1,16	139,13	0,01199	1,67

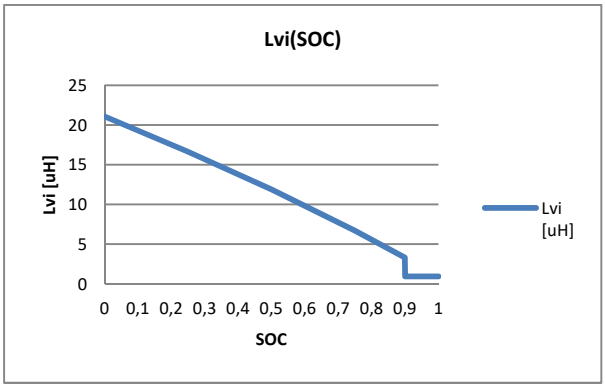

Fig. A.1 – $L_{vi}(SOC)$ theoretical values

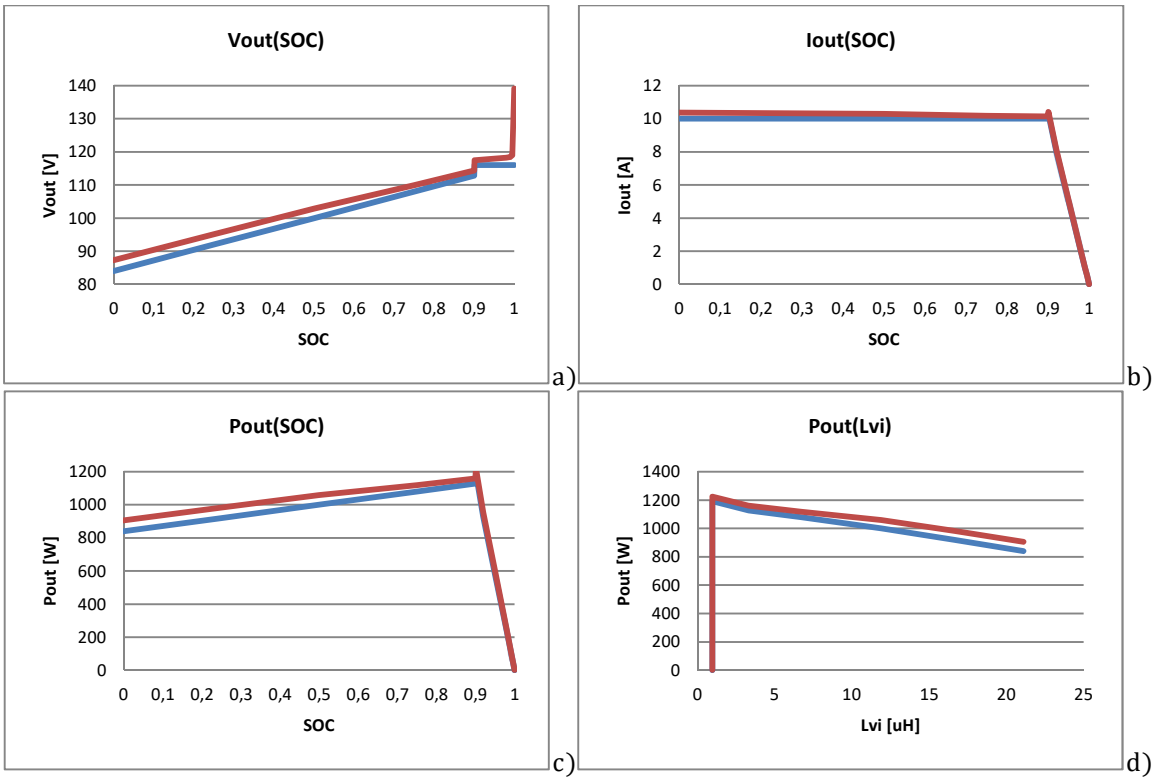

Fig. A.2 –Voltages, currents and Output Power as function of the SOC and L_{vi}, for theoretical and simulation at blue and red, respectively: a) V_{out}(SOC); b) I_{out}(SOC); c) $P_{out}(SOC)$ and d) $P_{out}(L_{vi})$

Step 8 - Select the Resonant Capacitor

$$I_{Cr\_RMS} := \sqrt{\left(\frac{\pi \cdot I_o}{2 \cdot \sqrt{2} \cdot n}\right)^2 + \left(\frac{n \cdot (V_o + 2 \cdot V_F)}{4 \cdot \sqrt{2} \cdot f_0 \cdot L_m}\right)^2} = 7.892$$

$$I_{Cr\_peak} := \sqrt{2} \cdot I_{Cr\_RMS} = 11.161$$

$I_{Cr\_peak} = 11.161$

$$V_{Cr\_max} := \frac{V_{in\_max}}{2} + \frac{I_{Cr\_peak}}{2 \cdot \pi \cdot f_0 \cdot C_r} = 359.344$$

$V_{Cr\_max} = 359.344$

$C_r = 89.983 \cdot 10^{-9}$

$C_r = 90 \cdot 10^{-9}$

$R_{ac} = 23.445$

$P := R_{ac} \cdot I_{Cr\_RMS}^2 = 1.46 \cdot 10^3$

Step 9 - Rectifier Network Design

$I_o = 10$

$f = 100 \cdot 10^3$

$V_o = 116$

$perc\_ripple := 1\%$

$V_{ripple} := V_o \cdot perc\_ripple = 1.16$

$V_{ripple} = 1.16$

$$C_o := \frac{I_o}{V_{ripple} \cdot 2 \cdot f} = 43.103 \cdot 10^{-6}$$

$C_o = 43 \cdot 10^{-6}$

Summary

- Design characteristics

$V_{in}=320$ $k=7$

$I_o=10$ $f=100\cdot10^3$

$V_o=116$ $f_0=100\cdot10^3$

$P_o=1.16\cdot10^3$

- Converter parameters

$M_{min}=1.143$ $n=1.58$ $R_{ac}=23.45$

$M_{max}=1.154$ $L_{lkp}=13\cdot10^{-6}$ $C_r=90\cdot10^{-9}$

$margin=0.1$ $L_m=91\cdot10^{-6}$ $L_r=28\cdot10^{-6}$

$M_{maxmax}=1.27$ $L_{lks}=5\cdot10^{-6}$ $L_p=104\cdot10^{-6}$

$Q=0.7544$ $C_o=43\cdot10^{-6}$

1st point: considering SOC = 0%
- Vo_min and Io_max

$V_{o\_min}=84$ $V_{o\_sim\_0}:=89.2$ $I_{o\_max}=10$ $I_{o\_sim\_0}:=10.62$

$P_{Lvi\_0}=840$ $P_{o\_sim\_0}:=947.51$ $R_{o\_Lvi\_0}=8.4$ $R_{ac\_Lvi\_0}=16.978$ $L_{vi\_0}=18.5\cdot10^{-6}$

2nd point: considering SOC = 90%
- Vo_90% and Io_max

$V_{o\_90}=112.8$ $V_{o\_sim\_90}:=114.30$ $I_{o\_max}=10$ $I_{o\_sim\_90}:=10.13$

$P_{Lvi\_90}=1128$ $P_{o\_sim\_90}:=1158.26$ $R_{o\_Lvi\_90}=11.28$ $R_{ac\_Lvi\_90}=22.799$ $L_{vi\_90}=5.6\cdot10^{-6}$

3rd point: considering SOC = 99.5%
- Vo_max and Io_float

$V_{o\_max}=116$ $V_{o\_sim\_100}:=118.95$ $I_{o\_99.5}=0.5$ $I_{o\_sim\_100}:=0.51$

$P_{Lvi\_99.5}=58$ $P_{o\_sim\_100}:=60.99$ $R_{o\_Lvi\_100}=1.16\cdot10^4$ $R_{ac\_Lvi\_100}=2.345\cdot10^4$ $L_{vi\_100}=3.5\cdot10^{-6}$

-> Teorethical values:
> Vin = 320V
> f = 100kHz
> for the 3 operation points 0%, 90% and 100%

-> Simulation results in PSIM:
> Vin = 320V
> f = 100kHz
> for the 3 operation points 0%, 90% and 100%

$V_{in}=320$ $V_{in}:=80$ $R_o:=5.6$

$R_{ac}:=\frac{8\cdot n^2}{\pi^2}\cdot R_o=11.318$

$$P_{Lvi\_g\_80V}(L_{vi\_g}):=\frac{V_{in}^2}{4\cdot n^2\cdot R_{ac}\cdot\frac{\pi^2}{8\cdot n^2}}\cdot\left|\frac{R_{ac}}{\left(\frac{1}{j\cdot\omega\cdot C_r}+j\cdot\omega\cdot L_{lkp}+j\cdot\omega\cdot L_{vi\_g}+j\cdot\omega\cdot L_m\right)\cdot\left(\frac{R_{ac}+n^2\cdot j\cdot\omega\cdot L_{lks}}{j\cdot\omega\cdot L_m}+1\right)-j\cdot\omega\cdot L_m}\right|^2$$

$L_{vi\_min}:=5.77\cdot10^{-6}$ $P_{o\_max}:=139$

$L_{vi\_max}:=17.66\cdot10^{-6}$ $P_{o\_min}:=62$

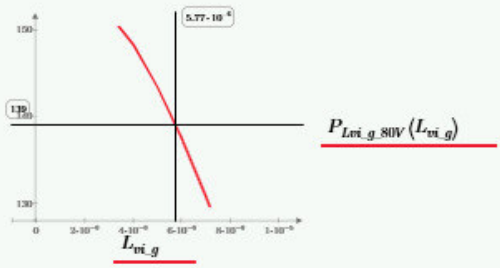

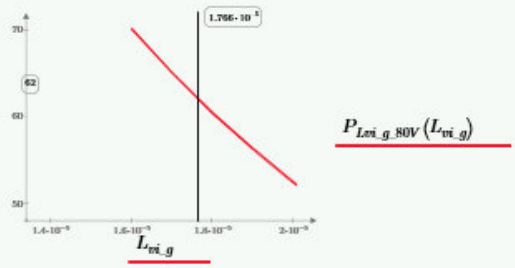

$V_{o\_max} := \sqrt{P_{o\_max} \cdot R_o} = 27.9$ $V_{o\_min} := \sqrt{P_{o\_min} \cdot R_o} = 18.63$

$I_{o\_max} := \sqrt{\frac{P_{o\_max}}{R_o}} = 4.98$ $I_{o\_min} := \sqrt{\frac{P_{o\_min}}{R_o}} = 3.33$

$V_{o\_max} = 27.9$ $I_{o\_max} = 4.98$ $P_{o\_max} = 139$

$V_{o\_min} = 18.63$ $I_{o\_min} = 3.33$ $P_{o\_min} = 62$

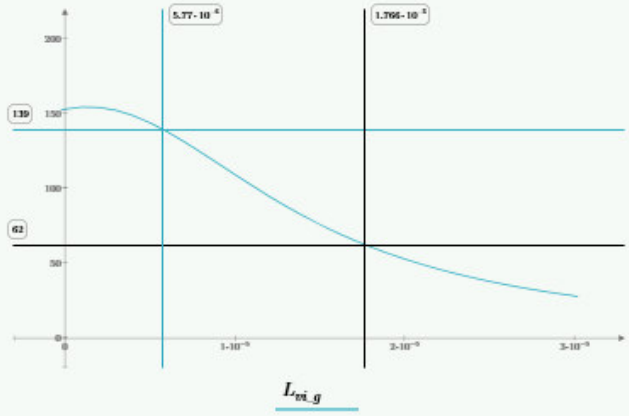

$P_{Lvi\_g\_80V}(L_{vi\_g})$

L_{vi_g}

f	100	$[kHz]$
$deadtime$	100	$[ns]$

	Vin = 80V										
	Lvi [uH]	Idc [A]	Vin [V]	Iin [A]	Pin [VA]	Vout [V]	Iout [A]	Pout [VA]	rend [%]	R = U/I [Ω]		SOC [%]
max	17,66	0	79,4	0,96	29,1	8,65	1,37	11,7	40,20619	5,6	Resist.Preta	0
aprox.	5,6	1,45	76,4	1,48	60,6	23,6	1,91	44,6	73,59736	11,28	Electronic load	90
min	5,56	1,5	80,8	0,512	7,8	29,1	0,0935	2,44	31,28205	232	Electronic load	100
VI c.c.	0	0	80,8	0,571	9,37	31,6	0,102	3,07	32,76414	232	Electronic load	100

$R_{o1} := 5.6$ $R_{ac1} := \frac{8 \cdot n^2}{\pi^2} \cdot R_{o1} = 11.318$

$R_{o2} := 11.28$ $R_{ac2} := \frac{8 \cdot n^2}{\pi^2} \cdot R_{o2} = 22.799$

$R_{o3} := 232$ $R_{ac3} := \frac{8 \cdot n^2}{\pi^2} \cdot R_{o3} = 468.906$

$$P_{Lvi\_g\_80V\_1}(L_{vi\_g}) := \frac{V_{in}^2}{4 \cdot n^2 \cdot R_{ac1} \cdot \frac{\pi^2}{8 \cdot n^2}} \cdot \left| \frac{R_{ac1}}{\left(\frac{1}{j \cdot \omega \cdot C_r} + j \cdot \omega \cdot L_{lkp} + j \cdot \omega \cdot L_{vi\_g} + j \cdot \omega \cdot L_m\right) \cdot \left(\frac{R_{ac1} + n^2 \cdot j \cdot \omega \cdot L_{lks}}{j \cdot \omega \cdot L_m} + 1\right) - j \cdot \omega \cdot L_m} \right|^2$$

$$P_{Lvi\_g\_80V\_2}(L_{vi\_g}) := \frac{V_{in}^2}{4 \cdot n^2 \cdot R_{ac2} \cdot \frac{\pi^2}{8 \cdot n^2}} \cdot \left| \frac{R_{ac2}}{\left(\frac{1}{j \cdot \omega \cdot C_r} + j \cdot \omega \cdot L_{lkp} + j \cdot \omega \cdot L_{vi\_g} + j \cdot \omega \cdot L_m\right) \cdot \left(\frac{R_{ac2} + n^2 \cdot j \cdot \omega \cdot L_{lks}}{j \cdot \omega \cdot L_m} + 1\right) - j \cdot \omega \cdot L_m} \right|^2$$

$$P_{Lvi\_g\_80V\_3}(L_{vi\_g}) := \frac{V_{in}^2}{4 \cdot n^2 \cdot R_{ac3} \cdot \frac{\pi^2}{8 \cdot n^2}} \cdot \left| \frac{R_{ac3}}{\left(\frac{1}{j \cdot \omega \cdot C_r} + j \cdot \omega \cdot L_{lkp} + j \cdot \omega \cdot L_{vi\_g} + j \cdot \omega \cdot L_m\right) \cdot \left(\frac{R_{ac3} + n^2 \cdot j \cdot \omega \cdot L_{lks}}{j \cdot \omega \cdot L_m} + 1\right) - j \cdot \omega \cdot L_m} \right|^2$$

$L_{vi\_1} := 17.66 \cdot 10^{-6}$ $P_{o\_1} := 62$

$L_{vi\_2} := 5.6 \cdot 10^{-6}$ $P_{o\_2} := 70.5$

$L_{vi\_3} := 5.56 \cdot 10^{-6}$ $P_{o\_3} := 3.45$

$L_{vi\_4} := 0$ $P_{o\_4} := 3.97$

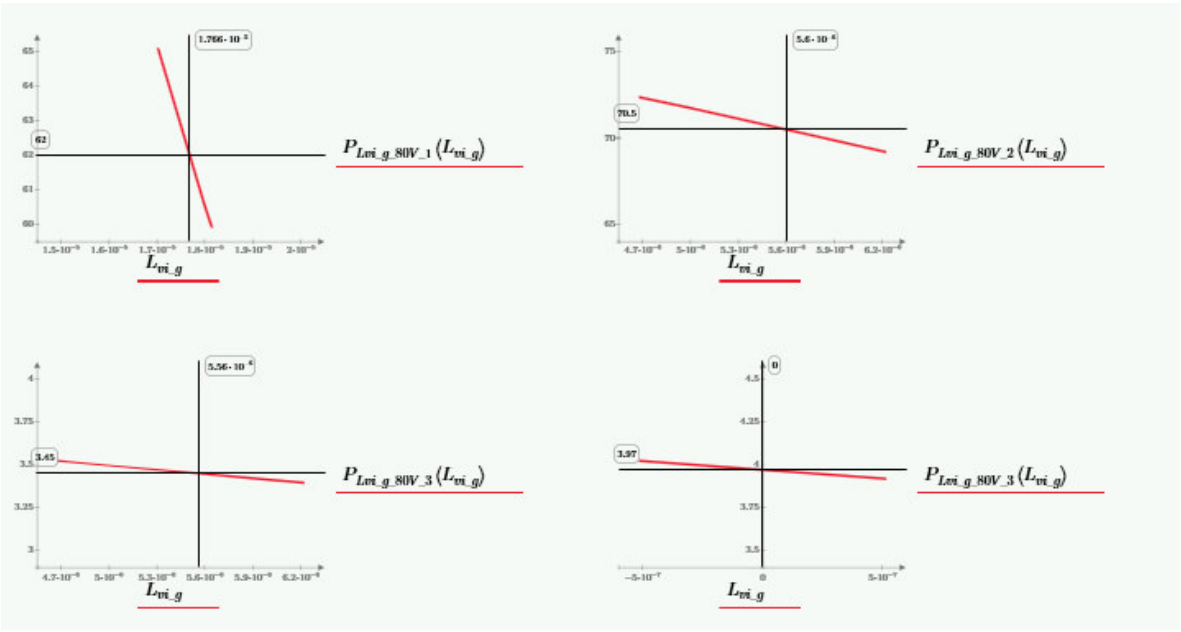

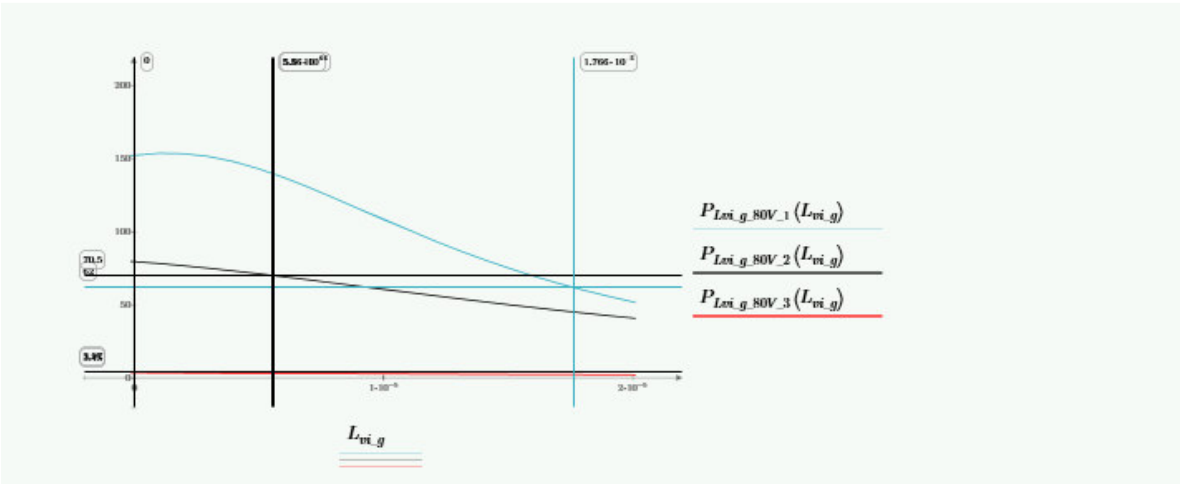

$V_{o\_1} := \sqrt{P_{o\_1} \cdot R_{o1}} = 18.63$ $V_{o\_2} := \sqrt{P_{o\_2} \cdot R_{o2}} = 28.2$ $V_{o\_3} := \sqrt{P_{o\_3} \cdot R_{o3}} = 28.29$ $V_{o\_4} := \sqrt{P_{o\_4} \cdot R_{o3}} = 30.35$

$I_{o\_1} := \sqrt{\frac{P_{o\_1}}{R_{o1}}} = 3.33$ $I_{o\_2} := \sqrt{\frac{P_{o\_2}}{R_{o2}}} = 2.5$ $I_{o\_3} := \sqrt{\frac{P_{o\_3}}{R_{o3}}} = 0.12$ $I_{o\_4} := \sqrt{\frac{P_{o\_4}}{R_{o3}}} = 0.13$

$V_{o\_1} = 18.63$	$I_{o\_1} = 3.33$	$P_{o\_1} = 62$
$V_{o\_2} = 28.2$	$I_{o\_2} = 2.5$	$P_{o\_2} = 70.5$
$V_{o\_3} = 28.29$	$I_{o\_3} = 0.12$	$P_{o\_3} = 3.45$
$V_{o\_4} = 30.35$	$I_{o\_4} = 0.13$	$P_{o\_4} = 3.97$

$V_{in} := 320$

Frequency control

$f := 100 \cdot 10^3$ $f_0 := 100 \cdot 10^3$ $f_p := 51.909 \cdot 10^3$ $L_{vi} := 0$

$f_{sw\_min} := 0$

$f_{sw\_max} := 200 \cdot 10^3$

$f_{sw\_g} := 0, 1000 .. 200 \cdot 10^3$

$$P_{fsw\_g\_0}(f_{sw\_g}) := \frac{V_{in}^2}{4 \cdot n^2 \cdot R_{ac\_Lvi\_0} \cdot \frac{\pi^2}{8 \cdot n^2}} \cdot \left| \frac{R_{ac\_Lvi\_0}}{\left(\frac{1}{j \cdot (2 \cdot \pi \cdot f_{sw\_g}) \cdot C_r} + j \cdot (2 \cdot \pi \cdot f_{sw\_g}) \cdot (L_{lkp} + L_{vi} + L_m)\right) \cdot \left(\frac{R_{ac\_Lvi\_0} + n^2 \cdot j \cdot (2 \cdot \pi \cdot f_{sw\_g}) \cdot L_{lks}}{j \cdot (2 \cdot \pi \cdot f_{sw\_g}) \cdot L_m} + 1\right)} - j \cdot (2 \cdot \pi \cdot f_{sw\_g}) \cdot L_m \right|^2$$

$$P_{fsw\_g\_25}(f_{sw\_g}) := \frac{V_{in}^2}{4 \cdot n^2 \cdot R_{ac\_Lvi\_25} \cdot \frac{\pi^2}{8 \cdot n^2}} \cdot \left| \frac{R_{ac\_Lvi\_25}}{\left(\frac{1}{j \cdot (2 \cdot \pi \cdot f_{sw\_g}) \cdot C_r} + j \cdot (2 \cdot \pi \cdot f_{sw\_g}) \cdot (L_{lkp} + L_{vi} + L_m)\right) \cdot \left(\frac{R_{ac\_Lvi\_25} + n^2 \cdot j \cdot (2 \cdot \pi \cdot f_{sw\_g}) \cdot L_{lks}}{j \cdot (2 \cdot \pi \cdot f_{sw\_g}) \cdot L_m} + 1\right)} - j \cdot (2 \cdot \pi \cdot f_{sw\_g}) \cdot L_m \right|^2$$

$$P_{fsw\_g\_50}(f_{sw\_g}) := \frac{V_{in}^2}{4 \cdot n^2 \cdot R_{ac\_Lvi\_50} \cdot \frac{\pi^2}{8 \cdot n^2}} \cdot \left| \frac{R_{ac\_Lvi\_50}}{\left(\frac{1}{j \cdot (2 \cdot \pi \cdot f_{sw\_g}) \cdot C_r} + j \cdot (2 \cdot \pi \cdot f_{sw\_g}) \cdot (L_{lkp} + L_{vi} + L_m)\right) \cdot \left(\frac{R_{ac\_Lvi\_50} + n^2 \cdot j \cdot (2 \cdot \pi \cdot f_{sw\_g}) \cdot L_{lks}}{j \cdot (2 \cdot \pi \cdot f_{sw\_g}) \cdot L_m} + 1\right)} - j \cdot (2 \cdot \pi \cdot f_{sw\_g}) \cdot L_m \right|^2$$

$$P_{fsw\_g\_75}(f_{sw\_g}) := \frac{V_{in}^2}{4 \cdot n^2 \cdot R_{ac\_Lvi\_75} \cdot \frac{\pi^2}{8 \cdot n^2}} \cdot \left| \frac{R_{ac\_Lvi\_75}}{\left(\frac{1}{j \cdot (2 \cdot \pi \cdot f_{sw\_g}) \cdot C_r} + j \cdot (2 \cdot \pi \cdot f_{sw\_g}) \cdot (L_{lkp} + L_{vi} + L_m)\right) \cdot \left(\frac{R_{ac\_Lvi\_75} + n^2 \cdot j \cdot (2 \cdot \pi \cdot f_{sw\_g}) \cdot L_{lks}}{j \cdot (2 \cdot \pi \cdot f_{sw\_g}) \cdot L_m} + 1\right)} - j \cdot (2 \cdot \pi \cdot f_{sw\_g}) \cdot L_m \right|^2$$

$$P_{fsw\_g\_90}(f_{sw\_g}) := \frac{V_{in}^2}{4 \cdot n^2 \cdot R_{ac\_Lvi\_90} \cdot \frac{\pi^2}{8 \cdot n^2}} \cdot \left| \frac{R_{ac\_Lvi\_90}}{\left(\frac{1}{j \cdot (2 \cdot \pi \cdot f_{sw\_g}) \cdot C_r} + j \cdot (2 \cdot \pi \cdot f_{sw\_g}) \cdot (L_{lkp} + L_{vi} + L_m)\right) \cdot \left(\frac{R_{ac\_Lvi\_90} + n^2 \cdot j \cdot (2 \cdot \pi \cdot f_{sw\_g}) \cdot L_{lks}}{j \cdot (2 \cdot \pi \cdot f_{sw\_g}) \cdot L_m} + 1\right)} - j \cdot (2 \cdot \pi \cdot f_{sw\_g}) \cdot L_m \right|^2$$

$$P_{fsw\_g\_90\_2}(f_{sw\_g}) := \frac{V_{in}^2}{4 \cdot n^2 \cdot R_{ac\_Lvi\_90\_2} \cdot \frac{\pi^2}{8 \cdot n^2}} \cdot \left| \frac{R_{ac\_Lvi\_90\_2}}{\left(\frac{1}{j \cdot (2 \cdot \pi \cdot f_{sw\_g}) \cdot C_r} + j \cdot (2 \cdot \pi \cdot f_{sw\_g}) \cdot (L_{lkp} + L_{vi} + L_m)\right) \cdot \left(\frac{R_{ac\_Lvi\_90\_2} + n^2 \cdot j \cdot (2 \cdot \pi \cdot f_{sw\_g}) \cdot L_{lks}}{j \cdot (2 \cdot \pi \cdot f_{sw\_g}) \cdot L_m} + 1\right)} - j \cdot (2 \cdot \pi \cdot f_{sw\_g}) \cdot L_m \right|^2$$

$$P_{fsw\_g\_92}(f_{sw\_g}) := \frac{V_{in}^2}{4 \cdot n^2 \cdot R_{ac\_Lvi\_92} \cdot \frac{\pi^2}{8 \cdot n^2}} \cdot \left| \frac{R_{ac\_Lvi\_92}}{\left(\frac{1}{j \cdot (2 \cdot \pi \cdot f_{sw\_g}) \cdot C_r} + j \cdot (2 \cdot \pi \cdot f_{sw\_g}) \cdot (L_{lkp} + L_{vi} + L_m)\right) \cdot \left(\frac{R_{ac\_Lvi\_92} + n^2 \cdot j \cdot (2 \cdot \pi \cdot f_{sw\_g}) \cdot L_{lks}}{j \cdot (2 \cdot \pi \cdot f_{sw\_g}) \cdot L_m} + 1\right)} - j \cdot (2 \cdot \pi \cdot f_{sw\_g}) \cdot L_m \right|^2$$

$$P_{fsw\_g\_95}(f_{sw\_g}) := \frac{V_{in}^2}{4 \cdot n^2 \cdot R_{ac\_Lvi\_95} \cdot \frac{\pi^2}{8 \cdot n^2}} \cdot \left| \frac{R_{ac\_Lvi\_95}}{\left(\frac{1}{j \cdot (2 \cdot \pi \cdot f_{sw\_g}) \cdot C_r} + j \cdot (2 \cdot \pi \cdot f_{sw\_g}) \cdot (L_{lkp} + L_{vi} + L_m)\right) \cdot \left(\frac{R_{ac\_Lvi\_95} + n^2 \cdot j \cdot (2 \cdot \pi \cdot f_{sw\_g}) \cdot L_{lks}}{j \cdot (2 \cdot \pi \cdot f_{sw\_g}) \cdot L_m} + 1\right)} - j \cdot (2 \cdot \pi \cdot f_{sw\_g}) \cdot L_m \right|^2$$

$$P_{fsw\_g\_98}(f_{sw\_g}) := \frac{V_{in}^2}{4 \cdot n^2 \cdot R_{ac\_Lvi\_98} \cdot \frac{\pi^2}{8 \cdot n^2}} \cdot \left| \frac{R_{ac\_Lvi\_98}}{\left(\frac{1}{j \cdot (2 \cdot \pi \cdot f_{sw\_g}) \cdot C_r} + j \cdot (2 \cdot \pi \cdot f_{sw\_g}) \cdot (L_{lkp} + L_{vi} + L_m)\right) \cdot \left(\frac{R_{ac\_Lvi\_98} + n^2 \cdot j \cdot (2 \cdot \pi \cdot f_{sw\_g}) \cdot L_{lks}}{j \cdot (2 \cdot \pi \cdot f_{sw\_g}) \cdot L_m} + 1\right)} - j \cdot (2 \cdot \pi \cdot f_{sw\_g}) \cdot L_m \right|^2$$

$$P_{fsw\_g\_99}(f_{sw\_g}) := \frac{V_{in}^2}{4 \cdot n^2 \cdot R_{ac\_Lvi\_99} \cdot \frac{\pi^2}{8 \cdot n^2}} \cdot \left| \frac{R_{ac\_Lvi\_99}}{\left(\frac{1}{j \cdot (2 \cdot \pi \cdot f_{sw\_g}) \cdot C_r} + j \cdot (2 \cdot \pi \cdot f_{sw\_g}) \cdot (L_{lkp} + L_{vi} + L_m)\right) \cdot \left(\frac{R_{ac\_Lvi\_99} + n^2 \cdot j \cdot (2 \cdot \pi \cdot f_{sw\_g}) \cdot L_{lks}}{j \cdot (2 \cdot \pi \cdot f_{sw\_g}) \cdot L_m} + 1\right)} - j \cdot (2 \cdot \pi \cdot f_{sw\_g}) \cdot L_m \right|^2$$

$$P_{fsw\_g\_99.5}(f_{sw\_g}) := \frac{V_{in}^2}{4 \cdot n^2 \cdot R_{ac\_Lvi\_99.5} \cdot \frac{\pi^2}{8 \cdot n^2}} \cdot \left| \frac{R_{ac\_Lvi\_99.5}}{\left(\frac{1}{j \cdot (2 \cdot \pi \cdot f_{sw\_g}) \cdot C_r} + j \cdot (2 \cdot \pi \cdot f_{sw\_g}) \cdot (L_{lkp} + L_{vi} + L_m)\right) \cdot \left(\frac{R_{ac\_Lvi\_99.5} + n^2 \cdot j \cdot (2 \cdot \pi \cdot f_{sw\_g}) \cdot L_{lks}}{j \cdot (2 \cdot \pi \cdot f_{sw\_g}) \cdot L_m} + 1\right)} - j \cdot (2 \cdot \pi \cdot f_{sw\_g}) \cdot L_m \right|^2$$

$$P_{fsw\_g\_100}(f_{sw\_g}) := \frac{V_{in}^2}{4 \cdot n^2 \cdot R_{ac\_Lvi\_100} \cdot \frac{\pi^2}{8 \cdot n^2}} \cdot \left| \frac{R_{ac\_Lvi\_100}}{\left(\frac{1}{j \cdot (2 \cdot \pi \cdot f_{sw\_g}) \cdot C_r} + j \cdot (2 \cdot \pi \cdot f_{sw\_g}) \cdot (L_{lkp} + L_{vi} + L_m)\right) \cdot \left(\frac{R_{ac\_Lvi\_100} + n^2 \cdot j \cdot (2 \cdot \pi \cdot f_{sw\_g}) \cdot L_{lks}}{j \cdot (2 \cdot \pi \cdot f_{sw\_g}) \cdot L_m} + 1\right)} - j \cdot (2 \cdot \pi \cdot f_{sw\_g}) \cdot L_m \right|^2$$

$f_{sw\_0} := 145 \cdot 10^3$

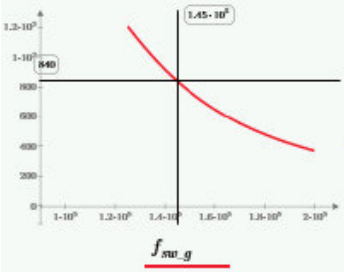

$P_{fsw\_g\_0}(f_{sw\_g})$

f_{sw_g}

$f_{sw\_25} := 138 \cdot 10^3$

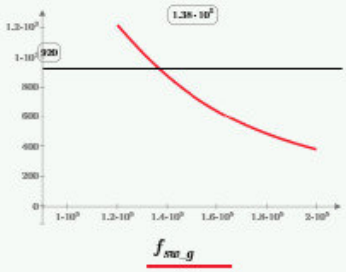

$P_{fsw\_g\_25}(f_{sw\_g})$

f_{sw_g}

$f_{sw\_50} := 129 \cdot 10^3$

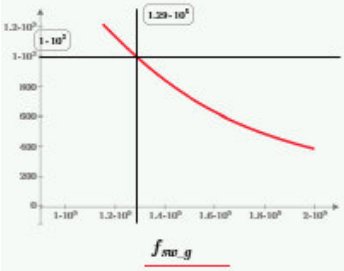

$P_{fsw\_g\_50}(f_{sw\_g})$

f_{sw_g}

$f_{sw\_75} := 118 \cdot 10^3$

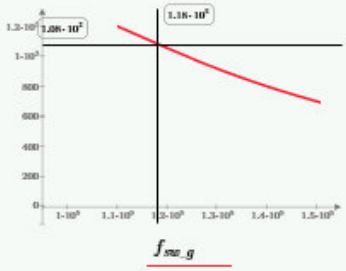

$P_{fsw\_g\_75}(f_{sw\_g})$

f_{sw_g}

$f_{sw\_90} := 112 \cdot 10^3$

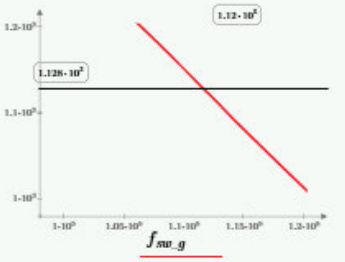

$P_{fsw\_g\_90}(f_{sw\_g})$

f_{sw_g}

$f_{sw\_90\_2} := 107.5 \cdot 10^3$

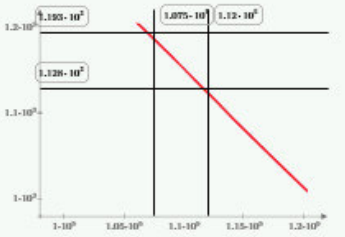

$P_{Loi\_90\_2} = 1.193 \cdot 10^3$

$V_{o\_90\_2} = 116$

$I_{o\_90\_2} = 10.284$

$R_{o\_Loi\_90\_2} = 11.28$

$f_{sw\_92} := 107.5 \cdot 10^3$

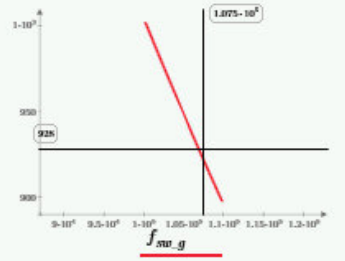

$P_{fsw\_g\_92}(f_{sw\_g})$

f_{sw_g}

$f_{sw\_95} := 107.5 \cdot 10^3$

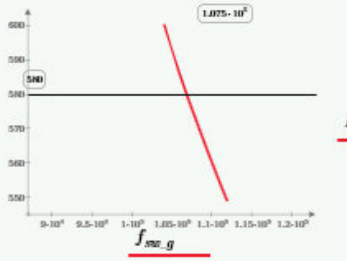

$P_{fsw\_g\_95}(f_{sw\_g})$

f_{sw_g}

$f_{sw\_98} := 107.5 \cdot 10^3$

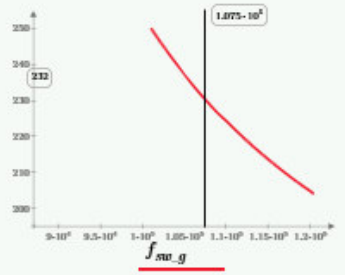

$P_{fsw\_g\_98}(f_{sw\_g})$

f_{sw_g}

$f_{sw\_99} := 107.5 \cdot 10^3$

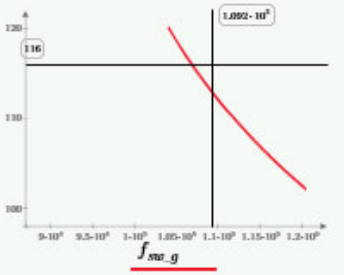

$P_{fsw\_g\_99}(f_{sw\_g})$

f_{sw_g}

$f_{sw\_99.5} := 107.5 \cdot 10^3$

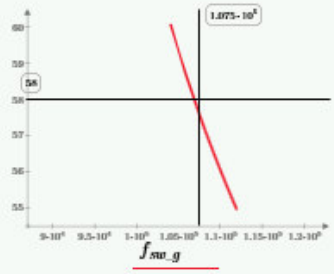

$P_{fsw\_g\_99.5}(f_{sw\_g})$

$f_{sw\_100} := 107.5 \cdot 10^3$

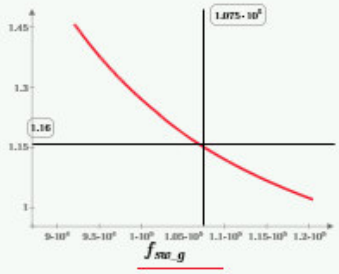

$P_{fsw\_g\_100}(f_{sw\_g})$

$f_{sw\_0} = 145 \cdot 10^3$ $f_{sw\_75} = 118 \cdot 10^3$ $f_{sw\_95} = 107.5 \cdot 10^3$ $f_{sw\_99.5} = 107.5 \cdot 10^3$

$f_{sw\_25} = 138 \cdot 10^3$ $f_{sw\_90} = 112 \cdot 10^3$ $f_{sw\_98} = 107.5 \cdot 10^3$ $f_{sw\_100} = 107.5 \cdot 10^3$

$f_{sw\_50} = 129 \cdot 10^3$ $f_{sw\_92} = 107.5 \cdot 10^3$ $f_{sw\_99} = 107.5 \cdot 10^3$

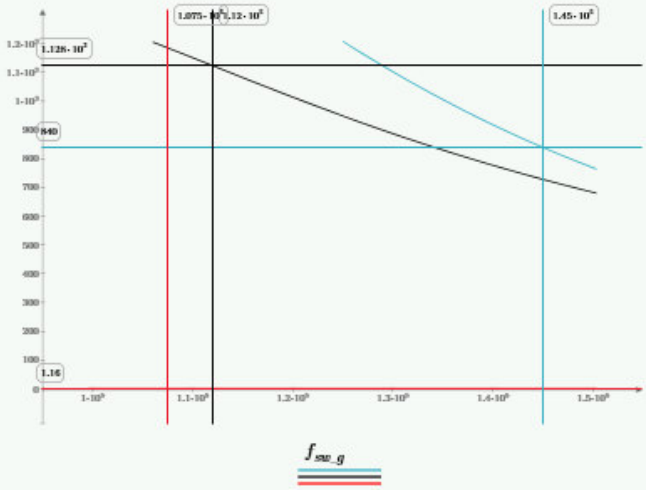

$P_{fsw\_g\_0}(f_{sw\_g})$

$P_{fsw\_g\_90}(f_{sw\_g})$

$P_{fsw\_g\_100}(f_{sw\_g})$

f_{sw_g}

1st point: considering SOC = 0%
- Vo_min and Io_max

$V_{o\_min} = 18.633$ $V_{o\_sim\_0} := 94.92$ $I_{o\_max} = 4.982$ $I_{o\_sim\_0} := 11.30$

$P_{Lvi\_0} = 840$ $P_{o\_sim\_0} := 1072.68$ $R_{o\_Lvi\_0} = 8.4$ $R_{ac\_Lvi\_0} = 16.978$ $f_{sw\_0} = 145 \cdot 10^3$

2nd point: considering SOC = 90%
- Vo_90% and Io_max

$V_{o\_90} = 112.8$ $V_{o\_sim\_90} := 114.04$ $I_{o\_max} = 4.982$ $I_{o\_sim\_90} := 10.11$

$P_{Lvi\_90} = 1128$ $P_{o\_sim\_90} := 1153$ $R_{o\_Lvi\_90} = 11.28$ $R_{ac\_Lvi\_90} = 22.799$ $f_{sw\_90} = 112 \cdot 10^3$

3rd point: considering SOC = 99.5%
- Vo_max and Io_float

$V_{o\_max} = 27.9$ $V_{o\_sim\_100} := 118.26$ $I_{o\_99.5} = 0.5$ $I_{o\_sim\_100} := 0.51$

$P_{Lvi\_99.5} = 58$ $P_{o\_sim\_100} := 60.28$ $R_{o\_Lvi\_100} = 1.16 \cdot 10^4$ $R_{ac\_Lvi\_100} = 2.345 \cdot 10^4$ $f_{sw\_100} = 107.5 \cdot 10^3$

-> Teorethical values:
> Vin = 320V
> Lvi = 0H
> for the 3 operation points 0%, 90% and 100%

-> Simulation results in PSIM:
> Vin = 320V
> Lvi = 0H
> for the 3 operation points 0%, 90% and 100%

Simulation parameters summary:

$V_{in}=320$

$f=100\cdot10^{3}$	$L_{vi}=0$	$L_{lkp}=13\cdot10^{-6}$	$C_o=43\cdot10^{-6}$
$L_{vi\_0}=18.5\cdot10^{-6}$	$f_{sw\_0}=145\cdot10^{3}$	$L_{lks}=5\cdot10^{-6}$	
$L_{vi\_90}=5.6\cdot10^{-6}$	$f_{sw\_90}=112\cdot10^{3}$	$L_m=91\cdot10^{-6}$	
$L_{vi\_100}=3.5\cdot10^{-6}$	$f_{sw\_100}=107.5\cdot10^{3}$	$n=1.58$	
		$R_p=1.66$	$R_{p\_sim}:=0.001$
$C_r=90\cdot10^{-9}$		$R_s=0.63$	$R_{s\_sim}:=0.001$

Both control variables simultaneously:

$L_{vi}:=0$

$$M_{100\_Lvi\_0}(f_{sw\_g}):=\left|\frac{R_{ac\_100}}{\left(\frac{1}{j\cdot(2\cdot\pi\cdot f_{sw\_g})\cdot C_r}+j\cdot(2\cdot\pi\cdot f_{sw\_g})\cdot(L_{lkp}+L_{vi}+L_m)\right)\cdot\left(\frac{R_{ac\_100}+n^2\cdot j\cdot(2\cdot\pi\cdot f_{sw\_g})\cdot L_{lks}}{j\cdot(2\cdot\pi\cdot f_{sw\_g})\cdot L_m}+1\right)-j\cdot(2\cdot\pi\cdot f_{sw\_g})\cdot L_m}\right|$$

$$P_{fsw\_g\_0}(f_{sw\_g}):=\frac{V_{in}^{\ 2}}{4\cdot n^2\cdot R_{ac\_100}\cdot\frac{\pi^2}{8\cdot n^2}}\cdot\left|\frac{R_{ac\_100}}{\left(\frac{1}{j\cdot(2\cdot\pi\cdot f_{sw\_g})\cdot C_r}+j\cdot(2\cdot\pi\cdot f_{sw\_g})\cdot(L_{lkp}+L_{vi}+L_m)\right)\cdot\left(\frac{R_{ac\_100}+n^2\cdot j\cdot(2\cdot\pi\cdot f_{sw\_g})\cdot L_{lks}}{j\cdot(2\cdot\pi\cdot f_{sw\_g})\cdot L_m}+1\right)-j\cdot(2\cdot\pi\cdot f_{sw\_g})\cdot L_m}\right|^2$$

$L_{vi\_10u}:=10\cdot10^{-6}$

$$M_{100\_Lvi\_10u}(f_{sw\_g}):=\left|\frac{R_{ac\_100}}{\left(\frac{1}{j\cdot(2\cdot\pi\cdot f_{sw\_g})\cdot C_r}+j\cdot(2\cdot\pi\cdot f_{sw\_g})\cdot(L_{lkp}+L_{vi\_10u}+L_m)\right)\cdot\left(\frac{R_{ac\_100}+n^2\cdot j\cdot(2\cdot\pi\cdot f_{sw\_g})\cdot L_{lks}}{j\cdot(2\cdot\pi\cdot f_{sw\_g})\cdot L_m}+1\right)-j\cdot(2\cdot\pi\cdot f_{sw\_g})\cdot L_m}\right|$$

$$P_{fsw\_g\_10u}(f_{sw\_g}):=\frac{V_{in}^{\ 2}}{4\cdot n^2\cdot R_{ac\_100}\cdot\frac{\pi^2}{8\cdot n^2}}\cdot\left|\frac{R_{ac\_100}}{\left(\frac{1}{j\cdot(2\cdot\pi\cdot f_{sw\_g})\cdot C_r}+j\cdot(2\cdot\pi\cdot f_{sw\_g})\cdot(L_{lkp}+L_{vi\_10u}+L_m)\right)\cdot\left(\frac{R_{ac\_100}+n^2\cdot j\cdot(2\cdot\pi\cdot f_{sw\_g})\cdot L_{lks}}{j\cdot(2\cdot\pi\cdot f_{sw\_g})\cdot L_m}+1\right)-j\cdot(2\cdot\pi\cdot f_{sw\_g})\cdot L_m}\right|^2$$

$L_{vi\_20u}:=20\cdot10^{-6}$

$$M_{100\_Lvi\_20u}(f_{sw\_g}):=\left|\frac{R_{ac\_100}}{\left(\frac{1}{j\cdot(2\cdot\pi\cdot f_{sw\_g})\cdot C_r}+j\cdot(2\cdot\pi\cdot f_{sw\_g})\cdot(L_{lkp}+L_{vi\_20u}+L_m)\right)\cdot\left(\frac{R_{ac\_100}+n^2\cdot j\cdot(2\cdot\pi\cdot f_{sw\_g})\cdot L_{lks}}{j\cdot(2\cdot\pi\cdot f_{sw\_g})\cdot L_m}+1\right)-j\cdot(2\cdot\pi\cdot f_{sw\_g})\cdot L_m}\right|$$

$$P_{fsw\_g\_20u}(f_{sw\_g}):=\frac{V_{in}^{\ 2}}{4\cdot n^2\cdot R_{ac\_100}\cdot\frac{\pi^2}{8\cdot n^2}}\cdot\left|\frac{R_{ac\_100}}{\left(\frac{1}{j\cdot(2\cdot\pi\cdot f_{sw\_g})\cdot C_r}+j\cdot(2\cdot\pi\cdot f_{sw\_g})\cdot(L_{lkp}+L_{vi\_20u}+L_m)\right)\cdot\left(\frac{R_{ac\_100}+n^2\cdot j\cdot(2\cdot\pi\cdot f_{sw\_g})\cdot L_{lks}}{j\cdot(2\cdot\pi\cdot f_{sw\_g})\cdot L_m}+1\right)-j\cdot(2\cdot\pi\cdot f_{sw\_g})\cdot L_m}\right|^2$$

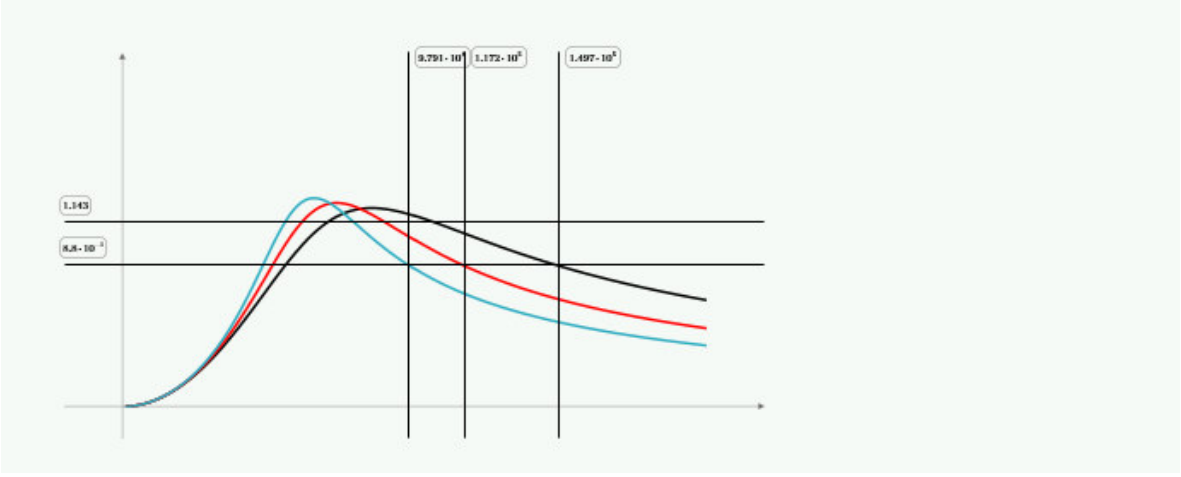

Auxiliary Matlab Code for the Determination of the Q Parameter:

```
%%%%%%%%%%%%%%%%%%%%%%%%%%%%%%%%%%%%%%%%%%%%%%%%%%%%%%%%%%%%%%%%%%%%%%%%%%%%%%%
% Auxiliar calculations for the converter design - Parameters Q
%%%%%%%%%%%%%%%%%%%%%%%%%%%%%%%%%%%%%%%%%%%%%%%%%%%%%%%%%%%%%%%%%%%%%%%%%%%%%%%
clear all
clc

%%%%%%%%%%%%%%%%%%%%%%%%%%%%%%%%%%%%%%%%%%%%%%%%%%%%%%%%%%%%%%%%%%%%%%%%%%%%%%%
% Parameters
%%%%%%%%%%%%%%%%%%%%%%%%%%%%%%%%%%%%%%%%%%%%%%%%%%%%%%%%%%%%%%%%%%%%%%%%%%%%%%%
k=7;
Mg_min = 1.143;
margin = 0.1;
Mg_max2 = 1.154;
Mg_maxmax2 = (1+margin)*Mg_max2
f = 100e3;
f0 = 100e3;
fp = 48.412e3;
w = 2*pi*f;
w0 = 2*pi*f0;
wp = 2*pi*fp;

%%%%%%%%%%%%%%%%%%%%%%%%%%%%%%%%%%%%%%%%%%%%%%%%%%%%%%%%%%%%%%%%%%%%%%%%%%%%%%%
% Plot of the maximum gain curves as function of Q for various values of k
%%%%%%%%%%%%%%%%%%%%%%%%%%%%%%%%%%%%%%%%%%%%%%%%%%%%%%%%%%%%%%%%%%%%%%%%%%%%%%%
fs = [0.1:100:100e3];
Qv = [0.01:0.05:2];
Qv2 = [0.01:0.0005:2];
Qp = 0.6315;

k5=5;
k6=6;
k7=7;
k8=8;
k9=9;
k10=10;

M5=zeros(length(fs),length(Qv));
M6=zeros(length(fs),length(Qv));
M7=zeros(length(fs),length(Qv));
M8=zeros(length(fs),length(Qv));
M9=zeros(length(fs),length(Qv));
M10=zeros(length(fs),length(Qv));

for y=1:length(Qv)
    for x=1:length(fs)
        M5(x,y) =
abs(((((2*pi*fs(x))^2)/wp^2)*(k5/(k5+1)))/((i*(((2*pi*fs(x))/w0)*(1-
(((2*pi*fs(x))^2)/w0^2))*Qv(y)*(((k5+1)^2)/(2*k5+1))))+(1-
(((2*pi*fs(x))^2)/wp^2))));
        M6(x,y) =
abs(((((2*pi*fs(x))^2)/wp^2)*(k6/(k6+1)))/((i*(((2*pi*fs(x))/w0)*(1-
(((2*pi*fs(x))^2)/w0^2))*Qv(y)*(((k6+1)^2)/(2*k6+1))))+(1-
(((2*pi*fs(x))^2)/wp^2))));
        M7(x,y) =
abs(((((2*pi*fs(x))^2)/wp^2)*(k7/(k7+1)))/((i*(((2*pi*fs(x))/w0)*(1-
(((2*pi*fs(x))^2)/w0^2))*Qv(y)*(((k7+1)^2)/(2*k7+1))))+(1-
(((2*pi*fs(x))^2)/wp^2))));
        M8(x,y) =
abs(((((2*pi*fs(x))^2)/wp^2)*(k8/(k8+1)))/((i*(((2*pi*fs(x))/w0)*(1-
(((2*pi*fs(x))^2)/w0^2))*Qv(y)*(((k8+1)^2)/(2*k8+1))))+(1-
(((2*pi*fs(x))^2)/wp^2))));
        M9(x,y) =
abs(((((2*pi*fs(x))^2)/wp^2)*(k9/(k9+1)))/((i*(((2*pi*fs(x))/w0)*(1-
(((2*pi*fs(x))^2)/w0^2))*Qv(y)*(((k9+1)^2)/(2*k9+1))))+(1-
(((2*pi*fs(x))^2)/wp^2))));
        M10(x,y) =
abs(((((2*pi*fs(x))^2)/wp^2)*(k10/(k10+1)))/((i*(((2*pi*fs(x))/w0)*(1-
(((2*pi*fs(x))^2)/w0^2))*Qv(y)*(((k10+1)^2)/(2*k10+1))))+(1-
(((2*pi*fs(x))^2)/wp^2))));
```

```
    end
end

for y=1:length(Qv)
    m5(y)=max(M5(:,y));
    m6(y)=max(M6(:,y));
    m7(y)=max(M7(:,y));
    m8(y)=max(M8(:,y));
    m9(y)=max(M9(:,y));
    m10(y)=max(M10(:,y));
end

%%%%%%%%%%%%%%%%%%%%%%%%%%%%%%%%%%%%%%%%%%%%%%%%%%%%%%%%%%%%%%%%%%%%%%%%%%%%%%%
% Plot of the maximum gain curves as function of Q for various values of k
%%%%%%%%%%%%%%%%%%%%%%%%%%%%%%%%%%%%%%%%%%%%%%%%%%%%%%%%%%%%%%%%%%%%%%%%%%%%%%%
figure(1)
plot(Qv,m5,'k-^')
hold on
plot(Qv,m6,'k-o')
hold on
plot(Qv,m7,'k-s',...
    'LineWidth',2,...
    'MarkerSize',5,...
    'MarkerEdgeColor','k',...
    'MarkerFaceColor','w')
hold on
plot(Qv,m8,'k-+')
hold on
plot(Qv,m9,'k-*')
hold on
plot(Qv,m10,'k-x')
hold on

plot(Qv2,Mg_maxmax2,'k')
hold on;
legend('k = 5','k = 6','k = 7','k = 8','k = 9','k = 10','M_m_a_x_m_a_x')
plot(Qp,Mg_maxmax2,'ko',...
    'LineWidth',1,...
    'MarkerSize',10,...
    'MarkerEdgeColor','k',...
    'MarkerFaceColor','k')
plot(Qp,1.1,'k')
plot(Qp,1.125,'k')
plot(Qp,1.15,'k')
plot(Qp,1.175,'k')
plot(Qp,1.2,'k')
plot(Qp,1.225,'k')
plot(Qp,1.25,'k')
hold on;
title({'Peak gain curve for various k values'});
xlabel('Q');
ylabel('M_p_e_a_k');
grid on;
axis([0.3 1 1.1 1.8]);

%%%%%%%%%%%%%%%%%%%%%%%%%%%%%%%%%%%%%%%%%%%%%%%%%%%%%%%%%%%%%%%%%%%%%%%%%%%%%%%
% Plot of the maximum gain curve as function of Q for k = 7
%%%%%%%%%%%%%%%%%%%%%%%%%%%%%%%%%%%%%%%%%%%%%%%%%%%%%%%%%%%%%%%%%%%%%%%%%%%%%%%
figure(2)
% Plot M(Q) for k = 7
plot(Qv,m7,'k-s',...
    'LineWidth',2,...
    'MarkerSize',5,...
    'MarkerEdgeColor','k',...
    'MarkerFaceColor','w')
hold on

% Trace of Mmaxmax gain curve
plot(Qv2,Mg_maxmax2,'k')
hold on;
```

```
% % Traces of Mmin, Mmax e Mmaxmax gains
% plot(Qv2,Mg_min,'r')
% hold on;
% plot(Qv2,Mg_max2,'r')
% hold on;
% plot(Qv2,Mg_maxmax2,'r')
% hold on;

% % Plot of the crossing point between M(Q) curve with Mmaxmax trace
% plot(0.63,Mg_maxmax2,'m-o')
% plot(0.63,Mg_maxmax2,'m-+')
% plot(0.6315,Mg_maxmax2,'y-o')
% plot(0.6315,Mg_maxmax2,'y-+')
% plot(0.635,Mg_maxmax2,'k-o')
% plot(0.635,Mg_maxmax2,'k-+')
% plot(Qp,Mg_maxmax2,'g-o')
% plot(Qp,Mg_maxmax2,'g-+')

% Plot of the crossing point between M(Q) curve with Mmaxmax trace
plot(Qp,Mg_maxmax2,'ko',...
    'LineWidth',1,...
    'MarkerSize',10,...
    'MarkerEdgeColor','k',...
    'MarkerFaceColor','k')
plot(Qp,1.1,'k')
plot(Qp,1.125,'k')
plot(Qp,1.15,'k')
plot(Qp,1.175,'k')
plot(Qp,1.2,'k')
plot(Qp,1.225,'k')
plot(Qp,1.25,'k')
hold on;

% Figure legends
legend('k = 7','M_m_a_x_m_a_x')

% Plot titule and axis informations
title({'Peak gain curve for k = 7'});
xlabel('Q');
ylabel('M_p_e_a_k');
grid on;
axis([0.3 1 1.1 1.8]);

fprintf('\n\n#################################################\n');
fprintf('\tMmaxmax = %1.3f \n',Mg_maxmax2);
fprintf('\tQ = %1.5f \n',Qp);
fprintf('#################################################\n\n');
```

Fig. A.3 shows the peak gain curves as function of the Q value for different k values obtained using the code above.

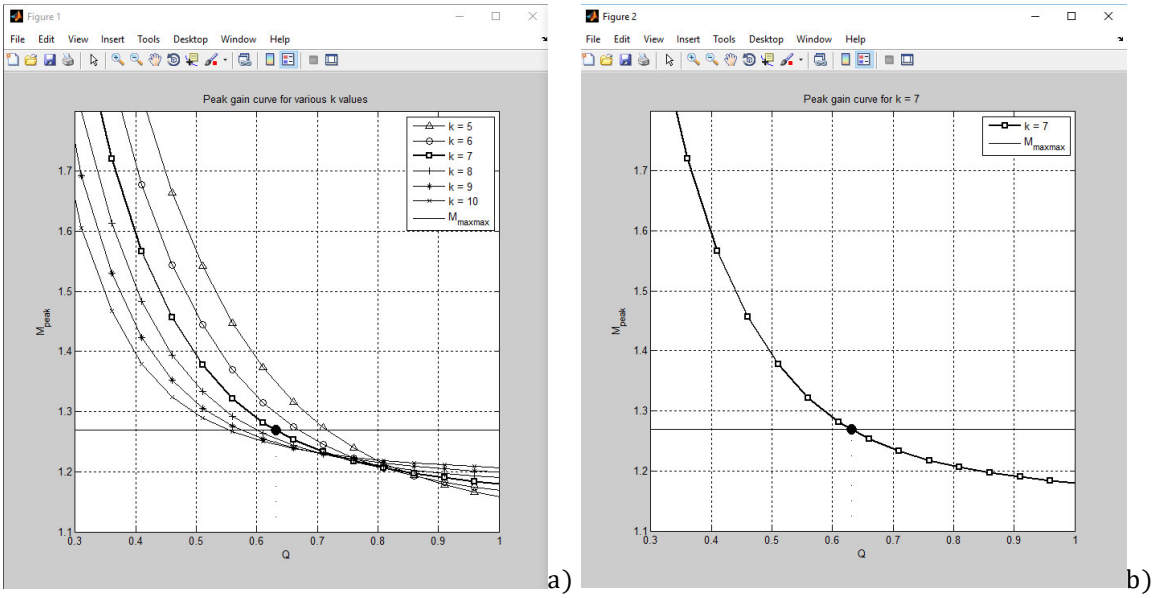

Fig. A.3 – Peak gain curves as function of the Q parameter: a) $M_{peak}(Q)$ for different k values; b) $M_{peak}(Q)$ for different $k = 7$

A.2. Analysis of the k Parameter Impact in the Converter Design

At this point, an analysis of the k parameter impact in the converter design $\left(k = \frac{L_m}{L_{lkp}}\right)$ is shown as well as an analysis of the behavior of the two resonant frequencies, f_0 and f_p as function of the VI inductance value.

This analysis is made considering the same design used to obtain the curves from Figure 3.15 but, in this case, the design was made four times with four different values of the k parameter as shown in Fig. A.4.

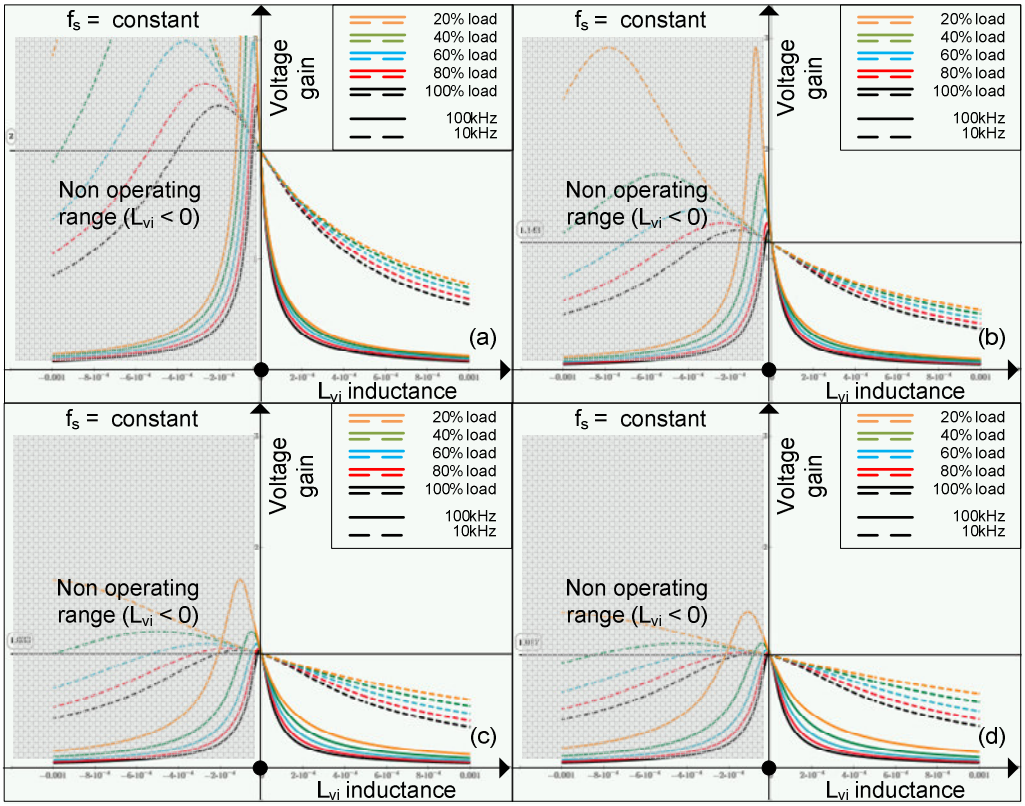

Fig. A.4 – Gain curves as function of L_{vi} at 10 kHz and 100 kHz at different load values and for 4 values of k for design: a) $M(L_{vi})$ for $k = 1$; b) $M(L_{vi})$ for $k = 7$, c) $M(L_{vi})$ for $k = 30$; d) $M(L_{vi})$ for $k = 60$

From the curves in Fig. A.4, it can be seen that the value of M_{min} depends of the k value:

Tab. A.2 – Gain as function of the k parameter

k	M_{min}
1	2
7	1.143
30	1.033
60	1.017

From the results shown in Fig. A.4 and Tab. A.2 it can be seen that:

→ The gain decreases with the increase of the VI inductance value.

→ The gain for $L_{vi} = 0$, M_{min} decreases with the increase of the k value.

→ For lower values of k the gain $M(L_{vi})$, is less load dependent.

→ For lower values of k is possible to have a higher output regulation with the same range of variation of L_{vi}, which means more gain variation leading to higher output regulation.

→ For higher frequencies (design frequency f_s) it is possible to have higher output regulation (higher gain variation) with the same variation of the VI inductance L_{vi}.

Now, a similar analysis, for the same four values of the k parameter is shown but, in this case, the goal is to see the behavior of both resonant frequencies f_p and f_0 of the LLC resonant converter as function of the L_{vi} inductance as shown in Fig. A.5.

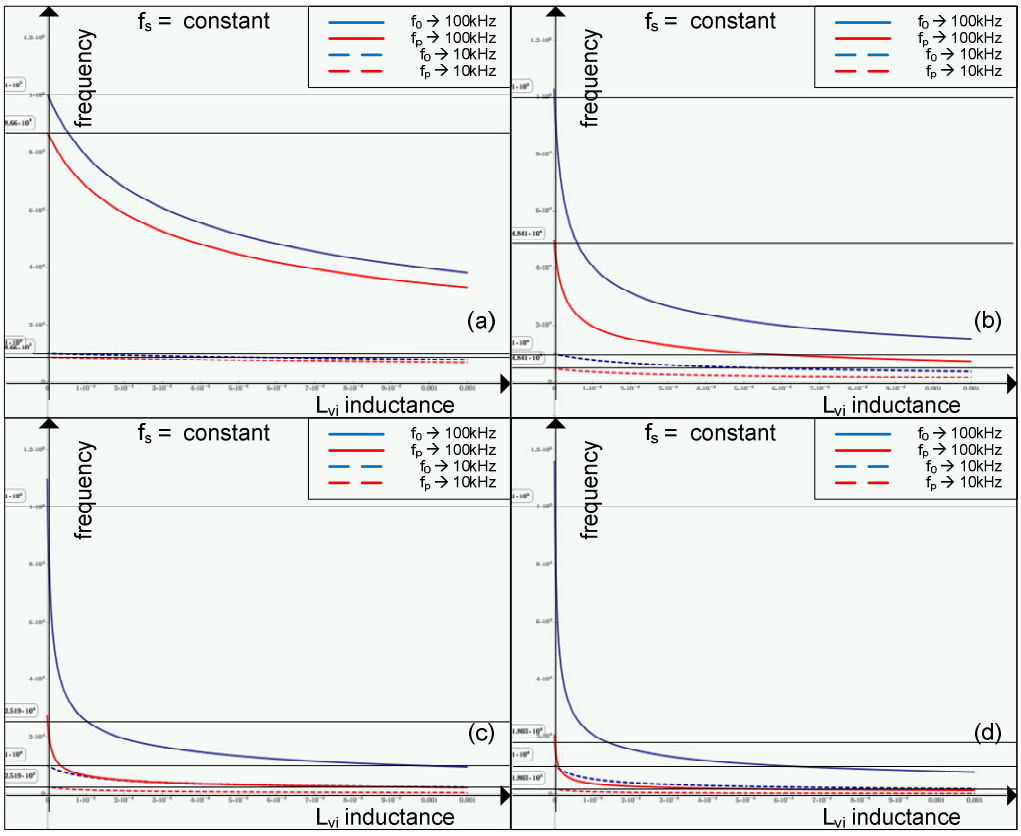

Fig. A.5 – Resonant frequency curves as function of L_{vi} at 10 kHz and 100 kHz for 4 values of k for design: a) $f_s(L_{vi})$ and $f_0(L_{vi})$ for $k = 1$; b) $f_s(L_{vi})$ and $f_0(L_{vi})$ for $k = 7$, c) $f_s(L_{vi})$ and $f_0(L_{vi})$ for $k = 30$; d) $f_s(L_{vi})$ and $f_0(L_{vi})$ for $k = 60$

From the curves shown in Fig. A.5, it can be seen that the value of f_0 and f_p depend of the k value:

Tab. A.3 – Resonant frequency as function of the k parameter

f_s $[kHz]$	k	f_0 $[kHz]$	f_p $[kHz]$
10	1	10	8.66
	7	10	4.841
	30	10	2.519
	60	10	1.803
100	1	100	86.603
	7	100	48.412
	30	100	25.194
	60	100	18.033

From the results shown in Fig. A.5 and Tab. A.3 it can be seen that:

→ The resonant frequencies f_0 and f_p decrease as the VI inductance value increases.

→ For $L_{vi} = 0$, the resonant frequency f_0 is equal to the design switching frequency f_s, which means that, at this point, the circuit is operating at resonance.

→ The resonant frequency f_p for $L_{vi} = 0$, decreases with the increase of the k value.

→ For $L_{vi} = 0$, the f_p value is closer to the f_0 frequency value for lower values of k. As k increases, f_p value decreases and goes away from the f_0 value. For low values of k the variation between the maximum and minimum values of f_p is higher when compare to higher values of k.

→ For lower design frequencies value f_s, the resonant frequencies are not so variable with the VI inductance L_{vi}. As the design frequency value increases, the resonant frequencies values are more variable with the variation of the L_{vi} value.

B. Variable Inductor Design

This section of the appendix presents the calculation performed using Mathcad Prime 3.1 and in LabVIEW software to obtain the VI construction parameters.

Mathcad Prime 3.1 Design Procedure for the VI Project:

The Mathcad file used for design the VI was adopted from a previous file used by another student Marco Martins, during his Master Thesis [17].

ETD core 44/22/15

$comp1 := 43.8$

$comp2 := 32.5$

$comp3 := 15.2$

$alt1 := 22.5$

$alt2 := 16.1$

$r := \frac{comp3}{2} = 7.6$

$area1 := \pi \cdot r^2 = 181.458$

$area2 := (alt1 - alt2) \cdot comp3 = 97.28$

$area3 := \left(\frac{comp1 - comp2}{2}\right) \cdot comp3 = 85.88$

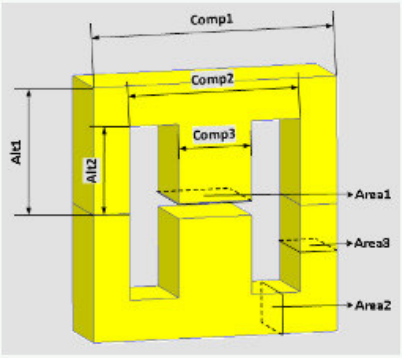

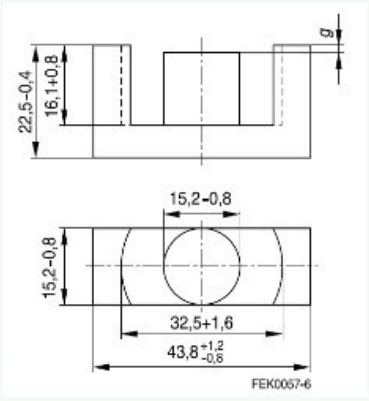

Results:

$comp1 = 43.8$	$comp2 = 32.5$	$comp3 = 15.2$
$alt1 = 22.5$	$alt2 = 16.1$	
$area1 = 181.5$	$area2 = 97.3$	$area3 = 85.9$

Core parameters

$Ae := 173 \cdot 10^{-6}$		effective magnetic cross section (m^2)
$g := 0.5 \cdot 10^{-3}$		ar gap (m)
$le := 103 \cdot 10^{-3}$		effective magnetic path length (m)
$Bs := 0.49$	0.49	saturation magnetization (T)
$I_{dc} := 0.5$		maximum control current (A)
$\mu_0 := 4 \cdot \pi \cdot 10^{-7}$		air permeability
$\mu_r := 1650$		relative permeability (initial)

$Wa := alt2 \cdot (comp2 - comp3) = 278.53$

$Wa := 279$	area of window (m^2)

$lext := ((alt1 \cdot 2) + (alt2 \cdot 2) + ((alt2 - 0.5) \cdot 2) + comp1 + (comp1 - comp2 + comp3)) \cdot 10^{-3} = 0.1787$

$lext := 179 \cdot 10^{-3}$	external path (m)

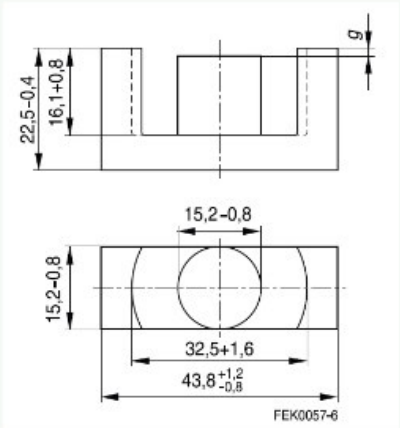

Values of the core dimensions are relative to one half of the core

Core: ETD 44/22/15
Material: N87
gap: 0.5mm

Magnetic fiels density and maximum ac current

$I_{ac\_max} := 15$ — Maximum acceptable value in terms of resonant current

$B_{max} := \frac{Bs}{5} = 0.098$

Magnetic parameters

$\delta := 6$ — Current density (A/m^2) for a wire isolated from free air
(maximum 6, and 4 to non free air isolated)

$L_{max} := 30 \cdot 10^{-6}$ — Required maximum inductance value

Number of turns of the main winding

$N_{ac} := \frac{L_{max} \cdot I_{ac\_max}}{B_{max} \cdot Ae}$ — Number of turns of the main winding — $N_{ac} = 26.542$

$d := \sqrt{\frac{4 \cdot I_{ac\_max}}{\pi \cdot \delta}}$ — Diameter of wire of the main winding (mm) — $d = 1.784$

$s_{ac} := \pi \cdot \left(\frac{d}{2}\right)^2 = 2.5$ — Cross section of wire of the main winding (mm^2)

Number of turns of the control winding

$k := 0.8$ — Decreasing permeability factor

$\mu_{k\_Bsat} := \mu_r \cdot k$ — $\mu_{k\_Bsat} := 330$ — $\mu_r = 1650$ — $\mu_{k\_Bsat} = 330$

$N_{dc} := \frac{k \cdot Bs \cdot lext}{2 \cdot \mu_{k\_Bsat} \cdot \mu_0 \cdot I_{dc}}$ — Number of turns of the control winding — $N_{dc} = 169.206$

$dc := \sqrt{\frac{4 \cdot I_{dc}}{\pi \cdot \delta}}$ — Diameter of wire of the control winding (mm) — $dc = 0.326$

$s_{dc} := \pi \cdot \left(\frac{dc}{2}\right)^2 = 0.083$ — Cross section of wire of the control winding (mm^2)

ac and dc winding area ocupation

$A_W := N_{ac} \cdot \frac{\pi \cdot d^2}{4} + N_{dc} \cdot \frac{\pi \cdot dc^2}{4}$ — Ocupied area by tthe main winding — $A_W = 80.457$

$Ku := \frac{A_W}{Wa}$ — it is within the limit value (0.4), no needs for a second itration — $Ku = 0.288$

gap

$gap := \frac{\left(N_{ac}^2 \cdot \mu_r \cdot Ae - le \cdot L_{max}\right) \cdot \mu_0}{L_{max} \cdot \mu_r}$ — gap larger than the one available! — $gap = 5.105 \cdot 10^{-3}$

$gap_2 := 0.5 \cdot 10^{-3}$ — available air gap value for the core — $gap_2 = 500 \cdot 10^{-6}$

$N_{ac\_2} := \sqrt{\frac{\left(gap_2 \cdot L_{max} \cdot \frac{\mu_r}{\mu_0} + le \cdot L_{max}\right)}{\left(\mu_r \cdot Ae\right)}}$ — new value of ac turns — $N_{ac\_2} = 8.306$

new ac and dc winding area ocupation

$A_W := N_{ac\_2} \cdot \frac{\pi \cdot d^2}{4} + N_{dc} \cdot \frac{\pi \cdot dc^2}{4}$ — Ocupied area by tthe main winding — $A_W = 34.867$

$Ku := \frac{A_W}{Wa}$ — $Ku = 0.125$

Calculation of inductance

$L := \frac{N_{ac\_2}^2}{\frac{le}{\mu_r \cdot \mu_0 \cdot Ae} + \frac{gap_2}{\mu_0 \cdot Ae}}$ — Inductance of the main winding — $L = 26.67 \cdot 10^{-6}$

Experimental prototype

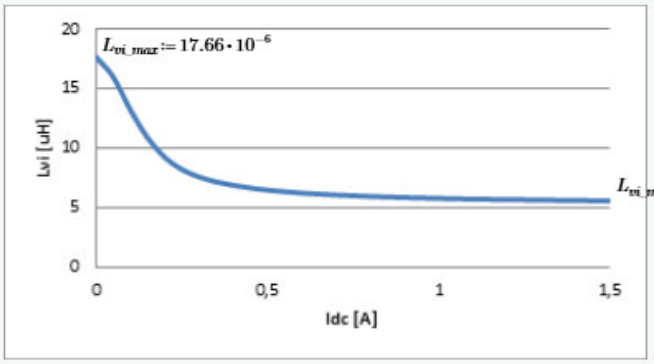

$L_{vi\_max} := 17.66 \cdot 10^{-6}$

$L_{vi\_min} := 5.56 \cdot 10^{-6}$

Magnetic flux density in the core

$$B(I) := \frac{N_{ac} \cdot I_{ac\_max}}{\frac{le}{\mu_r \cdot \mu_0} + \frac{gap}{\mu_0}}$$

$\frac{B(I_{ac\_max})}{Bs} = 0.198$ $\quad B(I_{ac\_max}) = 0.097$

Summary of the Variable Inductor Prototype

$N_{dc} = 169$		$N_{ac\_2} = 8$		$N_{dc} = 169$	
$dc = 0.326$	mm	$d = 1.784$	mm	$dc = 0.326$	mm
$s_{dc} = 0.083$	mm^2	$s_{ac} = 2.5$	mm^2	$s_{dc} = 0.083$	mm^2

From Labview file: calc_ind_v1.3_ETD442215.vi

$N_{ac\_vi} = 8$

$L_{max\_vi} = 28.22 \cdot 10^{-6}$

$L_{min\_vi} = 4.98 \cdot 10^{-6}$

Core dimensions

Window:

$h_w := alt2 \cdot 2 = 32.2$

$l_w := \frac{(comp2 - comp3)}{2} = 8.65$

$A_{half\_W} := h_w \cdot l_w = 278.53$

$A_{W\_tot} := 2 \cdot A_{half\_W} = 557.06$

Free window:

$h_{wf} := 22$

$l_{wf} := 5$

$A_{half\_Wf} := h_{wf} \cdot l_{wf} = 110$

$A_{W\_totf} := 2 \cdot A_{half\_Wf} = 220$

Margin

$k_{marg} := 20\%$ 20% margin to do the calculation

ac Winding

Central mounting piece dimensions

$h_{p\_ac} := 29.5$

$d_{p\_ac} := 17.3$

$P_{ac} := 2 \cdot \pi \cdot \left(\frac{d_{p\_ac}}{2}\right) = 54.35$

$h_{p\_ac} = 29.5$

$P_{ac} = 54.35$

Ocupied area by the ac winding

$N_{ac} := N_{ac\_2} = 8.306$

$N_{ac} := 8$

$s_{ac} = 2.5$

$s_{ac\_p} := 1$

$d_{ac\_p} := \sqrt{\frac{4 \cdot s_{ac\_p}}{\pi}} = 1.128$

$d_{ac\_p} = 1.128$

$N_{turns\_col} := \frac{h_{p\_ac} \cdot (1 - k_{marg})}{d_{ac\_p}} = 20.915$

$N_{turns\_col\_p} := 20$

$N_{col\_ac} := \frac{N_{ac}}{N_{turns\_col}} = 0.383$

$N_{col\_ac\_p} := 1$

$A_{ocup\_ac} := (d_{ac\_p} \cdot N_{turns\_col\_p}) \cdot (d_{ac\_p} \cdot N_{col\_ac\_p}) = 25.465$

$A_{ocup\_ac} = 25.465$

dc Winding

Mounting pieces dimensions

$h_{p\_dc} := 22$

$l_{p\_dc} := 11$

$c_{p\_dc} := 20$

$P_{dc} := 2 \cdot (l_{p\_dc} + c_{p\_dc}) = 62$

$h_{p\_dc} = 22$

$P_{dc} = 62$

Ocupied area by the dc winding

$N_{dc} = 169.206$

$N_{dc} := 170$

$s_{dc} = 0.083$

$s_{dc\_p} := 0.1$

$d_{dc\_p} := \sqrt{\frac{4 \cdot s_{dc\_p}}{\pi}} = 0.357$

$d_{dc\_p} = 0.357$

$N_{turns\_col\_dc} := \frac{h_{p\_dc} \cdot (1 - k_{marg})}{d_{dc\_p}} = 49.324$

$N_{turns\_col\_dc\_p} := 49$

$N_{col\_dc} := \frac{N_{dc}}{N_{turns\_col\_dc\_p}} = 3.469$

$N_{col\_dc\_p} := 3$

$A_{ocup\_dc} := (d_{dc\_p} \cdot N_{turns\_col\_dc\_p}) \cdot (d_{dc\_p} \cdot N_{col\_dc\_p}) = 18.717$

$A_{ocup\_dc} = 18.717$

Total free area

$A_{half\_W} := h_w \cdot l_w = 278.53$ Core free area (half)

$A_{half\_Wf} = 110$ Free area with the mounting pieces in place (half)

$A_{half\_free\_total} := A_{half\_Wf} - A_{ocup\_ac} - A_{ocup\_dc} = 65.819$ Free area with the mounting pieces in place and with the windings done (half)

$A_{half\_free\_total} = 65.819$ If Afree > 0, OK
If Afree < 0, NOK

$l_{wf} = 5$

$l_{ocup\_ac} := d_{ac\_p} \cdot N_{col\_ac\_p} = 1.128$

$l_{ocup\_dc} := d_{dc\_p} \cdot N_{col\_dc\_p} = 1.07$

$l_{free} := l_{wf} - l_{ocup\_ac} - l_{ocup\_dc} = 2.801$

$l_{free} = 2.801$

If Afree > 0, OK
If Afree < 0, NOK

Quantity of wire needed:
- ac winding

$P_{ac} = 54.35$

$N_{turns\_col\_p} = 20$

$N_{col\_ac\_p} = 1$

$W_{ac} := P_{ac} \cdot N_{turns\_col\_p} \cdot N_{col\_ac\_p} \cdot (1 + k_{marg}) = 1.304 \cdot 10^3$

$W_{ac\_m} := W_{ac} \cdot 10^{-3} = 1.304$

$W_{ac\_m} := 1.4$

- dc winding

$P_{dc} = 62$

$N_{turns\_col\_dc\_p} = 49$

$N_{col\_dc\_p} = 3$

$W_{dc} := P_{dc} \cdot N_{turns\_col\_dc\_p} \cdot N_{col\_dc\_p} \cdot (1 + k_{marg}) = 10.937 \cdot 10^3$

$W_{dc\_m} := W_{dc} \cdot 10^{-3} = 10.937$

$W_{dc\_m} := 11$

$W_{dc\_tot\_m} := W_{dc\_m} \cdot 2 = 22$

$W_{dc\_tot\_m} := 22$

Summary

$N_{dc} = 170$	$N_{ac} = 8$	$N_{dc} = 170$	turns
$d_{dc\_p} = 0.357$	$d_{ac\_p} = 1.128$	$d_{dc\_p} = 0.357$	mm
$s_{dc\_p} = 0.1$	$s_{ac\_p} = 1$	$s_{dc\_p} = 0.1$	mm^2
$W_{dc\_m} = 11$	$W_{ac\_m} = 1.4$	$W_{dc\_m} = 11$	m

$W_{ac\_m} = 1.4$ meters of wire with cross section of $s_{ac\_p} = 1$

$W_{dc\_tot\_m} = 22$ meters of wire with cross section of $s_{dc\_p} = 0.1$

Legend

To insert
OK values
From datasheet
From Labview file

LabVIEW Software Application for the VI Project and Design:

The software in LabVIEW used for design the VI was previously made by another student Samuel Ferreira, during his Master Thesis [16].

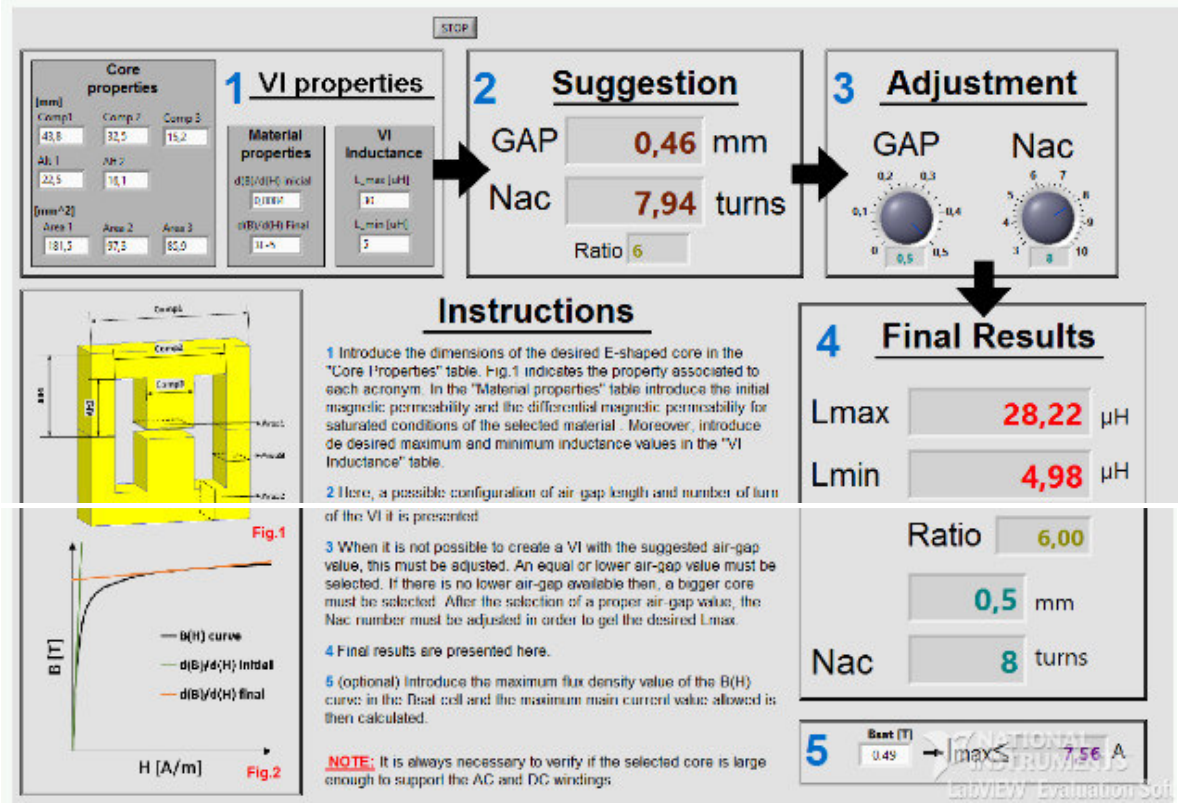

C. Prototype Construction Details

In this section of the appendix, the details of the designed PCBs are shown. The schematics and board drawings in EAGLE 7.5.0 Light Edition Software, as well as the necessary components list, for the construction of the LLC resonant converter prototype are presented. The design of the PCBs is briefly presented below using the schematics, board drawings and the picture of the boards with and without the components. In addition, the transformer and the VI construction is shown by pictures and finally the global assembly of the converter prototype is shown.

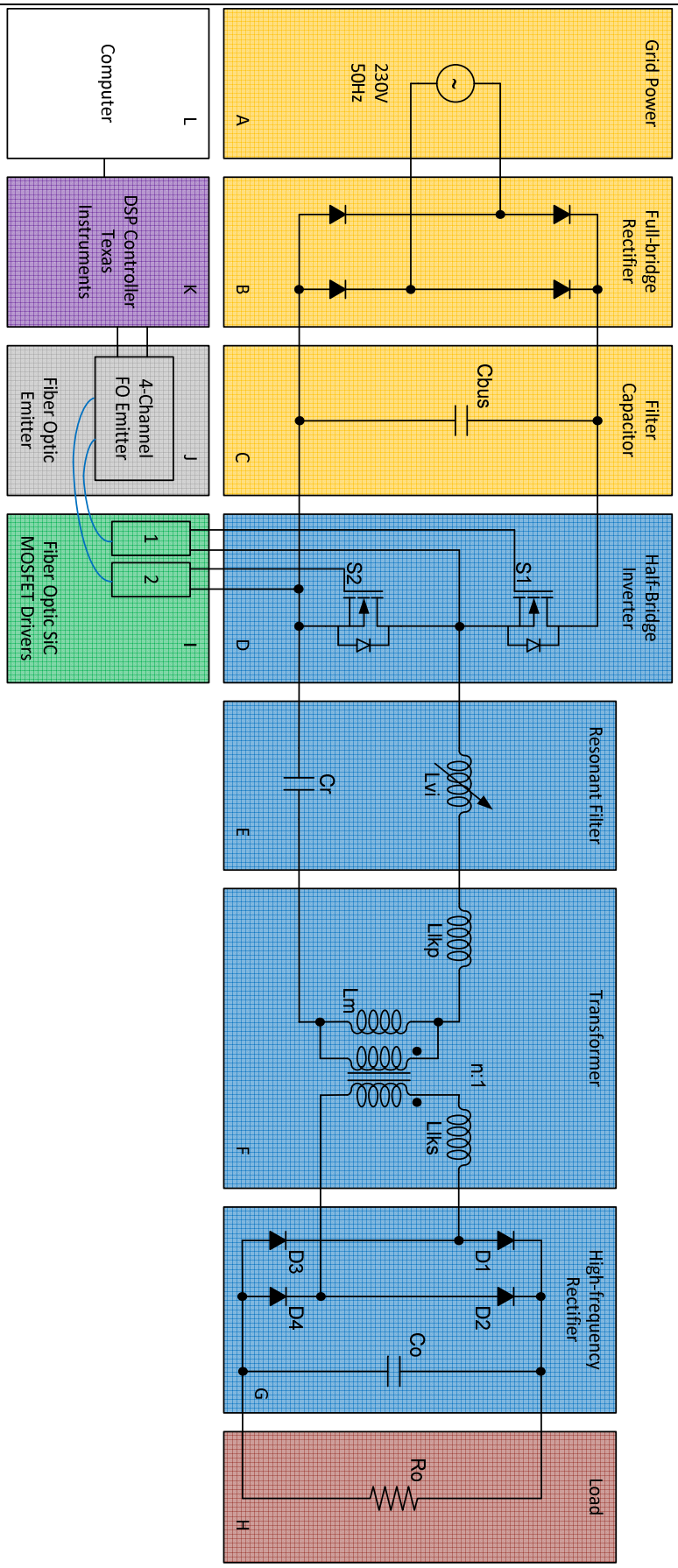

Fig. C.1 – Block diagram of the built prototype

C.1. DC Bus generator

To generate the DC Bus used to feed the LLC-VI resonant converter (V_{in}) the circuit shown in Fig. C.2 a) is used. Block A corresponds to the national grid power. Block B corresponds to full-bridge rectifier and is implemented by the white box shown in the right picture. Block C corresponds to the filter capacitor and is implemented by the black capacitors in the right picture.

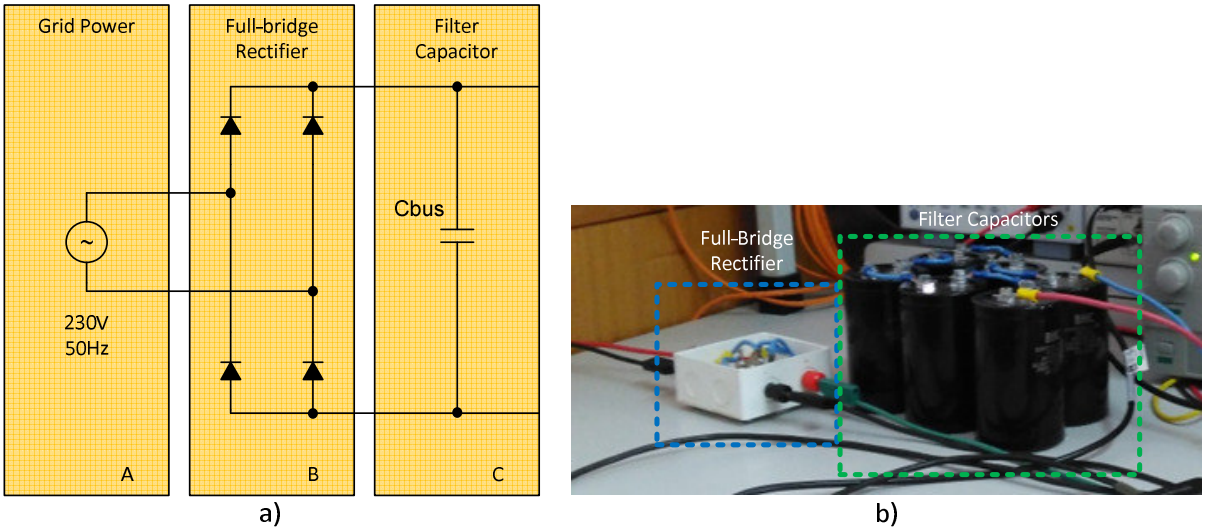

Fig. C.2 – Schematic of the DC bus generator [ref]

C.2. LLC-VI Resonant Converter

The LLC-VI resonant converter is composed by: half-bridge inverter, resonant filter, high-frequency transformer, and high-frequency full-bridge rectifier. The following figures present the schematics of the electrical circuits and PCB project and pictures of the build PCBs.

Half-Bridge Inverter:

Fig. C.3 shows the schematic for the half-bridge inverter PCB and, Fig. C.4 shows the board design, the PCB prototype top and bottom layer and, the PCB full-assembly.

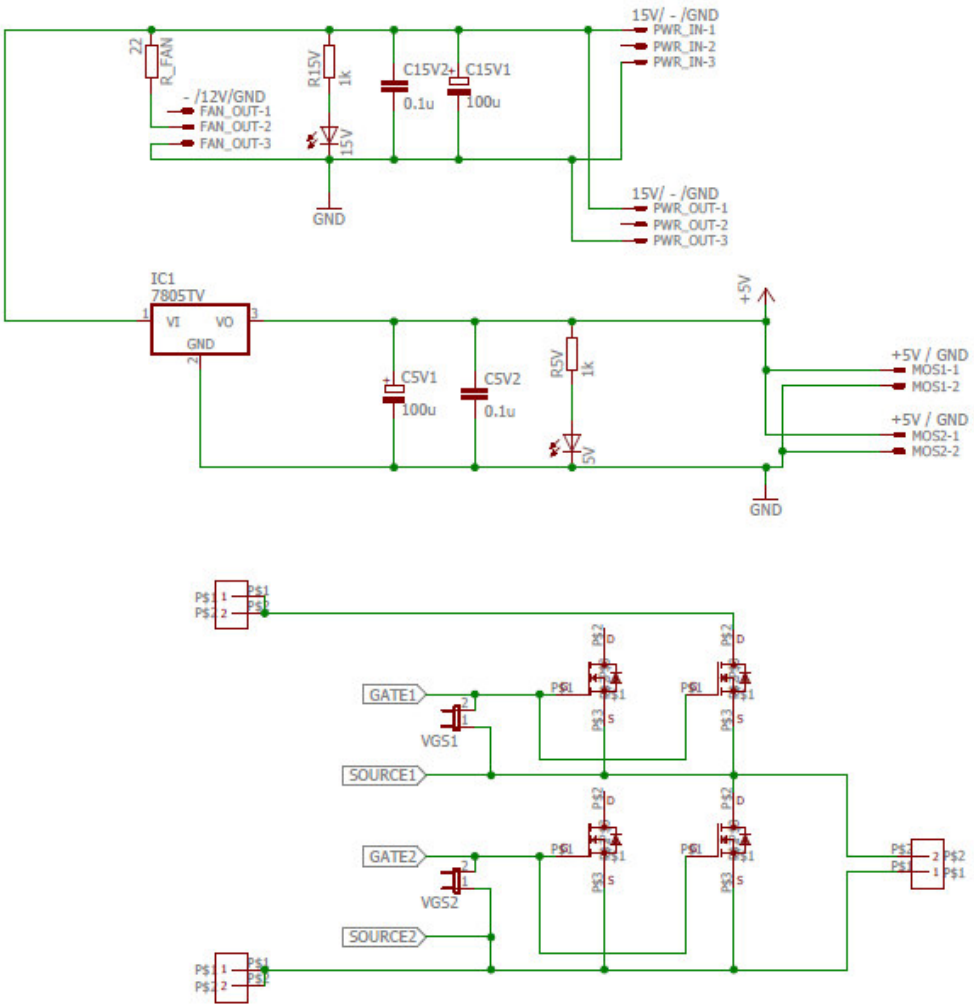

Fig. C.3 – Half-bridge inverter schematic

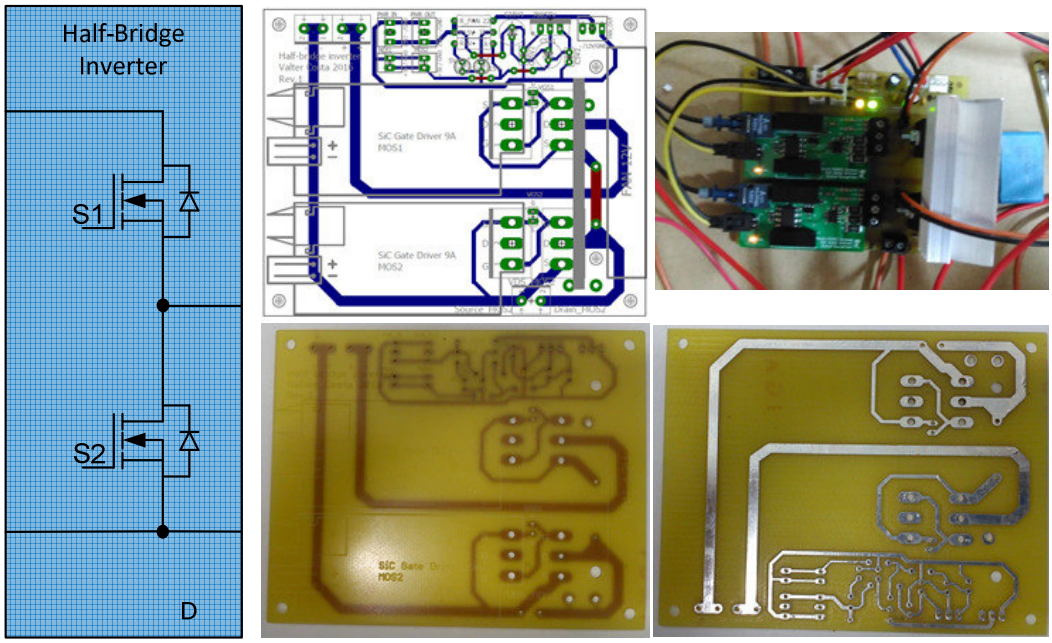

Fig. C.4 – Half-bridge inverter PCB prototype (100 x 80 mm), Board design; PCB Top and Bottom Layer and PCB full assembly

The Block D in Fig. C.4 shows the half-bridge inverter schematic. The top picture in the middle shows the board design in the Eagle software. In the bottom, the pictures show the top

and bottom layer of the manufactured PCB. Finally, the top right picture is the PCB full-assembly. Tab. C.1 shows the components list for the PCB board.

Tab. C.1 – Half-bridge inverter components list

Board	
Name	Half-bridge inverter Rev.1
Dimension	100 x 80 mm
Number of layers	2 - Top + Bottom
Observation	Half-bridge inverter board

	Schematic description	Value	Component	Observation
1	PWR_IN	15V / - / GND		Power in +15V
2	PWR_OUT	15V / - / GND		Power out +15V
3	C15V1	100u	Electrolitic capacitor	
4	C15V2	0,1u	Ceramic capacitor	
5	R15V	1k	Resistor	
6	15V		LED	15V
7	R_FAN	22	Resistor	
8	FAN_OUT	- / 12V / GND		Fan power +12V
9	IC1	7805	Voltage regulator 5V	
10	C5V1	100u	Electrolitic capacitor	
11	C5V2	0,1u	Ceramic capacitor	
12	R5V	1k	Resistor	
13	5V		LED	5V
14	MOS1	+5V / GND		Power for MOSFET Drivers
15	MOS2	+5V / GND		Power for MOSFET Drivers
16	Input +			+ from DC Bus
17	Input -			- from DC Bus
18	VGS1		Jumper	Measure Vgs1
19	VGS2		Jumper	Measure Vgs2
20	SiC Gate Driver 9A MOS1	PCB board - Driver for the Silicon Carbide Power MOSFETs		
21	SiC Gate Driver 9A MOS1	PCB board - Driver for the Silicon Carbide Power MOSFETs		
22	MOSFET 1	C2M0025120	MOSFET N-Channel	
23	MOSFET 2	C2M0025120	MOSFET N-Channel	
24	Output	Output of the MOSFET arm		
25	Heatsink MOS1, MOS2	3 x 63 x 55 (exp x comp x alt)		
26	FAN	DC 12V 0,21A		

Resonant Filter:

Fig. C.5 shows the schematic for the resonant filter PCB and, Fig. C.6 shows the board design, the PCB prototype top and bottom layer and, the PCB full-assembly. The resonant filter PCB includes the VI and the resonant capacitor and also a buck converter to control, in close-loop operation, the DC current for controlling the inductance value of the VI.

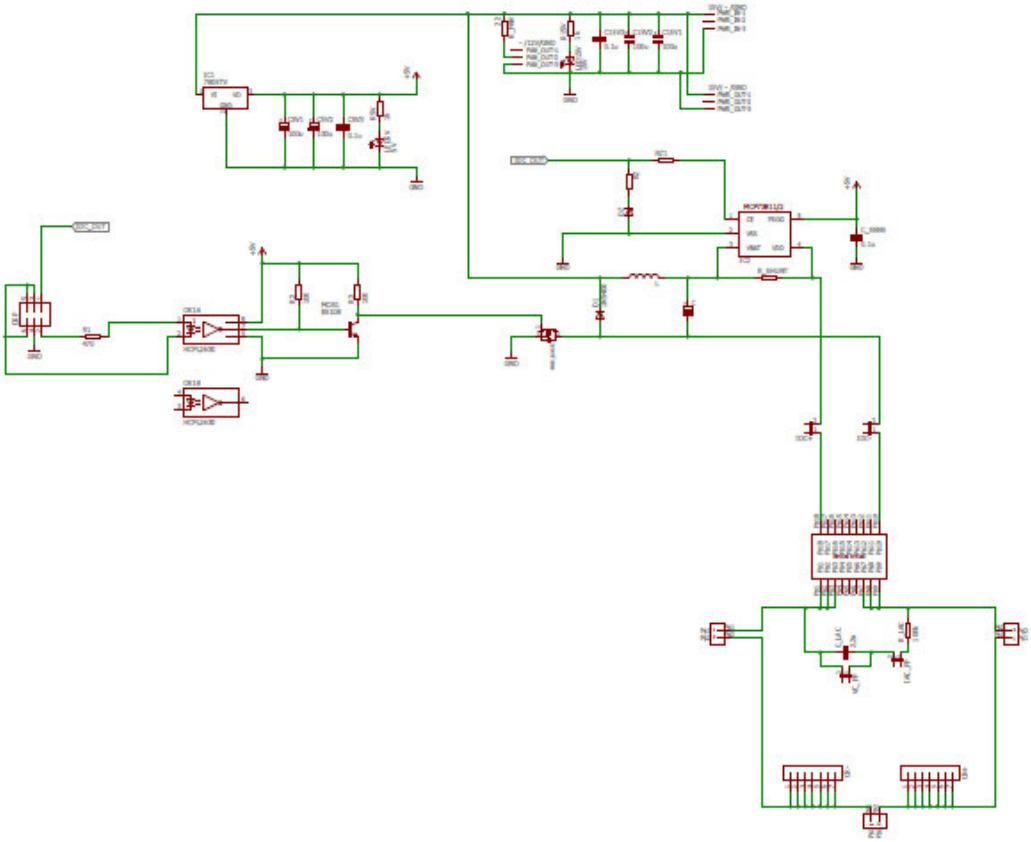

Fig. C.5 –Resonant filter schematic

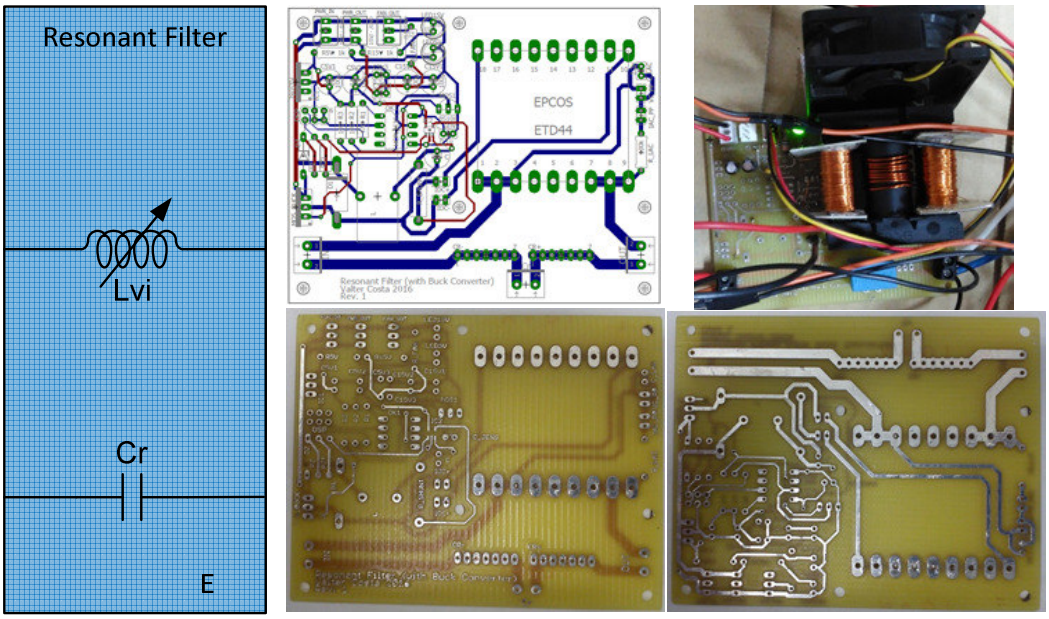

Fig. C.6 – Resonant filter PCB prototype (100 x 80 mm), Board design; PCB Top and Bottom Layer and PCB full assembly

Block E in Fig. C.6 shows the resonant filter schematic. The top picture in the middle shows the board design in the Eagle software. In the bottom, the pictures show the top and bottom layer of the manufactured PCB. Finally, the top right picture is the PCB full-assembly. Tab. C.2 shows the components list for the PCB board.

Tab. C.2 – Resonant filter components list

Board	
Name	Resonant Filter Rev.1
Dimension	100 x 80 mm
Number of layers	2 - Top + Bottom
Observation	Resonant Filter board

	Schematic description	Value	Component	Observation
1	PWR_IN	15V / - / GND		Power in +15V
2	PWR_OUT	15V / - / GND		Power out +15V
3	C15V1	100u	Electrolitic capacitor	
4	C15V2	100u	Electrolitic capacitor	
5	C15V3	0,1u	Ceramic capacitor	
6	R15V	1k	Resistor	
7	LED15V			15V
8	R_FAN	22	Resistor	
9	FAN_OUT	- / 12V / GND		Fan power +12V
10	IC1	7805	Voltage regulator 5V	
11	C5V1	100u	Electrolitic capacitor	
12	C5V2	0,1u	Ceramic capacitor	
13	C5V3	0,1u	Ceramic capacitor	
14	R5V	1k	Resistor	
15	5V		LED	5V
16	DSP	6 pins (2x3)	Male conector	
17	R15V	470	Resistor	
18	OK1	HCPL2630	Optocoupler	
19	R2	100	Resistor	
20	R3	100	Resistor	
21	MOS1	BS108	MOSFET N-Channel	
22	RZ		Resistor	
23	DZ		Zener Diode	
24	IC2	INA193	Current Shunt monitor -16V to +80V Common-Mode Range	
25	C_SENS	0,1u	Ceramic capacitor	
26	R_SHUNT		Resistor	Buck Converter
27	MOS_BUCK	IRFZ44N	MOSFET N-Channel	
28	D1	80SQ040	Schottky Rectifier Diode	
29	L		Inductor	
30	C		Ceramic Capacitor	
31	IDC+		Jumper	IDC from PCB or EXT
32	IDC-		Jumper	IDC from PCB or EXT
33	EPCOS ETD44		Variable Inductor	ETD 44/22/15 ferrite core
34	VC_PP	Measure VC_PP	Jumper	Integrator circuit used to obtain the values for the Lac characteristic curve
35	IAC_PP	Measure IAC_PP	Jumper	
36	R_LAC	100k	Resistor	
37	C_LAC	2,2n	Ceramic capacitor	
38	CR-			Holes for Cr capacitor connection
39	CR+			
40	IN		Terminal block 2x5mm	
41	Cr		Terminal block 2x5mm	
42	OUT		Terminal block 2x5mm	
43	FAN	DC 12V 0,21A		

Fig. C.7 shows the VI components and assembly. Fig. C.7 b) shows the coiling machine used to make the VI coils (this machine was already existent in the laboratory and was previously built by other students for coiling the windings for VIs and transformers).

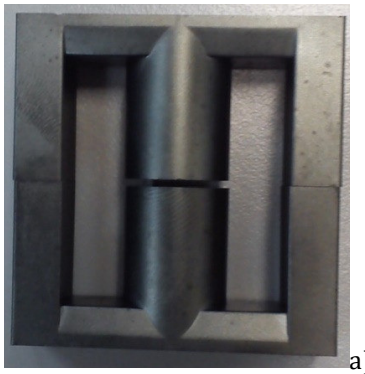
a)

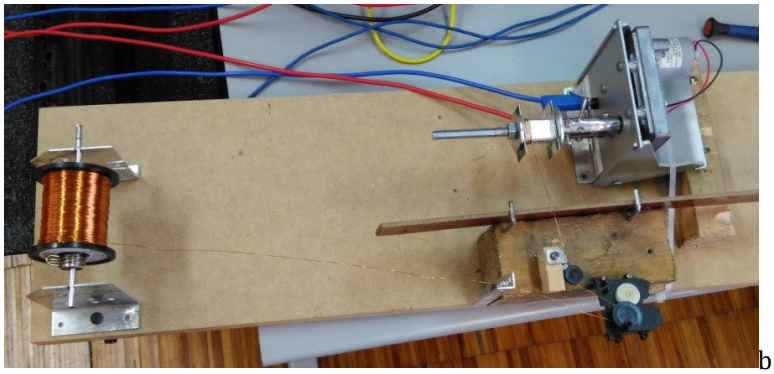
b)

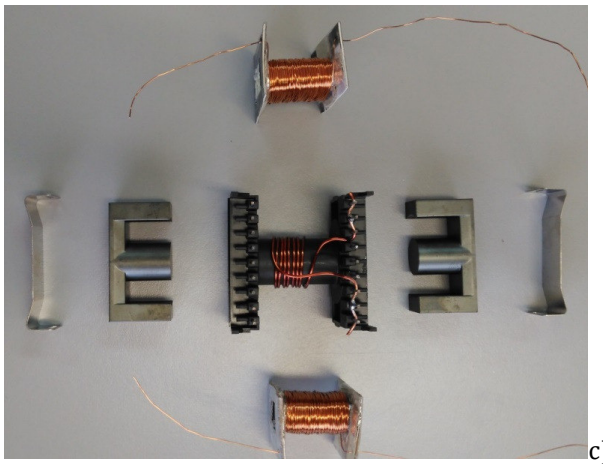
c)

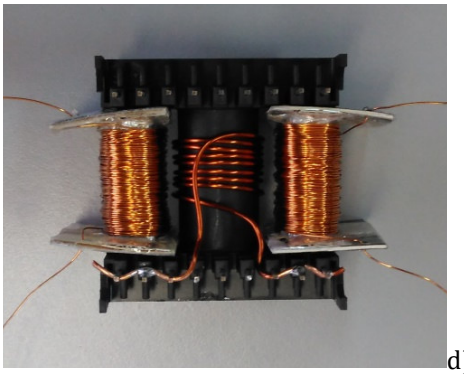
d)

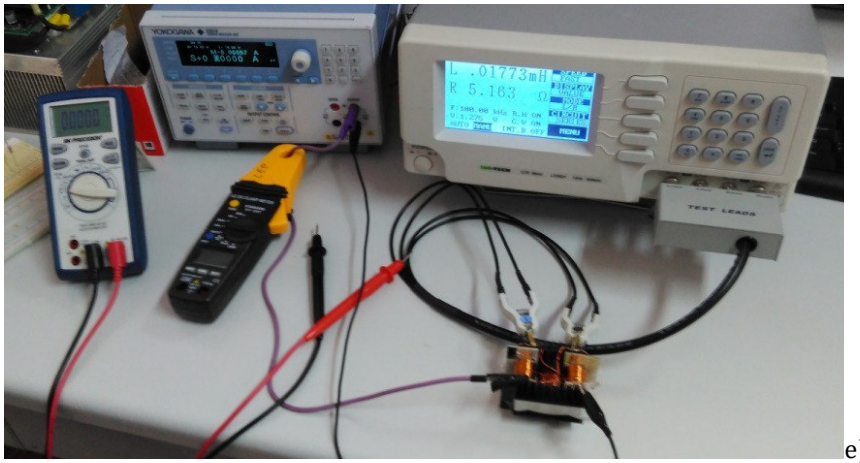
e)

Fig. C.7 – VI parts, assembly and tests: a) ETD 44/22/15 ferrite core; b) Coiling machine; c) VI parts; d) VI full assembly; e) Tests of the VI

Fig. C.7 e) shows a picture during the experimental tests to the VI. Using a current source – YOKOGAWA GS610 Source Measure Unit – (top left) and a LCR meter – ISO-TECH LCR Meter LCR821 – (top right) it was possible to measure the inductance values as function of the DC control current $L(I_{dc})$ to characterize the VI – Small-Signal Analysis. The $L(I_{dc})$ curve (Small-signal characteristics), shown in Fig. C.8, was obtained for a I_{dc} variation between 0 and 1.5A and the range obtained (measured with the LCR meter) for a frequency of 100 kHz was from 5.56 μH to 17.66 μH, corresponding to the maximum and minimum values of I_{dc}, respectively as in Tab. C.3.

Tab. C.3 – $L_{vi}(I_{dc})$ measured values

I_{dc} [A]	L_{vi} [μH]
0.00	17.66
0.05	15.97
0.10	13.21
0.15	10.87
0.20	9.22
0.25	8.21
0.30	7.58
0.35	7.16
0.40	6.87
0.45	6.65
0.50	6.47
0.60	6.22
0.70	6.05
0.80	5.93
0.90	5.84
1.00	5.77
1.10	5.71
1.25	5.65
1.50	5.56

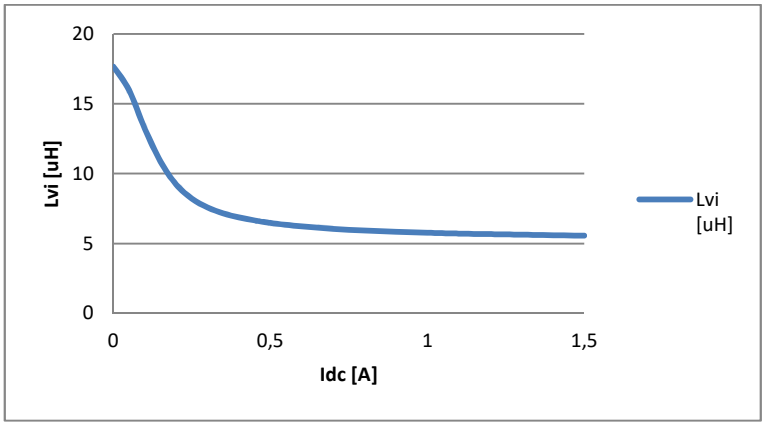

Fig. C.8 – $L_{vi}(I_{dc})$ measured curved

Transformer:

Fig. C.9 shows the schematic for the transformer PCB and, Fig. C.10 shows the board design, the PCB prototype top and bottom layer, the PCB full-assembly and the transformer prototype during some experimental tests.

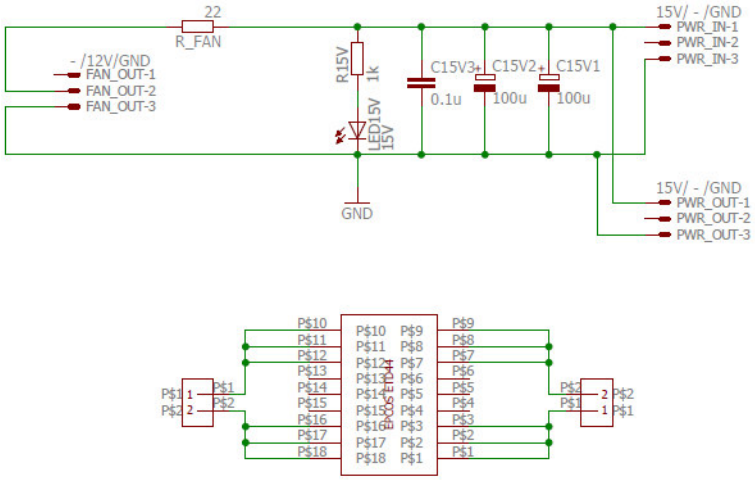

Fig. C.9 – Transformer PCB schematic

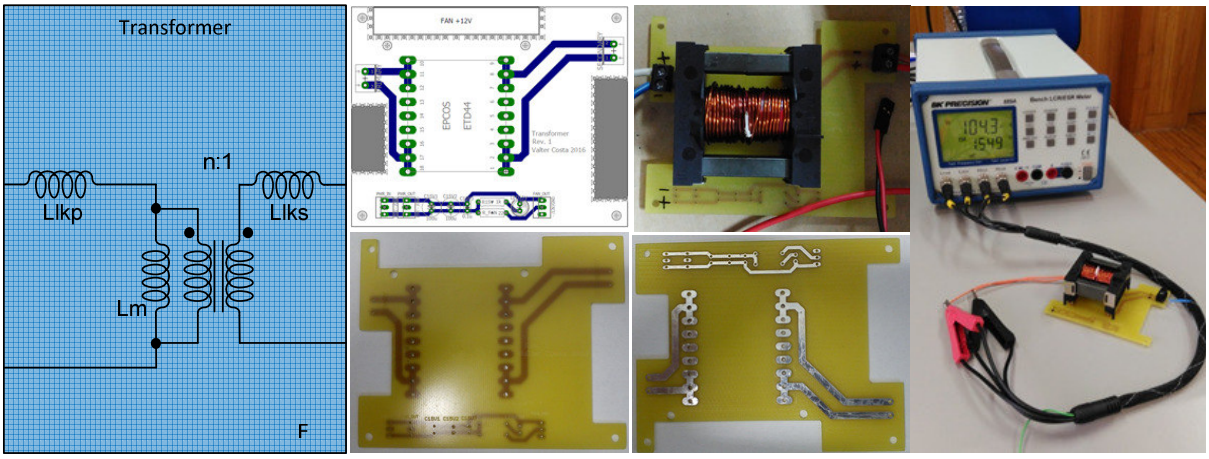

Fig. C.10 – Transformer PCB prototype (100 x 80 mm), Board design; PCB Top and Bottom Layer and PCB full assembly and transformer prototype during experimental tests

Block F in Fig. C.10 shows the transformer schematic. The top picture in the middle left shows the board design in the Eagle software. In the bottom, the pictures show the top and bottom layer of the manufactured PCB. The top middle picture in the right is the PCB full-assembly and finally, the left picture shows the transformer during some experimental tests. Using a LCR meter – BK PRECISION Model 889B Bench LCR/ESR Meter – it was possible to measure the inductance values for L_r and L_p used in the calculations for the converter design. The transformer characteristics were previously presented in Table 5..Tab. C.4 shows the components list for the PCB board.

Tab. C.4 – Transformer PCB components list

Board	
Name	Transformer Rev.1
Dimension	100 x 80 mm
Number of layers	1 - Bottom
Observation	Transformer board

	Schematic description	Value	Component	Observation
1	PWR_IN	15V / - / GND		Power in +15V
2	PWR_OUT	15V / - / GND		Power out +15V
3	C15V1	100u	Electrolitic capacitor	
4	C15V2	100u	Electrolitic capacitor	
5	C15V3	0,1u	Ceramic capacitor	
6	R15V	1k	Resistor	
7	LED15V			15V
8	R_FAN	22	Resistor	
9	FAN_OUT	- / 12V / GND		Fan power +12V
10	Primary		Terminal block 2x5mm	
11	Secondary		Terminal block 2x5mm	
12	EPCOS ETD44	ETD 44/22/15 ferrite core		
13	FAN	DC 12V 0,21A		

Full-bridge rectifier:

Fig. C.11 shows the schematic for the full-bridge rectifier PCB and, Fig. C.12 shows the board design, the PCB prototype top and bottom layer, and the PCB full-assembly.

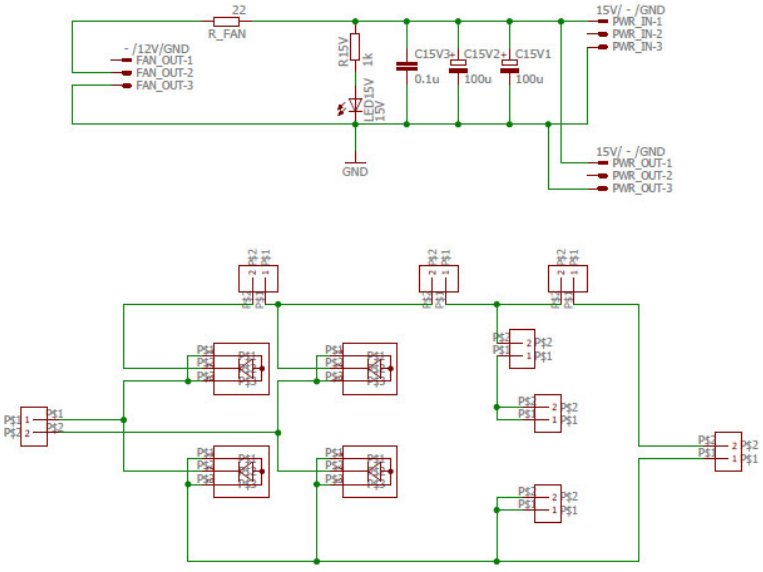

Fig. C.11 – Full-bridge rectifier board schematic

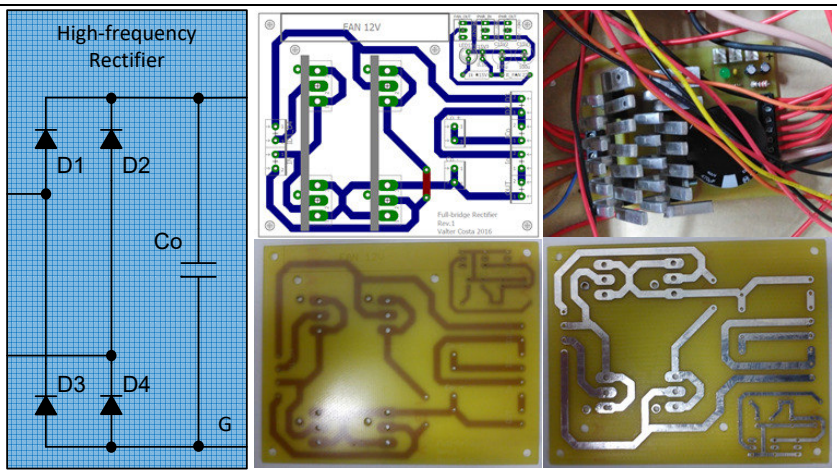

Fig. C.12 – High-frequency Full-Bridge rectifier PCB prototype (100 x 80 mm), Board design; PCB Top and Bottom Layer and PCB full assembly

Block G in Fig. C.12 shows the high-frequency full-bridge rectifier schematic. The top picture in the middle shows the board design in the Eagle software. In the bottom, the pictures show the top and bottom layer of the manufactured PCB. Finally, the top right picture is the PCB full-assembly. Tab. C.5 shows the components list for the PCB board.

Tab. C.5 – Full-bridge rectifier components list

Board	
Name	Full-bridge Rectifier Rev.1
Dimension	100 x 80 mm
Number of layers	2 - Top + Bottom
Observation	Full-bridge rectifier

	Schematic description	Value	Component	Observation
1	PWR_IN	15V / - / GND		Power in +15V
2	PWR_OUT	15V / - / GND		Power out +15V
3	C15V1	100u	Electrolitic capacitor	
4	C15V2	100u	Electrolitic capacitor	
5	C15V3	0,1u	Ceramic capacitor	
6	R15V	1k	Resistor	
7	LED15V			15V
8	R_FAN	22	Resistor	
9	FAN_OUT	- / 12V / GND		Fan power +12V
10	IN		Terminal block 2x5mm	
11	ID1_D4		Terminal block 2x5mm	
12	Co +		Terminal block 2x5mm	
13	Co -		Terminal block 2x5mm	
14	ID2_D3		Terminal block 2x5mm	
15	ICo		Terminal block 2x5mm	
16	Io		Terminal block 2x5mm	
17	OUT		Terminal block 2x5mm	
18	D1	80EPF12	Rectifier Diode	
19	D2	80EPF12	Rectifier Diode	
20	D3	80EPF12	Rectifier Diode	
21	D4	80EPF12	Rectifier Diode	
22	FAN	DC 12V 0,21A		
23	Heatsink D1, D3	3 x 63 x 55 (exp x comp x alt)		
24	Heatsink D2, D4	3 x 63 x 55 (exp x comp x alt)		

C.3. Load

To emulate the load behavior two resistors were used as shown in Fig. C.13.

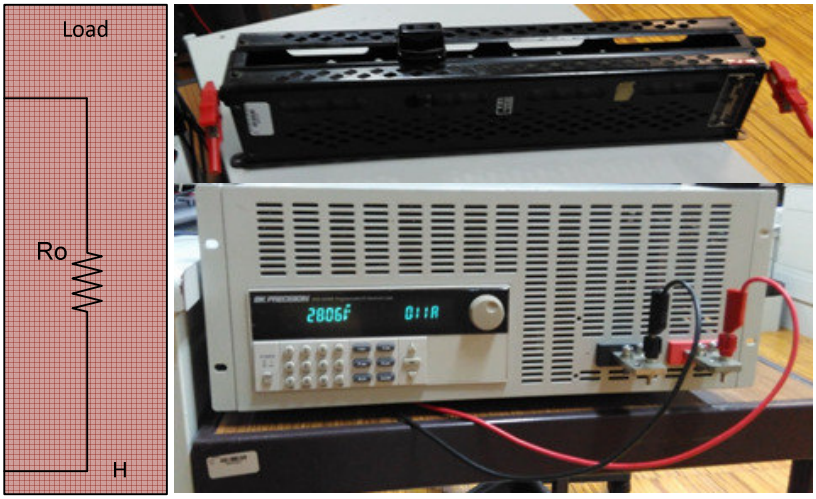

Fig. C.13 – Converter load: a) Resistive 5.6 Ω load; b) Programmable DC Electronic Load – BK PRECISION 8522 2400W

Block H in Fig. C.13 shows the load schematic. Theoretical, simulation and experimental analysis was made using a resistive load to simulate the battery behavior.

The top picture in the left, shows the variable resistor used – 5.6 Ω / 6A. In the bottom left, is shown a Programmable DC Electronic Load – BK PRECISION 8522 2400W.

C.4. Controller

Fig. C.14 shows the block diagram of the controller used to control the switching of the SiC MOSFET switches in the half-bridge inverter.

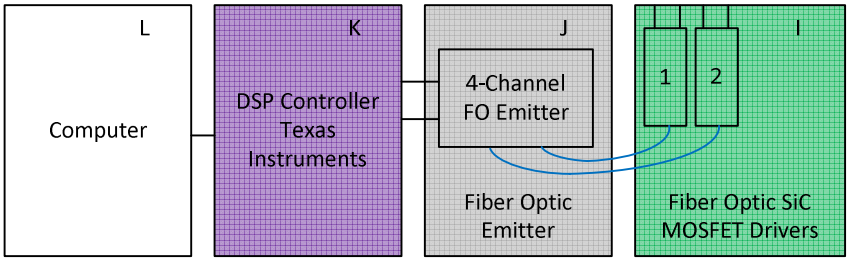

Fig. C.14 – Block diagram of the controller

The controller is composed by four blocks:

- I represents the SiC MOSFET Drivers to generate the electric signals to drive SiC MOSFET switches.
- J represents the Fiber Optic Emitter PCB;
- K represents the DSP control board;
- L represents a computer used to program the DSP control board;

SiC MOSFET Drivers:

The SiC MOSFET from the half-bridge inverter are driven each one, by a fiber optic driver. The PCB board of the drivers is shown in Fig. C.15. The SiC MOSFET Drivers were already existent in the Laboratory and were used in this work because they allow controlling the SiC MOSFET switches with a frequency limited to 100 kHz.

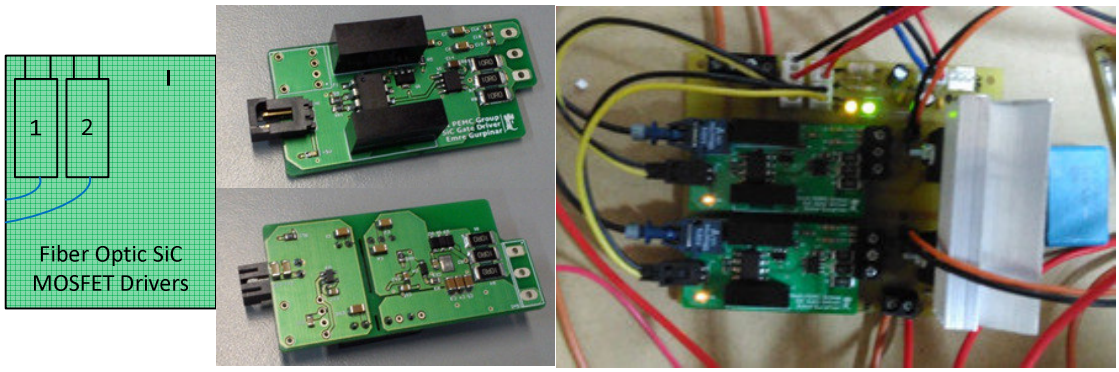

Fig. C.15 – Fiber optic drivers PCB, Top and Bottom view and, the assembled drivers in the half-bridge inverter PCB

The SiC MOSFET Drivers are assembled in the half-bridge inverter PCB as shown in Fig. C.15 in the right. The drivers convert the electric signals from the DSP control board to optic signals to the input of the SiC MOSFET drivers.

Fiber optic emitter:

Fig. C.16 shows the schematic for the Fiber Optic Emitter PCB and, Fig. C.17 shows the board design, the PCB prototype top and bottom layer, the PCB full-assembly and the transformer prototype during some experimental tests.

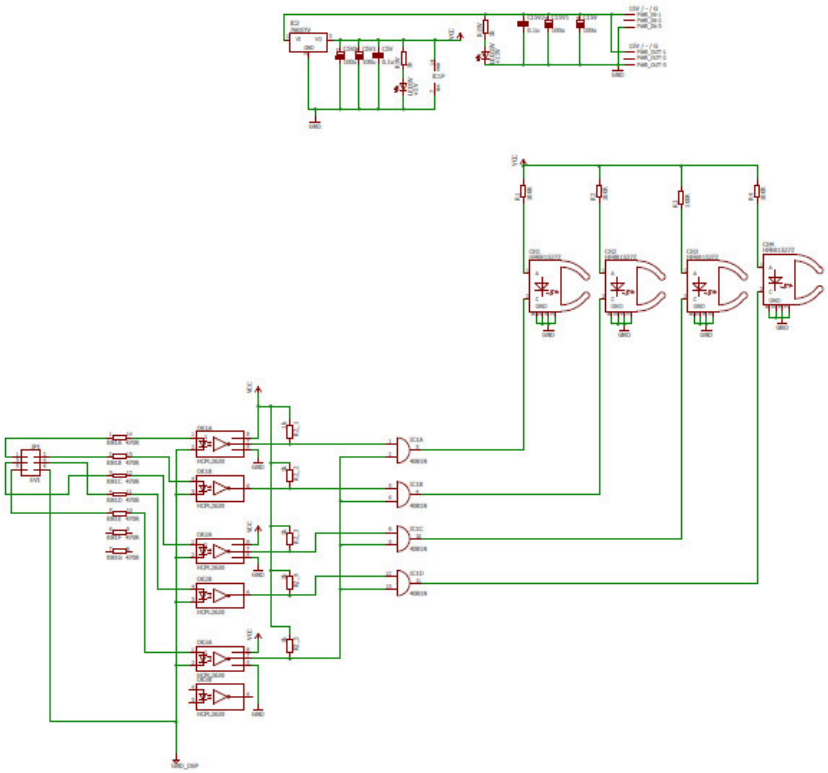

Fig. C.16 – Fiber optic emitter board schematic

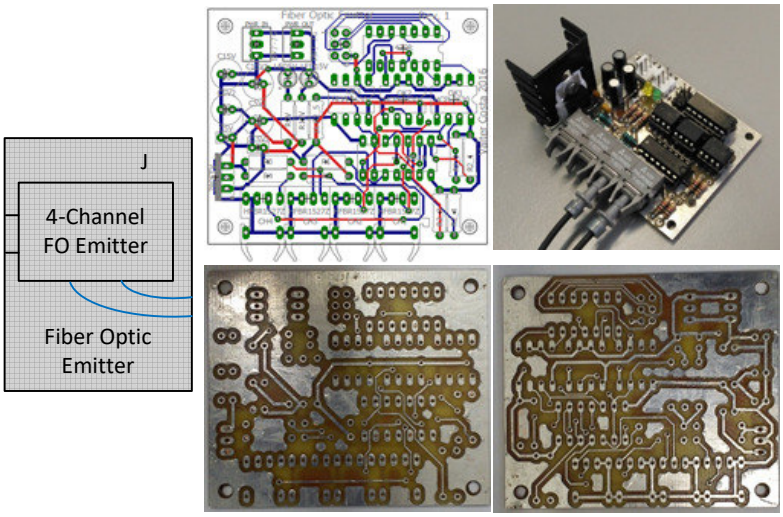

Fig. C.17 – Fiber Optic Emitter PCB prototype (62x52 mm), Board design; PCB Top and Bottom Layer and PCB full assembly

Block J in Fig. C.17 shows the Fiber Optic Emitter board schematic. The top picture in the middle shows the board design in the Eagle software. In the bottom, the pictures show the top and bottom layer of the manufactured PCB. Finally, the top right picture is the PCB full-assembly. Tab. C.6 shows the components list for the PCB board.

Tab. C.6 – Fiber optic emitter components list

Board	
Name	Fiber Optic Emitter Rev.1
Dimension	62 x 52 mm
Number of layers	2 - Top + Bottom
Observation	4 Channels fiber optic emitter with enable pin

	Schematic description	Value	Component	Observation
1	PWR_IN	15V / - / GND		Power in +15V
2	PWR_OUT	15V / - / GND		Power out +15V
3	C15V	100u	Electrolitic capacitor	
4	C15V1	100u	Electrolitic capacitor	
5	C15V3	0,1u	Ceramic capacitor	
6	R15V	1k	Resistor	
7	LED15V			15V
8	IC2	7805	Voltage regulator 5V	
9	C5V2	100u	Electrolitic capacitor	
10	C5V1	100u	Electrolitic capacitor	
11	C5V	0,1u	Ceramic capacitor	
12	R5V	1k	Resistor	
13	LED5V			5V
14	R1	100	Resistor	
15	R2	100	Resistor	
16	R3	100	Resistor	
17	R4	100	Resistor	
18	CH1	HFBR1527Z	Fiber Optic Transmitter	
19	CH2	HFBR1527Z	Fiber Optic Transmitter	
20	CH3	HFBR1527Z	Fiber Optic Transmitter	
21	CH4	HFBR1527Z	Fiber Optic Transmitter	
22	JP1			header 6 pins (3x2)
23	RN1	7x470	CI resistor	
24	OK1	HCPL2630	Optocoupler	
25	OK2	HCPL2631	Optocoupler	
26	OK3	HCPL2632	Optocoupler	
27	R2_1	1k	Resistor	
28	R2_2	1k	Resistor	
29	R2_3	1k	Resistor	
30	R2_4	1k	Resistor	
31	R2_5	1k	Resistor	
32	IC1	CD4071	CI Logic Ports OR (4x)	

Before the full assembly of the half-bridge inverter some experimental tests were perform to verify the drivers and the fiber emitter board operation as shown in Fig. C.18.

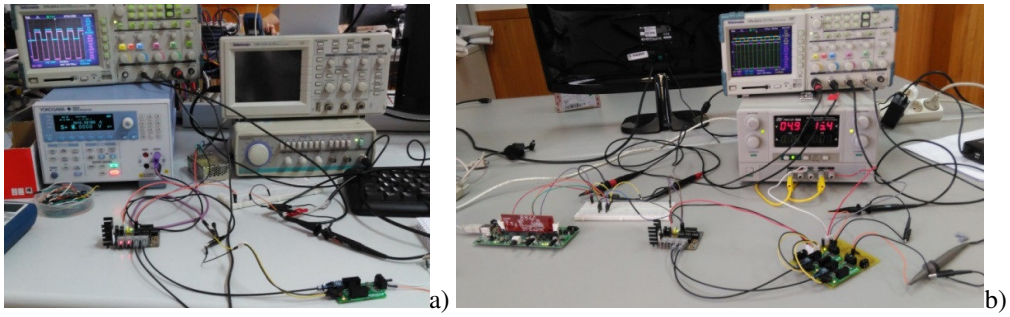

a) b)

Fig. C.18 – Fiber optic emitter and SiC MOSFET drivers experimental test prototype: a) Driver testing; b) Half-bridge inverter testing

DSP Control Board:

In order to control the converter, a DSP control board from Texas Instruments, shown in Fig. C.19, was used.

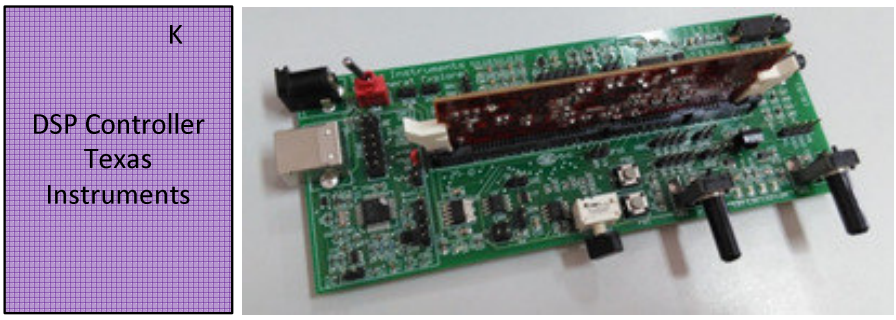

Fig. C.19 – DSP board from Texas Instruments (150 x 65 mm)

The DSP control board is used to generate the electric signals to the Fiber Optic Emitter PCB to control the SiC MOSFET switching. The DSP generates two square wave electric signals with 100 kHz frequency and 50% duty cycle. The signals are then used to control the switching of the SiC MOSFET switches. The SiC MOSFET drivers receive fiber optic signals. An interface board was design and built – Fiber Optic Emitter. The block diagram in Matlab/Simulink used to create the PWM signal at 100 kHz and 50% duty cycle is shown in Fig. C.21.

Computer:

In order to program the DSP control board (Fig. C.19) a computer existent in the laboratory was used. Matlab software and Matlab/Simulink library were used to build a block program for the SiC MOSFET transistors and it was compiled for C language and transfer to the DSP control board using Code Composer Studio (CCS) software shown in Fig. C.20.

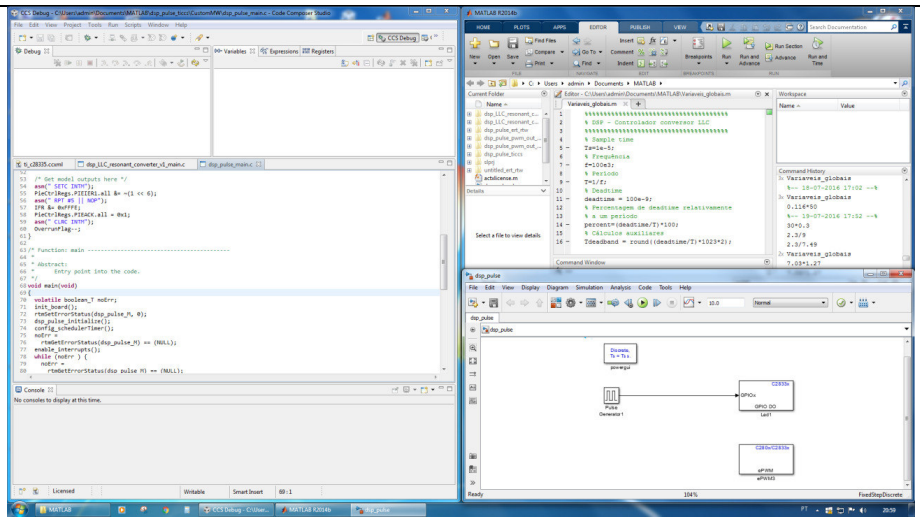

Fig. C.20 – Print screen of the computer monitor. CCS workspace (left), Matlab workspace (Top right) and, Matlab/Simulink block program (Bottom right)

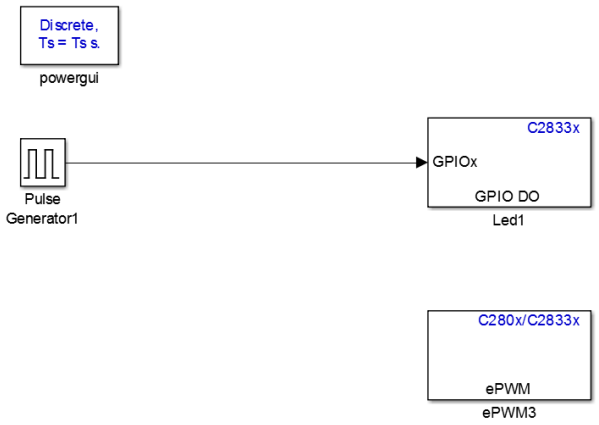

Fig. C.21 – Block diagram in Matlab/Simulink

In order to choose the switching frequency and the dead-time of the square waves for controlling the SiC MOSFET switching, an auxiliary code in Matlab was used as shown below:

```
%%%%%%%%%%%%%%%%%%%%%%%%%%%%%%%%%%%%%%%%
% DSP - Controlador conversor LLC
%%%%%%%%%%%%%%%%%%%%%%%%%%%%%%%%%%%%%%%%
% Sample time
Ts=1e-5;
% Frequência
f=100e3;
% Período
T=1/f;
% Deadtime
deadtime = 100e-9;
% Percentagem de deadtime relativamente
% a um período
percent=(deadtime/T)*100;
% Cálculos auxiliares
Tdeadband = round((deadtime/T)*1023*2);
```

D. Published Articles

This section of the appendix presents the articles published in the 51st International Universities' Power Engineering Conference (UPEC 2016, Coimbra, Portugal) entitled **"Analysis and Simulation of the LLC Resonant Converter under Different Control Methods"** and the article published in the 42nd Annual Conference of the IEEE Industrial Electronics Society (IECON 2016, Florence, Italy) entitled **"Evaluation of a Variable-Inductor-Controlled LLC Resonant Converter for Battery Charging Applications"**.

Analysis and Simulation of the LLC Resonant Converter under Different Control Methods

Valter S. Costa[1,2], M. S. Perdigão[1,2], A. S. Mendes[1]
[1]Instituto de Telecomunicações, University of Coimbra, DEEC, Coimbra,
[2]IPC, Instituto Superior de Engenharia de Coimbra, ISEC, DEE, Portugal, valter.costa@isec.pt, perdigao@isec.pt

J. M. Alonso
University of Oviedo, Electrical Eng. Dept., Tecnología Electrónica, Spain
marcos@uniovi.es

***Abstract* — This paper presents the analysis and design methodology for a LLC resonant converter controlled using two different control methods, switching frequency and VI (Variable Inductor). In order to compare both control techniques a battery charger is analyzed and simulation results are presented. In order to control the converter gain, the converter is regulated in the first case by varying the switching frequency and, in the second case, is regulated through a variable resonant tank. The design methodology is presented and simulation results were obtained and compared with the theoretical ones considering a simple battery charger application.**

Keywords—DC-DC power converters, Resonant inverters, Battery chargers

I. Introduction

The number of researchers reporting or analyzing the performance of the LLC resonant converter has increased drastically in recent years. A high number of applications have demonstrated that the LLC resonant converter is highly performing. From high-density dc-dc converters to mid to low power LED drivers [1],[2], or classical 48 V telecom power sources [3], the resonant mode of operation is pointed out as a main advantage for its high efficiency at the resonant frequency and its inherent capability of reducing switching losses due to ZVS (Zero Voltage Switching) characteristics. Battery chargers are also referred as benefiting from the inherent LLC characteristics. In addition, high reliability, high efficiency and low component cost can all be provided by choosing this topology [4]-[6]. This paper analysis the classical LLC converter topology controlled by the switching frequency, f_s and controlled with a variable resonant tank, using a VI as shown in Fig. 1. Depending on the operating conditions, the paper will analyze the performance, ZVS and ZCS, full-load and no-load operation. Another explored condition is to mix both control variables, frequency and variable resonant tank in order to verify the impact on the output regulation.

II. LLC Resonant Converter

The proposed converter topology is based on the half-bridge inverter feeding an LLC resonant tank. The converter generally provides galvanic isolation by using an isolation transformer, which is followed by a rectifier stage. For the purpose of this work, the load will be a battery bank.

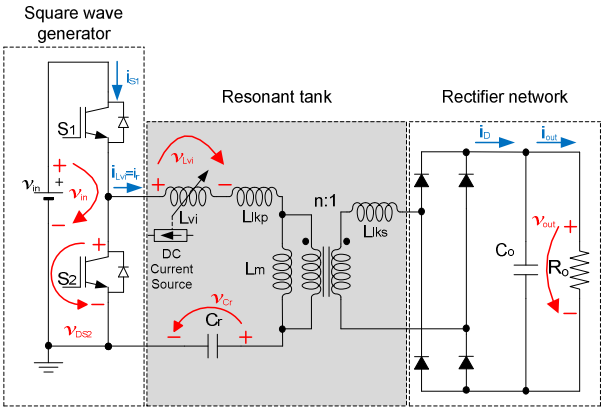

Fig. 1. Proposed LLC resonant converter

The typical LLC resonant converter can be divided in three modules as shown in Fig. 1 [7]. Fig. 1 presents the adopted current and voltage definitions. By turning the switches S_1 and S_2 with 50% duty cycle and complementary to each other a square voltage wave v_{DS2} is created at the input of the resonant network. In the present case a half-bridge inverter is used, but a full-bridge inverter could also be used. Typically the resonant tank has three components: a resonant inductor, L_r, the magnetizing inductance of the transformer, L_m and a resonant capacitor, C_r. In the case of the VI control, the role of the resonant inductor is done by the variable inductor L_{vi}, as opposed to the classical topology where the leakage inductance of the transformer L_{lkp} is used. In the classic topology this is done to avoid using two magnetic components. In this case, adding a new magnetic device allows the converter to operate at constant switching frequency (f_s) or even to use both control variables f_s and L_{vi} to regulate the ouput. The goal of the resonant tank is to filter the higher harmonic currents in order to allow only the fundamental component of the current to flow through the resonant tank, even when a square wave voltage is applied to the input.

A. Behaviour of the LLC Resonant Converter

The LLC resonant converter is known to be capable of providing a wide output voltage range and safe-operation from no-load to short-circuit conditions [7]. When f_s is the control variable, it is natural to operate the converter around the resonant frequency, $f_0 = \frac{1}{2*\pi*\sqrt{L_r C_r}}$ associated to the series elements of the resonant tank, L_r and C_r. Around this frequency, the gain characteristics are almost independent of

978-1-5090-4650-8/16/$31.00 ©2016 IEEE

the load [7]. Traditionally, the control is made by varying f_s. The required f_s range will be relatively small to guarantee enough controllability of the output gain (depending on the application) [7]. Therefore narrow f_0 range with light load and ZVS capability with even no load are commonly described as key benefits. It can also be seen that the gain changes with the load when f_s is different from f_0. The border between ZVS and ZCS operation is given by the peak gain, i.e. ZCS to the left and ZVS to the right, respectively. In case of no-load, the peak gain is maximum and it occurs when $f_s = f_p = \frac{1}{2*\pi*\sqrt{L_p C_r}}$ associated to the series-parallel elements of the resonant tank, L_p and C_r. Operating above f_0 the resonant tank is inductive and the input current, i_r lags the voltage applied to the resonant tank, v_{DS2}. The converter operates similar to a series resonant converter and therefore at f_0 the converter has only one operating point, which means no output regulation. Above f_0, switching losses will be minimized, due to ZVS. Working near resonance has the advantage of near sinusoidal waveforms. Below f_0 and above the boundary between ZVS/ZCS, formed by the peak of the family load vs. gain curves, the converter still operates in ZVS. This will not be the case if the converter is operated below the boundary leading to a capacitive operation [8].

B. *General Analysis using FHA and Design Methodology*

In order to use the first harmonic approximation (FHA) it is assumed that the filtering action of the resonant network is enough so that only the fundamental component of the square wave voltage v_{DS2} contributes to the power transfer to the output. Fig. 2a) shows the AC equivalent circuit for the LLC-VI and, Fig. 2b) shows the simplified AC equivalent circuit for the LLC resonant converter [11]. If f_s is adopted as control variable, L_{vi} is assumed to be zero.

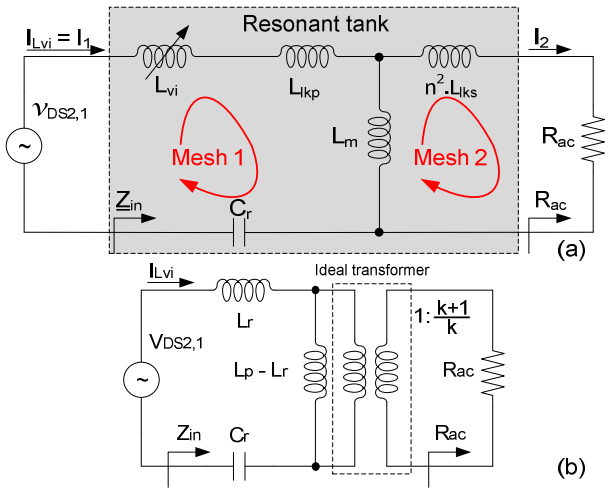

Fig. 2. LLC resonant converter: a) AC equivalent circuit; b) Simplified AC eqivalent circuit

Following the design procedure from [11], the converter equations needed for the design using FHA are shown in TABLE I. k is a ratio between L_m and L_{lkp} and is typically $k \in [5;10]$ according to [11]. From (2), a minimum voltage gain at ω_0 can be obtained as $M_{\omega\to\omega_0} = M_{min} = \frac{k+1}{k}$ and, considering an allowed voltage variation at the input, a maximum gain can be obtained and depends on the input voltage and the minimum gain, $M_{max} = \frac{V_{in\_min}}{V_{in\_max}} * M_{min}$. Finally, Fig. 2a) may be redesigned in terms of L_p and L_r as shown in Fig. 2b), where an ideal transformer is included and $L_r = L_{lkp} + L_m // L_{lkp}$ and $L_p = L_{lkp} + L_m$.

The next section will analyse the impact of the f_s and the VI on the design methodology and converter operation.

TABLE I. LLC CONVERTER EQUATIONS

General Equations for the LLC-VI	Mesh analysis	$\underline{V}_{in} = \left(\frac{1}{j\omega C_r} + j\omega L_{lkp} + j\omega L_{vi} + j\omega L_m\right)\cdot \underline{I}_1 - j\omega L_m \cdot \underline{I}_2$ $0 = \left(R_{ac} + j\omega n^2 L_{lks} + j\omega L_m\right)\cdot \underline{I}_1 - j\omega L_m \cdot \underline{I}_2 \quad ; \quad \underline{V}_o = \underline{I}_2 \cdot R_{ac}$
	Voltage gain	$M(j\omega) = \frac{\underline{V}_o}{\underline{V}_{in}} = \frac{R_{ac}}{\left(\frac{1}{j\omega C_r} + j\omega L_{lkp} + j\omega L_{vi} + j\omega L_m\right)\cdot\left(\frac{R_{ac} + n^2\cdot j\omega L_{lks}}{j\omega L_m} + 1\right) - j\omega L_m}$ (1)
LLC f_s control method [11]	Voltage gain	$M(j\omega) = \frac{2n\cdot V_o}{V_{in}} = \left\lvert \frac{\left(\frac{\omega^2}{\omega_p^2}\right)\frac{k}{k+1}}{j\left(\frac{\omega}{\omega_0}\right)\cdot\left(1-\frac{\omega^2}{\omega_0^2}\right)\cdot Q\frac{(k+1)^2}{2k+1} + \left(1-\frac{\omega^2}{\omega_p^2}\right)} \right\rvert$ (2)
		$Q = \frac{\sqrt{L_r/C_r}}{R_{ac}} \quad ; \quad k = \frac{L_m}{L_{lkp}} \quad ; \quad R_{ac} = \frac{8n^2}{\pi^2}R_o \quad ; \quad R_o = \frac{V_o}{I_o} \quad ; \quad n = \frac{N_p}{N_s}$
Resonant tank		$C_r = \frac{1}{2\pi Q\cdot f_0\cdot R_{ac}} \; ; \; L_r = \frac{1}{(2\pi f_0)^2 C_r} \; ; \; L_p = \frac{(k+1)^2}{(2k+1)}\cdot L_r \; ; \; n = \frac{V_{in\_max}}{2(V_o + 2\cdot V_F)}\cdot M_{min}$

III. Control Variables Impact on The LLC Resonant Converter

A. LLC Resonant Converter for Battery Charger Application

In order to prove the design methodology presented in this paper and considering both control techniques a simple battery charger application is considered. Fig. 3 shows the battery voltage and current profiles. The voltage and current are dependent on the state-of-charge (SOC) of the battery or battery bank. For this reason, during charging, the battery voltage v_{out} is not constant. The converter must cope with these changes and therefore must be capable of providing a wide output voltage range and safe-operation from no-load to short-circuit conditions [7]. The LLC isolated converter is capable of dealing with these requirements, since ZVS is guaranteed in the primary side and ZCS is assured in the secondary [4]. These requirements will also be kept with the LLC-VI.

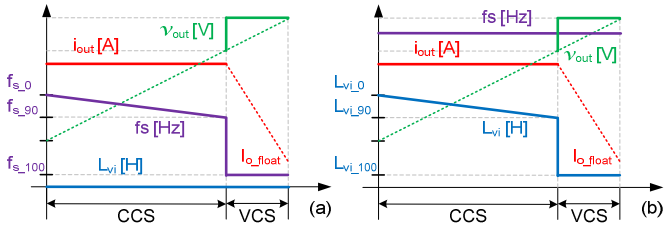

Fig. 3. Battery voltage and current profiles and, behavior of L_{vi} and f_s values along the charging process: (a) f_s control and, (b) L_{vi} control

Fig. 3a) and Fig. 3b) show the voltage and current profiles and, behavior of L_{vi} and f_s considering frequency and VI control, respectively.

Using the VI control method, in the charging stage the goal is to have a constant charging current, starting with an initial value for L_{vi}. Since the battery voltage is not constant, the controller needs to act on the inductance value to compensate the effect of the voltage variation. In this case, as the voltage increases from a minimum value, L_{vi} needs to decrease from L_{vi_0} (SOC ~0%), to maintain a constant charging current until an acceptable SOC is achieved (SOC~90% at L_{vi_90}). This mode is identified as current charging stage, CCS. In the next stage, identified as VCS (voltage charging stage), when the battery is almost fully charged, the voltage needs to be maintained at a constant maximum value as the charging current tends to decrease naturally to its floating level I_{o_float}. At this point, L_{vi} tends to its minimum value L_{vi_100} (SOC → 100%). During the whole process f_s is kept constant. This simple approach is sufficient to prove the converter performance, however more complex charge control algorithms can be implemented to improve the efficiency of the application itself.

Using the frequency control method, the charging profile is similar to the previous case but, in this case, the resonant inductor L_{vi} from Fig. 1 is not considered in the circuit and, the resonant inductor paper is done using the leakage inductance of the transformer.

The control variable is f_s. During CCS, f_s varies from f_{s_0} (SOC ~0%) to, f_{s_90} (SOC ~90%), to maintain a constant charging current as the battery voltage increases. During VCS, f_s tends to its minimum value f_{s_100} (SOC → 100%) maintaining the voltage at is maximum value as the charging current tends do its floating level I_{o_float}.

The simple approach presented in Fig. 3 is sufficient to prove the converter performance; however more complex charge control algorithms can be implemented to improve the efficiency of the application itself.

Having a battery bank as load, inductive operation is needed, therefore the converter will operate only at or above resonance. Above resonance, ZVS operation appears but the waveforms have more distortion.

B. VI Control Method

Fig. 4 presents the gain curves as function of L_{vi}, $M(L_{vi})$ at 10 kHz and 100 kHz using (1) from TABLE I. Fig. 4a) presents these curves for different load values. It is possible to observe that a higher frequency leads to a narrower voltage gain peak. The previous resonance point considered in the design methodology, for $f_s = f_0$, occurs now when L_{vi} is zero. At this point, the voltage gain is independent of load and frequency variation. In this case since the value of L_{vi} changes, so does the resonance frequency. Mathematically, resonance may occur for negative values of L_{vi}. Since a negative value of L_{vi} is not possible, it implies that the real operating region will always be a ZVS inductive region. From Fig. 4b) it can be seen that for a given voltage gain variation, ΔM, when the frequency is higher $(100\ kHz)$ the variation of inductance needed to obtain that gain variation (ΔL_{vi}) is smaller when compared to a lower frequency $(10\ kHz)$ gain curve. Therefore, for the same inductance range, a higher value of f_s will lead to a higher controllable range of the output. Increasing f_s enables circuit miniaturization and operating at constant f_s facilitates the design of the EMI filter.

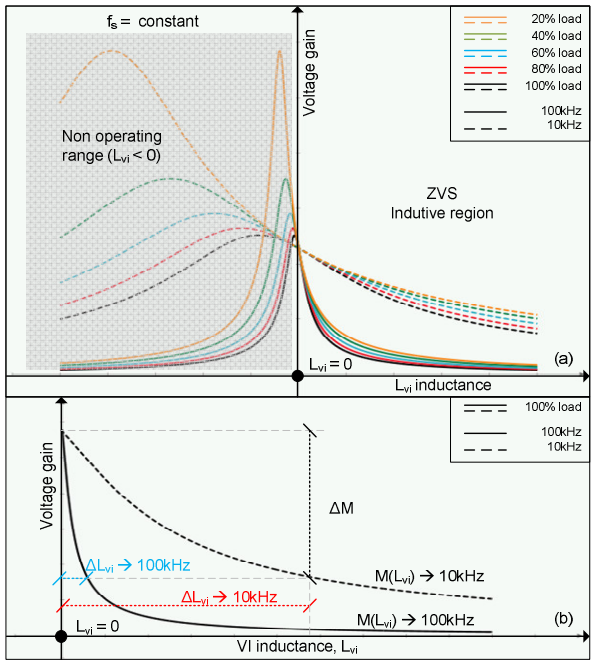

Fig. 4. Gain curves as function of L_{vi} at 10 kHz and 100 kHz: a) $M(L_{vi})$ at different load levels; b) $M(L_{vi})$ at full-load

This converter has inherent no-load and short-circuit protection. For short-circuit conditions, the resonant current would be limited by L_{vi}. For no-load, this current is equal to the magnetizing current of the transformer. Therefore, using the variable inductance concept, the converter can provide a controllable output and be operated at constant switching frequency f_s, advantageous in EMC (electromagnetic

compatibility) and miniaturization issues, without compromising reliability and performance [9].

C. Switching Frequency Control Method

In order to analyse the impact of the switching frequency on the LLC converter operation, the voltage gain must be obtained as a function of the switching frequency.

Similar to the VI control method, (1) can be used to obtain the gain curves as function of f_s. In this case, L_{vi} is not considered and is set to be zero in (1). The variation of f_s is made by knowing that $\omega = 2 * \pi * f_s$. Fig. 5 presents the gain curves as function of f_s, $M(f_s)$ considering a design for $10\,kHz$ and $100\,kHz$. Fig. 5a) presents these curves for different load values. In this case unlike the previous case it is possible to observe that considering the design for a lower frequency leads to a narrower voltage gain peak. At and around resonance, the voltage gain is independent of the load and frequency variation. As the resonant filter components are constant, f_0 is always constant even with f_s variation. Since the converter is designed initially to operate at resonance considering the maximum power in the output at this point, and that in normal operation, it will only operate at or above f_0 to regulate the output, ZVS is always guaranteed. From Fig. 5b) it can be seen that for a given voltage gain variation, ΔM, when the design frequency is higher $(100\,kHz)$ the variation of f_s needed to obtain that gain variation (Δf_s) is higher when compared to a lower frequency design $(10\,kHz)$ gain curve. Therefore, for the same f_s range, when the design is for a lower value of f_s it will lead to a higher controllable range of the output. Nevertheless, from Fig. 5a) above resonance, if the frequency of design is higher, the operation is less load dependent although it allows less output regulation with the same variation of f_s. Another advantage of increasing the design frequency is that enables circuit miniaturization.

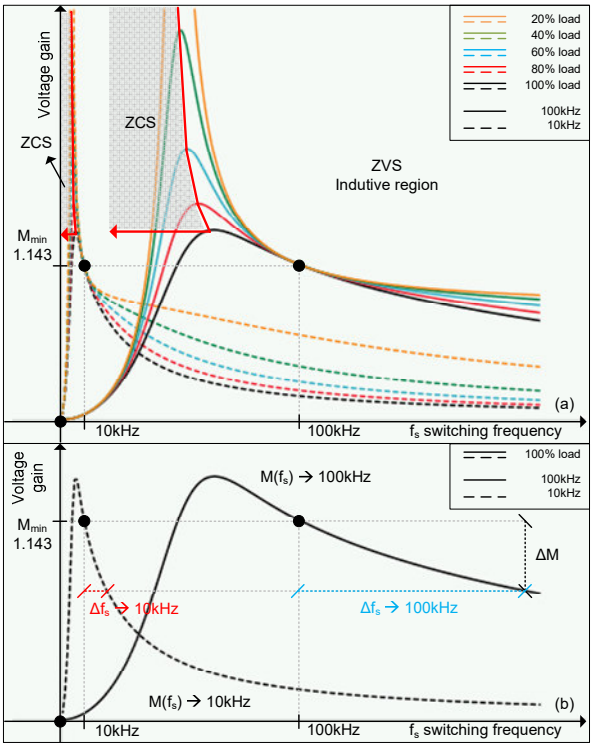

Fig. 5. Gain curves as function of f_s for 10 kHz and 100 kHz design: a) $M(f_s)$ at different load levels; b) $M(f_s)$ at full-load

D. Control Variables Range

In order to identify the required inductance and frequency range for the application, the output power must be calculated. Using (1) and knowing that $M = \frac{2*n*V_o}{V_{in}}$ from [7] the output converter power can be obtained as:

$$P_o = \frac{V_o^2}{R_o} = \frac{\left(\frac{V_{in}}{2n}\right)^2}{R_o} \cdot \left|M\left(j\omega\right)\right|^2 \quad (3)$$

1) VI control range

Considering the voltage and current profiles presented in Fig. 3a), the output power for the three levels of SOC corresponding to L_{vi_0}, L_{vi_90} and, L_{vi_100} can be obtained by using (3). The results are shown in Fig. 6.

By intersecting the gain curves of Fig. 6 with the defined power levels, L_{vi_0}, L_{vi_90} and, L_{vi_100} are obtained. The inductance range is defined with L_{vi_0} and L_{vi_100}. The procedure for the construction of the VI can be find in previous literature [9].

2) Frequency Control Range

Similar to the previous case, in order to identify the required frequency range for the application, the output power must be calculated. In this case, the output power is calculated using (3) and the gain $M(j\omega)$ is also obtained using (1) where $\omega = 2 * \pi * f_s$ and, L_{vi} is kept at zero ($L_{vi} = 0$). In this case, f_s is the control variable.

Considering the voltage and current profiles presented in Fig. 3b), the output power for the three levels of SOC corresponding to f_{s_0}, f_{s_90} and, f_{s_100} can be obtained using (3). The results are shown in Fig. 7.

By intersecting the gain curves of Fig. 7 with the defined power levels, f_{s_0}, f_{s_90} and, f_{s_100} are obtained. The frequency range is defined with f_{s_0} and f_{s_100}.

3) VI and Frequency Control

Fig. 8 presents the gain curves as function of f_s, $M(f_s)$ considering a design for 100 kHz. From Fig. 8, it can be seen that using both control methods simultaneously can be advantageous. It is possible to obtain the same gain M with a smaller value of f_s by increasing the L_{vi} value. This would imply pushing the operating point from A to B or C as shown in Fig. 8.

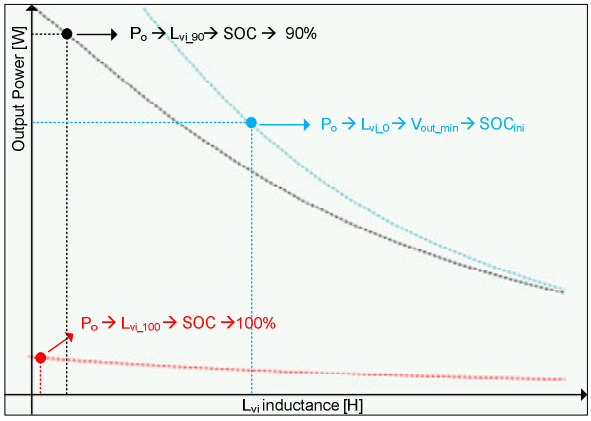

Fig. 6. Output power as function of of L_{vi}, $P_o(L_{vi})$ for the operating points corresponding to L_{vi_0}, L_{vi_90} and L_{vi_100}

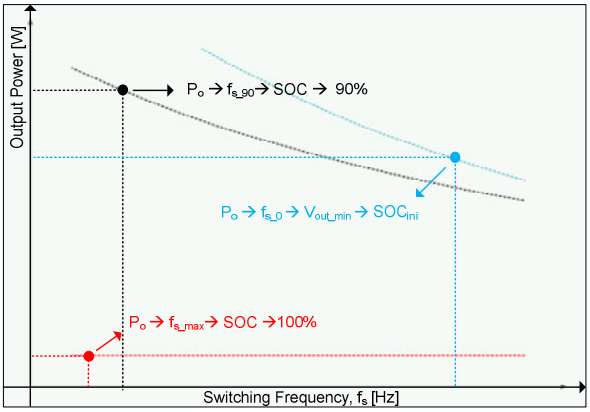

Fig. 7. Output power as function of of f_s, $P_o(f_s)$ for the operating points corresponding to f_{s_0}, f_{s_90} and f_{s_100}

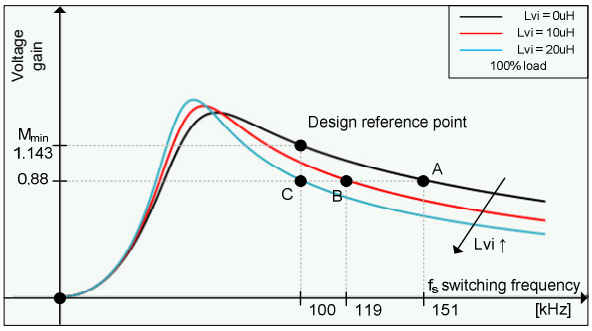

Fig. 8. Gain curves as function of f_s for 100 kHz design for three different values of L_{vi} at full-load (100% load)

IV. Simulation Results

In order to validate the proposed topology, simulations in PSIM were carried out considering the converter parameters shown in TABLE II. , which were obtained by applying the proposed methodology. The simulation results shown in Fig. 9 and Fig. 10 were obtained under open-loop control and are referred to VI and frequency control methods, respectively.

TABLE II. Converter Parameters for Simulation

Description		Specification
Main parameters		$V_{in} = 400V$; $f_s = 100kHz$; $d = 0.5$
Magnetic devices	L_{vi}	$L_{vi\_min} = 0.8\mu H$; $L_{vi\_max} = 21.1\mu H$
	Transformer	$k = 7$; $n = 1.95$
		$L_{lkp} = 15.11\mu H$; $L_{lks} = 3.97\mu H$
		$L_m = 105.75\mu H$
C_r , C_o , Load		$89.42nF$; $43\mu F$; $R_o \geq 8.4\Omega$

The simulation results referred to the VI control method are shown in Fig. 9 and are referred to operating points L_{vi_0}, L_{vi_90} and L_{vi_100} (red, green and blue, respectively) obtained from Fig. 3b). Fig. 9a) and Fig. 9b) show respectively the driver signals for S1 and S2, $v_{GS1}$and v_{GS2} and the resonant filter input voltage, v_{DS2}. Fig. 9c), Fig. 9d), Fig. 9f) and Fig. 9g) show respectively the input current, i_{S1}, the current in the resonant tank, i_{Lvi}, the current in the rectifier diodes, i_D and the output current, i_{out}. Finally, Fig. 9e) and Fig. 9h) show respectively the voltage at the VI terminals, v_{Lvi} and the output voltage, v_{out}.

During the CCS the range of the VI is $[L_{vi\_0}; L_{vi\_90}]$. When charging begins, $L_{vi} = L_{vi\_0}$, $I_{out} = 10A$ and $V_{out} = 84V$ which corresponds to its minimum value.

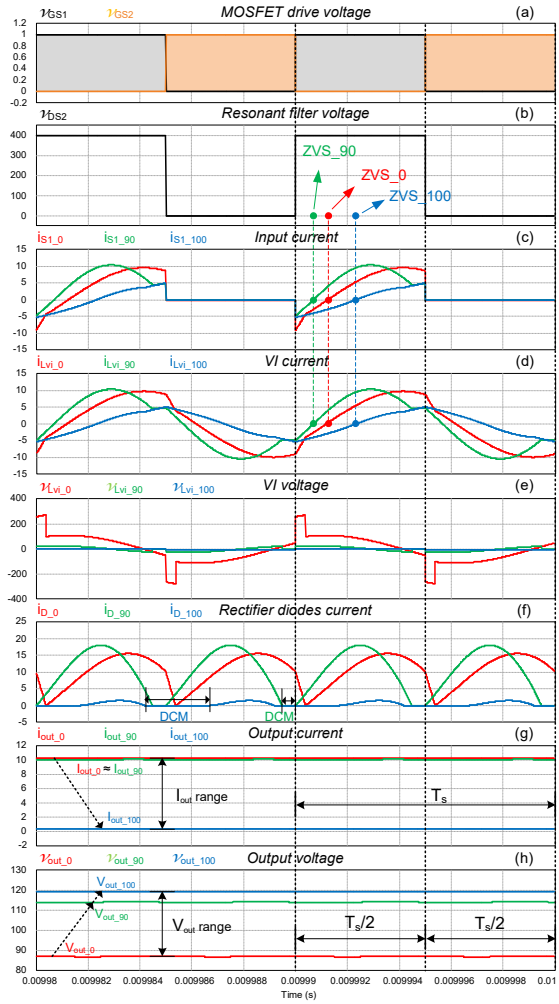

Fig. 9. Waveforms from simulation which represent the three points of operation correspondent to L_{vi_0}, L_{vi_90} and L_{vi_100}, in red, green and blue, respectively: (a) $v_{GS1}$and v_{GS2}; (b) v_{DS2} ; (c) i_{S1}; (d) i_{Lvi}; (e) v_{Lvi}; (f) i_D; (g) i_{out}; (h) v_{out}

When CCS ends, $L_{vi} = L_{vi\_90}$, $I_{out} = 10A$ and $V_{out} = 112{,}8V$ (SOC $\approx$ 90%). The controller switches from CCS to VCS, and the battery voltage increases to its maximum value, $V_{out} = 116V$ and the charging current tends naturally to its float value. At this point, $L_{vi} \rightarrow L_{vi\_100}$. The converter operates always above resonance with ZVS. When the charging process begins the rectifier diodes operate in CCM (continuous conduction mode). The analysis of i_D shows however that the converter enters in DCM (discontinuous conduction mode). When the batteries are almost fully charged the behavior of the converters tends to an open circuit and the current through the VI, i_{Lvi_100} exhibits a triangular shape waveform similar to what would be expected for the magnetizing current, i_{Lm}.

The simulation results referred to the frequency control method are shown in Fig. 10 and are referred to operating points f_{s_0}, f_{s_90} and f_{s_100} (red, green and blue, respectively) obtained from Fig. 3a). Fig. 10a) to Fig. 10c) show respectively the driver signals for S1 and S2, $v_{GS1}$and v_{GS2}, for f_{s_0}, f_{s_90} and f_{s_100} respectively. Fig. 10d) shows the resonant filter input voltage, v_{DS2}. Fig. 10e), Fig. 10f), Fig. 10g) and Fig. 10h) show respectively the input current, i_{S1}, the current in the resonant tank, i_{Lvi}, the current in the rectifier diodes, i_D and the output current, i_{out}. Finally, Fig. 10i) shows the output voltage, v_{out}.

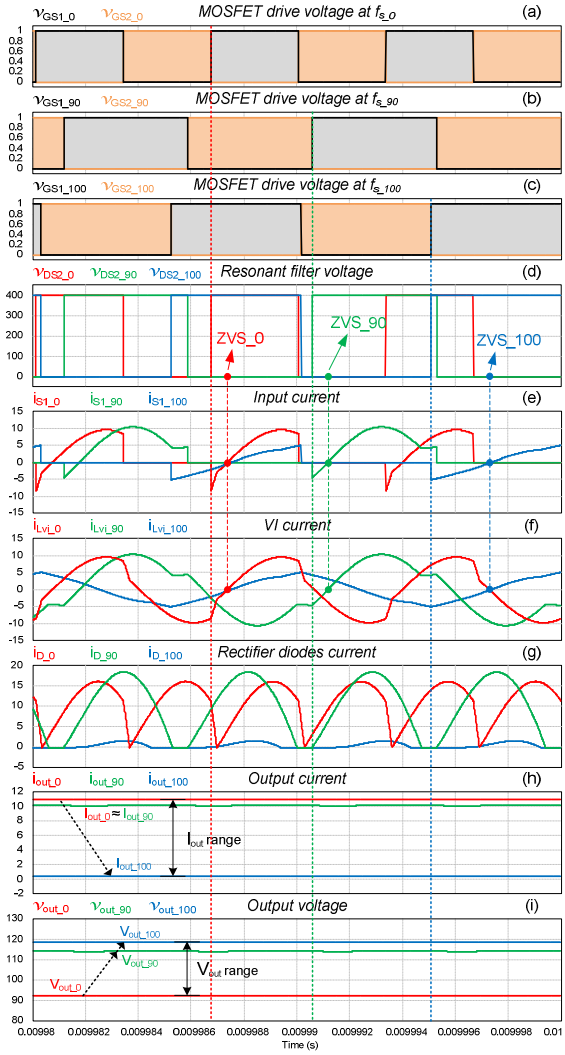

Fig. 10. Waveforms from simulation which represent the three points of operation correspondent to L_{vi_0}, L_{vi_90} and L_{vi_100}, in red, green and blue, respectively: (a) $v_{GS1}$and v_{GS2} for f_{s_0}; (b) $v_{GS1}$and v_{GS2} for f_{s_90}; (c) $v_{GS1}$and v_{GS2} for f_{s_100}; (d) v_{DS2} ; (e) i_{S1}; (f) i_{Lvi}; (g) i_D; (h) i_{out}; (i) v_{out}

TABLE III. show the theoretical and simulation results considering VI and frequency control methods for the converter design parameters defined in TABLE II. As can be seen the simulation results are similar to the expected theoretical results and the results for VI control are very similar to the results for frequency control.

TABLE III. THEORETICAL AND SIMULATION RESULTS

		Theoretical				Simulation		
SOC [%]	L_{vi} [μH]	f_s [kHz]	V_{out} [V]	I_{out} [A]	P_{out} [W]	V_{out} [V]	I_{out} [A]	P_{out} [W]
≈ 0	21.1	100	84	10	840	87.23	10.38	906
≈ 90	3.3	100	112.8	10	1128	114.41	10.14	1161
≈ 100	0.98	100	116	0.5	58	118.99	0.51	61
≈ 0	–	151	84	10	840	92.5	11.01	1019
≈ 90	–	106.3	112.8	10	1128	114.41	10.14	1161
≈ 100	–	101.65	116	0.5	58	118.99	0.51	61
≈ 0	10	120	84	10	840	89.38	10.64	951

From TABLE III. the necessary range to regulate the output is about $20\mu H$ considering only VI control, $50kHz$ considering only f_s control and, $10\mu H$ and $20kHz$ considering VI and f_s control simultaneously. In conclusion, using both control techniques simultaneously allows the range of each control variable to be smaller when compared to the case of using only one control method.

V. CONCLUSIONS

The goal of this paper is to analyze the LLC resonant converter and compare its behavior when using either the traditional frequency control or, using a variable resonant tank through a VI. The advantages of using simultaneously both control techniques were discussed. The converter parameters are first determined considering the traditional design methodology (used for frequency control) and then, depending on the chosen control method, the output power expression is used to determine either the necessary VI or f_s range to control the converter output. A simple charging profile was followed. A careful theoretical and simulation analysis of the converter is presented for different switching frequencies, including the analysis of the converter output power as function of both control variables. Theoretical results were confronted with simulation and a good agreement was found. In conclusion both control parameters can be used to control the output of the LLC resonant converter achieving always ZVS: using a VI while keeping f_s constant or using f_s while the resonant parameters are kept constant. A higher f_s leads to converter miniaturization and the range of the VI needed to obtain a specific output regulation will be smaller. However, if f_s is the control variable, the range is higher. A mix between both controls methods leads to an improved performance

REFERENCES

[1] Y. Wang, Y. Guan, J. Huang, W. Wang and D. Xu, "A Single-Stage LED Driver Based on Interleaved Buck–Boost Circuit and LLC Resonant Converter," in *IEEE Journal of Emerging and Selected Topics in Power Electronics*, vol. 3, no. 3, pp. 732-741, Sept. 2015.

[2] Shuze Zhao, Jiale Xu and O. Trescases, "Burst-Mode Resonant LLC Converter for an LED Luminaire With Integrated Visible Light Communication for Smart Buildings," in *IEEE Transactions on Power Electronics*, vol. 29, no. 8, pp. 4392-4402, Aug. 2014.

[3] R. L. Lin and C. W. Lin, "Design criteria for resonant tank of LLC DC-DC resonant converter," *IECON 2010 - 36th Annual Conference on IEEE Industrial Electronics Society*, Glendale, AZ, 2010, pp. 427-432. doi: 10.1109/IECON.2010.5674988

[4] Z. Fang, T. Cai, S. Duan and C. Chen, "Optimal Design Methodology for LLC Resonant Converter in Battery Charging Applications Based on Time-Weighted Average Efficiency," in *IEEE Transactions on Power Electronics*, vol. 30, no. 10, pp. 5469-5483, Oct. 2015.

[5] Musavi, F.; Craciun, M.; Gautam, D.S.; Eberle, W.; Dunford, W.G., "An LLC Resonant DC–DC Converter for Wide Output Voltage Range Battery Charging Applications," in *Power Electronics, IEEE Transactions on* , vol.28, no.12, pp.5437-5445, Dec. 2013

[6] Shafiei, N.; Ordonez, M.; Craciun, M.; Botting, C.; Edington, M., "Burst Mode Elimination in High-Power LLC Resonant Battery Charger for Electric Vehicles," in *Power Electronics, IEEE Transactions on* , vol.31, no.2, pp.1173-1188, Feb. 2016.

[7] Hangseok Choi, "AN-4151, Half-Bridge LLC Resonant Converter Design Using FSFR-Series Fairchild Power Switch (FPS™)", 2007.

[8] Helen Ding, "AN-1160, Design of Resonant Half-Bridge Converter using IRS2795(1,2) Control IC", International Rectifier.

[9] M. S. Perdigao, S. F. Ferreira, M. Martins, A. S. Mendes and J. M. Alonso, "Finite element analysis of a variable inductor for an RSCC based LED lamp driver," *Industry Applications Society Annual Meeting, 2015 IEEE*, Addison, TX, 2015, pp. 1-8.

[10] C. A. Cheng, H. W. Chen, E. C. Chang, C. H. Yen and K. J. Lin, "Efficiency study for a 150W LLC resonant converter," *Power Electronics and Drive Systems, 2009. PEDS 2009. International Conference on*, Taipei, 2009, pp. 1261-1265.

[11] Hangseok Choi, " Design Considerations for an LLC resonant Converter," Farichild Power Seminar 2007

Evaluation of a Variable-Inductor-Controlled LLC Resonant Converter for Battery Charging Applications

Valter S. Costa[1,2], M. S. Perdigão[1,2], A. S. Mendes[1]
[1]Instituto de Telecomunicações, University of Coimbra, DEEC, Coimbra,
[2]IPC, Instituto Superior de Engenharia de Coimbra, ISEC, DEE, Portugal, perdigao@isec.pt

J. M. Alonso
University of Oviedo, Electrical Eng. Dept., Tecnología Electrónica, Spain
marcos@uniovi.es

***Abstract* — Based on the respective merits of the LLC resonant converter and the VI (Variable Inductor), a new battery charger topology is proposed. This paper presents a design methodology for the LLC resonant converter controlled with a VI. The output of the converter is regulated through a variable resonant tank in order to control the charging process. A small-scale prototype fed by a 50V DC input, with an IGBT based inverter working at 11.3 kHz was built in order to test the proposed control method. Experimental results are presented.**

Keywords—LLC resonant converter, variable inductor, battery charger.

I. Introduction

The number of researchers reporting or analyzing the performance of the LLC resonant converter has increased drastically in recent years. A high number of applications have demonstrated that the LLC resonant converter is highly performing. From high-density dc-dc converters to mid to low power LED drivers [1],[2], or classical 48 V telecom power sources [3], the resonant mode of operation is pointed out as a main advantage for its high efficiency at the resonant frequency and its inherent capability of reducing switching losses due to ZVS (Zero Voltage Switching) characteristics. Battery chargers are also referred as benefiting from the inherent LLC characteristics. Battery chargers requirements are somehow different from other applications since the converter must provide low high-frequency current ripple to maximize the battery life, a wide output voltage to cope with typical battery voltage profiles and a flexible control in order to design appropriate charging algorithms. In addition, high reliability, high efficiency and low component cost can all be provided by choosing this topology [4]-[6].

This paper is inspired in the classical LLC converter topology by exploring a new control method, based on a variable resonant tank as shown in Fig. 1. Fig. 1 presents also the adopted current and voltage definitions.

Using the variable inductance concept, the converter can provide a controllable output and be operated at constant switching frequency f_s, advantageous in EMC (electromagnetic compatibility) and miniaturization issues, without compromising reliability and performance. ZVS is guaranteed and the whole strategy is demonstrated by a simple charging concept.

II. LLC Resonant Converter

The proposed converter topology is based on the half-bridge inverter feeding an LLC resonant tank. The converter generally provides galvanic isolation by using an isolation transformer, which is followed by a rectifier stage. For the purpose of this work, the load will be a battery bank.

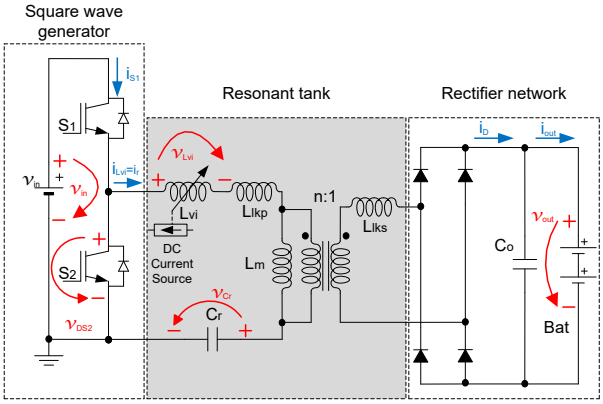

Fig. 1. Proposed LLC resonant converter

The typical LLC resonant converter can be divided in three modules as shown in Fig. 1 [7]. By turning the switches S_1 and S_2 with 50% duty cycle and complementary to each other a square voltage wave v_{DS2} is created at the input of the resonant network. In the present case a half-bridge inverter is used, but a full-bridge inverter could also be used. Typically the resonant tank has three components: a resonant inductor, L_r, the magnetizing inductance of the transformer, L_m and a resonant capacitor, C_r. In this case, the role of the resonant inductor is done by the variable inductor L_{vi}, as opposed to the classical topology where the leakage inductance of the transformer L_{lkp} is used. In the classic topology this is done to avoid using two magnetic components. In this case, adding a new magnetic device allows the converter to operate at constant switching frequency (f_s) or even to use both control variables f_s and L_{vi} to regulate the ouput. The goal of the resonant tank is to filter the higher harmonic currents in order to allow only the fundamental component of the current to flow through the resonant tank, even when a square wave voltage is applied to the input.

A. Advantages and Behaviour of the LLC Resonant Converter

The LLC resonant converter is known to be capable of providing a wide output voltage range and safe-operation from no-load to short-circuit conditions [7]. When f_s is the control variable, it is natural to operate the converter around the resonant frequency, $f_0 = \frac{1}{2*\pi*\sqrt{L_r C_r}}$ associated to the series elements of the resonant tank, L_r and C_r. Around this frequency, the gain characteristics are almost independent of the load, as seen in Fig. 2. Traditionally, the control is made by varying f_s. The required f_s range will be relatively small to guarantee enough controllability of the output gain (depending on the application) [7]. Therefore narrow f_0 range with light load and ZVS capability with even no load are commonly described as key benefits. It can also be seen that the gain changes with the load when f_s is different from f_0. The border between ZVS and ZCS operation is given by the peak gain, i.e. ZCS to the left and ZVS to the right, respectively. In case of no load, the peak gain is maximum and it occurs when $f_s = f_p = \frac{1}{2*\pi*\sqrt{L_p C_r}}$ associated to the series-parallel elements of the resonant tank, L_p and C_r, where L_p is defined as the sum of the primary leakage inductance and the magnetizing inductance.

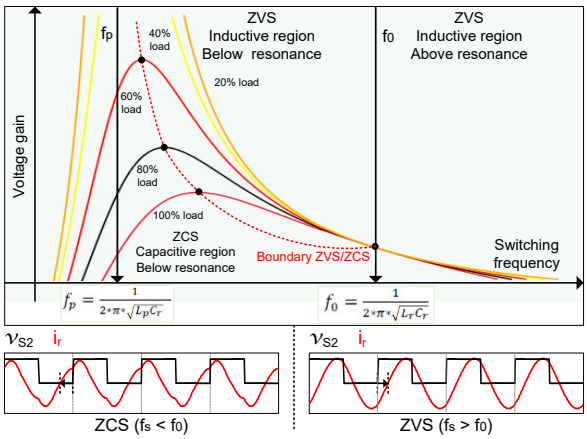

Fig. 2. Typical gain curves of LLC resonant converter for various loads and capacitive and inductive region waveforms

It is also noticed that operating above f_0 the resonant tank is inductive and the input current, i_r lags the voltage applied to the resonant tank, v_{DS2}. The converter operates similar to a series resonant converter and therefore at f_0 the converter has only one operating point, which means no output regulation. Above f_0, switching losses will be minimized, due to ZVS. Working near resonance has the advantage of near sinusoidal waveforms. Below f_0 and above the boundary between ZVS/ZCS, formed by the peak of the family load vs. gain curves, the converter still operates in ZVS. This will not be the case if the converter is operated below the boundary leading to a capacitive operation [8].

B. LLC Resonant Converter with VI Control

In the present case study an LLC resonant converter with Variable Inductor (LLC-VI) control is described. The L_{vi} is connected in series with the transformer primary side, but the rest of the topology is kept. As response to a dc control current, the global reluctance of the magnetic L_{vi} core is varied, and therefore the differential inductance of the inductor is controlled. Thus, the role of the L_{vi} is to change the characteristics of the resonant tank in order to have a controllable output in a similar manner to the classical f_s control. The L_{vi} principle of operation may be found in prior literature and will not be further addressed in this paper [9]. In this case, the f_s will be kept constant, which benefits the converter design (EMC and control design). However, if necessary these two control variables might act together to improve the performance of the converter.

Besides small size, low component cost and high reliability, charging applications have specific requirements that are directly related to the battery voltage and current profile as exemplified in Fig. 3. These characteristics are strongly dependent on the state-of-charge (SOC) of the battery or battery bank. For this reason, during charging, the battery voltage v_{out} is not constant. The converter must cope with these changes and therefore must be capable of providing a wide output voltage range and safe-operation from no-load to short-circuit conditions [7]. The LLC isolated converter is capable of dealing with these requirements, since ZVS is guaranteed in the primary side and ZCS is assured in the secondary [4]. These requirements will also be kept with the LLC-VI. In the charging stage the goal is to have a constant charging current, starting with an initial value for L_{vi}. Since the battery voltage is not constant, the controller needs to act on the inductance value to compensate the effect of the voltage variation. In this case, as the voltage increases from a minimum value, L_{vi} needs to decrease from L_{vi_0} (SOC ~0%), to maintain a constant charging current until an acceptable SOC is achieved (SOC~90% at L_{vi_90}). This mode is identified as current charging stage, CCS. In the next stage, identified as VCS (voltage charging stage), when the battery is almost fully charged, the voltage needs to be maintained at a constant maximum value as the charging current tends to decrease naturally to its floating level I_{o_float}. At this point, L_{vi} tends to its minimum value L_{vi_100} (SOC → 100%). During the whole process f_s is kept constant. This simple approach is sufficient to prove the converter performance, however more complex charge control algorithms can be implemented to improve the efficiency of the application itself.

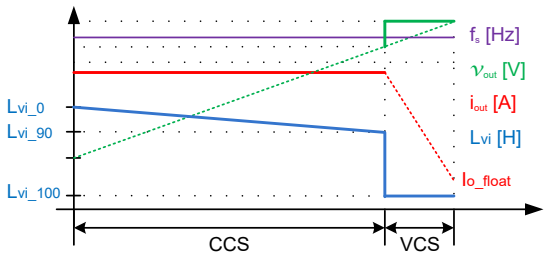

Fig. 3. Battery voltage and current profiles and, behavior of L_{vi} and f_s values along the charging process

Having a battery bank as load, inductive operation is needed, therefore the converter will operate only at or above resonance. Above resonance, ZVS operation appears but the waveforms have more distortion.

III. Analysis and Design of the LLC-VI

In this section the analysis and design of the converter will be discussed considering the proposed VI control method. The approach will be based on the evaluation of the converter using the fundamental harmonic approximation (FHA).

A. General Analysis using FHA and Design Methodology

In order to use the first harmonic approximation (FHA) it is assumed that the filtering action of the resonant network is enough so that only the fundamental component of the square wave voltage v_{DS2} contributes to the power transfer to the output. Fig. 4 shows the AC equivalent circuit for the LLC-VI.

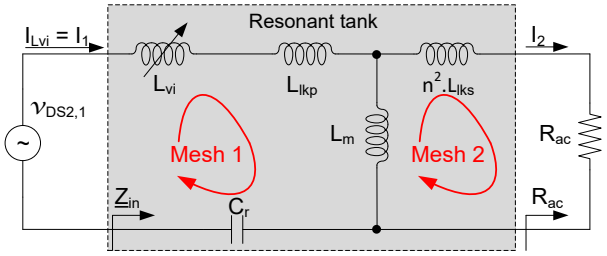

Fig. 4. AC equivalent circuit for LLC resonant converter

Considering the transformer turns ratio $n = N_p/N_s$, the rectifier and the load, an equivalent resistance R_{ac} is defined that includes the effect of the output rectifier and load resistance:

$$R_{ac} = \frac{8n^2}{\pi^2} R_o \tag{1}$$

where $R_o = V_o/I_o$ is the load resistance (that represents the battery bank).

The design methodology starts by determining the resonant tank parameters (L_r, L_p and C_r) assuming the traditional FHA method followed by [11], considering the nominal operating point as reference. The following condition is considered at the nominal operating point: $L_{vi} = 0$. As previously mentioned, the LLC converter has two resonant frequencies: $\omega_0 = 2\pi f_0$ determined by L_r and C_r and $\omega_p = 2\pi f_p$, determined by L_p and C_r, where $L_m = L_p - L_{lkp}$ and $L_r = L_{lkp} + L_m // (n^2 L_{lks})$. In a transformer, if the secondary side winding is open or short-circuited, L_p and L_r can be measured, respectively. Following the procedure presented in [11] and assuming that $L_{lkp} = n^2 L_{lks}$ the voltage gain for this converter can be expressed as:

$$M(j\omega) = \frac{2n \cdot V_o}{V_{in}} = \left| \frac{\left(\frac{\omega^2}{\omega_p^2}\right)\frac{k}{k+1}}{j\left(\frac{\omega}{\omega_0}\right)\cdot\left(1-\frac{\omega^2}{\omega_0^2}\right)\cdot Q\frac{(k+1)^2}{2k+1}+\left(1-\frac{\omega^2}{\omega_p^2}\right)} \right| \tag{2}$$

Where $Q = \frac{\sqrt{L_r/C_r}}{R_{ac}}$ and $k = \frac{L_m}{L_{lkp}}$ and is typically $k \in [5;10]$ according to [11]. With this simplification, a minimum voltage gain at ω_0 can be obtained as $M_{\omega\to\omega_0} = M_{min} = \frac{k+1}{k}$. Finally, Fig. 4 may be redesigned in terms of L_p and L_r as shown in Fig. 5, where an ideal transformer is included and $L_r = L_{lkp} + L_m // L_{lkp}$ and $L_p = L_{lkp} + L_m$.

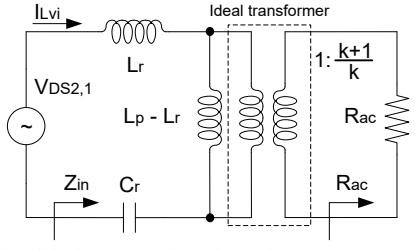

Fig. 5. Simplified AC eqivalent circuit for LLC resonant converter

Assuming an input voltage variation of 10% to 15%, the maximum gain can be calculated as:

$$M_{\max} = \frac{V_{in\_\max}}{V_{in\_\min}} \cdot M_{\min} \tag{3}$$

In order to identify the value of Q (for the calculation of the resonant parameters), it is necessary to find the peak gain curves as function of Q and intersect them with the specified maximum gain (assuming a variable range for V_{in}). These curves for different k values are shown in Fig. 6, as obtained from (2). For a selected Q range the voltage gain is determined and the peak gain value is identified. This is repeated for different values of k.

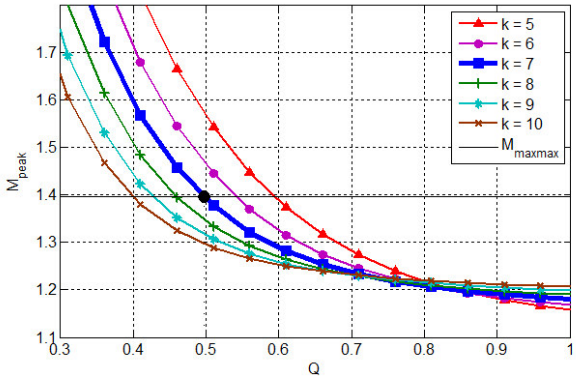

Fig. 6. Peak gain (maximum attainable gain) versus Q for different k values

The final value of Q is obtained from the intersection of the maximum gain, considering a margin of 10% ($M_{maxmax} = 1.1 * M_{max}$), and the peak gain curve for the selected k as shown in Fig. 6. Knowing the value of Q, considering f_s and f_0, the resonant parameters can be calculated as:

$$C_r = \frac{1}{2\pi Q \cdot f_0 \cdot R_{ac}} \tag{4}$$

$$L_r = \frac{1}{(2\pi f_0)^2 C_r} \tag{5}$$

$$L_p = \frac{(k+1)^2}{(2k+1)} \cdot L_r \tag{6}$$

Considering an output voltage ripple of 1%, the output capacitor C_o can be calculated as:

$$C_o = \frac{I_o}{V_{ripple} \cdot 2 \cdot f_s} \tag{7}$$

Finally, the transformer turns ratio is determined. Considering the diode rectifier voltage drop V_F, the transformer turns ratio can be determined as:

$$n = \frac{N_p}{N_s} = \frac{V_{in\_\max}}{2(V_o + 2 \cdot V_F)} \cdot M_{\min} \tag{8}$$

The next section will analyse the impact of the VI on the design methodology and converter operation.

B. VI Control Impact on the Design Methodology

In order to analyse the impact of the VI on the LLC converter operation, the voltage gain must be obtained as a function of this new control parameter.

Applying Kirchhoff's Laws to mesh 1 and mesh 2, referred previously in Fig. 4, (9) and (10) can be written. Considering the output voltage $\underline{V_O} = \underline{I_2} * R_{ac}$, and the two mesh equations, the voltage gain is obtained as in (11).

$$\underline{V}_{in} = \left(\frac{1}{j\omega C_r} + j\omega L_{lkp} + j\omega L_{vi} + j\omega L_m \right) \cdot \underline{I}_1 - j\omega L_m \cdot \underline{I}_2 \tag{9}$$

$$0 = \left(R_{ac} + j\omega n^2 L_{lks} + j\omega L_m \right) \cdot \underline{I}_1 - j\omega L_m \cdot \underline{I}_2 \tag{10}$$

$$M(j\omega) = \frac{\underline{V}_o}{\underline{V}_{in}} = \frac{R_{ac}}{\left(\frac{1}{j\omega C_r} + j\omega L_{lkp} + j\omega L_{vi} + j\omega L_m \right) \cdot \left(\frac{R_{ac} + n^2 \cdot j\omega L_{lks}}{j\omega L_m} + 1 \right) - j\omega L_m} \tag{11}$$

Fig. 7 presents the gain curves as function of L_{vi}, $M(L_{vi})$ at 10 kHz and 100 kHz. Fig. 7a) presents these curves for different load values. It is possible to observe that a higher frequency leads to a narrower voltage gain peak. The previous resonance point considered in the design methodology, for $f_s = f_0$, occurs now when L_{vi} is zero. At this point, the voltage gain is independent of load and frequency variation. In this case since the value of L_{vi} changes, so does the resonance frequency. Mathematically, resonance may occur for negative values of L_{vi}. Since a negative value of L_{vi} is not possible, it implies that the real operating region will always be a ZVS inductive region. From Fig. 7b) it can be seen that for a given voltage gain variation, ΔM, when the frequency is higher $(100\ kHz)$ the variation of inductance needed to obtain that gain variation (ΔL_{vi}) is smaller when compared to a lower frequency $(10\ kHz)$ gain curve. Therefore, for the same inductance range, a higher value of f_s will lead to a higher controllable range of the output. Increasing f_s enables circuit miniaturization and operating at constant f_s facilitates the design of the EMI filter.

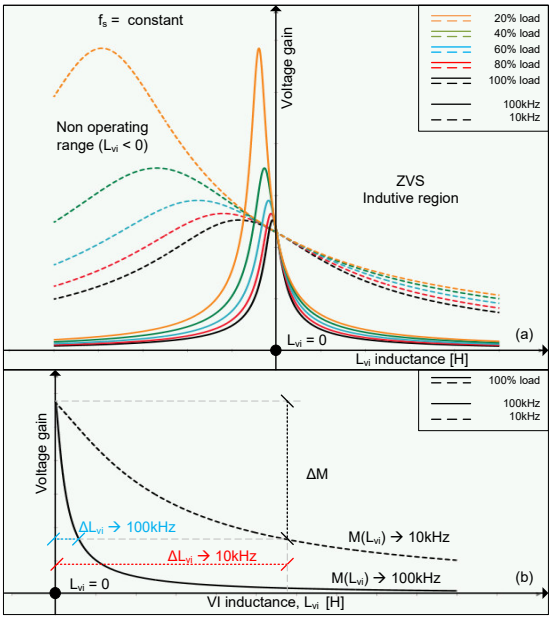

Fig. 7. Gain curves as function of L_{vi} at 10 kHz and 100 kHz: a) $M(L_{vi})$ at different load levels; b) $M(L_{vi})$ at full-load

However, this converter has inherent no-load and short-circuit protection. For short-circuit conditions, the resonant current would be limited by L_{vi}. For no-load, this current is equal to the magnetizing current of the transformer.

C. VI Control Range

In order to identify the required inductance range for the application, the output power must be calculated. Using (11) and knowing that $M = \frac{2*n*V_o}{V_{in}}$ from [7] the output converter power can be obtained as:

$$P_o = \frac{V_o^2}{R_o} = \frac{\left(\frac{V_{in}}{2n} \right)^2}{R_o} \cdot \left| M(j\omega) \right|^2 \tag{12}$$

For the LLC battery charger and considering the voltage and current profiles presented in Fig. 3, the output power for the three levels of SOC corresponding to L_{vi_0}, L_{vi_90} and, L_{vi_100} can be obtained by using (12). The results are shown in Fig. 8.

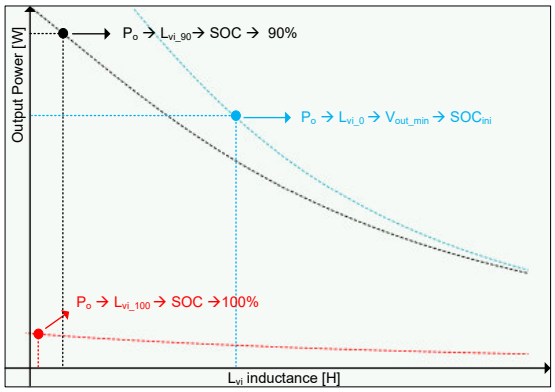

Fig. 8. Output power as function of of L_{vi}, $P_o(L_{vi})$ for the operating points corresponding to L_{vi_0}, L_{vi_90} and L_{vi_100}

By intersecting the gain curves of Fig. 8 with the defined power levels, L_{vi_0}, L_{vi_90} and, L_{vi_100} are obtained. The inductance range is defined with L_{vi_0} and L_{vi_100}. The procedure for the construction of the VI can be find in previous literature [9].

IV. Simulation Results

In order to validate the proposed topology, simulations in PSIM were carried out considering the converter parameters shown in Table I, which were obtained by applying the proposed methodology. The simulation results shown in Fig. 9 were obtained under open-loop control.

TABLE I. Converter Parameters for Simulation

Description		Specification
Main parameters		$V_{in} = 400V$; $f_s = 100kHz$; $d = 0.5$
Magnetic devices	L_{vi}	$L_{vi\_min} = 0.8\mu H$; $L_{vi\_max} = 21.1\mu H$
	Transformer	$k = 7$; $n = 1.95$
		$L_{lkp} = 15.11\mu H$; $L_{lks} = 3.97\mu H$
		$L_m = 105.75\mu H$
C_r , C_o , Load		$89.42nF$; $43\mu F$; $R_o \geq 8.4\Omega$

The simulation results are referred to operating points L_{vi_0}, L_{vi_90} and L_{vi_100} (red, green and blue, respectively) obtained from Fig. 3. Fig. 9a) and Fig. 9b) show respectively the driver signals for S1 and S2, $v_{GS1}$and v_{GS2} and the resonant filter input voltage, v_{DS2}. Fig. 9c), Fig. 9d), Fig. 9f) and Fig. 9g) show respectively the input current, i_{S1}, the current in the resonant tank, i_{Lvi}, the current in the rectifier diodes, i_D and the output current, i_{out}. Finally, Fig. 9e) and Fig. 9h) show

respectively the voltage at the VI terminals, v_{Lvi} and the output voltage, v_{out}.

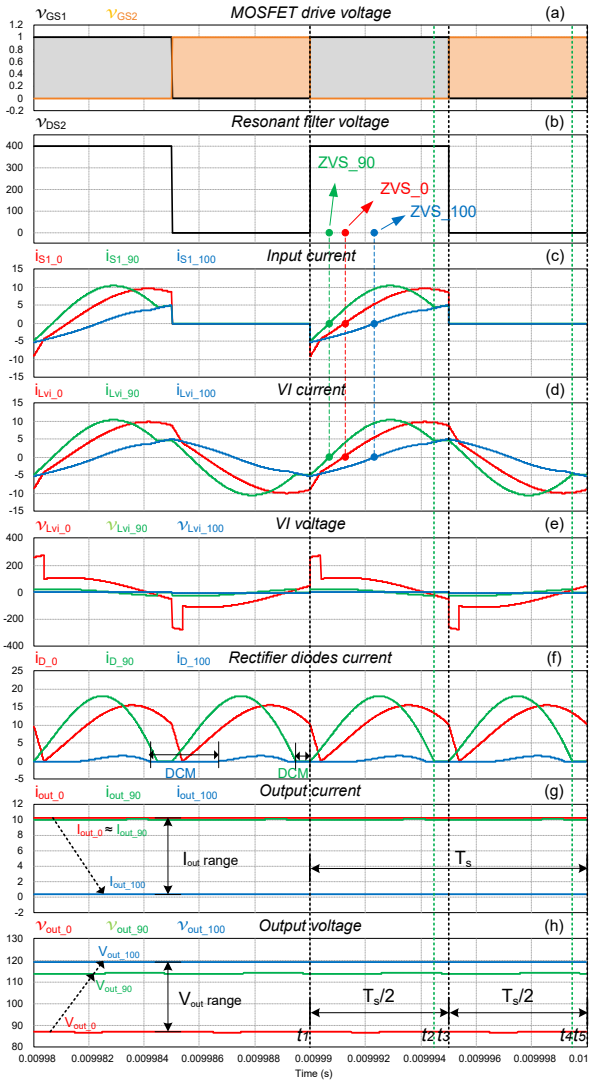

Fig. 9. Waveforms from simulation which represent the three points of operation correspondent to L_{vi_0}, L_{vi_90} and L_{vi_100}, in red, green and blue, respectively: (a) $v_{GS1}$and v_{GS2}; (b) v_{DS2} ; (c) i_{S1}; (d) i_{Lvi}; (e) v_{Lvi}; (f) i_D; (g) i_{out}; (h) v_{out}

During the CCS the range of the VI is $[L_{vi\_0}; L_{vi\_90}]$. When charging begins, $L_{vi} = L_{vi\_0}$, $I_{out} = 10A$ and $V_{out} = 84V$ which corresponds to its minimum value. When CCS ends, $L_{vi} = L_{vi\_90}$, $I_{out} = 10A$ and $V_{out} = 112{,}8V$ (SOC ≈ 90%). The controller switches from CCS to VCS, and the battery voltage increases to its maximum value, $V_{out} = 116V$ and the charging current tends naturally to its float value. At this point, $L_{vi} \rightarrow L_{vi\_100}$. The converter operates always above resonance with ZVS. When the charging process begins the rectifier diodes operate in CCM (continuous conduction mode). The analysis of i_D shows however that the converter enters in DCM (discontinuous conduction mode). When the batteries are almost fully charged the behavior of the converters tends to an open circuit and the current through the VI, i_{Lvi_100} exhibits a triangular shape waveform similar to what would be expected for the magnetizing current, i_{Lm}.

Table II shows the theoretical and simulation results for the converter design parameters defined in Table I. As can be seen the simulation results are similar to the expected theoretical results.

TABLE II. THEORETICAL AND SIMULATION RESULTS

	Theoretical				Simulation		
SOC [%]	L_{vi} [μH]	V_{out} [V]	I_{out} [A]	P_{out} [W]	V_{out} [V]	I_{out} [A]	P_{out} [W]
≈ 0	21.1	84	10	840	87.23	10.38	906
≈ 90	3.3	112.8	10	1128	114.41	10.14	1161
≈ 100	0.98	116	0.5	58	118.99	0.51	61

V. SMALL-SCALE LLC CONVERTER TEST RESULTS

In order to validate the proposed topology an experimental small-scale prototype was built using a half-bridge IGBT based inverter. The results were obtained without closed-loop control. The converter input was fed by a DC voltage source (YOKOGAWA GS610) at constant f_s. To simulate the load a Programmable DC Electronic Load was used (BK PRECISION 8522 2400W). The system specifications and converter parameters are shown in Table III. The purpose was to verify experimentally the ability to control the output of the LLC-VI. The design methodology was followed but only two operating points were considered.

TABLE III. CONVERTER PARAMETERS FOR SIMULATION AND EXPERIMENTAL PROTOTYPE

Description		Specification
Main parameters		$V_{in} = 50V$; $f_s = 11.3kHz$; $d = 0.5$
$IGBT_1$ and $IGBT_2$		SEMiX202GB066HDs ; $600V$; $274A$; $6m\Omega$
D_1 , D_2, D_3 and D_4		80EPF12 ; $V_F = 1{,}2V$; $40A$; $1200V$
Theoretical design		
Magnetic devices	L_{vi}	$L_{vi\_min} = 3\mu H$; $L_{vi\_max} = 81\mu H$
	Transformer	$k = 31$; $n = 2$
		$L_{lkp} = 7.86\mu H$; $L_{lks} = 3.14\mu H$
		$L_m = 242\mu H$
C_r , C_o , Load		$5.21uF$; $381\mu F$; $R_o = 11.6\Omega$
Simulation and experimental parameters		
Magnetic devices	L_{vi}	$L_{vi} = 14.52\mu H \rightarrow 73.785\mu H$
		$N_{ac} = 13$; $N_{dc} = 111$ (2 ×)
		ETD44/22/15 core ; $0.5mm$ gap
	Transformer	$n = 2$; $N_p = 8$; $N_s = 4$
		$L_{lkp} = 7{,}86\mu H$; $L_{lks} = 3{,}135\mu H$
		$L_m = 242\mu H$
C_r , C_o , Load		$3\mu F$; $680\mu F$; $R_o = 11.6\Omega$

The obtained simulation and experimental waveforms presented in Fig. 10 and Fig. 11, show the operation of the converter at the two VI prototype limits, L_{vimin} and L_{vimax}. For this test the load was kept constant. Fig. 10 shows v_{DS2} and, i_{Lvi} for L_{vimin} and L_{vimax}. Between these two limits the converter operates at ZVS.

Fig. 11 shows v_{in}, v_{out}, i_{Lvi} and i_{out}, for L_{vimin} and L_{vimax}. It can be seen that by adjusting the VI control current I_{dc} and regulating the inductance value it is possible to control the converter output. In Fig. 11e) the converter operates in DCM (when $i_{Lvi} = i_{Lm}$ the rectifier diodes are not conducting), and in Fig. 11f) operates in CCM. For L_{vimax} the converter operates closer to resonance since the i_{Lvi} is closer to a sinusoidal. Table IV shows the theoretical, simulation and experimental results for the small-scale prototype. As expected the simulation results are very close to the theoretical results. The experimental values exhibit some variation essentially due to coupling losses in the power transformer and due to the prototype efficiency. For current and voltage values the error between the experimental and simulation results is around 24 % and 21 %, respectively. Nevertheless at this point, it was only intended to prove the capability of this topology regarding output regulation.

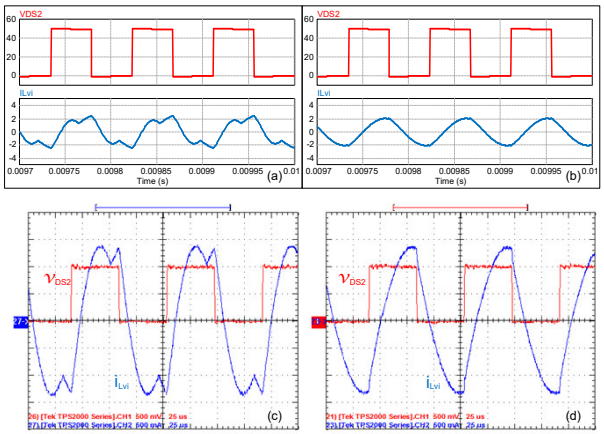

Fig. 10. v_{DS2} and, i_{Lvi}, red and blue respectively: (a) and (c) for L_{vimin}; (b) and (d) for L_{vimax}, simulation and experimental tests, respectively. Experimental results, 25V/div, 0,5A/div, 25us/div

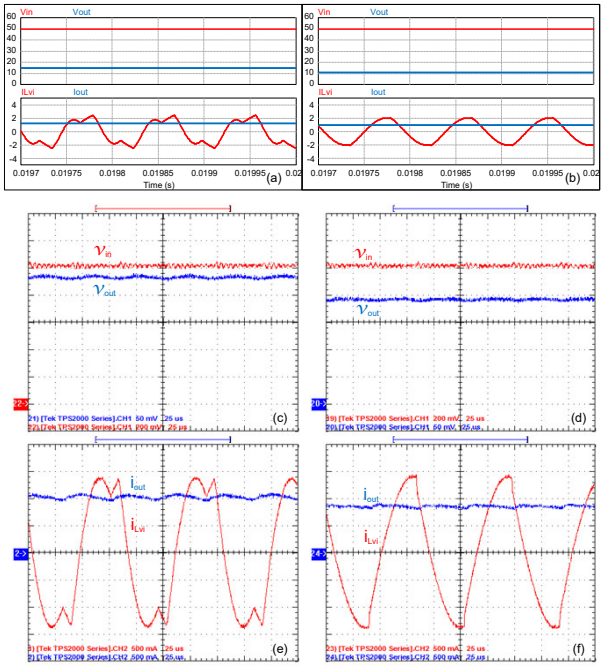

Fig. 11. v_{in}, v_{out} (red and blue, respectively), i_{Lvi} and i_{out} (red and blue, respectively): (a), (c) and (e) for L_{vimin} and (b), (d) and (f) for L_{vimax}. Experimental results v_{in} and v_{out}, 10V/div, 2.5V/div, respectively. i_{Lvi} and i_{out}, 0.5A/div, 0.5A/div respectively, 25us/div

TABLE IV. CONVERTER PARAMETERS FOR SIMULATION AND EXPERIMENTAL PROTOTYPE

VI prototype range	**Theoretical results**	**Simulation Results**			**Experimental Results**		
L_{vi} [μH]	P_{out} [W]	V_{out} [V]	I_{out} [A]	P_{out} [W]	V_{out} [V]	I_{out} [A]	P_{out} [W]
14.52	19.9	15.1	1.3	19.6	11.4	0.922	10.9
73.785	11.8	11.4	0.98	11.2	9.35	0.796	7.3

VI. CONCLUSIONS

This paper proposes an LLC resonant converter for battery charging with VI control. Two main goals were identified: the first was to explore the possibility to regulate the LLC converter output with a variable resonant tank and the second one, to apply this control technique to a battery charger. It was demonstrated that a variable inductance based LLC converter provides output power regulation and allows controlling the charging process. Taking as reference the traditional design methodology (used for frequency control) it was possible to determine the converter parameters and the required inductance range. A simple charging profile was followed, during CCS a constant output current was maintained while the V_{out} increases (with increasing SOC) and, during VCS, I_{out} tends naturally to its float value as V_{out} reaches its maximum value. In this case the inductance is used to keep a constant output voltage (as SOC reaches its maximum). A careful analysis of the methodology is presented for different switching frequencies, including the analysis of the converter output power as function of the control variable. Theoretical results were confronted with simulation and a good agreement was found. The experimental tests of the small-scale LLC-VI allowed verifying the proposed approach. Experimental waveforms are very close to the simulation ones. An output range of variation from 67% to 100% was obtained at constant frequency. In this case, a relatively small output regulation was obtained, due to poor coupling in the transformer and efficiency losses in the converter. This is the main reason why there is some distance between the experimental values (in terms of voltage and current levels) and the simulation ones. If f_s increases, the converter will be miniaturized and the range of the VI needed to obtain a specific output regulation will be smaller. A proper design of the magnetic components and the converter parameters (seeking efficiency) will lead to the expected values (according to the design methodology). In conclusion, the VI can be used to control the output of the LLC resonant converter achieving always ZVS while f_s is kept constant.

REFERENCES

[1] Y. Wang, Y. Guan, J. Huang, W. Wang and D. Xu, "A Single-Stage LED Driver Based on Interleaved Buck–Boost Circuit and LLC Resonant Converter," in *IEEE Journal of Emerging and Selected Topics in Power Electronics*, vol. 3, no. 3, pp. 732-741, Sept. 2015.

[2] Shuze Zhao, Jiale Xu and O. Trescases, "Burst-Mode Resonant LLC Converter for an LED Luminaire With Integrated Visible Light Communication for Smart Buildings," in *IEEE Transactions on Power Electronics*, vol. 29, no. 8, pp. 4392-4402, Aug. 2014.

[3] R. L. Lin and C. W. Lin, "Design criteria for resonant tank of LLC DC-DC resonant converter," *IECON 2010 - 36th Annual Conference on IEEE Industrial Electronics Society*, Glendale, AZ, 2010, pp. 427-432. doi: 10.1109/IECON.2010.5674988

[4] Z. Fang, T. Cai, S. Duan and C. Chen, "Optimal Design Methodology for LLC Resonant Converter in Battery Charging Applications Based on Time-Weighted Average Efficiency," in *IEEE Transactions on Power Electronics*, vol. 30, no. 10, pp. 5469-5483, Oct. 2015.

[5] Musavi, F.; Craciun, M.; Gautam, D.S.; Eberle, W.; Dunford, W.G., "An LLC Resonant DC–DC Converter for Wide Output Voltage Range Battery Charging Applications," in *Power Electronics, IEEE Transactions on* , vol.28, no.12, pp.5437-5445, Dec. 2013

[6] Shafiei, N.; Ordonez, M.; Craciun, M.; Botting, C.; Edington, M., "Burst Mode Elimination in High-Power LLC Resonant Battery Charger for Electric Vehicles," in *Power Electronics, IEEE Transactions on* , vol.31, no.2, pp.1173-1188, Feb. 2016.

[7] Hangseok Choi, "AN-4151, Half-Bridge LLC Resonant Converter Design Using FSFR-Series Fairchild Power Switch (FPS™)", 2007.

[8] Helen Ding, "AN-1160, Design of Resonant Half-Bridge Converter using IRS2795(1,2) Control IC", International Rectifier.

[9] M. S. Perdigao, S. F. Ferreira, M. Martins, A. S. Mendes and J. M. Alonso, "Finite element analysis of a variable inductor for an RSCC based LED lamp driver," *Industry Applications Society Annual Meeting, 2015 IEEE*, Addison, TX, 2015, pp. 1-8.

[10] C. A. Cheng, H. W. Chen, E. C. Chang, C. H. Yen and K. J. Lin, "Efficiency study for a 150W LLC resonant converter," *Power Electronics and Drive Systems, 2009. PEDS 2009. International Conference on*, Taipei, 2009, pp. 1261-1265.

[11] Hangseok Choi, " Design Considerations for an LLC resonant Converter," Farichild Power Seminar 2007